**Uniwersytet Gdański**

**Wydział Matematyki, Fizyki i Informatyki**

**Instytut Fizyki Doświadczalnej**

**Michał Mońka**

**Procesy fotofizyczne i fotochemiczne oraz efekt ciężkiego atomu w związkach organicznych wykazujących termicznie aktywowaną opóźnioną fluorescencję (TADF) i emisję indukowaną agregacją (AIE)**

**Rozprawa doktorska**

Promotor:

**dr hab. Aleksander Kubicki, prof. UG**

Promotor pomocniczy:

**dr Illia E. Serdiuk**

**Gdańsk 2022**

# Spis treści

# Wykaz skrótów oraz stosowanych oznaczeń

- ESIPT (*ang.* Excited-State Intramolecular Proton Transfer) – wewnątrzmolekularne przeniesienie protonu w stanie wzbudzonym
- AIE (*ang.* Aggregation Induced Emission) – emisja spowodowana agregacją
- TADF (*ang.* Thermally Activated Delayed Fluorescence) – termicznie aktywowana opóźniona fluorescencja
- OLED (*ang.* Organic Light Emitting Diodes) – organiczna dioda elektroluminescencyjna
- PLQY (*ang.* Photoluminescence Quantum Yield) – wydajność kwantowa fotoluminescencji [%]
- HAE – (*ang.* Heavy-Atom Effect) – efekt ciężkiego atomu
- ACQ (*ang.* Aggregation Caused Quenching) – wygaszanie spowodowane agregacją
- ISC (*ang.* Intersystem Crossing) – przejście międzysystemowe
- rISC (*ang.* Reverse Intersystem Crossing) – odwrotne przejście międzysystemowe
- $k_B$ – stała Boltzmanna [eV/K]
- $A$ – stała pre-eksponencyjna
- T – temperatura [K]
- $\Delta E_{ST}$ – przerwa energetyczna pomiędzy stanem $T^*$ i $S^*$
- SOC (*ang.* Spin-Orbit Coupling) – sprzężenie spinowo-orbitalne
- $V$ – stała sprzężenia spinowo-orbitalnego
- $^3CT$ – wzbudzony stan trypletowy utworzony przez przejście z przeniesieniem ładunku
- $^1CT$ – wzbudzony stan singletowy utworzony przez przejście z przeniesieniem ładunku
- $^3LE_D$ – wzbudzony stan trypletowy utworzony przez przejście zlokalizowane na donorowym fragmencie emitera
- $k_{rISC}$ – stała szybkości odwrotnego przejścia międzysystemowego
- $k_{ISC}$ – stała szybkości przejścia międzysystemowego
- $k_r$ – stała szybkości dezaktywacji promienistej ze stanu singletowego
- $k_{nr}$ – stała szybkości dezaktywacji bezpromienistej ze stanu singletowego
- $\lambda$ – energia reorganizacji
- $f$ – siła oscylatora
- $T^*$ – wzbudzony stan trypletowy
- $S^*$ – wzbudzony stan singletowy
- $T_1$ – pierwszy elektronowy wzbudzony stan trypletowy
- $S_1$ – pierwszy elektronowy wzbudzony stan singletowy

# Wykaz publikacji

[**P1**] M. Mońka, I. E. Serdiuk, A. Kubicki, P. Bojarski. Not only AIE: Light-sensitivity of 4-dimethylamino-2′-hydroxychalcones beneficial to highly efficient photochemical synthesis of 4′-dimethylaminoflavanones. J. Mol. Liq. 2020, 313, 113526 DOI: 10.1016/j.molliq.2020.113526

[**P2**] I. E. Serdiuk, M. Mońka, K. Kozakiewicz, B. Liberek, P. Bojarski, S. Y. Park. Vibrationally Assisted Direct Intersystem Crossing between the Same Charge-Transfer States for Thermally Activated Delayed Fluorescence: Analysis by Marcus–Hush Theory Including Reorganization Energy. J. Phys. Chem. B, 2021, 125, 10, 2696–2706 DOI: 10.1021/acs.jpcb.0c10605

[**P3**] M. Mońka, I. E. Serdiuk, K. Kozakiewicz, E. Hoffman, J. Szumilas, A. Kubicki, S. Y. Park, P. Bojarski. Understanding the internal heavy-atom effect on thermally activated delayed fluorescence: application of Arrhenius and Marcus theories for spin–orbit coupling analysis. J. Mater. Chem. C, 2022,10, 7925-7934 DOI: 10.1039/D2TC00476C

[**P4**] M. Mońka, D. Grzywacz, E. Hoffman, V. Ievtukhov, K. Kozakiewicz, R. Rogowski, A. Kubicki, B. Liberek, P. Bojarski, I.E. Serdiuk. Decisive role of heavy-atom orientation for efficient enhancement of spin–orbit coupling in organic thermally activated delayed fluorescence emitters. J. Mater. Chem. C, 2022,10, 11719-11729 DOI: 10.1039/D2TC01729F

# Streszczenie

Wraz z rozwojem technologii, urządzenia elektroniczne stały się istotnym elementem w działalności współczesnego człowieka, towarzysząc mu w większości sfer jego życia. Powszechność telefonów komórkowych, tabletów czy komputerów jest na to najlepszym dowodem. Działanie wielu z nich wiąże się z użyciem materiałów, zdolnych do emisji światła pod wpływem dostarczenia im energii z zewnątrz, co ma miejsce na przykład w wyświetlaczach. Makroskopowe cechy takich urządzeń emitujących światło jak barwa, jasność czy trwałość, są uzależnione od rodzaju użytych związków chemicznych (emiterów) i ich właściwości fotofizycznych na poziomie molekularnym. Dzięki zgromadzonej do tej pory wiedzy na ich temat, współcześnie projektowane emitery charakteryzują się bardzo dobrymi parametrami, a żywotność urządzeń zbudowanych z takich związków, nie stanowi ograniczenia w ich funkcyjności.

Problem w tym, że kluczowe materiały wszystkich powszechnie dostępnych urządzeń optoelektronicznych zbudowane są z nieorganicznych lub hybrydowych związków, zawierających w swojej strukturze ciężkie metale takie jak iryd, platynę, ziemie rzadkie itd. Ograniczony dostęp tych pierwiastków uzależniony od czynników geograficznych, politycznych i ekonomicznych to jeden z kluczowych powodów, dla którego koszty produkcji tych urządzeń są na wysokim poziomie. Co więcej, toksyczność metali przejściowych dyskwalifikuje takie materiały z niektórych z zastosowań oraz komplikuje metody ich utylizacji. W związku z powyższym, inwestycje we wdrażanie mniej szkodliwych i łatwiej dostępnych materiałów stanowią jeden z aktualnych wiodących kierunków naukowych i uznany priorytet badawczo-rozwojowy. Niestety, technologia wytwarzania urządzeń opartych o przyjazne środowisku materiały organiczne nie osiągnęła jeszcze wymaganego przez przemysł poziomu dojrzałości. Do głównych problemów przez które do tej pory nie udało się zastąpić kluczowych elementów ich organicznymi odpowiednikami należą niska wydajność oraz stabilność organicznych związków, z których buduje się komponenty takich urządzeń. Dotyczy to między innymi nowoczesnych materiałów emitujących światło będących przedmiotem badań niniejszej dysertacji.

Rozprawa doktorska dotyczy badań właściwości fotofizycznych i fotochemicznych wybranych związków organicznych emitujących światło, odznaczających się wysokim potencjałem aplikacyjnym w urządzeniach optoelektronicznych. Podstawowym jej celem jest zrozumienie mechanizmów fotoindukowanych procesów zachodzących w stanach wzbudzonych, warunkujących wydajność emisji światła oraz odpowiedzialnych za fotostabilność emiterów.

Pierwsza część pracy poświęcona jest opisowi przeprowadzonych badań nad związkami z grupy 2'-hydroksychalkonów, w których zachodzi zjawisko wewnątrzmolekularnego przeniesienia protonu w stanie wzbudzonym (ESIPT) oraz zjawisko emisji indukowanej agregacją (AIE). Pomimo bardzo atrakcyjnych właściwości fotofizycznych, molekuły te są wyjątkowo niestabilne i łatwo ulegają licznym

fotoindukowanym procesom, prowadzącym do utworzenia nowych cząsteczek, pozbawionych korzystnych cech emisyjnych. Ponieważ stabilność jest kluczowym parametrem decydującym o możliwości zastosowania związków w optoelektronice, przestawione w pracy badania dostarczają szczegółowej wiedzy o mechanizmie fotodegradacji z uwzględnieniem poszczególnych jej etapów a także sposobach jej kontroli. Używając standardowych metod doświadczalnych oraz współczesnych narzędzi teoretycznych, dokonano opisu sześcioetapowej ścieżki, składającej się wielu pojedynczych procesów takich jak transfer protonu, izomeryzacja *s-cis – s-trans* i cyklizacja. Zebrane dane i podjęte próby badawcze dowodzą temu, że reakcję można całkowicie zatrzymać na wczesnym jej etapie, co w przyszłości ułatwi wdrażanie na rynek tych (i podobnych) emiterów.

Druga część rozprawy dotyczy organicznych emiterów, w których zachodzi zjawisko termicznie aktywowanej opóźnionej fluorescencji (TADF), stanowiących w tej chwili bardzo młodą, ale dynamicznie rozwijaną klasę obiektów, głównie zorientowaną na zastosowanie w nowoczesnych OLED. Przedstawione badania koncentrują się na próbie rozwiązania aktualnego problemu w tych związkach, związanego ze zbyt wolnym odwrotnym przejściem międzysystemowym. Przedmiotem badań są niebieskie i czerwone emitery cieszące się największym zapotrzebowaniem na moment przygotowywania rozprawy. Konkretniej, doświadczalnej weryfikacji zostaje poddany koncept udoskonalenia właściwości fotofizycznych emiterów TADF, polegający na wprowadzeniu do ich struktury łatwo dostępnych ciężkich atomów w celu wzmocnienia sprzężenia spin-orbita i przyspieszenia konwersji wzbudzonych stanów trypletowych do singletowych, wskutek czego możliwa jest wydajna elektroluminescencja. Na podstawie przeprowadzonych pomiarów fotofizycznych oraz dzięki opracowanej metodologii analizy danych doświadczalnych ustalono, że tzw. efekt ciężkiego atomu, w określonych warunkach korzystnie wpływa na parametry luminescencyjne zmodyfikowanych emiterów. Za pomocą szczegółowych obliczeń teoretycznych skorelowanych z obserwacjami doświadczalnymi, określono jaki jest mechanizm zjawiska TADF i wskazano najbardziej istotne czynniki, wpływające na jego wydajność.

# Abstract

With the development of technology, electronic devices have become relevant element in activity of modern human, accompanying him in most areas of his life. Commonness of mobile phones, tablets and computers is the best proof of this. The operation of many of them is based on use of materials, that are able to emission of light when external energy is applied, which take place for example, in displays. The macroscopic features of such light-emitting devices, such as color, brightness or stability, depend on the type of chemical compounds (emitters) used and their photophysical properties at the molecular level. Thanks to the knowledge gathered so far, the currently designed emitters show very good parameters, and the lifetime of devices made of such compounds is not a limitation in their functionality.

The problem is that the key components of all commonly available optoelectronic devices are made of inorganic or hybrid compounds, containing in their structure heavy metals such as iridium, platinum, rare earths, etc. The limited access of these elements, depending on geographical, political and economic factors, is one of the key reasons why the production cost of these devices is very high. What is more, the toxicity of transition metals disqualifies such materials from some application and complicates the methods of their waste management. With respect to this, investments devoted to implementation of less harmful and more accessible materials are one of the current leading scientific directions and a well known research and development priority. Unfortunately, fabrication of friendly organic materials technology has not reached the sufficient level required by the industry. The low efficiency and stability of pure organic compounds remain currently the main problems, because of which replacement of the key elements with their organic analogs have failed so far. Especially, it is true for light-emitting materials, which are the subject of this dissertation.

The doctoral thesis is devoted to photophysical and photochemical investigations of selected organic light-emitting compounds, with high applicative potential in optoelectronic devices. The fundamental aim of this work is to understand the mechanisms of photoinduced processes occuring in excited state, which determine emission efficiency and photostability of emitters.

First part of this work is based on description of performed investigations of 2'-hydroxychalcones derivatives, which show excited-state intramolecular proton transfer (ESIPT) and aggregation induced emission (AIE). Despite showing attracvite photophysical features, these compounds are extremely unstable and can easily undergo photoinduced processes, leading to formation of molecules without beneficial emissive properties. Since stability is a crucial parameter determining the possibility of using compounds in optoelectronics, described research here provides detailed knowledge about the mechanism of photodegradation taking into account individual stages and ways to control it.

By using conventional experimental methodology and advanced theoretical tools, description of six-stage phototransformation has been made, including proton transfer, s-cis – s-trans isomerization and

cyclization processes. The collected data and undertaken attempts unambiguosly prove, that photodegradation can be stopped at its early stage, therefore it could facilitate the implementation of this (and similar) compounds in devices in the near future.

Second part of dissertation concerns organic emitters with thermally activated delayed fluorescence (TADF), being currently relatively young, but dynamically developed class of objects, mainly devoted to application in OLED industry. Presented research here is focused on solving problem in TADF compounds, related to slow reverse intersystem crossing (rISC). At the moment, red and blue emitters are strongly demanded, thus they are the subject of presented research. More precisely, the concept of improving the photophysical properties of blue and red TADF emitters based on introducing well accessible heavy atoms (HA) into their structure was experimentally verified. It assumes that incorporation of HA can enhance spin-orbit coupling (SOC) and will accelerate conversion of triplet excited states into singlet ones, from which efficient electroluminescence can occur. Based on performed photophysical measurements and thanks to originally developed analysis methodology it was evidenced that so called heavy-atom effect in some specific cases can have a positive impact on luminescent parameters of modified compounds. By using detailed theoretical calculations correlated with experimental observations, the mechanism of TADF was revealed with identification of most important factors that affects its efficiency.

# Wstęp

Za sprawą rosnącego zapotrzebowania na nowoczesne organiczne materiały o wysokiej wydajności, obecnie wiele uwagi poświęca się rozwojowi organicznej optoelektroniki. Wiele wskazuje, że sukces tej dziedziny w niedalekiej przyszłości przeniesie społeczeństwu wiele wymiernych korzyści. Jedną z nich, będzie wdrożenie do powszechnego użytku nowoczesnych organicznych urządzeń optoelektronicznych, takich jak panele fotowoltaiczne, tranzystory polowe czy wyświetlacze OLED (*Organic Light Emitting Diodes*).

Zastosowanie materiałów opartych o czysto organiczne związki posiada wiele istotnych zalet, które trudno przecenić. Do najważniejszych z nich należą: niskie koszty produkcji, wysoka dostępność pierwiastków, niska toksyczność, biokompatybilność, łatwiejsza utylizacja po zakończeniu użytkowania, oraz względnie łatwiejsze technologicznie metody produkcji. Wymienionych cech absolutnie nie można przypisać materiałom nieorganicznym, do budowy których używa się pierwiastków metali szlachetnych (takich jak np. iryd i platyna). Dlatego, w dzisiejszych czasach, kiedy problemy zanieczyszczenia środowiska oraz oddziaływanie szkodliwych związków na człowieka stają się coraz bardziej odczuwalne w skutkach, inwestycje we wdrażanie mniej toksycznych materiałów stanowią jeden z wiodących kierunków technologicznych i uznany priorytet badawczo-rozwojowy.

Z drugiej strony, parametry współczesnych organicznych urządzeń optoelektronicznych niestety wciąż nie są na wystarczającym dla wdrożenia poziomie. Ich niska wydajność oraz stabilność są głównymi problemami, przez które do tej pory nie udało się zastąpić kluczowych elementów urządzeń, ich organicznymi odpowiednikami, co dotyczy między innymi nowoczesnych materiałów emitujących światło (emiterów), będących obiektem badań niniejszej rozprawy. Należy wyraźnie podkreślić, że obie wymienione przeszkody wynikają wprost z właściwości fotofizycznych i fotochemicznych organicznych związków, których używa się do budowy warstw emisyjnych urządzeń. Dlatego, problem względnie słabych parametrów w organicznych związkach emitujących światło (względem nieorganicznych materiałów) musi być rozwiązany jeszcze na poziomie molekularnym.

Rozprawa doktorska dotyczy badań właściwości fotofizycznych i fotochemicznych wybranych związków organicznych emitujących światło, o wysokim potencjale aplikacyjnym. Podstawowym celem pracy jest zrozumienie mechanizmów fotoindukowanych procesów w stanach wzbudzonych, warunkujących wydajność emisji światła oraz odpowiedzialnych za fotostabilność emiterów.

Rozprawa została podzielona na dwie części: pierwsza część dotyczy grupy związków, w których zachodzi zjawisko wewnątrzmolekularnego przeniesienia protonu w stanie wzbudzonym (ESIPT) oraz zjawisko emisji indukowanej agregacją (AIE). Badaniami zostały objęte pochodne 2'- hydroksychalkonów, które dzięki swoim unikalnym właściwościom emisyjnym, stanowią obiecującą grupę fluoroforów, o szerokim zastosowaniu, np. w laserach organicznych [1, 2]. Jednakże,
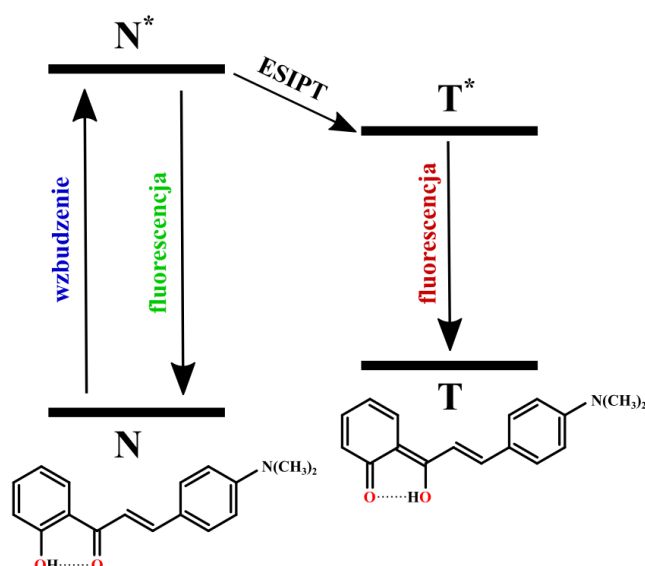
w niektórych środowiskach o niskiej lepkości (zwłaszcza w roztworach), molekuły te łatwo ulegają licznym fotoindukowanym procesom (m. in. fotoizomeryzacja cis-trans), prowadzącym do utworzenia nowych cząsteczek, pozbawionych (lub o zmienionych) konkretnych właściwości emisyjnych. Ponieważ stabilność jest kluczowym parametrem decydującym o możliwości zastosowania związków w optoelektronice, wiedza o tym w jaki sposób można wpłynąć na wydajność (i ją kontrolować) konkretnych niepożądanych reakcji, może w przyszłości ułatwić i przyspieszyć wdrażanie na rynek tych (i podobnych) emiterów. Bez szczegółowej wiedzy o mechanizmie tych reakcji, trudno jednak wyobrazić sobie jakiekolwiek świadome działania, zmierzające w kierunku poprawy parametrów w tych związkach. Dlatego celem badań w tej grupie związków jest identyfikacja produktów wspomnianych fotoreakcji, określenie jej wydajności oraz wskazanie czynników mogących potencjalnie ją zahamować. Ponadto, używając współczesnych teoretycznych narzędzi chemii kwantowej, została zaproponowana najbardziej prawdopodobna ścieżka fotodegradacji, obejmująca struktury stanów pośredniczących. Szczegółowy opis badań z ich wynikami znajduje się w pracy **P1**.

Druga część rozprawy poświęcona jest opisowi przeprowadzonych badań nad organicznymi emiterami, w których dochodzi do zjawiska termicznie aktywowanej opóźnionej fluorescencji (TADF). Szczególnie duża (i wciąż rosnąca) uwaga, jaką od kilku lat poświęca się emiterom TADF jest wynikiem kombinacji wielu zalet, które łączą w sobie te związki sprawiając, że stanowią one w tej chwili osobną i dynamicznie rozwijaną klasę obiektów, głównie zorientowaną na zastosowanie w OLED. Jednakże, parametry zdecydowanej większości znanych organicznych emiterów TADF wciąż nie są na wdrożeniowym i satysfakcjonującym odbiorców poziomie. Ich krótka żywotność w OLED to aktualnie największy problem z jakim trzeba się mierzyć. Aby materiały TADF osiągnęły dostatecznie wysoki poziom gotowości technologicznej, której wymaga przemysł, niezbędna jest szczegółowa wiedza o mechanizmie tego zjawiska, na podstawie której będzie możliwe sformułowanie odpowiedzi na podstawowe i bardzo ogólne pytanie: jak projektować wydajne, stabilne i w pełni organiczne materiały emisyjne wykorzystujące zjawisko TADF? Aktualnie, brak wystarczającej ilości systematycznych i podstawowych badań nad mechanizmem, uniemożliwia zbudowanie spójnej teorii o TADF, a dotychczasowo opracowany tzw. trójpoziomowy model posiada dużo ograniczeń i w opinii autora tej rozprawy stanowi raczej „przedmiot umiarkowanego sporu”, niż kompletny i solidny aparat matematyczny zdolny dalej rozwijać dziedzinę zaawansowanych organicznych materiałów emisyjnych. Zgodnie z powyższym, celem podjętych badań w tej grupie związków jest przede wszystkim dostarczenie doświadczalnych danych o zjawisku TADF na przykładzie najbardziej obiecujących emiterów, propozycja sposobu udoskonalenia ich właściwości fotofizycznych wraz z jego weryfikacją a także wytłumaczenie obserwowanych efektów za pomocą współczesnych narzędzi teoretycznych (obliczeń kwantowo-chemicznych). Realizacja wymienionych zadań, które zostały szczegółowo opisane w **P2, P3 i P4**, pomoże w sformułowaniu jasnych i spójnych zasad projektowania molekularnego, przyczyniając się do lepszego zrozumienia mechanizmu i w przyszłości skonstruowaniu

kompletnego modelu dla organicznych związków wykorzystujących w swoim działaniu zjawisko TADF.

# Część I. Emitery z ESIPT i AIE

Jednym z poważniejszych problemów w konstruowaniu współczesnych urządzeń emitujących światło, opartych o organiczne związki jest zjawisko znacznego spadku wydajności kwantowej fotoluminescencji (PLQY) spowodowane agregacją molekuł, która zazwyczaj ma miejsce w ośrodkach stałych (ACQ – Aggregation Caused Quenching) [3]. Większość znanych fluoroforów ulega temu zjawisku, niekorzystnemu z punktu widzenia zastosowania w optoelektronice. Pochodne 2'-hydroksychalkonów należą do nielicznej grupy związków, wykazujących odwrotny efekt (AIE - Aggregation Induced Emission) od wyżej wymienionego: kryształy tych związków odznaczają się znacznie wyższą wartością PLQY w porównaniu do ich roztworów [4, 5]. Te interesujące właściwości sprawiają, że takie obiekty (w fazie sztywnej) są szczególnie interesujące pod względem aplikacji optoelektronicznych jako emiterów w OLED [6-9], w tym szczególnie w zakresie bliskiej podczerwieni (NIR) [10, 11].



**Rys. 1.** Ogólny schemat dla zjawiska ESIPT i struktura pochodnej 2'-hydroksychalkonu w odpowiadających jej dwóch formach: **N** i **T**.

Z drugiej strony, 2'-hydroksychalkony wykazują ciekawe właściwości nie tylko w ośrodkach sztywnych. W roztworach, związki te ulegają zjawisku wewnątrzmolekularnego przeniesienia protonu w stanie wzbudzonym (ESIPT), które może zachodzić wzdłuż wiązania wodorowego, utworzonego pomiędzy donorem i akceptorem wodoru [12-14]. W wielu wypadkach, reakcję ESIPT klasyfikuje się jako proces bardzo szybki (dzięki brakowi bariery stała szybkości $k_{ESIPT} > 10^{12}$ s$^{-1}$) [15], który jak przedstawiono na **Rys. 1**, pod wpływem wzbudzenia cząsteczki zazwyczaj prowadzi do utworzenia dwóch wzbudzonych jej form (**N**$^*$ oraz **T**$^*$)**,** z których możliwa jest dezaktywacja promienista (fluorescencja) do stanu podstawowego (**N** i **T**). Z tego powodu, emisja światła ma zazwyczaj charakter dualny, tzn. widmo fluorescencji składa się z dwóch pasm, których maksima są wyraźnie odseparowane od siebie, a ich wzajemna odległość zależy przede wszystkim od energii wzbudzonych poziomów energetycznych form **N**$^*$ i **T**$^*$. Ponieważ proces przeniesienia protonu w stanie wzbudzonym jest ekstremalnie wrażliwy na warunki środowiska w którym zachodzi, obiekty ulegające temu zjawisku znalazły mnóstwo szerokich aplikacji w różnych dziedzinach. Do najbardziej znanych przykładów z literatury należą między innymi zastosowania związków z ESIPT w chemii analitycznej jako sensorów

i markerów fluorescencyjnych, pozwalających wykrywać konkretne substancje [16-19]. Ponadto, dzięki korzystnie dużemu przesunięciu Stokesa, minimalizującego efekty reabsorpcji, fluorofory z ESIPT stosuje się w badaniach obiektów biologicznych, gdzie są wykorzystywane między innymi do obrazowania [20-23]. Poza tym, niektóre z podobnych związków wykazują spory potencjał aplikacyjny w bateriach słonecznych a także w materiałach emisyjnych, w tym także emitujących białe światło (dzięki dwupasmowej fluorescencji) [24-28].

Poza opisanymi wyżej zjawiskami, 2'-hydroksychalkony w roztworach bardzo łatwo ulegają innym fotoindukowanym bezpromienistym procesom (fotoizomeryzacja trans-cis, obroty wokół pojedynczych wiązań C-C, oraz cyklizacja) [29], co zostało podkreślone we wcześniejszych pracach [30-32]. Zróżnicowane preferencje relaksacyjne 2'-hydroksychalkonów stanowią spore wyzwanie dla inżynierii materiałowej, gdyż wiele z fotoindukowanych procesów wiąże się z nieodwracalnymi (lub częściowo odwracalnymi) zmianami w ich strukturze i utratą lub zmianą pierwotnych właściwości. Ponieważ współcześnie wiele etapów wytwarzania urządzeń optoelektronicznych przebiega w ośrodkach o niskiej lepkości (np. w roztworach – *solution processing*), tym bardziej należy zwrócić szczególną uwagę na możliwości występowania procesów pobocznych, prowadzących do fotodegradacji. Dogłębne zrozumienie jej mechanizmu oraz sformułowanie spójnych wniosków dotyczących sposobów eliminacji niepożądanych procesów, stanowi główną motywację do podjęcia badań w celu udoskonalania organicznych emiterów światła, co zostało opisane szczegółowo w pracy **P1**.

## Wybór obiektów i dane doświadczalne

Do badań nad fotostabilnością 2'-hydroksychalkonów zostały wybrane związki, których struktury przedstawione zostały na **Rys. 2**.
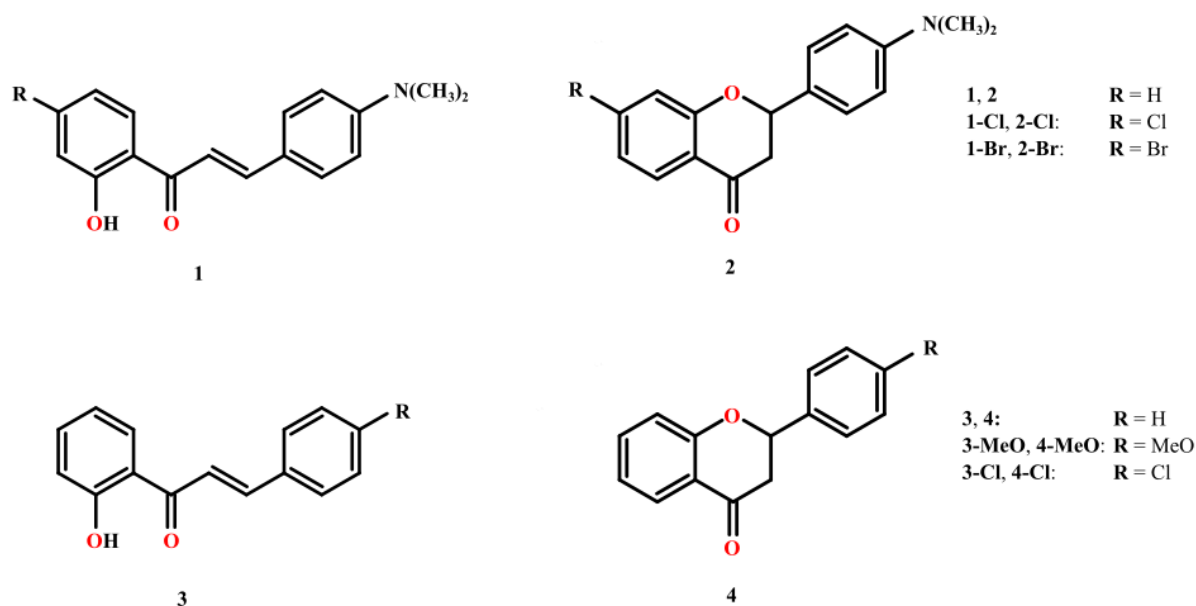
**Rys. 2.** Struktury badanych związków.

Zaczynając od doświadczalnych dowodów, w pierwszym kroku przeprowadzono test fotostabilności 4′-dimethylamino-2-hydroksychalkonu (**1**) w roztworach dichlorometanu (DCM) i cykloheksanu (CH), polegający na ciągłym jego naświetlaniu światłem monochromatycznym i kontroli postępu fotoreakcji za pomocą pomiarów absorpcji oraz chromatografii cienkowarstwowej (TLC). Widoczny spadek głównego pasma absorpcji (którego maksimum przypada w okolicach 410 nm i 445 nm odpowiednio dla roztworów w CH i DCM) oznacza zmianę koncentracji związku wyjściowego **1** (a więc jego
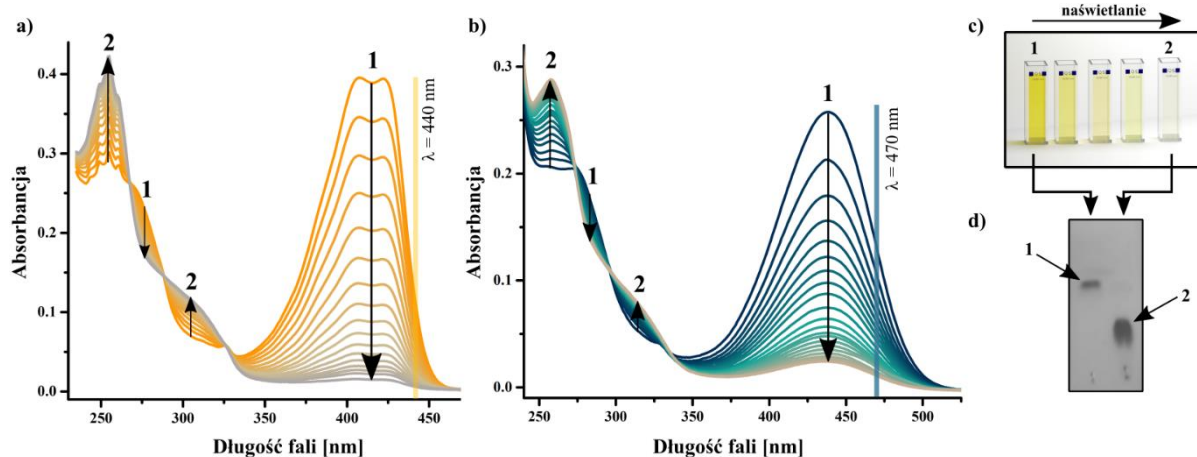


**Rys. 3.** Zmiany w pomiarach absorpcji podczas procesu naświetlania roztworu **1** w CH (**a**) i DCM (**b**), widoczna i kontrola na papierku TLC.

fotodegradację), natomiast narastające pasmo (widoczne w ok. 250 nm i 305 nm) jest spowodowane tworzeniem się nowego produktu **2**, który został wyizolowany i zidentyfikowany za pomocą metod chromatograficznych, spektrometrii masowej (LCMS) oraz protonowego jądrowego rezonansu magnetycznego ($^1$H NMR) jako 4'-dimethyloaminoflavanon (**2**). Rejestrując zmiany w absorpcji

degradującego **1** w funkcji czasu stwierdzono, że jest to reakcja kinetyczna pierwszego rzędu, której szybkość wyraźnie zależy od polarności: degradacja zachodzi prawie dwukrotnie szybciej w CH, niż w polarnym DCM. Co interesujące, powstały produkt **2** poddany dalszej ekspozycji na światło z zakresu UV (254nm) również ulega fototransformacji, prowadzącej w znacznej części (87%) do utworzenia związku wyjściowego **1**. Na podstawie tych obserwacji sformułowano wniosek, że reakcja **1→2** jest odwracalna a kierunek jej przebiegu zależy od długości fali światła, na którego działanie zostaje wystawiony roztwór. Analogicznie, na podstawie analiz LCMS i $^1$H NMR stwierdzono, że 2'-hydroksychalkon (**3**) i inne jego pochodne (**3-MeO** i **3-Cl**) także ulegają fotodegradacji do flawanonów (**4**, **4-MeO** i **4-Cl**).

Badanie mechanizmu fotodegradacji **1** rozpoczęto od stacjonarnych pomiarów fotoluminescencji. Jak wspomniano wcześniej, obecność dwóch pasm widocznych na widmie fluorescencji przedstawionym na **Rys. 4**, wynika ze zjawiska ESIPT, któremu ulega **1**. Utworzenie formy tautomerycznej (**T***) w stanie wzbudzonym, objawia się obecnością dodatkowego pasma, którego maksimum emisji jest przesunięte w stronę długofalową względem formy **N***.
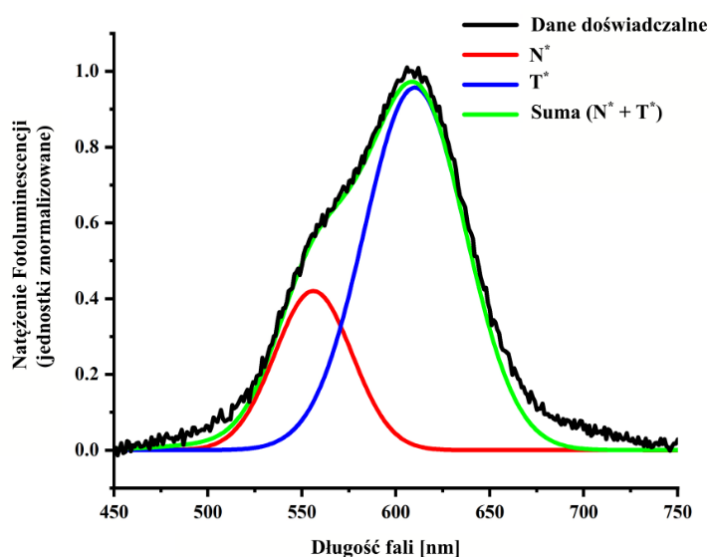


**Rys. 4.** Zarejestrowane widmo fluorescencji dla **1** w roztworze DCM.

W celu weryfikacji, czy ESIPT bierze udział w fotodegradacji **1**, badaniu fotostabilności poddano pochodne **1**, do których wprowadzono ciężkie atomy w celu przyspieszenia przejścia międzysystemowego (ISC) w tych związkach (**1-Cl**, **1-Br**), wywołanego tzw. efektem ciężkiego atomu [33]. Ponieważ nie stwierdzono znaczących zmian we właściwościach fotofizycznych i fotochemicznych tych pochodnych, a związki **1-Cl** i **1-Br** również ulegają fotodegradacji, od doświadczalnej strony można

sugerować bezkonkurencyjność ESIPT, jego kluczową rolę w mechanizmie fotodegradacji i wykluczyć znaczącą rolę stanów trypletowych w jej przebiegu.

## Obliczenia teoretyczne

Z uwagi na brak możliwości szczegółowego zbadania dalszych ścieżek fotodegradacji obejmujących stany pośrednie za pomocą dostępnych metod eksperymentalnych, analiza kolejnych etapów fotoreakcji **1→2** została przeprowadzona z wykorzystaniem narzędzi teoretycznych, w tym przypadku obliczeń DFT (Density Functional Theory).

W pierwszym kroku za pomocą optymalizacji struktury **1** ustalono, że w stanie podstawowym $S_0$, uprzywilejowaną termodynamicznie formą **1** jest $N_{s\text{-}cis}$, jak przedstawiono na **Rys. 5**. Następnie udało się potwierdzić, że bezpośrednio po wzbudzeniu ($N_{s\text{-}cis} \rightarrow N^*_{s\text{-}cis}$) do stanu $S_1$, ESIPT ($N^*_{s\text{-}cis} \rightarrow T^*_{Z,E}$) jest procesem bezbarierowym i dlatego, w zestawieniu z innymi możliwymi bezpromienistymi procesami w stanie wzbudzonym (ISC, izomeryzacja), stanowi najbardziej energetycznie korzystną ścieżkę prowadzącą do utworzenia wzbudzonej formy tautomerycznej $T^*_{Z,E}$. Jest to zgodne z ww. danymi doświadczalnymi. Po utworzeniu $T^*_{Z,E}$, cząsteczka poprzez obrót wokół kąta torsyjnego D1 o 90° ($T^*_{Z,E} \rightarrow T^*_{twist}$), łatwo może przejść do stanu podstawowego ($T^*_{twist} \rightarrow T_{twist}$), dzięki przecinaniu się powierzchni energii potencjalnych w tym punkcie (tzw. *conical intersection*). Z tego miejsca w stanie podstawowym, możliwe są dwie ścieżki o bliskim prawdopodobieństwie dzięki braku barier energetycznych:

1) Powrót do formy tautomerycznej ($T_{twist} \rightarrow T_{Z,E}$) czemu odpowiada zmniejszenie kąta D1 do pierwotnej wartości ok. 0°, z dalszym odwrotnym przeniesieniem protonu w stanie podstawowym ($T_{Z,E} \rightarrow N_{s\text{-}cis}$) i powrotem do formy $N_{s\text{-}cis}$. Ta ścieżka nie wywołuje więc fotodegradacji.

2) Dalsze zwiększanie kąta D1 do wartości 180° ($T_{twist} \rightarrow T_{E,E}$), a następnie izomeryzacja *s-cis – s-trans* oraz cyklizacja. Chociaż izomeryzacja jest wyraźnie procesem endotermicznym, ($\Delta G[T_{s\text{-}trans} - T_{E,E}] = +25.1$ kJ/mol) to następująca po nim cyklizacja ($T_{s\text{-}trans} \rightarrow 2_{PT}$) prowadząca do $2_{PT}$ ostatecznie obniża energię układu ($\Delta G[2_{PT} - T_{E,E}] = -5.1$ kJ/mol). Ostatnim etapem na ścieżce **1**→**2** jest transfer protonu ($2_{PT} \rightarrow 2$), prawdopodobnie przez efekt tunelowy wskutek dużej bariery energetycznej.
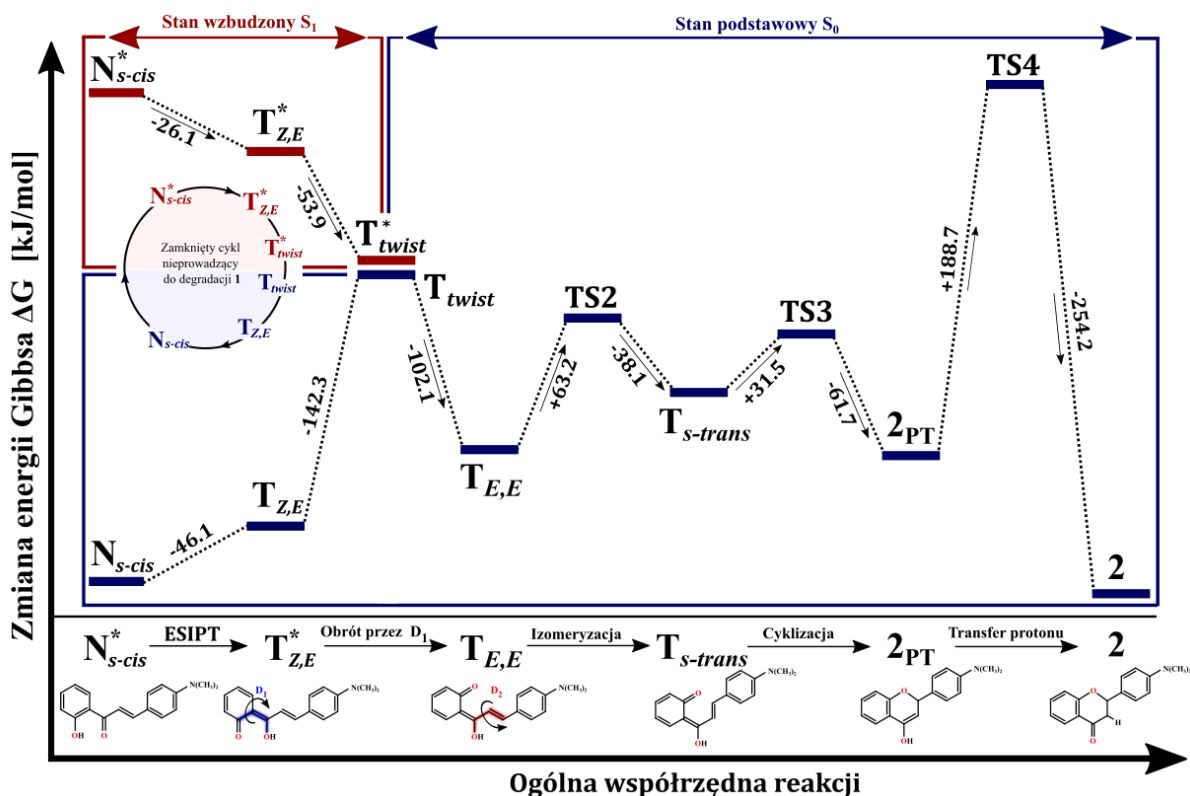
**Rys. 5.** Ogólny schemat fotoreakcji **1→ 2** z uwzględnieniem struktur w poszczególnych jej etapach

Znając wszystkie etapy szlaku fotodegradacji **1** (**Rys. 5**), zwrócono szczególną uwagę na dwa procesy, w których dochodzi do redystrybucji lub rozerwania wewnątrzcząsteczkowego wiązania wodorowego: ESIPT: ($N^*_{s\text{-}cis} \rightarrow T^*_{Z,E}$) oraz obrót wokół kąta D1 ($T^*_{Z,E} \rightarrow T_{E,E}$). Wiadomo, że niektóre protyczne rozpuszczalniki (jak np. MeOH) są zdolne do tworzenia kompleksów poprzez międzymolekularne wiązania wodorowe, mogąc potencjalnie wpływać na wysokość bariery energetycznej wyżej wymienionych dwóch procesów [34, 35].  Sugerując się tym, przeprowadzono test fotostabilności **1** z dodaniem śladowych ilości MeOH do roztworu. W wyniku naświetlania roztworu **1** w DCM z 1% MeOH nie stwierdzono fotodegradacji (**Rys. 6a**). Aby rozstrzygnąć, czy drastyczny wzrost fotostabilności **1** jest wynikiem zahamowania ESIPT ($N^*_{s\text{-}cis} \rightarrow T^*_{Z,E}$), przeprowadzono pomiar widma fotoluminescencji dla tego roztworu (**Rys. 6b**). Ponieważ na zarejestrowanym widmie wyraźnie widoczne jest pasmo pochodzące od formy **T***, dlatego stwierdzono, że fotodegradacja nie jest hamowana na etapie zjawiska ESIPT.
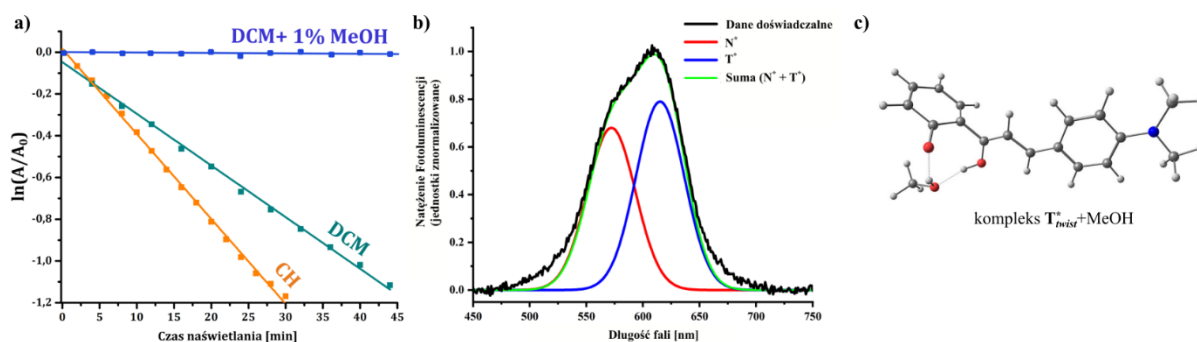
**Rys. 6. a)** wykres przedstawiający zmiany w absorpcji dla badanych roztorów **1** pod wpływem oświetlania w funkcji czasu, **b)** zarejestrowane widmo fotoluminescencji **1** z dodaniem 1% MeOH, **c)** zoptymalizowana struktura kompleksu $T^*_{twist}$ z MeOH.

Na podstawie obliczeń ustalono, że utworzenie międzycząsteczkowych wiązań wodorowych pomiędzy $T^*_{twist}$ (**Rys. 6c**) utrudnia formację $T_{E,E}$ i tym samym przyczynia się do wzrostu fotostabilności **1** (szczegóły w pracy **P1**). Obecność protycznych cząsteczek w zasięgu molekuł **1** należy więc wskazać jako jeden ze sposobów na eliminacje drastycznej wrażliwości **1** na światło, co może być stosowane w procesie technologicznym.

Ekspozycji na światło zostały również poddane kryształy **1** (a także kryształy jego pochodnych: **1-Cl** i **1-Br**), jednakże nie stwierdzono w nich żadnych zmian we właściwościach fotofizycznych przed i po przeprowadzonej próbie fotostabilności, co stanowi o braku wrażliwości na światło tych związków, tworzących agregaty w fazie krystalicznej. Dzięki temu, usztywnienie struktury w fazie krystalicznej w 2'-hydroksychalkonach nie tylko przyczynia się do poprawy ich właściwości emisyjnych poprzez zjawisko AIE, ale także zapewnia im wysoką fotostabilność.

# Część II. Emitery do OLED na bazie organicznych związków z TADF

Organiczne diody elektroluminescencyjne (OLED) stanowią jeden z najbardziej fascynujących przykładów współczesnych zastosowań materiałów organicznych w elektronice. Widoczny postęp w branży nowoczesnych wyświetlaczy i giętkich paneli dotykowych jest rezultatem progresywnych badań m. in. fotofizycznych, mających podstawowe znaczenie dla rozwoju tej dziedziny. W obszarze powierzchniowych źródeł światła, pośród różnych technologii konwersji energii elektrycznej w świetlną, obecnie największe oczekiwania wiąże się z OLEDami.

W porównaniu do aktualnie rozpowszechnionych (chociaż sukcesywnie wypieranych z obiegu) wyświetlaczy LCD (Liquid Crystal Display), OLED są lepsze zarówno pod względem parametrów fotometrycznych jak i fizycznych [36]. Wśród tych pierwszych, do największych zalet OLED należą, wysoki kontrast kolorów, szeroki kąt widzenia, krótki czas reakcji matrycy. Ponadto, w OLED nie występuje problem odwzorowania „pełnej czerni", ponieważ piksele nie potrzebują dodatkowego podświetlenia, jak ma to miejsce w przypadku ekranów LCD, co wpływa także na wyższą energooszczędność OLED [37, 38]. Mając na uwadze właściwości fizyczne, wyświetlacze OLED mogą przyjmować różne kształty, są znacznie cieńsze niż LCD, a związki, na bazie których konstruuje się kluczowe komponenty urządzeń, są łatwiejsze pod względem preparatyki zarówno w procesie wytwarzania (np. na etapie wytwarzania urządzeń pojawia się możliwość stosowania bardziej oszczędne metody, tzw. *solution processing* [39]), jak i w ich późniejszej utylizacji.

Jednakże, pomimo istotnej przewagi OLED nad alternatywnymi rozwiązaniami, technologii tej daleko do doskonałości: aktualnie przez obecność ciężkich metali w ich konstrukcji. Należy wyraźnie podkreślić, że emitery w obecnych na rynku urządzeniach OLED, oparte są głównie na nieorganicznych kompleksach, zawierających przeważnie iryd lub platynę [40] (z chemicznego punktu widzenia nie są to w pełni organiczne związki a nazewnictwo OLED jest tu wynikiem pewnego marketingowego uproszczenia). Konieczność stosowania ciężkich metali wynika przede wszystkim z potrzeby uzyskiwania wymaganego wysokiego **poziomu stabilności oraz wydajności urządzeń, którego nie osiągnęły jeszcze OLEDy na bazie w pełni organicznych związków**. Z drugiej strony, jak wspomniano we wstępie, użycie nieorganicznych materiałów wpływa między innymi na zdecydowanie wyższe koszty produkcji OLED i późniejszej ich utylizacji, ponieważ są to pierwiastki o ograniczonym dostępie, uzależnionym od czynników geograficznych, ekonomicznych i politycznych.

Problem niskiej stabilności i wydajności w organicznych OLED wynika wprost z właściwości fotofizycznych związków, których użyto do budowy warstwy emisyjnej urządzenia. Dlatego problem względnie słabych parametrów w organicznych OLED (widoczny szczególnie w niebieskim oraz czerwonym zakresie), musi być rozwiązany na poziomie molekularnym.

W urządzeniach emitujących światło, stan wzbudzony emitera (nazywany ekscytonem) osiąga się dzięki rekombinacji nośników ładunku: elektronu (ujemnego) oraz dziury (dodatniego). W zależności od konfiguracji spinowej ekscytonu, można wyróżnić wzbudzony stan singletowy ekscytonu $S^*$ oraz wzbudzony stan trypletowy $T^*$. Wykazano, że udział ekscytonów singletowych $S^*$ i trypletowych $T^*$ zawsze wyraża się proporcją 1:3 tzn. na każde 100 rekombinujących elektronów, produkowanych jest 25 ekscytonów $S^*$ i 75 ekscytonów $T^*$. Z fizycznego punktu widzenia, oba rodzaje powstałych stanów wzbudzonych wykazują odmienne preferencje procesów relaksacyjnych: w warunkach temperatury pokojowej, w czysto organicznych związkach, na ogół jedynie stany singletowe zdolne są do dezaktywacji promienistej, podczas gdy wydajność przejść promienistych ze stanów trypletowych jest o kilka rzędów mniejsza (stany trypletowe nie są wydajnym źródłem przejść, którym towarzyszy emisja światła – fosforescencja jest procesem zabronionym). W takim wypadku, 75% rekombinujących par nośników ładunku ulega bezpromienistej dezaktywacji do stanu podstawowego, a energia niezbędna do utworzenia stanu wzbudzonego jest bezpowrotnie tracona. W związku z powyższym powstają dwa istotne problemy:

1) Po pierwsze, bazując tylko na konwersji ekscytonów singletowych, tzw. wewnętrzna wydajność kwantowa $\eta_{int}$ może przyjmować wartość co najwyżej 25%, **co stanowi ograniczenie co do wydajności świecenia** OLED.

2) Po drugie, w materiałach organicznych, stany trypletowe są z reguły stanami długożyjącymi. Długi czas życia stanów wzbudzonych powoduje nagromadzenie ekscytonów, co sprzyja występowaniu innych procesów fotofizycznych, konkurencyjnych do pożądanych przejść promienistych. W szczególności, część z nich odpowiada za nieodwracalne zmiany w strukturze emiterów prowadząc do utraty ich funkcji co **przyczynia się do krótkiej żywotności OLED** [41].

Znakiem tego, ukształtowały się III główne strategie projektowania emiterów, różniące się między sobą mechanizmem utylizowania stanów trypletowych i sposobem pozyskiwania przejść promienistych.

Historycznie, tzw. pierwsza generacja OLED, zapoczątkowana przez Tang i Slyke [42] w 1987 roku, oparta była na konwencjonalnych organicznych fluoroforach, w których do generacji światła wykorzystuje się jedynie krótko żyjące stany singletowe $S_1$, pozyskiwane bezpośrednio z rekombinacji nośników ładunku. W przytaczanej pracy, zaprezentowano urządzenie oparte o tri-8-hydroxyquinoline aluminium (Alq$_3$) emitujące zielone światło ($\lambda_{max}$ = 550nm) z wydajnością $\eta_{ext}$ wynoszącą ok. 1%, i krótką żywotnością (30% spadek intensywności świecenia w ciągu 10h).

Do tzw. II generacji OLED należą urządzenia oparte na związkach, będących najczęściej kompleksami organo-metalicznymi, w których generacja światła może zachodzić bezpośrednio ze wzbudzonego stanu trypletowego $T_1$. Stany singletowe nie biorą bezpośredniego udziału w emisji, ponieważ obecność ciężkich metali powoduje natychmiastową konwersję $S^* \rightarrow T^*$. Aby w temperaturze pokojowej,

dezaktywacja promienista (fosforescencja) ze stanu $T_1$ charakteryzowała się względnie wysoką wydajnością, konieczne jest wprowadzenie pierwiastków metali przejściowych (iryd, platyna) do struktury takiego emitera. Jednym z pierwszych urządzeń opartych o fosforyzujący emiter, będący kompleksem porfirynowo-platynowym, zostało zaprezentowane w 1998 przez grupę S. R. Forresta i charakteryzowało się czerwoną emisją z wydajnością odpowiednio $\eta_{int}$=23.0 % i $\eta_{ext}$ = 4%. W roku 2001 Adachi i inni opublikowali pracę, w której przedstawili urządzenie oparte na fosforyzującym emiterze z imponującą wydajnością $\eta_{ext}$=19.0 % (i odpowiadającą $\eta_{int}$ = 87%).

## Zjawisko TADF
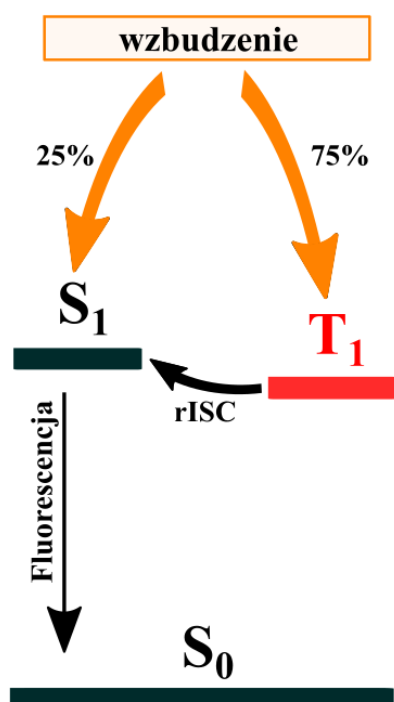


**Rys. 7.** Ogólny schemat zjawiska TADF

Jednym z najnowszych i póki co najbardziej obiecującym rozwiązaniem problemu użycia trypletowych ekscytonów w materiałach organicznych, jest użycie związków, w których przejścia pomiędzy stanami o różnej multipletowości z $T^*$ do $S^*$ zachodzą w zakresie mikro- i nanosekundowym. Aktualnie, od 2012 roku najlepszymi kandydatami do tego są organiczne związki, w których zachodzi zjawisko termicznie aktywowanej opóźnionej fluorescencji (ang. TADF – Thermally Activated Delayed Fluorescence) [43]. Urządzenia na bazie tych związków, w literaturze zyskały miano tzw. III generacji OLED [44].

Zjawisko TADF polega na emisji światła z najniższego stanu singletowego (fluorescencja), którą poprzedza tzw. odwrotne przejście międzysystemowe (rISC – reverse intersystem crossing) ze stanu trypletowego, występującego tu roli stanu pośredniego (**Rys. 7**). Dzięki temu, teoretycznie można „odzyskać" całą energię elektrycznego wzbudzenia, zmagazynowaną w stanach trypletowych. W celu osiągnięcia jak największej wydajności konwersji stanów $T^*$ do $S^*$, dąży się do maksymalizacji szybkości procesu rISC, którą mierzy się stałą $k_{rISC}$ [45]:

$$k_{rISC} = A \cdot e^{-\frac{\Delta E_{ST}}{k_B T}}, \tag{1}$$

gdzie:

- $k_B$ – stała Boltzmanna
- $A$ – stała pre-eksponencyjna,
- T – temperatura
- $\Delta E_{ST}$ – przerwa energetyczna pomiędzy stanem $T^*$ i $S^*$.

Zgodnie ze wzorem (1), aby w związkach nie zawierających ciężkich atomów, TADF zachodził dostatecznie wydajnie, różnica energii $\Delta E_{ST}$ pomiędzy stanem $T^*$ a $S^*$ powinna być możliwie jak
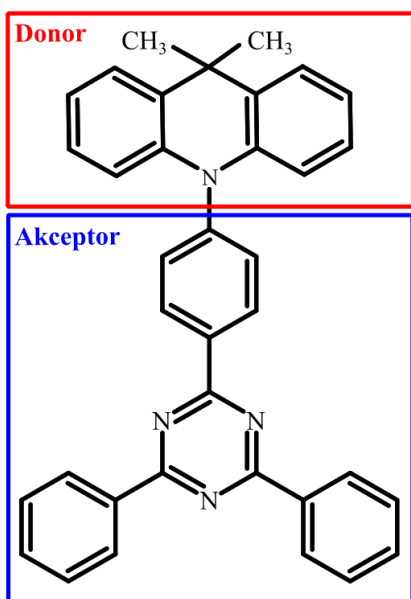
**Rys. 8.** Przykładowa struktura typowego emitera TADF o konstrukcji D-A: DMAC-TRZ.

najmniejsza. Dzięki temu, emiter TADF jest w stanie przy niewielkim wydatku energetycznym (porównywalnym z $k_B T$) przy temperaturze pokojowej przejść z niżej położonego stanu $T^*$ do stanu $S^*$.

Jeżeli chodzi o zasady projektowania molekularnego, minimalizacja $\Delta E_{ST}$ wymaga, przestrzennej separacji molekularnych orbitali granicznych: HOMO (Highest Occupied Molecular Orbital) i LUMO (Lowest Unoccupied Molecular Orbital). Elektronowe przejścia pomiędzy nimi tworzą najniższe stany wzbudzone $S^*$ i $T^*$. Współcześnie, separację orbitali granicznych osiąga się poprzez użycie silnie donorowych (D) i akceptorowych (A) fragmentów do konstrukcji emitera, którego przykładową strukturę prezentuje **Rys. 8**.

Z tego powodu, przeważająca liczba znanych emiterów TADF stanowią układy typu donor-akceptor (D-A), których najniższe stany wzbudzone S i T zostają utworzone przez przejście z przeniesieniem ładunku (charge transfer, odpowiednio stany ¹CT i ³CT). Takie związki z reguły charakteryzują się dużą zmianą momentu dipolowego podczas przejścia i dlatego większość z nich, odznacza się silnymi właściwościami solwatochromowymi, a kształt widma fluorescencji jest poszerzony i pozbawiony struktury oscylacyjnej.

### Model trójpoziomowy

W nieobecności ciężkich atomów, ze względu na zasadę zachowania całkowitego momentu pędu, przejścia pomiędzy stanami o tej samej naturze są zabronione regułami wyboru [46, 47], co potwierdzają liczne obliczenia kwantowo-chemiczne. W kontekście fotofizycznym oznacza to, że przejścia ¹CT↔³CT są zbyt wolne, żeby konkurować z innymi procesami dezaktywacyjnymi. Jak więc to możliwe, że doświadczalnie obserwuje się fluorescencję opóźnioną?

Dlatego, aktualnie w literaturze funkcjonuje ogólne przekonanie, że skoro przejścia ¹CT↔³CT są zabronione, w mechanizmie TADF istotną rolę pełni obecność innego trypletowego stanu, którego energia jest zbliżona do energii poziomu ¹CT. Aby proces międzysystemowy był dozwolony ze względu na reguły wyboru, musi to być stan o innej naturze (³LE, locally excited), utworzony poprzez orbitale zlokalizowane zazwyczaj na jednym z fragmentów emitera TADF (donorowy lub akceptorowy) lub stan z przeniesieniem ładunku (CT), lecz utworzony przez inne orbitale, niż te tworzące stan ¹CT [48]. Wśród znacznej części opublikowanych do tej pory wyników badań fotofizycznych dotyczących emiterów TADF o strukturze D-A, teoretyczny model uwzględniający obecność stanu ³LE znany dalej jako model trójpoziomowy (three-state model) pozwolił na wytłumaczenie danych doświadczalnych [49-52].

Dokładniejsze badania spektroskopowe ujawniły jednak, że kinetyka procesów międzysystemowych nie koreluje ściśle z wyżej wymienionymi oczekiwaniami. Szczegóły tych badań, w których autor tej rozprawy również asystował są opisane w **P2**. Nasze wyniki uzyskane na drodze eksperymentalnej a także obliczenia teoretyczne poddają w wątpliwość słuszność powszechnie proponowanego kierunku projektowania nowoczesnych emiterów, opartego o trójpoziomowy model, zakładający wiodącą rolę kanału $^3LE \leftrightarrow {}^1CT$ w mechanizmie TADF. Ponieważ kluczowe wyniki pracy doktorskiej są tłumaczone na podstawie teorii wytłumaczonej w **P2**, najważniejsze dowody i wnioski zostały przedstawione poniżej.

Zgodnie z ogólnym wzorem (1), teoria dopuszcza możliwość zachodzenia wydanych procesów międzysystemowych pomiędzy stanami S i T, jeżeli są one przede wszystkim zbliżone energetycznie (tzn. mają niską wartość $\Delta E_{ST}$). Ze względu na odmienną naturę, stany CT i LE charakteryzuje inna wrażliwość na zmianę polarności otoczenia: stan LE, ponieważ nie wiąże się z tak znaczną zmianą rozkładu gęstości elektronowej podczas przejścia, zazwyczaj wykazuje wobec niej niską czułość, podczas gdy energia poziomu CT ulega zależności, znanej w literaturze jako dodatni efekt solwatochromowy.

Dzięki tym różnym właściwościom stanów CT i LE, za pomocą zmiany polarności rozpuszczalnika, można wybiórczo dopasować energię poziomu CT i zewnętrznie wpłynąć na parametr $\Delta E_{1CT-3LE}$. W szczególności, stosując ośrodek o relatywnie niskiej polarności, można doprowadzić do energetycznego wyrównania obu poziomów, czyli $\Delta E_{1CT-3LE} \approx 0$. W takich warunkach, zgodnie ze wzorem (1), należałoby się spodziewać, że stała szybkości $k_{rISC}$ dla przejścia $^3LE \rightarrow {}^1CT$ powinna przyjmować wartość maksymalną. Z drugiej strony, dostatecznie duża polarność otoczenia skutecznie obniża poziom $^1CT$, oddalając go od stanu $^3LE$, a wynikiem wzrostu $\Delta E_{1CT-3LE}$ powinien być gwałtowny spadek stałej szybkości $k_{rISC}$ dla tego przejścia.

## Model dwupoziomowy $^3CT \rightarrow {}^1CT$: teoria rotamerów

*Na podstawie czego można sądzić, że model trójpoziomowy zakładający wiodącą rolę przejścia $^3LE \rightarrow {}^1CT$ w rISC nie jest do końca właściwy?*

Doświadczalne badania solwatochromowe przeprowadzone dla DMAC-TRZ, zorientowane na weryfikację powyższych założeń ujawniły dwie ważne doświadczalne obserwacje:

1) Brak maksimum wartości $k_{rISC}$ w sytuacji, kiedy $\Delta E_{1CT-3LE} \approx 0$.
2) W miarę zwiększania polarności otoczenia, wartość $k_{rISC}$ rośnie, natomiast stała dezaktywacji promienistej ze stanu $^1CT$ - $k_r$ - spada.

Pierwszy wynik wskazuje na niezależność $k_{rISC}$ od $\Delta E_{1CT-3LE}$ i tym samym istotnie podważa znaczącą rolę stanu $^3LE$ w zjawisku TADF. Druga obserwacja każe sądzić, że kluczowe dla rISC mogą być

jednak oddziaływania $^3CT \leftrightarrow ^1CT$. Wynika to między innymi z tego, że wzrost polarności sprzyja lepszej stabilizacji stanów $^1CT$ i $^3CT$, wpływając na skuteczniejszą separację gęstości elektronowej. Konsekwencją tego jest spadek $k_r$ i tym samym, hipotetyczne obniżenie $\Delta E_{1CT-3CT}$. Połączenie zależności $\Delta E_{1CT-3CT}$ z $k_{rISC}$ prowadzi do sformułowania wniosku o tym, że teoretycznie wzbronione przejście $^3CT \rightarrow ^1CT$, może mieć jednak decydujące znaczenie.

*Jaki jest zatem poprawny mechanizm TADF: $^1CT \leftrightarrow ^3CT$ czy $^1CT \leftrightarrow ^3LE$?*

Konfrontacja uzyskanych doświadczalnych wyników z aktualnie obowiązującym stanem wiedzy, tworzy wysoce niejasny obraz co do mechanizmu TADF. Z jednej strony, według klasycznych zasad fotofizycznych, w emiterach D-A nie może dochodzić do wydajnego rISC pomiędzy stanami o tej samej naturze ale różnej multipletowości $^3CT \leftrightarrow ^1CT$. Z drugiej strony, nasze doświadczalne obserwacje wskazują na szlak $^3CT \leftrightarrow ^1CT$ jako znacznie wydajniejszy niż $^3LE \leftrightarrow ^1CT$. Aby rozstrzygnąć te niezgodności, przeprowadzone zostały szczegółowe obliczenia teoretyczne.

Jak wspomniano wcześniej, w emiterach TADF o strukturze typu D-A, jednym z kluczowych czynników decydujących o szybkości przejścia interkombinacyjnego jest $\Delta E_{ST}$. Minimalną wartość tego parametru wpływającą na szybki rISC, osiąga się dzięki przestrzennej separacji orbitali HOMO oraz LUMO, której w znacznym stopniu pomaga wykręcenie jednostek D i A względem siebie o 90°, wzdłuż osi pojedynczego wiązania łączącego oba fragmenty. Stąd, wartość $\Delta E_{ST}$ silnie zależy od kąta torsyjnego $\theta_{DA}$ wyznaczonego przez płaszczyzny D oraz A.
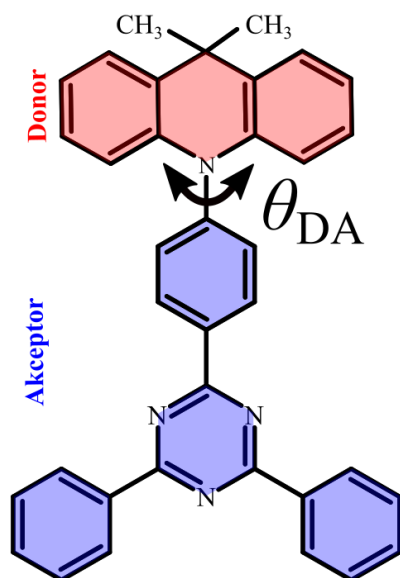


**Rys. 9.** Struktura emitera DMAC-TRZ z widocznym kątem $\theta_{DA}$.

Według aktualnego stanu wiedzy, w emiterach D-A o idealnie ortogonalnej strukturze ($\theta_{DA}$ = 90°, **Rys. 9**), pomimo minimalnego $\Delta E_{3CT-1CT}$, pomiędzy stanami o tej samej naturze ($^3CT \leftrightarrow ^1CT$) nie może jednak dochodzić do wydajnego rISC, ze względu na zerową wartość stałej sprzężenia spinowo-orbitalnego (SOC) *V*, co potwierdzają liczne obliczenia kwantowo-chemiczne.

Nowe światło na problem wydajności przejścia $^3CT \rightarrow ^1CT$ rzuciło uwzględnienie tzw. zjawiska izomerii rotacyjnej, czyli obecności różnych form jednego emitera TADF (tzw. rotamerów $\theta_{DA}$), różniących się między sobą wartością kąta $\theta_{DA}$, które są wynikiem molekularnych drgań $\omega(\theta_{DA})$ wzdłuż osi łączącej D i A. Obecność ich uzasadniona jest na gruncie termodynamicznym, a prawdopodobieństwo ich występowania wygodnie jest opisać za pomocą rozkładu Boltzmanna. Z tego powodu, zamiast rozpatrywać pojedynczą, „zamrożoną" konfigurację danej cząsteczki, na emiter TADF należy spojrzeć jako na dynamicznie

zmieniający się układ, w ramach pewnego rozkładu statystycznego w funkcji kąta torsyjnego $\theta_{DA}$ [53-55].

Odchylenie kąta $\theta_{DA}$ od ortogonalności powoduje przede wszystkim zwiększenie pokrywania się HOMO i LUMO, wzrost energii poziomu [1]CT a także $\Delta E_{3CT-1CT}$ [56]. Z drugiej strony okazuje się, że decydujący wpływ na rISC w ramach [3]CT→[1]CT może mieć jednak silna zależność stałej $V$ od wartości $\theta_{DA}$: w miarę przyrostu $\theta_{DA}$, przejście [3]CT→[1]CT staje się bardziej prawdopodobne ze względu na wzrost $V$. Ponieważ parametr ten występuje w drugiej potędze czynnika pre-eksponencyjnego (2), jego stosunkowo niewielki przyrost wywołuje dużą zmianę $k_{rISC}$.

Trzecim ważnym parametrem, wpływającym na $k_{rISC}$ (obok $\Delta E_{ST}$ i $V$), którego wartość także zależy od $\theta_{DA}$ jest energia reorganizacji $\lambda$. Według definicji, $\lambda$ jest pewną nadwyżką energii, niezbędną cząsteczce podczas konkretnego przejścia elektronowego, do optymalizacji swojej geometrii po osiągnięciu nowego docelowego stan [57]. Wartość $\lambda$ jest tym wyższa, im większych zmian w swojej strukturze musi dokonać molekuła, aby osiągnąć minimum energetyczne w danym stanie. Dlatego, z reguły jest ona wyższa dla przejść obejmujących dwa stany o różnej naturze (którym odpowiadają różne geometrie), niż w przypadku przejść pomiędzy zdegenerowanymi poziomami CT. Innymi słowy, parametr ten uprzywilejowuje kanał [3]CT→[1]CT, ponieważ emiter musi dokonać mniej kosztownych energetycznie zmian w swojej strukturze podczas tego przejścia, niż w przypadku [3]LE→[1]CT.

Biorąc pod uwagę powyższe, przeprowadzono obliczenia DFT (*Density Functional Theory*), na podstawie których określiliśmy teoretyczne wartości stałych szybkości dla rotamerów $\theta_{DA}$: $k_{ISC}$ ([1]CT→[3]CT i [1]CT→[3]LE) oraz $k_{rISC}$ ([3]CT→[1]CT i [3]LE→[1]CT) w różnych polarnościach.

Stałe szybkości zostały wyznaczone z równania Marcusa [58], będącego dokładniejszym rozwinięciem równania (1):

$$k_{(r)ISC} = \frac{V^2}{\hbar} \cdot \sqrt{\frac{\pi}{k_B T \lambda}} \exp\left(-\frac{(\Delta E_{ST} + \lambda)^2}{4 k_B T \lambda}\right), \tag{2}$$

gdzie:

- $k_B$ – stała Boltzmanna,
- $\lambda$ – energia reorganizacji,
- $V$ – stała sprzężenia spinowo-orbitalnego (SOC),
- T – temperatura,
- $\Delta E_{ST}$ – przerwa energetyczna pomiędzy stanem T i S.

Obliczenia zostały przeprowadzone uwzględniając przyczynki od rotamerów różniących się wartością $\theta_{DA}$ od 60° do 120°, a końcowa wartość dla każdego z przejść została wyznaczona jako suma statystyczna poszczególnych wkładów od każdego rotameru $\theta_{DA}$ (czynnikiem wagowym był rozkład Boltzmanna).

Z otrzymanych zależności widać wyraźnie, że zarówno $k_{rISC}$ jak i $k_{ISC}$ wyznaczone teoretycznie dla przejścia $^3CT \rightarrow {^1}CT$ doskonale korelują z wartościami otrzymanymi na drodze doświadczalnej. Wysokie wartości $k_{3CT-1CT}$ są wynikiem kombinacji trzech czynników. Przede wszystkim niezerowe wartości $V$ dla rotamerów $\theta_{DA} \neq 90°$ (*i*) a także niskie wartości $\Delta E_{3CT-1CT}$ (*ii*). Decydujący jednak wpływ ma energia reorganizacji $\lambda$ (*iii*), której niska wartość dla przejścia $^3CT \rightarrow {^1}CT$, wynika z niemal identycznych struktur DMAC-TRZ w stanie $S_1$ jak i $T_1$. Największe wartości $k_{rISC}$ przewiduje się dla bardziej polarnych rozpuszczalników, co jest wynikiem malejącego $\Delta E_{3CT-1CT}$ wraz ze wzrostem polarności.

Zdecydowanie niższe wartości $k_{rISC}$ obserwuje się dla przejścia $^3LE \rightarrow {^1}CT$. Dla wysokich polarności (np. *aceton*), z uwagi na skrajnie niskie obsadzenie (~ 0%) poziomu $^3LE$ względem stanu $^3CT$, udział szlaku $^3LE \rightarrow {^1}CT$ w rISC jest znikomy. Dla niższych polarności (*hexan*), kiedy poziom $^3CT$ jest drugim najniższym stanem wzbudzonym (trypletowym), obsadzenie poziomu $^3LE$ wynosi > 90% i przez to, obliczenia przewidują dominującą rolę szlaku $^3LE \rightarrow {^1}CT$ w rISC. Należy jednak zauważyć, że pomimo tego, najwyższa wyznaczona teoretycznie wartość $k_{rISC}$ dla $^3LE \rightarrow {^1}CT$ ($k_{rISC}$ = 0.085 x $10^7$ s$^{-1}$, *benzen-hexan ½*) jest nadal mniejsza, niż najwyższa obliczona $k_{rISC}$ dla przejścia $^3CT \rightarrow {^1}CT$ ($k_{rISC}$ = 0.387 x $10^7$ s$^{-1}$, *aceton*). Ten fakt świadczy o tym, że pomimo teoretycznie wyższych wartości $V$ dla przejścia $^3LE \rightarrow {^1}CT$, udział tego kanału może mieć jednak mniejsze znaczenie dla szybkiego rISC, ustępując teoretycznie zabronionemu przejściu $^3CT \rightarrow {^1}CT$.

Przedstawione wyżej obserwacje prowadzą do ważnego wniosku: **kompletny opis mechanizmu TADF w emiterach D-A jest niemożliwy bez uwzględnienia kanału $^3CT \rightarrow {^1}CT$**, aktywowanego przez drgania wokół kąta torsyjnego $\theta_{DA}$, wyznaczonego przez oś wiązania D-A. Kluczowa rola drgań molekularnych w procesach międzysystemowych znajduje wyraz w wysokiej korelacji pomiędzy wyznaczonymi teoretycznie stałymi szybkości, a tymi otrzymanymi na drodze doświadczalnej.

*Przejście rISC jest nadal wolne. Jak je przyspieszyć?*

Znając najbardziej prawdopodobny mechanizm zjawiska TADF w emiterach D-A, powstaje pytanie: w jaki sposób można na niego wpłynąć, aby przyspieszyć rISC? Autor tej rozprawy doktorskiej podjął się wyzwania, aby odpowiedzieć na to pytanie.

## Efekt ciężkiego atomu

Jednym ze sposobów na rozwiązanie tego problemu i przyspieszenie $k_{rISC}$, jest zwiększenie czynnika pre-eksponencyjnego $V$ we wzorze (1). Efekt ten może wywołać obecność pierwiastków o dużej liczbie atomowej Z w pobliżu emitera TADF, stąd w literaturze powszechnie przyjętym określeniem tego zjawiska jest termin tzw. efektu ciężkiego atomu (HAE).

Rozwiązaniem problemu wolnego rISC może być więc użycie materiałów hybrydowych, składających się z organicznych cząsteczek na bazie układu D-A, zmodyfikowanych poprzez wprowadzenie tanich i szeroko dostępnych ciężkich atomów do ich struktury. Koncepcja zastosowania efektu ciężkiego atomu stanowi niezwykle korzystną alternatywę dla innych sposobów podnoszenia parametrów emiterów do OLED, ponieważ hipotetycznie, pozwala na osiągnięcie wysokich wartości $k_{rISC}$ przy zachowaniu w pełni organicznej natury materiałów.

Pomimo bardzo obiecującej idei, istnieje dużo niejasności wokół tego podejścia. Kluczowym z punktu widzenia projektowania molekularnego jest wiedza o tym, w jaki sposób należy używać tego efektu do selektywnego wzmacniania pożądanych przejść międzysystemowych i od jakich czynników zależy jego efektywność. W szczególności, do jakich fragmentów należy wprowadzać ciężkie atomy, aby uzyskać korzystny wpływ na właściwości fotofizyczne? Jak struktura elektronowa poziomów energetycznych wpływa na HAE? Co decyduje o sile tego efektu i w jakich okolicznościach ma szanse być on użyteczny? Odpowiedzi na te podstawowe pytania są niezbędne do sformułowania spójnych wniosków, na gruncie których, możliwe będzie poznanie mechanizmu i ustalenie w przyszłości ogólnych zasad stosowania efektu ciężkiego atomu w organicznych emiterach TADF.

Warto podkreślić, że informacje o kinetyce przejść międzysystemowych to nie tylko obszar zainteresowania emiterów światła, ale także fotosensybilizatorów, używanych w różnych fotokatalitycznych reakcjach a także fotodynamicznej terapii nowotworów. Obie wymienione aplikacje stanowią nie mniej aktualny temat niż OLED, dlatego zgromadzona wiedza może pomóc w projektowaniu nowych, wydajniejszych i wolnych od ciężkich metali związków organicznych używanych nie tylko w optoelektronice, ale także w medycynie czy przemyśle nowoczesnych paliw.

## Efekt ciężkiego atomu w emiterach z TADF: przegląd literatury

*Co aktualnie wiadomo o efekcie ciężkiego atomu w organicznych związkach z TADF?*

Ze zgromadzonej do tej pory literatury na temat efektu ciężkiego atomu wynika, że przyspieszenie procesu rISC za pomocą wprowadzenia tanich i łatwo dostępnych ciężkich pierwiastków do struktury emitera TADF jest jak najbardziej możliwe. Chociaż przykładów jest stosunkowo niewiele, to jednak gwałtownie rosnąca liczba prac o świadczy o wysokim potencjale aplikacyjnym tego rozwiązania.

Jednym z pierwszych doniesień o pozytywnym wpływie wprowadzenia ciężkich atomów na właściwości fotofizyczne emiterów TADF była praca z 2015 roku [59], przedstawiająca wyniki badań dla halogenowych pochodnych (pojedynczo i podwójnie podstawione atomy Cl, Br lub I w donorowej części emitera) rozbudowanych zielonych emiterów TADF (4CzIPN), złożonych z czterech jednostek donorowych (karbazol, Cz) oraz centralnie umieszczonego akceptora (dicyjanobenzen). Z przeprowadzonych pomiarów czasoworozdzielczych fotoluminescencji wynika, że w miarę zwiększania ilości oraz liczby atomowej $Z$ ciężkich atomów wprowadzonych do emitera, obserwuje się

większe skrócenie czasu życia fotoluminescencji. Niestety, w pracy nie zostały oszacowane stałe szybkości konkretnych przejść międzysystemowych, a podane w pracy wartości czasów życia fotoluminescencji odnoszą się prawdopodobnie do fluorescencji opóźnionej, dlatego nie można jednoznacznie stwierdzić, z którego wzbudzonego stanu następuje przyspieszona dezaktywacja. Na uwagę natomiast zasługują wysokie wartości PLQY, wynoszące dla wszystkich pochodnych powyżej 85%.

Bardziej szczegółowe badania dotyczące mechanizmu a także weryfikacja w OLED dla tych związków zostały przeprowadzone dopiero w 2021 roku [60]. Na ich podstawie ustalono, że zgodnie z oczekiwaniami, największe przyspieszenie rISC (około 200 - krotne) zaobserwowano dla pochodnej z I ($k_{rISC} \sim 10^7$ s$^{-1}$).

Podobne wnioski można wyciągnąć analizując wyniki badań [61] dla pochodnych innego popularnego zielonego emitera (PXZPM), zawierających odpowiednio atom chloru oraz bromu w akceptorowym fragmencie. Oba związki wykazywały przyspieszenie zarówno ISC (około 1.6 – krotne względem PXZPM) jak i rISC (około 3.7-krotne przyspieszenie) przy jednoczesnym zachowaniu wysokiej wydajności kwantowej fotoluminescencji (PLQY) na poziomie około 90%.

Innym przykładem może być publikacja [62], w której autorzy dokonali doświadczalnej weryfikacji pomysłu wprowadzenia atomu(ów) bromu do struktury innego typowego emitera TADF zbudowanego z dwóch fragmentów karbazolowych oraz dwóch akceptorowych. – 2CzPN. W wyniku przeprowadzonych badań udało się ustalić, że skutkiem wprowadzenia jednego atomu Br (BrCzCzPN) jest około 3 – krotne przyspieszenie ISC porównaniu do niepodstawionego 2CzPN (2CzPN: $k_{ISC}$ = 3.01 x 10$^7$ s$^{-1}$, BrCzCzPN: $k_{ISC}$ = 9.52 x 10$^7$ s$^{-1}$) oraz tylko nieznaczne przyspieszenie rISC (2CzPN: $k_{rISC}$ = 0.79 x 10$^5$ s$^{-1}$, BrCzCzPN: $k_{rISC}$ = 0.90 x 10$^5$ s$^{-1}$). Co ciekawe, gdy wprowadzone zostają dwa atomu Br (2BrCzPN, wówczas struktura tak zmodyfikowanego emitera staje się bardziej symetryczna), $k_{ISC}$ nie zmienia się praktycznie wcale, pomimo wzrostu wartości SOC z 0.49 do 0.62 cm$^{-1}$, a także mniejszej $\Delta E_{ST}$ z 0.30 do 0.24 eV, a $k_{rISC}$ wzrasta do wartości 1.34 x 10$^5$ s$^{-1}$.

Znaczny wzrost $k_{rISC}$ oraz wyższą wartość PLQY uzyskano także dla pochodnych zawierających jeden atom Br (OBA-BrS i OBA-BrO) w donorowym fragmencie struktury emiterów (w porównaniu do swoich analogów bez Br: OBA-S i OBA-O) [63]. Przyspieszeniu jednak ulega także ISC, natomiast bezpośrednią przyczyną wzrostu $k_{ISC\,i}\,k_{rISC}$ jest raczej zmniejszenie przerwy energetycznej niż typowy HAE. Niemniej jednak, zauważalna poprawa właściwości fotofizycznych przeniosła się także na testy w urządzeniach OLED, w których pochodne z Br wypadły zdecydowanie lepiej.

Znaczne przyspieszenie rISC za pomocą wprowadzenia atomu(ów) Br uzyskano dla innego związku (CPT) [64]. Jednakże, pomimo przyspieszenia rISC (z $k_{rISC}$ = 0.54 x 10$^6$ s$^{-1}$ do $k_{rISC}$ = 4.56 x 10$^6$ s$^{-1}$) przy jednoczesnym braku zmiany w ISC ($k_{ISC}$ = 19 x 10$^6$ s$^{-1}$), testy w urządzeniach wykazały, że OLEDy na bazie zmodyfikowanych emiterów z Br, nie wykazały istotnej poprawy w stabilności.

Silny efekt ciężkiego atomu spowodowany wymianą atomu tlenu [65] na atom siarki [66] zaobserwowano w innych emiterach TADF, wykazującego z fotoluminescencję w niebieskim zakresie ($\lambda_{max}$ ~ 480 nm). Wzrost stałej szybkości z $k_{rISC} = 0.3 \times 10^7$ s$^{-1}$ do $k_{rISC} = 6.4 \times 10^7$ s$^{-1}$ przełożył się na wyniki w urządzeniach OLED: pochodna z siarką odznaczała się zdecydowanie lepszymi parametrami emisyjnymi z w porównaniu do związku z tlenem.

Podobnie w innej pracy [67], wyraźnie lepszą odporność na degradację oraz wyższą EQE (z 17.7% do 25.2%) wykazywała pochodna zawierająca atom siarki w porównaniu do jej analogu z tlenem.

Kolejnym przykładem poprawy kinetycznych parametrów za pomocą (zewnętrznego) efektu ciężkiego atomu może być praca [68], w której ciężkie atomy (Br) zostały wprowadzone do struktury hosta (czyli ośrodka dyspersyjnego, w którym umieszcza się emiter).

Niezwykle szybki proces rISC ($k_{rISC}$ ~ $10^8$ s$^{-1}$) uzyskano dzięki wprowadzeniu atomu Se do struktury innego emitera TADF [69], co stanowi wzrost stałej $k_{rISC}$ o 4 rzędy wielkości, w porównaniu z pochodną zawierającą tlen.

Warto podkreślić, że oprócz poprawy zdolności emisyjnych związków wykazujących TADF (poprzez przyspieszanie rISC), efekt ciężkiego atomu był także z powodzeniem stosowany w celu zwiększenia skuteczności przejścia S$_1$ $\rightarrow$ T$_1$ (przyspieszanie ISC) [70] na przykład w fotodynamicznej terapii [71] skierowanej przeciwko komórkom nowotworowym, a także w materiałach wykazujących fosforescencję w temperaturze pokojowej (RTP) [72-78].

Z drugiej strony, część badań wskazuje, że samo wprowadzenie ciężkich atomów do emitera nie gwarantuje przyspieszenia procesów międzysystemowych [79]. Na przykład, wymiana lżejszego atomu Si na cięższy Ge w emiterze skutkuje zmniejszeniem stałej z $k_{rISC} = 3.3 \times 10^7$ s$^{-1}$ do $k_{rISC} = 1.6 \times 10^7$ s$^{-1}$ [80].

Co zaskakujące, inne badania pokazują, że możliwy jest także zupełnie odwrotny efekt (anty-efekt ciężkiego atomu) [81]. W cytowanej pracy autorzy nie odnotowali spodziewanego wzrostu *V*, nawet dla pochodnych zawierających 4 atomy jodu w swojej strukturze.

Jak widać z powyższych przykładów, do sformułowania spójnych wniosków na temat stosowania efektu ciężkiego atomu w organicznych związkach z TADF wciąż brakuje wystarczającej ilości danych doświadczalnych, a podstawie których możliwe byłoby opracowanie teoretycznego modelu.

## Niebieskie emitery TADF

W związku z niejasnym wpływem efektu ciężkiego atomu na właściwości fotofizyczne emiterów TADF, przeprowadzone zostały szczegółowe badania dotyczące natury tego zjawiska. Pierwszym problemem badawczym jaki podjęto w pracy [**P3**] jest więc pytanie o **wpływ HAE na właściwości fotofizyczne związków z TADF wykazujących emisję w niebieskim zakresie**. Drugim ogólnym zagadnieniem, które poruszono było **opracowanie spójnej metodologii badawczej do analizy mechanizmu TADF na podstawie danych doświadczalnych**.

Aby umożliwić sformułowanie odpowiedzi na wyżej postawione dwa problemy, niezbędnym była weryfikacja dwóch podstawowych pytań:

*(i)*      Który z procesów międzysystemowych – (rISC czy ISC) - jest bardziej podatny na ten efekt i wrażliwy na wprowadzenie ciężkich atomów?

*(ii)*      Za pośrednictwem którego ze szlaków ($^3$LE↔$^1$CT czy $^3$CT↔$^1$CT) odbywają się oba wymienione procesy w związkach z ciężkimi atomami?

Do badań nad efektem ciężkiego atomu zostały wybrane dwie halogenowe pochodne **diCl** oraz **diBr** niebieskiego emitera TADF **H** (**Rys. 10a**), analogu DMAC-TRZ, którego właściwości fotofizyczne zostały dobrze poznane i opisane w omówionych wcześniej badaniach [**P2**].
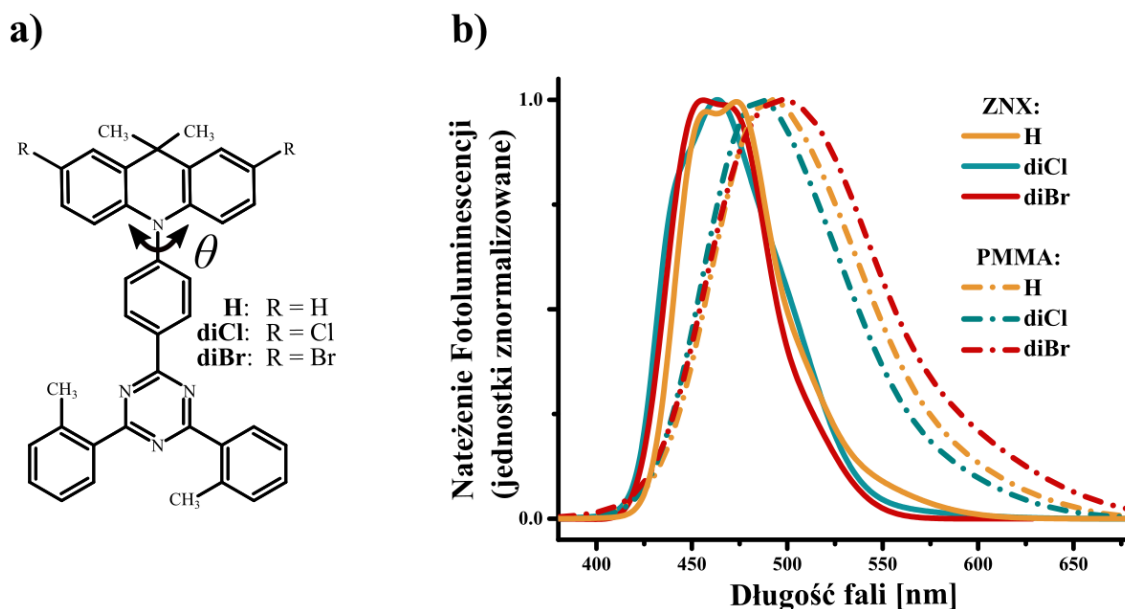


**Rys. 10. a)** Struktury emiterów objętych badaniami, **b)** stacjonarne widma fotoluminescencji zarejestrowane w dwóch ośrodkach o różnej polarności: ZNX i PMMA.

W pierwszym kroku, za pomocą stacjonarnych pomiarów widm fotoluminescencji, ustalono naturę oraz kolejność elektronowych stanów wzbudzonych w każdym z badanych związków, dla dwóch ośrodków o różnej polarności – ZNX (zoenex) oraz PMMA (polimetakrylan metylu). Na **Rys. 10b** przedstawiono wyniki tych pomiarów.

W niepolarnym ZNX, widma emisji wszystkich związków wykazują podobne cechy zarówno co do ich kształtu jak i lokalizacji – widma są względnie wąskie z maksimum mieszczącym się w zakresie 462 – 467 nm. W polarnym PMMA, są one przesunięte w kierunku dłuższych fal (maksimum widm emisji znajduje się w okolicach 492 – 499 nm), wyraźnie poszerzone a także pozbawione tzw. struktury oscylacyjnej. Wymienione cechy (wspólne dla wszystkich związków) świadczą o utworzeniu stanu wzbudzonego $S_1$, który powstaje przez przejście z silnym przeniesieniem ładunku (CT, charge transfer). Opisana tendencja, szerzej znana jako dodatni efekt solwatochromowy, jest typowa dla większości znanych emiterów TADF o budowie D-A.

Przechodząc do zmian spowodowanych wprowadzeniem ciężkich atomów, jedyna różnica widoczna w stacjonarnych pomiarach PL, polega na subtelnym przesunięciu widm emisji w kierunku fal krótkich dla **diCl** i **diBr** względem **H**, wynikającego z efektu indukcyjnego halogenów. Z tego powodu, energie poziomów $^1$CT dla emiterów **diCl** i **diBr** są usytuowane wyżej (**diCl**, **diBr**: $E_{1CT} = 2.97$ eV oraz $E_{1CT} = 2.90$ eV odpowiednio w ZNX i PMMA) względem **H** ($E_{1CT} = 2.93$ eV oraz $E_{1CT} = 2.88$ eV odpowiednio w ZNX i PMMA) jak widać na **Rys. 11a** i **11b**.
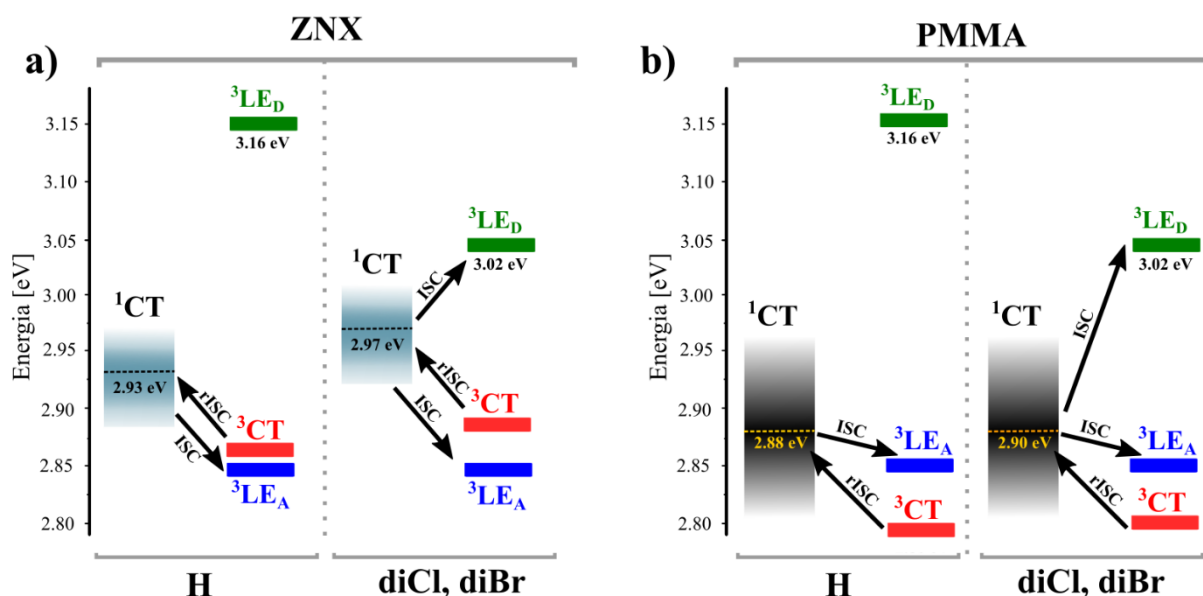


**Rys. 11.** Schemat przedstawiający ułożenie poziomów energetycznych w badanych emiterach w **a)** ZNX w **b)** PMMA.

Podobna identyfikację natury oraz lokalizację poziomów energetycznych przeprowadzono dla stanów trypletowych. W tym celu, dla wszystkich emiterów, a także osobno dla fragmentów donorowych i akceptora, zostały zmierzone widma fosforescencji w temperaturze 10 K. Na podstawie uzyskanych

wyników ustalono, że najniższym wzbudzonym stanem trypletowym w niepolarnym ZNX jest stan utworzony poprzez przejście zlokalizowane na akceptorowym fragmencie emiterów ($^3LE_A$), którego energia wynosi (E = 2.84 eV) i nie ulega zmianie pod wpływem wprowadzenia halogenów. W PMMA, widma fosforescencji wykazują podobne cechy do fluorescencji pochodzącej ze stanu $^1CT$, co oznacza że najniższy wzbudzony stan trypletowy jest tej samej natury ($^3CT$). Z uwagi na względnie wysoką energie poziomów trypletowych dla stanów zlokalizowanych na donorowym fragmencie emiterów ($^3LE_D$), oszacowanie ich energii doświadczalnie możliwe jest tylko za pomocą pomiarów fosforescencji dla osobnych donorowych fragmentów. W związku z wprowadzeniem halogenów do donorowej części emiterów, energia tego poziomu $^3LE_D$ ulega silnemu obniżeniu od wartości 3.16 eV dla **H** do około 3.02 eV dla **diCl** i **diBr**. Wyznaczone energie poszczególnych stanów wzbudzonych posłużyły do określenia przerw energetycznych pomiędzy najniższymi poziomami energetycznymi, których wartości przedstawiono w **Tabeli 1**.

**Tabela 1.** Wydajności kwantowe fotoluminescencji (PLQY), wartości przerw energetycznych oraz kinetyczne parametry fotofizyczne badanych związków.

| | PLQY | $\Delta E_{1CT-3LE(A)}{}^a$ | $\Delta E_{1CT-3CT}{}^b$ | $\Delta E_{1CT-3LE(D)}{}^c$ | $\tau_{PF}{}^d$ | $\tau_{DF}{}^e$ | $k_r{}^f$ | $k_{ISC}{}^g$ | $k_{nr}{}^h$ | $k_{rISC}{}^i$ |
|---|---|---|---|---|---|---|---|---|---|---|
| | [%] | [meV] | [meV] | [meV] | [ns] | [us] | [$s^{-1}\,10^7$] | [$s^{-1}\,10^7$] | [$s^{-1}\,10^7$] | [$s^{-1}\,10^4$] |
| **ZNX** | | | | | | | | | | |
| **H** | 60 | 94 | - | -230 | 15.3 | 171 | 1.5 | 5.1 | 0.0 | 1.03 |
| **diCl** | 75 | 133 | - | -55 | 13.1 | 333 | 1.8 | 6.1 | 0.0 | 0.87 |
| **diBr** | 12 | 114 | - | -55 | 2.2 | 104 | 2.0 | 38.5 | 3.8 | 1.74 |
| **PMMA** | | | | | | | | | | |
| **H** | 99 | 46 | 85 | -278 | 17.1 | 96 | 2.0 | 3.8 | 0.0 | 2.92 |
| **diCl** | 85 | 72 | 95 | -116 | 16.0 | 139 | 2.0 | 4.1 | 0.1 | 1.85 |
| **diBr** | 21 | 60 | 86 | -109 | 2.8 | 38 | 2.1 | 30.8 | 3.1 | 8.23 |

$^{a,b,b}$ – przerwy energetyczna pomiędzy stanami odpowiednio $^1CT$ - $^3LE_A$, $^1CT$ - $^3CT$ oraz $^1CT$ - $^3LE_D$; $^{d,e}$ – wyznaczony średni czas życia fluorescencji oraz fluorescencji opóźnionej; $^{f,\ g,\ h,\ i}$ –stałe szybkości procesów fotofizycznych odpowiednio: dezaktywacji promienistej ze stanu singletowego, przejścia międzysystemowego, dezaktywacji bezpromienistej oraz odwrotnego przejścia międzysystemnowego.

W następnej kolejności, za pomocą pomiarów czasowo-rozdzielczych wykonanych przy użyciu kamery smugowej (szczegóły używanych metod pomiarowych są szczegółowo opisane w suplemencie pracy [**P3**]), dla każdego związku zidentyfikowano proces TADF, a następnie przeprowadzono szczegółową analizę ewolucji czasowej widm emisji (**Rys. 12**). Przesunięcie widm w kierunku fal długich (tzw. *redshift*) widoczne w zakresie pierwszych ok. 50 ns oraz późniejsze (w zakresie 50 ns – 5 ms) w kierunku fal krótkich (*blueshift*) jest wynikiem obecności statystycznego rozkładu stanów $^1CT$, potwierdzającym współistnienie rotamerów o różnych wartościach $\theta_{DA}$.

Kolejnym etapem badań, było wyznaczenie stałych szybkości poszczególnych procesów fotofizycznych zachodzących w stanach wzbudzonych. Kluczowe z punktu widzenia uzyskania odpowiedzi na sformułowane na początku pytania (*i*) i (*ii*) są wnioski:

1. Wprowadzenie halogenów powoduje skrócenie czasu życia fluorescencji $\tau_{PF}$, wskazując na przyspieszoną dezaktywację ze stanu $^1$CT w tych emiterach. Największy efekt wykazuje **diBr**, gdzie skrócenie czasu wynika głównie z przyspieszenia $k_{ISC}$ oraz $k_{nr}$.

2. Wydłużenie czasu życia fluorescencji opóźnionej w **diCl** względem **H j**est rezultatem spadku stałej szybkości $k_{rISC}$, podczas gdy w **diBr** obserwujemy wyraźne przyspieszenie rISC.
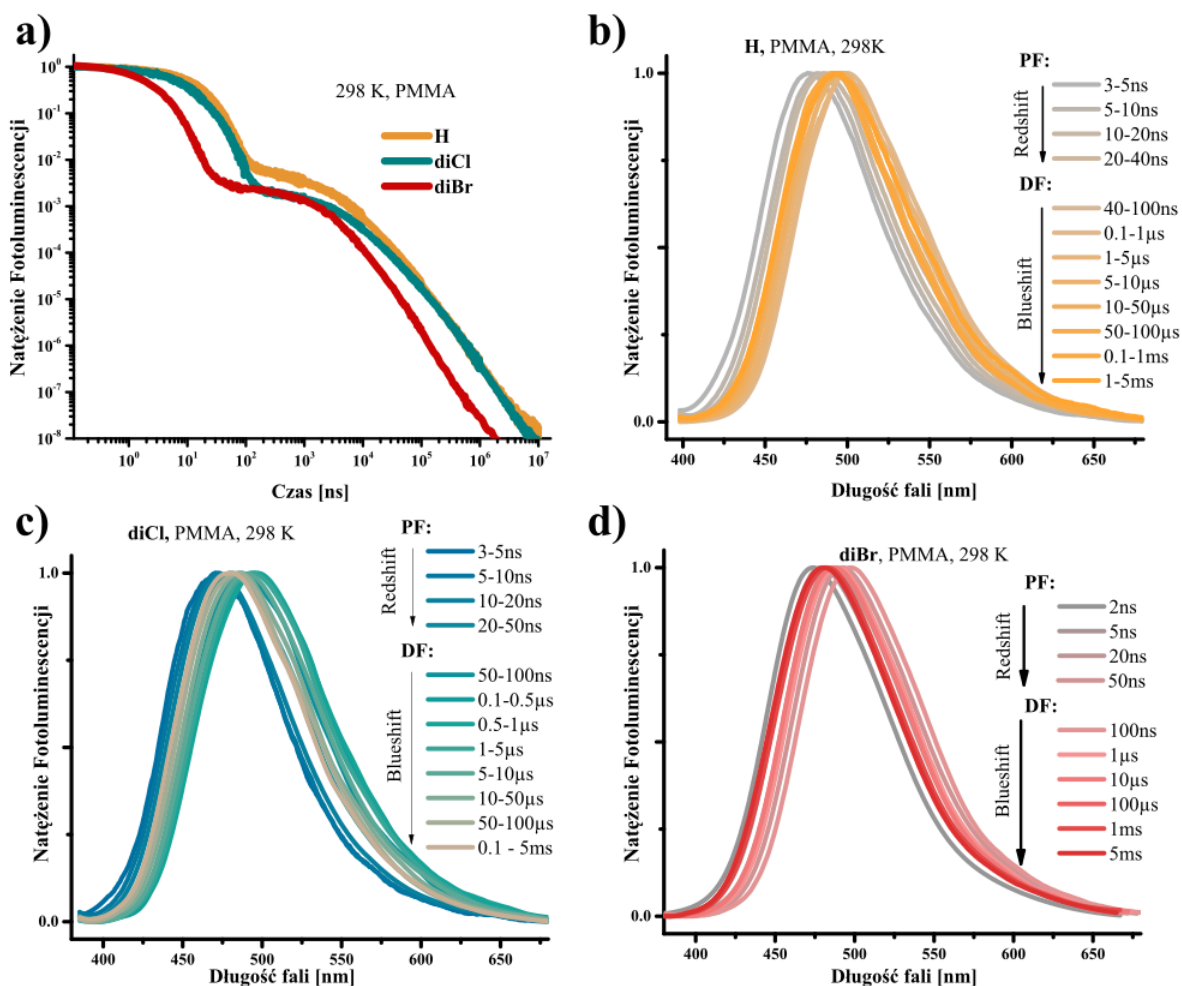


**Rys. 12.** Wyniki przeprowadzonych czasoworozdzielczych pomiarów fotoluminescencji: **a)** zarejestrowane zaniki natężenia fotoluminescencji, **b), c) i d)**: czasowa ewolucja widm emisji odpowiednio dla **H, diCl** i **diBr**.

Aby odpowiedzieć na pytanie o najbardziej prawdopodobny szlak w procesach ISC oraz rISC, przeprowadzono pomiary czasowo-rozdzielcze w różnych temperaturach. Dzięki temu, z równania Arrheniusa (1), udało się wyznaczyć energie aktywacji $E_a$ dla wspomnianych procesów, a także stałe pre-eksponencyjne A. Na **Rys. 13** przedstawiono wykresy, z których wyraźnie widać, że we wszystkich emiterach, zarówno w ZNX jak i PMMA, ISC przebiega bezbarierowo (energia aktywacji $E_a = 0$). Przechodząc do rISC, oszacowane wartości energi aktywacji dla **H, diCl** i **diBr** są zbliżone do siebie,

jednak widać wyraźną różnicę spowodowaną różnicą polarności: w ZNX we wszystkich emiterach, bariera energetyczna jest o około 30 meV wyższa niż w PMMA.
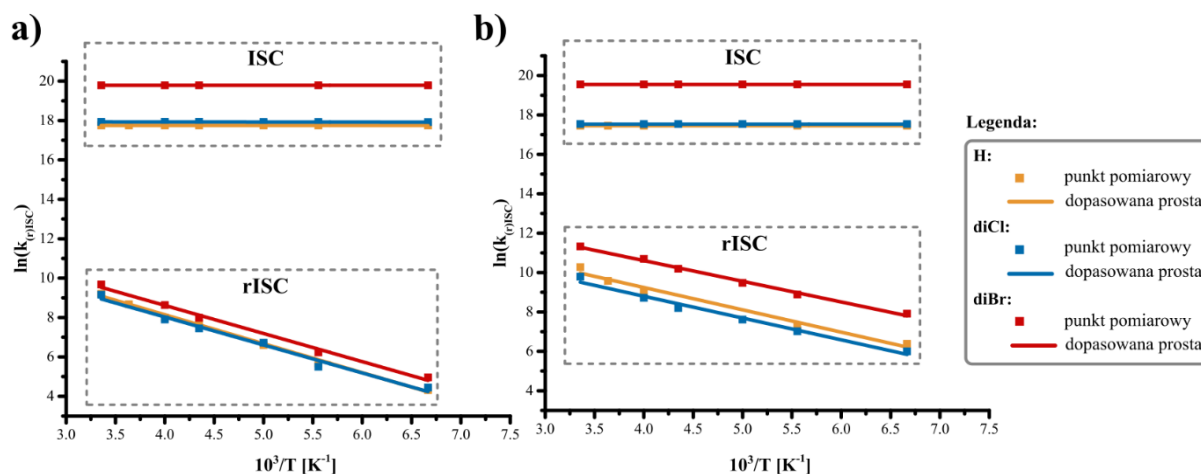


**Rys. 13.** Wyznaczone stałe szybkości dla ISC oraz rISC w funkcji temperatury na podstawie przeprowadzonych czasoworozdzielczych pomiarów fotoluminescencji w różnych temperaturach w **a)** ZNX oraz **b)** PMMA.

Jak wynika z porównania równań (1) i (2), wyznaczone wielkości $A$ i $E_a$ związane są z parametrami fotofizycznymi $\Delta E_{ST}$, $\lambda$ i $V$ następującymi relacjami:

$$A = \frac{V^2}{\hbar} \sqrt{\frac{\pi}{k_B T \lambda}}, \tag{3}$$

$$E_a = \frac{(\Delta E_{ST} + \lambda)^2}{4\lambda}. \tag{4}$$

W następnym kroku, wykorzystując te zależności, dla procesów ISC oraz rISC oszacowano wartości $\Delta E_{ST}$, $\lambda$ i $V$ (**Tabela 2**), które posłużyły do weryfikacji ścieżki, którą oba przejścia międzysystemowe zachodzą.

Przede wszystkim, z otrzymanych wyników widać wyraźną dysproporcję pomiędzy stałymi $V$ dla ISC oraz rISC, co świadczy o tym, że oba procesy najprawdopodobniej odbywają się różnymi szlakami. Ponieważ dla rISC są to wartości typowe dla tzw. przejść zabronionych, (<0.1 cm$^{-1}$) należy przypuszczać że proces ten odbywa się pomiędzy stanami o tej samej naturze, tzn. $^3$CT$\rightarrow$$^1$CT. Co więcej, brak wyraźnego wzrostu stałych $V$ w halogenowych pochodnych dla rISC sugeruje, aby wykluczyć jakikolwiek udział stanu $^3$LE$_D$ w tym przejściu międzysystemowym. Ten wniosek ma swoje uzasadnienie w innych badaniach [82], z których wynika, że przejście z udziałem stanu $^3$LE zlokalizowanego na fragmencie do którego wprowadzony jest ciężki atom (Br), powinno charakteryzować się większą wartością $V$, w porównaniu do emitera bez ciężkiego atomu. Odmiennie

dla ISC – względnie wysokie wartości $V$ wskazują na obecność tzw. dozwolonego procesu pomiędzy stanami o różnej naturze: $^{1}CT \rightarrow {}^{3}LE_A$ lub $^{1}CT \rightarrow {}^{3}LE_D$. Tym bardziej, zauważalny wzrost wartości z 0.29 cm$^{-1}$ dla **H** do 0.76 cm$^{-1}$ dla **diBr** może wskazywać na wiodącą rolę stanu $^{3}LE_D$ w mechanizmie ISC w **diBr**.

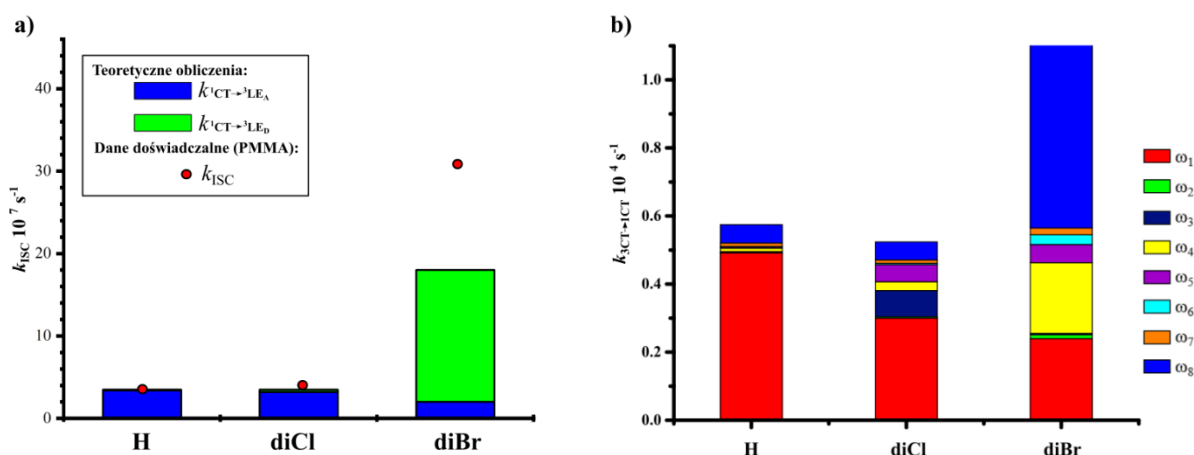**Tabela 2.** Parametry dla przejść ISC oraz rISC wyznaczone z równania Arrheniusa oraz równania Marcusa-Husha.

| | proces | Równanie Arrheniusa (1) | | Równanie Marcusa-Husha (2) | | | |
|---|---|---|---|---|---|---|---|
| | | $A$ | $E_a$ | $\Delta E_{ST}$ | $\lambda$ | $V$ | $V_{hal}/V_H$ |
| | | [s$^{-1}$ 10$^7$] | [meV] | [meV] | [meV] | [cm$^{-1}$] | |
| ZNX | | | | | | | |
| **H** | ISC | 5.09 | 0 | -122 | 122 | 0.29 | |
| **diCl** | | 6.12 | 0 | -127 | 127 | 0.31 | 1.0 |
| **diBr** | | 38.43 | 0 | -125 | 125 | 0.76 | 2.6 |
| **H** | rISC | 0.12 | 124 | 122 | 122 | 0.05 | |
| **diCl** | | 0.09 | 127 | 127 | 127 | 0.04 | 0.8 |
| **diBr** | | 0.16 | 126 | 125 | 125 | 0.05 | 1.1 |
| PMMA | | | | | | | |
| **H** | ISC | 3.83 | 0 | -93 | 93 | 0.29 | |
| **diCl** | | 4.11 | 0 | -97 | 97 | 0.30 | 1.0 |
| **diBr** | | 30.85 | 0 | -94 | 94 | 0.76 | 2.5 |
| **H** | rISC | 0.09 | 98 | 93 | 93 | 0.05 | |
| **diCl** | | 0.06 | 95 | 97 | 97 | 0.04 | 0.8 |
| **diBr** | | 0.26 | 92 | 94 | 94 | 0.07 | 1.5 |

Koncentrując się na wpływie ciężkiego atomu, dzięki porównaniu stosunków wyznaczonych stałych $V_{hal}/V_H$ można stwierdzić, że najsilniejszy efekt został wywołany dla procesu ISC (ok. 2.5 - krotny wzrost stalej $V$ dla **diBr** względem **H**). Zdecydowanie mniejsze wzmocnienie zanotowano dla rISC (ok. 1.1 dla ZNX i ok. 1.5 dla PMMA). Widać więc, że efekt ciężkiego atomu działa dość selektywnie – efekt jest silniejszy dla ISC, co z punktu widzenia projektowania organicznych emiterów do OLED jest czynnikiem niekorzystnym.

W kolejnym etapie badań, aby zweryfikować hipotezę o proponowanych szlakach dla ISC oraz rISC, przeprowadzono szczegółowe obliczenia DFT/TD-DFT. W obliczeniach użyto funkcjonału B3LYP z bazą Lan2LDZ. Głównym celem było stworzenie spójnego modelu teoretycznego, poprzez wyznaczenie teoretycznych wartości stałych szybkości, korelujących z danymi doświadczalnymi. Na podstawie tego, wytłumaczenie obserwowanego efektu i wskazanie kluczowych czynników wpływających na najważniejsze parametry fotofizyczne.

W związku z tym, analizę teoretyczną rozpoczęto od optymalizacji struktur w konkretnych stanach elektronowych. Następnie, za pomocą lokalizacji orbitali molekularnych tworzących stany wzbudzone, zidentyfikowano natury poziomów energetycznych. Obliczenia potwierdziły obecność stanów $^{1}CT$, $^{3}CT$, a także lokalnych $^{3}LE_A$ i $^{3}LE_D$, we wszystkich badanych związkach.

**ISC**. Dla rozpatrywanych przejść interkombinacyjnych $^1CT\rightarrow^3LE_A$ i $^1CT\rightarrow^3LE_D$, wyznaczono parametry fotofizyczne $\Delta E_{ST}$, $\lambda$, $V$, a także teoretyczne wartości stałych szybkości $k_{1CT\rightarrow3LE(A)}$ i $k_{1CT\rightarrow3LE(D)}$. Z otrzymanych rezultatów wynika, że obserwowane w **diBr** przyspieszenie ISC jest wynikiem (*i*) wzrostu stałej SOC pomiędzy stanami $^1CT$ i $^3LE_D$ (z 0.7 cm$^{-1}$ dla **H** do 3.3 cm$^{-1}$ w **diBr**) oraz (*ii*) zmniejszeniem wartości przerwy energetycznej $\Delta E_{1CT-3LED}$ (widoczne na **Rys. 11a** i **11b**). Przeprowadzone kalkulacje stałych szybkości dla alternatywnego szlaku $^1CT\rightarrow^3LE_A$ dobrze korelują z wynikami dla **H** oraz **diCl**. Jednakże, ponieważ wartość $V$ dla **diBr** ulega zmniejszeniu (z 0.63 cm$^{-1}$ w **H** do 0.49 cm$^{-1}$ w **diBr**), to szlak ten nie tłumaczy HAE dla ISC obserwowanego w **diBr**. Tym samym, za przyspieszenie ISC w **diBr** odpowiedzialny jest kanał $^1CT\rightarrow^3LE_D$. (**Rys. 14a**)
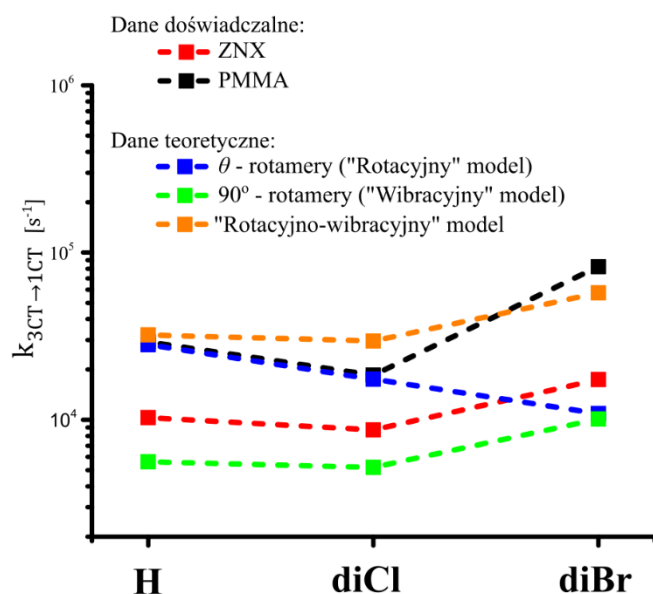


**Rys. 14**. Wyniki obliczeń DFT dla badanych emiterów: **a)** wykres prezentujący wkłady poszczególnych ścieżek ($^1CT\rightarrow^3LE_A$ i $^1CT\rightarrow^3LE_D$) w ISC, **b)** wkłady kolejnych drgań w rISC w ramach kanału $^3CT\rightarrow^3CT$.

Przechodząc do rISC, obliczenia DFT zdecydowanie wykluczyły udział stanów lokalnych $^3LE_A$ i $^3LE_D$ w tym procesie. Przede wszystkim, wyznaczone $V$ dla przejścia $^3LE_A \rightarrow$ $^1CT$ są równe dla **H** oraz **diBr**, (**H**, **diBr**: $V = 0.24$ cm$^{-1}$) co w połączeniu z wyższą energia reorganizacji, a także większą przerwą energetyczną (zarówno w ZNX jak i PMMA) dla **diBr** względem **H**, prowadzi do zmniejszenia stałej szybkości rISC, co stoi w sprzeczności z danymi doświadczalnymi. Szlak ten więc z całą pewnością nie tłumaczy obserwowanego przyspieszenia rISC w **diBr**.

W przypadku przejścia $^3LE_D \rightarrow$ $^1CT$, chociaż w wyznaczonych wartościach $V$ widać wyraźny wzrost (z 0.7 cm$^{-1}$ dla **H** do 3.1 cm$^{-1}$ dla **diBr**), to jego wkład należy uznać za marginalny, ze względu na znikome obsadzenie poziomu $^3LE_D$ (oszacowane za pomocą rozkładu Boltzmanna na ok. 0.1 % dla **diBr**). Co więcej, uzyskane podczas obliczeń wartości reorganizacji energii dla tego przejścia w **diBr** (**diBr**: $\lambda_{3LE(D)-1CT} = 0.28$ eV) powinny skutkować większą wrażliwością tego związku na zmianę temperatury (objawiającą się większą energią aktywacji), niż zostało to zarejestrowane w czasowo-rozdzielczych pomiarach temperaturowych.

Powyższe rezultaty świadczą o tym, że najbardziej prawdopodobnym szlakiem w rISC jest przejście $^3CT \rightarrow {}^1CT$. Zgodnie z wynikami z poprzednich badań [P2], najdokładniejszy opis zjawiska rISC opiera się na opracowanym wcześniej modelu rotacyjnym, który bazuje na obecności rotamerów $\theta_{DA}$, powstałych w wyniku drgań kąta torsyjnego $\omega_1$, wyznaczonego przez oś wiązania D-A. W związku z tym, w pierwszym kroku wyznaczono stałe szybkości $k_{3CT\rightarrow 1CT}$ w ramach tego modelu. Co zaskakujące - otrzymano wynik, który bardzo dobrze korelował tylko z wartościami doświadczalnymi uzyskanymi dla **H** oraz **diCl**, podczas gdy teoretyczna wartość dla pochodnej **diBr** wyraźnie odbiegała od eksperymentalnej, załamując obserwowany doświadczalnie trend.



**Rys. 15**. Porównanie danych doświadczalnych z opracowanymi teoretycznymi modelami, opisującymi rISC w ramach przejścia $^3CT\rightarrow{}^1CT$.

Dopiero szczegółowa analiza kolejnych wibracji wytłumaczyła przyczynę rozbieżności pomiędzy danymi doświadczalnymi a modelem rotacyjnym widoczną w **diBr**. Przejście $^3CT\rightarrow{}^1CT$ w **diBr** jest przyspieszone dzięki znacznemu wzmocnieniu SOC poprzez drgania wyższych rzędów $\omega_2$ - $\omega_8$. W szczególności najbardziej znaczące są wkłady pochodzące od wibracji $\omega_4$ i $\omega_8$. Uwzględnienie tych przyczynków w ramach modelu rotacyjno-wibracyjnego daje rezultat zgodny z doświadczeniem (**Rys. 15**).

Podsumowując, w wyniku przeprowadzonych badań udało się ustalić kilka ważnych wniosków, dotyczących wpływu efektu ciężkiego atomu na rISC w niebieskich emiterach wykazujących TADF.

Przede wszystkim, efekt ciężkiego atomu, najlepiej widoczny w **diBr** prowadzący do przyspieszenia obu procesów międzysystemowych jest zauważalnie silniejszy w przypadku ISC, niż w rISC, przez różną naturę tych przejść. Ściślej, analiza za pomocą równań Arrheniusa oraz Marcusa wykazała, że w ISC efekt ciężkiego atomu odbywa się z dominującym udziałem stanu $^3LE$ zlokalizowanego na fragmencie, do którego wprowadzony jest ciężki atom. Z drugiej strony, zarówno dane doświadczalne jak i szczegółowe obliczenia DFT jasno wskazują, że rISC najwyraźniej zachodzi poprzez szlak $^3CT\rightarrow{}^1CT$ i z tego powodu, przyspieszenie rISC nie jest tak silne, jak w przypadku ISC.

Opracowany model rotacyjno-wibracyjny świetnie koreluje z danymi doświadczalnymi i tym samym stanowi silny dowód na słuszność wcześniej proponowanego mechanizmu rISC, opartego o

oddziaływanie stanów wzbudzonych tej samej natury ($^3$CT-$^1$CT). Jeżeli w przypadku emiterów składających się z lekkich atomów, co można wytłumaczyć poprzez samo istnienie rotamerów $\theta_{DA}$, poprawny model rISC dla emiterów z ciężkimi atomami powinien uwzględniać wibracje wyższych rzędów. W szczególności, te drgania, które angażują ciężkie atomy, prowadzą do znacznego wzrostu stałych $V$ dla $^3$CT→$^1$CT i w rezultacie przyspieszają rISC.

Z aplikacyjnego punktu widzenia, przedstawione wnioski mają swoje istotne konsekwencje: po pierwsze, aby wpływ efektu ciężkiego atomu prowadził do poprawy parametrów fotofizycznych, należy unikać bliskości pomiędzy stanami $^3$LE i $^1$CT, ponieważ takie okoliczności sprzyjają przyspieszeniu ISC, co stanowi czynnik niepożądany w OLED gdyż skutkuje zwiększaniem populacji stanów trypletowych. Po drugie, zgodnie z przyjętym modelem rISC, ciężki atom powinien być zaangażowany w drgania molekularne o niskiej częstotliwości, aby skutecznie promować konwersję do stanu singletowego $S_1$.

## Czerwone emitery TADF

Przeprowadzone dotychczasowe badania prowadzą do wniosku, że kluczowym w przyspieszaniu procesu rISC jest przejście $^3CT \rightarrow ^1CT$. W związku z tym, aby uzyskać szybki rISC, zgodnie ze wzorem (1) należy dążyć do jak najmniejszych wartości $\Delta E_{ST}$ pomiędzy tymi stanami. Zgodnie z regułami wyboru, strategia minimalizowania $\Delta E_{ST}$ za pomocą przestrzennej separacji HOMO i LUMO niestety, powoduje obniżenie prawdopodobieństwa prześcia promienistego $S_1 \rightarrow S_0$. Ostatnie opisuje siła oscylatora $f$ – ważny parametr, którego wartość jest wprost proporcjonalna do stałej szybkości dezaktywacji promienistej $k_r$ z najniższego wzbudzonego stanu singletowego [83-84]:

$$k_r \sim f. \tag{5}$$

Niska wartość $f$ jest czynnikiem niepożądanym, ponieważ bezpośrednio przyczynia się do zmniejszenia skuteczności konwersji energii wzbudzenia na emisję światła, pogarszając w ten sposób ich właściwości emisyjne. W konsekwencji, oba parametry, istotne z punktu widzenia projektowania molekularnego są ze sobą związane i pozostają w stosunku do siebie w odwrotnej proporcji:

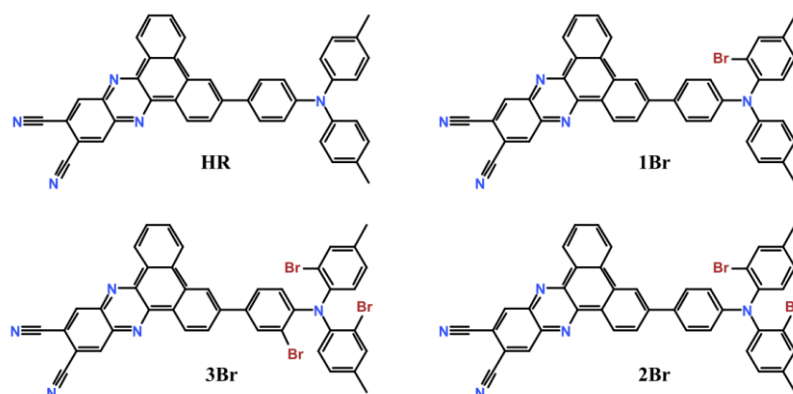$$f \sim \frac{1}{k_{rISC}}. \tag{6}$$

Taka relacja wymusza przyjęcie kompromisu, pomiędzy rozsądnie wysoką wartością siły oscylatora $f$ (aby zapewnić dostatecznie wysoką wydajność emisji światła), a akceptowalnie małą wartością przerwy energetycznej $\Delta E_{ST}$ (aby zapewnić wydajną konwersję stanów T do S, zgodnie ze wzorem (1)). Ograniczenie to stanowi obecnie poważny problem organicznych emiterów TADF o strukturze D-A.

Jednym z najbardziej atrakcyjnych sposobów na ominięcie konieczności bezwzględnego stosowania kompromisu pomiędzy $f$ oraz $\Delta E_{ST}$, jest selektywne zwiększenie czynnika przed eksponentą $A$ we wzorze (1), co jak pokazują wcześniejsze badania, można uzyskać za pomocą efektu ciężkiego atomu. Aby zweryfikować, czy ten koncept jest w stanie pozytywnie wpłynąć na parametry fotofizyczne związków z TADF wykazujących emisję w czerwonym zakresie (tzn. przyspieszyć rISC, zachowując wysoką wartość $f$ oraz PLQY), autor tej rozprawy przeprowadził szczegółowe badania spektroskopowe w opisanych dalej krokach.

**Wybór obiektów i stacjonarne charakterystyki fotoluminescencji.**

Do badań nad efektem ciężkiego atomu w czerwonym zakresie zostały wybrane pochodne znanego emitera **HR** (**Rys. 16**), który dzięki częściowo pokrywającym się HOMO i LUMO, posiada względnie wysoką wartość $f$, lecz odznacza się stosunkowo wolnym rISC [85]. W celu selektywnego przyspieszenia rISC i zwiększenia w ten sposób jego potencjału aplikacyjnego jako emitera TADF,

zaprojektowano 3 jego pochodne (**1Br**, **2Br** i **3Br** przedstawione na **Rys. 16**), różniące się między sobą liczbą wprowadzonych atomów Br w donorowym fragmencie związków.



**Rys. 16**. Struktury badanych emiterów.

Fotoluminescencyjne właściwości emiterów zostały zbadane w CBP (w stężeniu ok. 6%), często używanym jako materiał dyspersyjny (tzw. host) w warstwie emisyjnej czerwonych OLED. W pierwszym kroku, w celu określenia układu poziomów energetycznych, ustalenia natury stanów wzbudzonych, a także wyznaczenia wydajności kwantowych fotoluminescencji, dla wszystkich związków przeprowadzono serię stacjonarnych pomiarów emisji. Jak widać na **Rys. 17a**, zarejestrowane widma fotoluminescencji stopniowo przesuwają się w kierunku fal krótkich (maksimum widm zmienia się od $\lambda_{max} = 692$ nm dla **HR** do $\lambda_{max} = 602$ nm dla **3Br**), wraz ze wzrostem liczby atomów Br wprowadzanych do struktury emiterów. Obserwowana tendencja wynika ze wzrostu energii poziomu $S_1$ (**Tabela 3**), spowodowanego obecnością elektroujemnych atomów Br osłabiających fragment emitera. Natomiast z uwagi na zbliżony kształt zarejestrowanych widm przyjęto, że stany wzbudzone $S_1$ we wszystkich badanych związkach powstały wyniku przejść z przeniesieniem ładunku i dlatego odznaczają się tą samą naturą ($^1$CT).
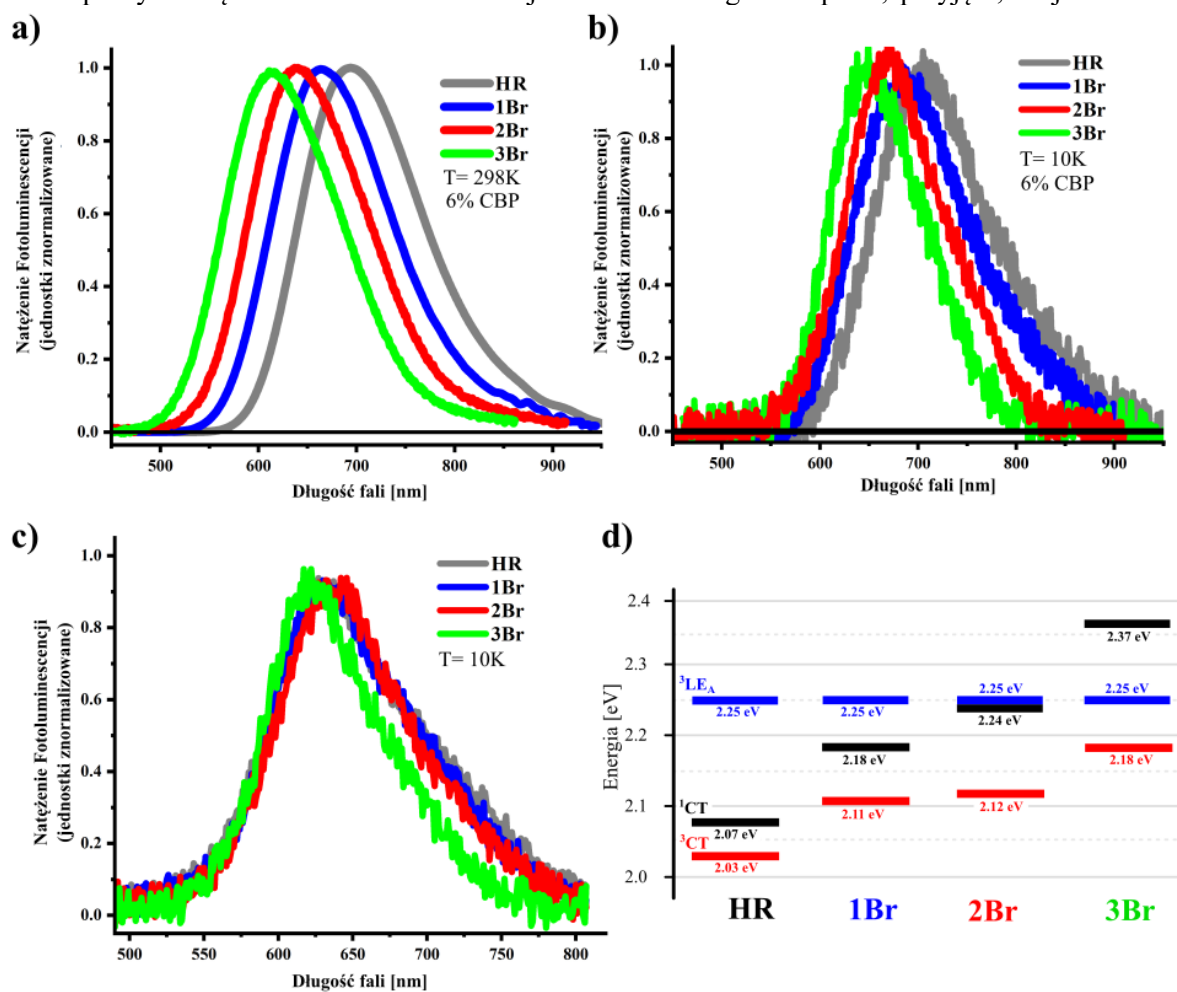
**Tabela 3**. Wydajności kwantowe fotoluminescencji (PLQY), energie poziomów energetycznych oraz wartości przerw energetycznych w badanych związkach.

|  | PLQY | $\lambda_{max}$ | energia $^1$CT | energia $^3$CT | energia $^3$LE | $\Delta E_{1CT-3CT}$ | $\Delta E_{1CT-3LE}$ |
|---|---|---|---|---|---|---|---|
|  | [%] | [nm] | [eV] | [eV] | [eV] | [eV] | [eV] |
| **HR** | 83 | 692 | 2.07 | 2.04 | 2.25 | 0.04 | -0.18 |
| **1Br** | 76 | 665 | 2.18 | 2.10 | 2.25 | 0.08 | -0.07 |
| **2Br** | 98 | 641 | 2.25 | 2.12 | 2.25 | 0.13 | 0.00 |
| **3Br** | 70 | 602 | 2.37 | 2.17 | 2.25 | 0.20 | 0.13 |

Energie stanów trypletowych określono za pomocą pomiarów fosforescencji (**Rys. 17b**) przy użyciu kamery smugowej. W CBP, z uwagi na bardzo zbliżony kształt widm zarejestrowanych w 10K oraz 298K, a także podobną tendencję przesuwania się maksimów w kierunku fal krótkich (wraz ze wzrostem liczby wprowadzanych atomów Br) przyjęto, że również najniższe stany $T_1$ dla wszystkich

emiterów powstały w wyniku przejść z przeniesieniem ładunku ($^3$CT). W celu wyznaczenia energii kolejnego stanu trypletowego (T$_2$), przeprowadzono analogiczne pomiary fosforescencji dla badanych związków w ośrodku o mniejszej polarności, polimerze – ZNX. W takim warunkach, zmierzone widma dla wszystkich emiterów są bardzo podobne zarówno pod względem kształtu jak i lokalizacji (**Rys. 17c**). W porównaniu do stanu $^3$CT, brak znaczących różnic w widmach fosforescencji pomiędzy badanymi związkami, wskazuje na odmienną od $^1$CT naturę stanu T$_2$. Ponieważ energia stanu trypletowego w ZNX (E=2.25 eV) nie ulega zmianie podczas wprowadzania atomu/ów Br, a kształt i położenie widma idealnie pokrywa się z widmem fosforescencji dla izolowanego akceptora, przyjęto, że jest to stan
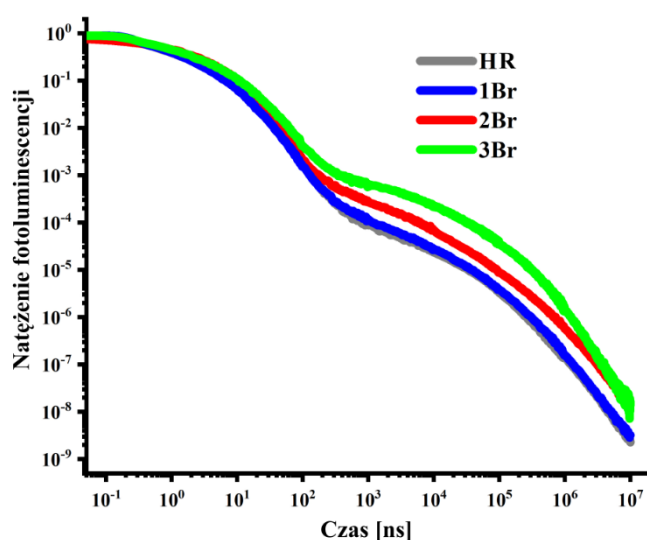


**Rys. 17**. Wyniki serii stacjonarnych pomiarów fotoluminescencji: **a)** widma fotoluminescencji zarejestrowane w 6% CBP w temperaturze pokojowej, **b)** widma fosforescencji w 6% CBP zmierzone w temperaturze 10K, **c)** widma fosforescencji w 10K w ZNX, **d)** schemat przedstawiający ułożenie poziomów energetycznych.

zlokalizowany na akceptorowym fragmencie ($^3$LE$_A$). W matrycy CBP jest on więc drugim stanem trypletowym (**Rys. 17d**).

Przechodząc do badań kinetyki fotoluminescencji, w celu określenia stałych szybkości procesów fotofizycznych zachodzących w stanach wzbudzonych, za pomocą pomiarów czasowo-rozdzielczych zarejestrowano zaniki natężenia fotoluminescencji (**Rys. 18**). W zakresie nanosekundowym, emitery **H**,

**1Br** oraz **2Br** wykazują podobną wartość czasu życia $\tau_{PF}$, w przybliżeniu równą 15 ns (**Tabela 4**). W **3Br** czas ulega wyraźnemu wydłużeniu do 27 ns, co jest spowodowane znacznym spadkiem $k_r$ względem pozostałych emiterów. Analizując proces ISC można zauważyć, że związki **2Br** i **3Br** wykazują największe wartości $k_{ISC}$, co najprawdopodobniej ma związek z bliskością stanów $^3$LE i $^1$CT. W porównaniu do **H**, średni czas życia fluorescencji opóźnionej $\tau_{DF}$ w **1Br** i **3Br** skraca około 1.5- krotnie, ponieważ w obu przypadkach zaobserwowano większy wzrost $k_{rISC}$ (odpowiednio 2- oraz 8- krotny dla **1Br** i **3Br** względem **HR**) niż $k_{ISC}$ (odpowiednio 1.5- oraz 2.5- krotny dla **1Br** i **3Br** względem **HR**).



**Rys. 18**. Zarejestrowane zaniki natężenia fotoluminescencji badanych związków w 6% CBP w temperaturze pokojowej.

**Tabela 4.** Czasy życia i stałe szybkości poszczególnych procesów fotofizycznych

|  | $\tau_{PF}$ [ns] | $\tau_{DF}$ [μs] | $k_r$ [s$^{-1}$ 10$^7$] | $k_{ISC}$ [s$^{-1}$ 10$^7$] | $k_{rISC}$ [s$^{-1}$ 10$^4$] |
|---|---|---|---|---|---|
| **HR** | 16.7 | 646 | 3.2 | 2.1 | 0.25 |
| **1Br** | 15.5 | 422 | 2.6 | 3.0 | 0.48 |
| **2Br** | 14.8 | 781 | 1.6 | 5.5 | 0.50 |
| **3Br** | 27.2 | 403 | 0.5 | 5.0 | 1.91 |

Odwrotną sytuację widać w **2Br** - w porównaniu do **HR**, $k_{rISC}$ wzrasta ok. 2- krotnie, podczas gdy $k_{ISC}$ prawie 3- krotnie, czego wynikiem jest dłuższy $\tau_{DF}$. Zebrane dane wskazują na brak addytywności efektu ciężkiego atomu ze względu na liczbę atomów **Br** wprowadzonych do struktury badanych związków. Zaprezentowane wyniki świadczą o tym, że poza samą obecnością ciężkich atomów, istotną rolę może pełnić ich wzajemna pozycja i orientacja w przestrzeni. W związku z tym, aby wskazać możliwe przyczyny obserwowanego nieregularnego wzrostu $k_{rISC}$, zostały przeprowadzone teoretyczne obliczenia kwantowo-chemiczne.

W pierwszym kroku tych obliczeń, przeprowadzono procedurę optymalizacji struktury dla każdego związku. Szczegółowa analiza geometrii pokazała, że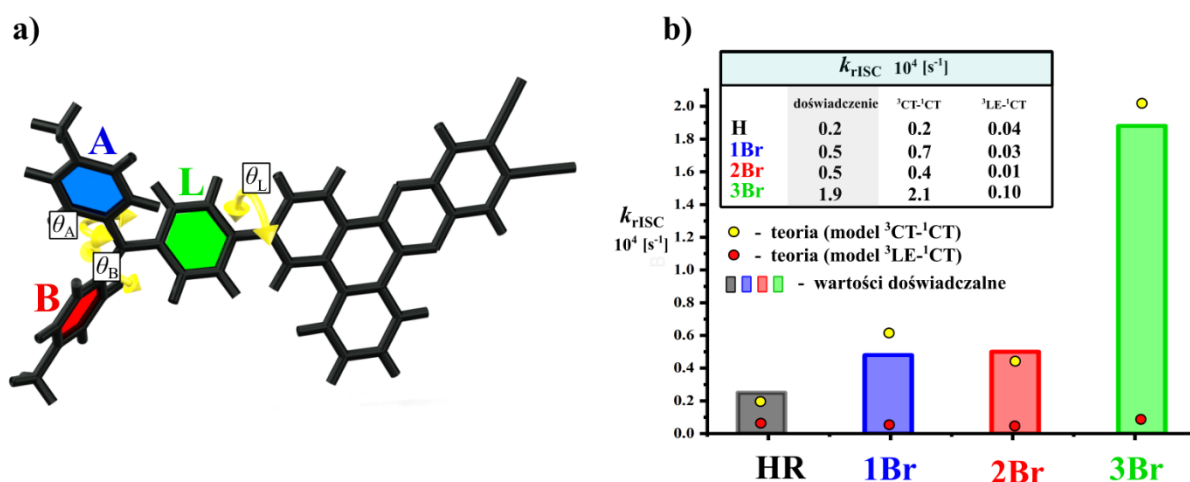 każdy z badanych emiterów, może istnieć w przynajmniej kilku swoich izomerach, w zależności od wzajemnej przestrzennej orientacji pierścieni (A, B i L **Rys. 19**) w donorze. W związku z dużym rozmiarem atomu Br, wprowadzenie ich do bocznych pierścieni aromatycznych A i B fragmentu donorowego, powoduje, że ich obroty są znacznie utrudnione. To prowadzi do ustabilizowania się różnych rotamerów każdego związku, dla których kluczowym czynnikiem różnicującym struktury są kąty torsyjne ($\theta_A$, $\theta_B$ i $\theta_L$ na **Rys. 19a**), wyznaczone przez płaszczyzny fragmentów do których wprowadzone są atomy Br. Uwzględnienie zjawiska izomerii rotacyjnej jest tym bardziej istotne, ponieważ w sztywnych ośrodkach o dużej lepkości (jakie się stosuje w OLED), rotacje tak dużych fragmentów przestają być swobodne gdyż wiążą się ze znacznym

wzrostem bariery energetycznej. Dlatego powstałe rotamery należy rozpatrywać jako odrębnie istniejące jednostki o indywidualnych właściwościach fotofizycznych.

Biorąc pod uwagę wszystkie możliwe kombinacje ułożenia bocznych pierścieni w badanych związkach, zoptymalizowano 2 stabilne rotamery dla **HR**, po 16 rotamerów dla **1Br** i **2Br** oraz 32 dla **3Br**, dla których w kolejnym kroku wyznaczono parametry dla przejść interkombinacyjnych $^3$CT→$^1$CT oraz $^3$LE$_A$→$^1$CT. Na podstawie otrzymanych wartości stałych $V$, przerw energetycznych $\Delta E_{ST}$ oraz reorganizacji energii, dla każdego rotameru, korzystając z równania Marcusa (2), określono indywidualne stałe szybkości dla procesu rISC (w ramach wspomnianych przejść: $k_{3CT→1CT}$ oraz $k_{3LE→1CT}$). Następnie, uwzględniając procentowe wkłady z populacji wszystkich izomerów (za pomocą rozkładu Boltzmanna), wyznaczono sumę statystyczną stałych szybkości, które zostały razem zestawione na **Rys 19b**. Porównując otrzymane wartości, przede wszystkim, widać bardzo dobrą korelację między wyznaczonymi teoretycznie $k_{3CT→1CT}$ ze stałymi szybkości $k_{rISC}$ uzyskanymi na drodze doświadczalnej. Stosunkowo niewielki wkład $k_{3LE→1CT}$ do rISC wynika głównie z niskiego obsadzenia poziomu $^3$LE, dlatego można wnioskować, że w każdym z badanych emiterów, dominującym szlakiem dla rISC jest przejście $^3$CT→$^1$CT.
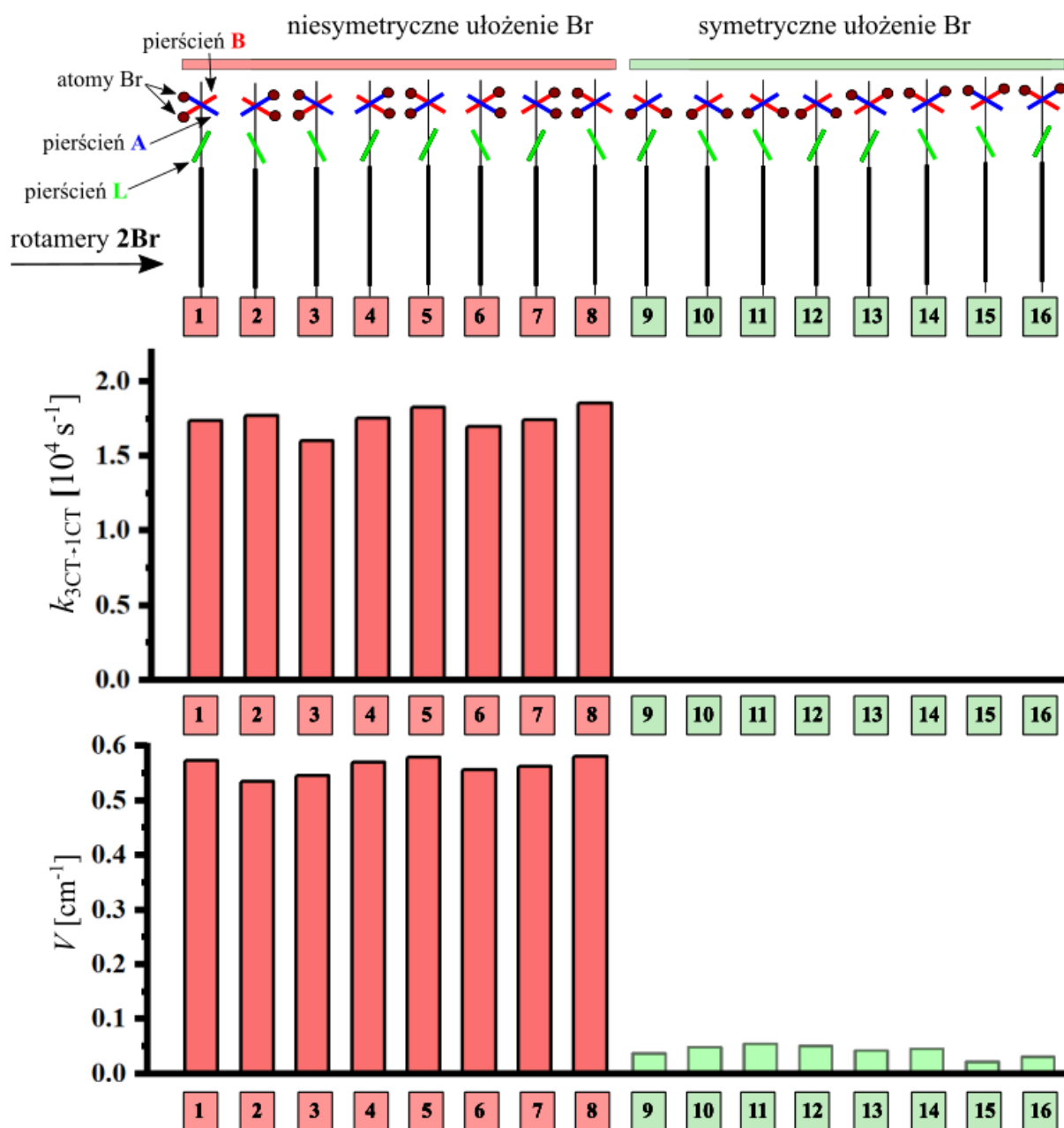


**Rys. 19**. **a)** struktura **HR** z oznaczonymi kątami torsyjnymi $\theta_A$, $\theta_B$ i $\theta_L$, **b)** porównanie wyników obliczeń teoretycznych uwzględniających modele $k_{3CT→1CT}$ oraz $k_{3LE→1CT}$ z wartościami $k_{rISC}$ uzyskanymi na drodze doświadczalnej.

Doszukując się bezpośrednich przyczyn dla których widać nieregularny trend $k_{3CT→1CT}$, przeprowadzono szczegółową analizę parametrów elektronowych w stanie wzbudzonym $^3$CT, w zależności od geometrii rotamerów dla każdego ze związków. Przede wszystkim, zaobserwowano drastyczne różnice w wartościach $V$ dla rotamerów **2Br** oraz **3Br**, wynikające ze sposobu rozmieszczenia atomów Br w strukturze tych związków.

W pochodnej **2Br**, udało się wyodrębnić dwie główne grupy rotamerów (po 8 rotamerów w każdej z grup), w których czynnikiem różnicującym jest obecność lub brak symetrii ułożenia atomów Br względem płaszczyzny akceptora. Jak widać na **Rys. 20**, w rotamerach z niesymetrycznym rozmieszczeniem ciężkich atomów (atomy Br są tylko po jednej stronie), wartości $V$ są wyraźnie większe ($V \approx 0.60$ cm$^{-1}$) od wartości wyznaczonych dla rotamerów, w których oba atomy Br są ułożone po obu stronach płaszczyzny akceptora ($V \approx 0.05$ cm$^{-1}$). Wartości innych parametrów takich jak $\Delta E_{ST}$ oraz reorganizacja energii $\lambda$ pozostają tu bez większych zmian, dlatego w konsekwencji, obserwujemy skrajnie różne wartości indywidualnych stałych szybkości $k_{3CT \to 1CT}$. Dla rotamerów z symetrycznym rozmieszczeniem Br $k_{3CT \to 1CT}$ osiąga 2.0 x 10$^4$ s$^{-1}$ podczas gdy najwyższa odpowiadająca wartość $k_{3CT \to 1CT}$ dla rotamerów z niesymetrycznym ułożeniem Br to zaledwie 2.7 x 10$^1$ s$^{-1}$.

Analogiczne wnioski można wyciągnąć analizując geometrię rotamerów emitera **3Br**, wykazującego najbardziej złożoną izomerię. Najmniejsze wartości $V$ (oraz indywidualne $k_{3CT \to 1CT}$) obserwuje się w sytuacji najbardziej symetrycznego rozmieszczenia atomów Br (np. $V = 0.58$ cm$^{-1}$, $k_{3CT \to 1CT} = 0.1$ x 10$^4$ s$^{-1}$), podczas gdy najwyższe wartości $V$ odpowiadają rotamerom, o wysoce niesymetrycznym ułożeniu ciężkich atomów, prowadząc do najwyższych dla tej grupy wartości $k_{3CT \to 1CT} = 8.2$ x 10$^4$ s$^{-1}$.

Poza opisanymi spostrzeżeniami należy podkreślić, że na podstawie obliczeń DFT oraz danych eksperymentalnych, w badanych emiterach stwierdzono brak związku pomiędzy $f$ oraz $k_{3CT \to 1CT}$. Pomimo bardzo różnych wartości $V$ (i odpowiadającym $k_{3CT \to 1CT}$), siła oscylatora $f$ pozostaje bez większych zmian. Tak więc, wprowadzenie ciężkiego atomu przyspiesza proces rISC (jak ustalono wcześniej, za pośrednictwem teoretycznie wzbronionego szlaku $^{3}CT \to {}^{1}CT$) i równocześnie nie powoduje zmniejszenia wartości siły oscylatora.



**Rys. 20**. Zestawienie 16 izomerów **2Br** z uwzględnieniem symetrii i odpowiadające im wartości $V$ oraz $k_{3CT \to 1CT}$.

Przedstawione wyżej obserwacje prowadzą do sformułowania kilku ważnych wniosków. Przede wszystkim, z uzyskanych danych doświadczalnych można sądzić, że wprowadzenie atomów Br do struktury emitera **HR** istotnie przyspiesza rISC, nie pogarszając znacząco właściwości emisyjnych (nie zaobserwowano drastycznego spadku PLQY oraz *f*). Co więcej, pochodna **3Br** odznacza się pożądaną selektywnością przyspieszania procesów międzysystemowych: zarejestrowano 8-krotne przyspieszenie rISC i zaledwie 2.5-krotne dla ISC. Z tego powodu, ten związek cechuje się najwyższą wartością aplikacyjną.

W wyniku przeprowadzonych obliczeń DFT ustalono, że ilość wprowadzonych ciężkich atomów do struktury emitera nie stanowi jedynego kryterium, gwarantującego poprawę kinetycznych parametrów fotofizycznych (w kontekście zjawiska TADF). Czynnikiem decydującym o sile efektu ciężkiego atomu okazuje się być sposób rozmieszczenia pierwiastków o dużej liczbie atomowej. Najlepszym przykładem są izomery emitera **2Br**: wysoka symetria w ułożeniu atomów Br prowadzi do kompensacji pola wywołanego przez te atomy i w rezultacie przyspieszenie przejść międzysystemowych nie występuje, podczas gdy inne rotamery **2Br** z niesymetrycznym rozmieszczeniem Br wykazują spodziewany znaczny wzrost stałych szybkości dla rISC oraz ISC.

Ponadto, odkrycie tej zależności może tłumaczyć wcześniej zaobserwowany efekt, który został nazwany przez autorów "anty-efektem ciężkiego atomu", gdzie w badanych związkach o wysokiej symetrii ułożenia ciężkich atomów nie dochodziło do oczekiwanego wzrostu *V* [81]. Na poparcie naszej hipotezy, w innych badanych przez nich związkach o niesymetrycznym rozmieszczeniu atomów Br efekt ciężkiego atomu został wyraźnie zaobserwowany.

Na zakończenie, podobnie jak w pracy [**P2**] i [**P3**] przeprowadzone tu teoretyczne obliczenia dla **HR** oraz jego pochodnych w ramach opracowanego wcześniej modelu rotacyjnego, przemawiają za słusznością proponowanego mechanizmu TADF zakładającego wiodącą rolę szlaku $^3CT \rightarrow {}^1CT$.

# Podsumowanie

W pierwszej części rozprawy przedstawiono opis przeprowadzonych badań nad pochodnymi 2'-hydroksychalkonów, w których zachodzi zjawisko wewnątrzmolekularnego przeniesienia protonu w stanie wzbudzonym (ESIPT) oraz zjawisko emisji indukowanej agregacją (AIE). Ustalono, że w aprotycznych rozpuszczalnikach, 2'-hydroksychalkony są wyjątkowo niestabilne i ulegają złożonemu fotoindukowanemu procesowi degradacji, który w rezultacie prowadzi do powstania flawanonów, pozbawionych zdolności emisyjnych. Reakcja ta obejmuje wiele etapów, między innymi ESIPT, izomeryzację, cyklizację oraz transfer protonu w stanie podstawowym. Za pomocą przeprowadzonych badań na pochodnych 2'-hydroksychalkonów zawierających w swojej strukturze ciężki atom (Cl, Br), wykluczono znaczący udział stanów trypletowych w procesie fotodegradacji. Stwierdzono wysoką wrażliwość tej reakcji na warunki środowiska w których zachodzi: jej kinetyka wyraźnie zależy od polarności, a obecność protycznych cząsteczek metanolu całkowicie hamuje reakcję dzięki utworzeniu międzymolekularnych wiązań wodorowych. Ustalono, że fotodegradacja jest procesem odwracalnym, którego kierunek można kontrolować za pomocą długości fali światła. W fazie krystalicznej, z powodu usztywnienia struktury, zbadane 2'-hydroksychalkony odznaczają się wysoką fotostabilnością, a pochodne zawierające grupę dimetyloaminową wykazują silną emisję w czerwonym zakresie dzięki zjawisku AIE.

Druga część rozprawy poświęcona jest opisowi wykonanych badań nad organicznymi emiterami, w których zachodzi zjawisko termicznie aktywowanej opóźnionej fluorescencji (TADF). W wyniku przeprowadzonych pomiarów doświadczalnych skorelowanych z wynikami obliczeń teoretycznych dla związku DMAC-TRZ ustalono, że prawidłowy opis mechanizmu TADF w emiterach o strukturze typu donor-akceptor jest niemożliwy, bez uwzględnienia teoretycznie zabronionego szlaku dla odwrotnego przejścia międzysystemowego (rISC) pomiędzy stanami o tej samej naturze $^3$CT$\rightarrow$$^1$CT. Na podstawie tych wniosków, doświadczalnej weryfikacji i szczegółowej analizie teoretycznej został poddany koncept, polegający na przyspieszeniu rISC za pomocą wywołania efektu ciężkiego atomu (HAE). W tym celu, zaprojektowano i otrzymano pochodne DMAC-TRZ, zawierające w swojej strukturze atomy Cl i Br. W wyniku przeprowadzonych pomiarów fotofizycznych stwierdzono, że najsilniejszy efekt wykazuje pochodna z Br, dla której odnotowano około 2.5-krotne przyspieszenie ISC i 1.5-krotne przyspieszenie rISC względem wyników uzyskanych dla związku wyjściowego - DMAC-TRZ. W celu ustalenia mechanizmu TADF w tych związkach, opracowano nową metodologię analizy danych doświadczalnych, umożliwiającą wyznaczenie wartości stałych sprzężenia spin-orbita na podstawie badania wrażliwości stałych szybkości przejść międzysystemowych na zamianę temperatury. Dzięki temu możliwe staje się określenie natury stanów wzbudzonych zaangażowanych w konkretny szlak.

Stosując opracowaną metodologię stwierdzono, że w ISC dominuje szlak obejmujący stany o różnej naturze, tj. $^1CT \rightarrow {}^3LE_D$, podczas gdy rISC głównie opiera się na przejściu $^3CT \rightarrow {}^1CT$. Jak ustalono, dominację kanału $^3CT \rightarrow {}^1CT$ w rISC można wytłumaczyć używając opracowanego modelu rotacyjno-wibracyjnego, który poza drganiami fragmentów donora i akceptora, uwzględnia także wibracje wyższych rzędów, w które szczególnie zaangażowane są atomy Br. Odnosząc się do wartości aplikacyjnej otrzymanych pochodnych, pomimo uzyskania przyspieszenia rISC w Br, to większa wrażliwość HAE na ISC (prawdopodobnie z uwagi na bliskość stanów $^3LE_D$ i $^1CT$) niż rISC, a także drastyczny spadek wydajności kwantowych fotoluminescencji (PLQY) niestety zmniejsza ich potencjał wdrożeniowy w nowoczesnych urządzeniach optoelektronicznych.

Kontynuując wątek zjawiska HAE w organicznych emiterach z TADF, szczegółowym badaniom zostały poddane inne związki z ciężkimi atomami z emisją w czerwonym zakresie, różniące się między sobą liczbą wprowadzonych do struktury atomów Br. Przede wszystkim, na podstawie wykonanych czasoworozdzielczych pomiarów fotoluminescencji ustalono, że stała szybkości dla rISC ($k_{rISC}$) zmienia się w sposób nieliniowy w zależności od liczby wprowadzonych atomów Br. Wyraźny brak addytywności zjawiska HAE wskazuje, że poza samą obecnością ciężkich atomów, istotną rolę w przyspieszaniu rISC muszą pełnić także inne czynniki. Przeprowadzone obliczenia teoretyczne ujawniły, że każdy z badanych emiterów, posiada przynajmniej kilka izomerów, zróżnicowanych pod względem przestrzennego rozmieszczenia bocznych pierścieni aromatycznych, do których wprowadzone są atomy Br. Ustalono, że wzajemna orientacja tych fragmentów ma kluczowe znaczenie dla rISC: wysoka symetria ułożenia ciężkich atomów prowadzi do kompensacji sprzężenia spinowo-orbitalnego i w rezultacie nie obserwuje się HAE, pomimo obecności ciężkich atomów. Zastosowanie wcześniej wypracowanego modelu rotacyjnego potwierdziło, że obserwowane doświadczalnie przyspieszenie rISC zachodzi głównie dzięki oddziaływaniu stanów tej samej natury $^3CT \rightarrow {}^1CT$. Dzięki około 8-krotnemu przyspieszeniu rISC oraz braku istotnego spadku PLQY, uzyskana pochodna zawierająca 3 atomy Br, odznacza się wyjątkowo wysoką wartością aplikacyjną.

# Literatura

[1] A. D'Aleo, A. Felouat, F. Fages. Boron difluoride complexes of 2'-hydroxychalcones and curcuminoids as fluorescent dyes and for photonic applications. Adv. Nat. Sci: Nanosci. Nanotechnol. 2014, **6**, 015009.

[2] X. Cheng, K. Wang, S. Huang, H. Zhang, H. Zhang, Y. Wang. Organic Crystals with Near-Infrared Amplified Spontaneous Emission Based on 2—hydroxychalcone Derivative: Subtle Structure Modifcation but Great Property Change. *Angew. Chem.* 2015, **54**, 8369-8373.

[3] G. R. Suman, M. Pandey, A. Chakravarthy. Review on new horizons of aggregation induced emission: from design to development. *Mater. Chem. Front.* 2021, **5**, 1541-1584.

[4] M. Dommett, M. Rivera, R. Crespo-Otero. How Inter- and Intramolecular Processes Dictate Aggregation-Induced Emission in Crystals Undergoing Excited-State Proton Transfer. *J. Phys. Chem. Lett.* 2017, **8**, 6148–6153.

[5] S. Kagatikar, D. Sunil. Aggregation induced emission of chalcones. *Chem. Pap.* 2021, **75**, 6147-6156.

[6] Y. Li, Z. Xu, X. Zhu, B. Chen, Z. Wang, B. Xiao, J. W. Y. Lam, Z. Zhao, D. Ma, B. Zhong Tang. Creation of Efficient Blue Aggregation-Induced Emission Luminogens for High-Performance Nondoped Blue OLEDs and Hybrid White OLEDs. *ACS Appl. Mater. Interfaces* 2019, **11**, 17592-17601.

[7] Z. Xu, J. Gu, X. Qiao, A. Qin, B. Zhong Tang, D. Ma. Highly Efficient Deep Blue Aggregation-Induced Emission Organic Molecule: A Promising Multifunctional Electroluminescence Material for Blue/Green/Orange/Red/White OLEDs with Superior Efficiency and Low Roll-Off. *ACS Photonics* 2019, **6**, 767-778.

[8] H. Zhang, A. Li, G. Li, B. Li, Z. Wang, S. Xu, B. Zhong Tang. Achievement of High-Performance Nondoped Blue OLEDs Based on AIEgens via Construction of Effective High-Lying Charge-Transfer State. *Adv. Opt. Mater.* 2020, **14**, 1902195.

[9] P. A. A. M. Vaz, J. Rocha, A. M. S. Silva, S. Guieu. Aggregation-induced emission enhancement in halochalcones. New J. Chem. 2016, **40**, 8198-8201.

[10] A. D'Aleo, E. Zaborova, F. Fages. Effect of Methoxy Substitution on Supramolecular Arrangement of Borondifluorides of 2'-Hydroxy Chalcones and their Solid-State NIR Fluorescence. *Croat. Chem. Acta* 2017, **90**, 583–588. DOI: 10.5562/cca3241

[11] A. D'Aleo, A. Saul, C. Attaccalite, F. Fages. Influence of halogen substitution on aggregationinduced near infrared emission of borondifluoride complexes of 2'-hydroxychalcones. *Mater. Chem. Front.* 2019, **3**, 86—92. DOI: 10.1039/c8qm00478a

[12] N. I. Zahid, M. S. Mahmood, B. Subramanian, S. M. Said, O. K. Abou-Zied. New Insight into the Origin of the Red/Near-Infrared Intense Fluorescence of a Crystalline 2-Hydroxychalcone Derivative: A Comprehensive Picture from the Excited-State Femtosecond Dynamics. *J. Phys. Chem. Lett.* 2017, **8**, 5603-5608. DOI: 10.1021/acs.jpclett.7b02601

[13] H. C. Joshi, L. Antonov. Excited-State Intramolecular Proton Transfer: A Short Introductory Review. *Molecules* 2021, **26**, 1475. DOI: 10.3390/molecules26051475

[14] L. Ma, Y. Yu, S. Duan, L. Yu, R. Zhang, Z. Wang, K. Lin. Enhanced solid-state photoluminescence and fluorescence spectral behaviors for an ESIPT molecule: An experimental and theoretical investigation *J. Mol. Liq.* 2020, **318**, 114176. DOI: 10.1016/j.molliq.2020.114176

[15] V. S. Padalkar, S. Seki. Excited-state intramolecular proton-transfer (ESIPT)-inspired solid state emitters. *Chem. Soc. Rev.* 2016, **45**, 169-202. DOI: 10.1039/c5cs00543d

[16] L. Wu, H-H. Han, L. Liu, J. E. Gardiner, A. C. Sedgwick, C. Huang, S. D. Bull, X.-P. He, T. D. James. ESIPT-based fluorescence probe for the rapid detection of peroxynitrite 'AND' biological thiols. *Chem. Commun.* 2018, **54**, 11336-11339. DOI: 10.1039/C8CC06917D

[17] H. Guan, A. Zhang, P. Li, L. Xia, F. Guo. ESIPT Fluorescence Probe Based on Double-Switch Recognition Mechanism for Selective and Rapid Detection of Hydrogen Sulfide in Living Cells. *ACS Omega* 2019, **4**, 9113-9119. DOI: 10.1021/acsomega.9b00934

[18] I. E. Serdiuk, M. Reszka, A. Synak, B. Liberek, P. Bojarski. Determination of low-activity hydrolases using ESIPT fluorescent indicators on silver surfaces. *Dyes Pigm.* 2018, **149**, 224-228. DOI: 10.1016/j.dyepig.2017.09.067

[19] M. K. Bera, C. Chakraborty, P. K. Singh, C. Sahu, K. Sen, S. Maji, A. K. Das, S. Malik. Fluorene-based chemodosimeter for "turn-on" sensing of cyanide by hampering ESIPT and live cel imaging *J. Mater. Chem. B* 2014, **2**, 4733 – 4739. DOI: 10.1039/c4tb00388h

[20] S. Goswami, A. Manna, S. Paul, A. K. Das, P. K. Nandi, A. K. Maity, P. Saha. A turn on ESIPT probe for rapid and ratiometric fluorogenic detection of homocysteine and cysteine in water with live cell-imaging. *Tetrahedron Lett.* 2014, **55**, 490-494. DOI: 10.1016/j.tetlet.2013.11.055

[21] L. Tang, M. Tian, H. Chen, X. Yan, K. Zhong, Y. Bian. An ESIPT-based mitochondria-targeted ratiometric and NIR-emitting fluorescent probe for hydrogen peroxide and its bioimaging in living cells. *Dyes Pigm.* 2018, **158**, 482-489. DOI: 10.1016/j.dyepig.2017.12.028

[22] J. E. Kwon, S. Y. Park. Advanced Organic Optoelectronic Materials: Harnessing Excited-State Intramolecular Proton Transfer (ESIPT) Process. *Adv. Mater.* 2011, **23**, 3615–3642. DOI: 10.1002/adma.201102046

[23] A. C. Sedgwick, L. Wu, H-H. Han, S. D. Bull, X-P. He, T. D. James, J. L. Sessler, B. Z. Tang, H. Tian, J. Yoon. Excited-state intramolecular proton-transfer (ESIPT) based fluorescence sensors and imaging agents. *Chem. Soc. Rev.,* 2018,**47**, 8842-8880. DOI: 10.1039/C8CS00185E

[24] S. Park, J. E. Kwon, S. H. Kim, J. Seo, K. Chung, S-Y. Park, D-J. Jang, B. M. Medina, J. Gierschner, S. Y. Park. A White-Light-Emitting Molecule: Frustrated Energy Transfer between Constituent Emitting Centers. *J. Am. Chem. Soc*. 2009**, 131**, 14043–14049. DOI: 10.1021/ja902533f

[25] K-C. Tang, M-J. Chang, T-Y. Lin, H-A. Pan, T-C. Fang, K-Y. Chen, W-Y. Hung, Y-H. Hsu, P. T. Chou. Fine Tuning the Energetics of Excited-State Intramolecular Proton Transfer (ESIPT): White Light Generation in A Single ESIPT System. *J. Am. Chem. Soc.* 2011, **133**, 17738–17745. DOI: 10.1021/ja2062693

[26] I. E. Serdiuk. White Light from a Single Fluorophore: A Strategy Utilizing Excited-State Intramolecular Proton-Transfer Phenomenon and Its Verification. *J. Phys. Chem. C* 2017, **121**, 5277–5286. DOI: 10.1021/acs.jpcc.7b00137

[27] V. Trannoy, A. Leaustic, S. Gadan, R. Gulliot, C. Allain, G. Clavier, S. Mazerat, B. Geffroy, P. Yu. A highly efficient solution and solid state ESIPT fluorophore and its OLED application. *New J. Chem*., 2021,**45**, 3014-3021. DOI: 10.1039/D0NJ05600F

[28] K-i. Sakai, T. Ishikawa, T. Akutagawa. A blue-white-yellow color-tunable excited state intramolecular proton transfer (ESIPT) fluorophore: sensitivity to polar–nonpolar solvent ratios. *J. Mater. Chem. C*, 2013, **1**, 7866-7871. DOI: 10.1039/C3TC31526F

[29] R. Matsushima, I. Hirao. Photocyclization of 2'-Hydroxychalcones to 4-Flavanones. *Bull. Chem. Soc. Jpn.* 1980, **53**, 518-522. DOI: 10.1246/bcsj.53.518

[30] P. T. Chou, M. L. Martinez, W. C. Cooper. Direct evidence of excited-state intramolecular proton transfer in 2'-hydroxychalcone and photooxygenation forming 3-hydroxyflavone. *Am. Chem. Soc*. 1992, **114**, 4943–4944. DOI: 10.1021/ja00038a091

[31] R. Matsushima, H. Kageyama. Photochemical Cyclization of 2'-Hydroxychalcones. *J. Chem. Soc. Perkin Trans. II 1985*, **2**, 743-748. DOI: 10.1039/P29850000743

[32] T. Teshima, M. Takeishi, T. Arai. Red fluorescence from tautomers of 2'-hydroxychalcones induced by intramolecular hydrogen atom transfer. *New J. Chem*. 2009, **33**, 1393–1401. DOI: 10.1039/B823431K

[33] IUPAC. Compendium of Chemical Terminology, 2nd ed. (the "Gold Book"). Compiled by A. D. McNaught and A. Wilkinson. Blackwell Scientific Publications, Oxford (1997). DOI: 10.1351/goldbook

[34] C. A. Kenfack, A. S. Klymchenko, G. Duportail, A. Burger, Y. Mely. Ab initio study of the solvent H-bonding effect on ESIPT reaction and electronic transitions of 3-hydroxychromone derivatives. *Phys. Chem. Chem. Phys.* 2012,**14**, 8910-8918. DOI: 10.1039/C2CP40869D

[35] D. Ghosh, S. Batuta, N. A. Begum, D. Mandal. Unusually slow intramolecular proton transfer dynamics of 4′-N,N-dimethylamino-3-hydroxyflavone in high n-alcohols: involvement of solvent relaxation. Photochem. Photobiol. Sci. 2016, **15**, 266–277. DOI: 10.1039/C5PP00377F

[36] https://noctiluca.eu/pl/ Data dostępu: 15.11.2022

[37] H-W. Chen, J-H. Lee, B-Y. Lin, S. Chen, S-T. Wu. Liquid crystal display and organic light-emitting diode display: present status and future perspectives. *Light Sci Appl*. 2018, **7**, 17168. DOI: 10.1038/lsa.2017.168

[38] U. Błaszczak, M. Zajkowski, Ł. Budzyński. Analiza parametrów kolorymetrycznych wybranych urządzeń z wyświetlaczami LCD/OLED w funkcji kąta obserwacji. Przegląd Elektrotechniczny 2015, **91**, 167-170. DOI:10.15199/48.2015.04.37

[39] K. Haase, M. Hambsch, C. Teixeira de Rocha, J. Zessin, S. C. B. Mannsfeld. Advances in solution processing of organic materials for devices. Handbook of Organic Materials for Electronic and Photonic Devices 2019, 553. DOI: 10.1016/B978-0-08-102284-9.00017-6

[40] G. Hong, X. Gan, C. Leonhardt, Z. Zhang, J. Seibert, J. M. Busch, S. Brase. A Brief History of OLEDs— Emitter Development and Industry Milestones. *Adv. Mater.* 2021, **33**, 2005630. DOI: 10.1002/adma.202005630

[41] M. Inoue, T. Serevicius, H. Nakatomani, K. Yoshida, T. Matsushima, S. Jursenas, C. Adachi. Effect of reverse intersystem crossing rate to suppress efficiency roll-off in organic light-emitting diodes with thermally activated delayed fluorescence emitters. *Chem. Phys. Lett.* 2016, **644**, 62-67. DOI: 10.1016/j.cplett.2015.11.042

[42] C. W. Tang, S. A. Van Slyke. Organic electroluminescent diodes. *Appl. Phys. Lett*. 1987, **51**, 913. DOI: 10.1063/1.98799

[43] H. Uoyama, K. Goushi, K. Shizu, H. Nomura, C. Adachi. Highly efficient organic light-emitting diodes from delayed fluorescence. *Nature* 2012, **492**, 234. DOI: 10.1038/nature11687.

[44] C. Adachi. Third-generation organic electroluminescence materials. *Jpn. J. Appl. Phys.* 2014, **53**, 060101. DOI: 10.7567/JJAP.53.060101

[45] J. Avo, T. Palmeira, F. B. Dias. Thermally Activated Delayed Fluorescence Emitters for Light-Emitting Diodes and Sensing Applications w B. Pedras, (eds) Fluorescence in Industry. Springer Series on Fluorescence, vol 18. DOI: 10.1007/4243_2019_8

[46] M. A. El Sayed. *J. Chem. Phys*. 1963, **38**, 2834 —2838 DOI: 10.1063/1.1733610

[47] C. M. Marian. Spin–orbit coupling and intersystem crossing in molecules. *WIREs Comput. Mol. Sci.* 2012, **2**, 187-203. DOI: 10.1002/wcms.83

[48] H. Noda, X-K. Chen, H. Nakatomani, T. Hosokai, M. Miyajima, N. Notsuka, J-L. Bredas, C. Adachi. Critical role of intermediate electronic states for spin-flip processes in charge-transfer-type organic molecules with multiple donors and acceptors. *Nat. Mater.* 2019, **18**, 1084-1090. DOI: 10.1038/s41563-019-0465-6

[49] P. K. Samanta, D. Kim, V. Coropceanu, J-L. Bredas. Up-Conversion Intersystem Crossing Rates in Organic Emitters for Thermally Activated Delayed Fluorescence: Impact of the Nature of Singlet vs Triplet Excited States. *J. Am. Chem. Soc*. 2017, **139**, 4042–4051. DOI: 10.1021/jacs.6b12124

[50] F. B. Dias, J. Santos, D. R. Graves, P. Data, R. S. Nobuyasu, M. A. Fox, A. S. Batsanov, T. Palmeira, M. N. Berberan-Santos, M. R. Bryce, A. P. Monkman. The Role of Local Triplet Excited States and D-A Relative

Orientation in Thermally Activated Delayed Fluorescence: Photophysics and Devices. *Adv. Sci*. 2016, **3**, 1600080. DOI: 10.1002/advs.201600080

[51] J. Gibson, A. P. Monkman, T. J. Penfold. The Importance of Vibronic Coupling for Efficient Reverse Intersystem Crossing in Thermally Activated Delayed Fluorescence Molecules. *Chem. Phys. Chem*. 2016, **17**, 2956-2961. DOI: 10.1002/cphc.201600662

[52] F. B. Dias, K. N. Bourdakos, V. Jankus, K. C. Moss, K. T. Kamtekar, V. Bhalla, J. Santos, M. R. Bryce, A. P. Monkman. *Adv. Mat*. 2013, **25**, 3707-3714. DOI: 10.1002/adma.201300753

[53] S-J. Woo, Y-H. Kim, J-J. Kim. Dihedral Angle Distribution of Thermally Activated Delayed Fluorescence Molecules in Solids Induces Dual Phosphorescence from Charge-Transfer and Local Triplet States. *Chem. Mater.* 2021, **33**, 5618-5630. DOI: 10.1021/acs.chemmater.1c01011

[54] I. Kim, S. O. Jeon, D. Jeong, H. Choi, W-J. Son, D. Kim, Y. M. Rhee, H. S. Lee. Spin–Vibronic Model for Quantitative Prediction of Reverse Intersystem Crossing Rate in Thermally Activated Delayed Fluorescence Systems. *J. Chem. Theory Comput*. 2020, **16**, 621–632. DOI: 10.1021/acs.jctc.9b01014

[55] D. Kelly, L. G. Franca, K. Stavrou, A. Danos, A. P. Monkman. Laplace Transform Fitting as a Tool To Uncover Distributions of Reverse Intersystem Crossing Rates in TADF Systems. *J. Phys. Chem. Lett*. 2022, **13**, 6981–6986. DOI: 10.1021/acs.jpclett.2c01864

[56] S-J. Woo, J-J. Kim. TD-DFT and Experimental Methods for Unraveling the Energy Distribution of Charge-Transfer Triplet/Singlet States of a TADF Molecule in a Frozen Matrix. *J. Phys. Chem. A* 2021, **125**, 1234–1242. DOI: 10.1021/acs.jpca.0c11322

[57] IUPAC. Compendium of Chemical Terminology, 2nd ed. (the "Gold Book"). Compiled by A. D. McNaught and A. Wilkinson. Blackwell Scientific Publications, Oxford (1997). DOI: 10.1351/goldbook.

[58] R. A. Marcus. On the Theory of Oxidation-Reduction Reactions Involving Electron Transfer I. *J. Chem. Phys.* 1956, **24**, 966–978 DOI: 10.1063/1.1742723

[59] A. Kretzschmar, C. Patze, S. T. Schwaebel, U. H. F. Bunz. Development of Thermally Activated Delayed Fluorescence Materials with Shortened Emissive Lifetimes. *J. Org. Chem.* 2015, **80**, 9126–9131. DOI: 10.1021/acs.joc.5b01496

[60] H. S. Kim, L. Y. Lee, S. Shin, W. Jeong, S. H. Lee, S. Kim, J. Lee, M. C. Suh, S. Yoo. Enhancement of Reverse Intersystem Crossing in Charge-Transfer Molecule through Internal Heavy Atom Effect. *Adv. Funct. Mater.* 2021, **31**, 2104646. DOI: 10.1002/adfm.202104646

[61] Y. Xiang, Y. Zhao, N. Xu, S. Gong, F. Ni, K. Wu, J. Luo, G. Xie, Z-H. Lu, C. Yang. Halogen-induced internal heavy-atom effect shortening the emissive lifetime and improving the fluorescence efficiency of thermally activated delayed fluorescence emitters. *J. Mater. Chem. C*, 2017, **5**, 12204-12210. DOI: 10.1039/C7TC04181K

[62] S. Gan, S. Hu, X-L. Li, J. Zeng, D. Zhang, T. Huang, W. Luo, W. Luo, Z. Zhao, L. Duan, S-J. Su, B. Z. Tang. Heavy Atom Effect of Bromine Significantly Enhances Exciton Utilization of Delayed Fluorescence Luminogens. ACS Appl. Mater. Interfaces 2018, **10**, 17327–17334. DOI: 10.1021/acsami.8b05389

[63] D. Song, Y. Yu, L. Yue, D. Zhong, Y. Zhang, X. Yang, Y. Sun, G. Zhou, Z. Wu. Asymmetric thermally activated delayed fluorescence (TADF) emitters with 5,9-dioxa-13b-boranaphtho[3,2,1-de]anthracene (OBA) as the acceptor and highly efficient blue-emitting OLEDs. *J. Mater. Chem. C*, 2019,**7**, 11953-11963. DOI: 10.1039/C9TC04115J

[64] T. Huang, X. Song, M. Cai, D. Zhang, L. Duan. Improving reverse intersystem crossing in exciplex-forming hosts by introducing heavy atom effect. *Mater.* 2021, **21**, 100705. DOI: 10.1016/j.mtener.2021.100705

[65] J. Lee, N. Aizawa, M. Numata, C. Adachi, T. Yasuda. Versatile Molecular Functionalization for Inhibiting Concentration Quenching of Thermally Activated Delayed Fluorescence. *Adv. Mater.* 2016, **29**, 1604856. DOI: 10.1002/adma.201604856

[66] Y. Ren, Y. Wada, K. Suzuki, Y. Kusakabe, J. Geldsetzer, H. Kali. Thioxanthone-based thermally activated delayed fluorescence emitters showing fast reverse intersystem crossing for efficient organic light-emitting diodes with small efficiency roll-off. *Europe PMC* 2021. 10.21203/rs.3.rs-289667/v1

[67] T. Hua, L. Zhan, N. Li, Z. Huang, X. Cao, Z. Xiao, S. Gong, C. Zhou, C. Zhong, C. Yang. Heavy-Atom Effect Promotes Multi-Resonance Thermally Activated Delayed Fluorescence. *Chem. Eng. J.* 2021, 426, 131169. DOI: 10.26434/chemrxiv.14046296.v1

[68] M. Einzinger, T. Zhu, P. de Silva, C. Belger, T. M. Swager, T. Van Voorhis, M. A. Baldo. Shorter Exciton Lifetimes via an External Heavy-Atom Effect: Alleviating the Effects of Bimolecular Processes in Organic Light-Emitting Diodes. *Adv. Mater.* 2017, **29**, 1701987. DOI: 0.1002/adma.201701987

[69] I. S. Park, H. Min, T. Yasuda. Ultrafast Triplet–Singlet Exciton Interconversion in Narrowband Blue Organoboron Emitters Doped with Heavy Chalcogens. *Angew. Chem.* 2022, 134, e202205684. DOI: 10.1002/ange.202205684

[70] J. Sivanarayanan, E. Sebastian, K. Vinod, F. Wurthner, M. Hariharan. Ultrafast Intersystem Crossing in Selenium-Annulated Perylene Bisimide. *J. Phys. Chem. C* 2022, **126**, 13319–13326. DOI: 10.1021/acs.jpcc.2c03847

[71] Y-F. Xiao, J-X. Chen, W-C. Chen, X. Zheng, C. Cao, J. Tan, X. Cui, Z. Yuan, S. Ji, G, Lu, W. Liu, P. Wang, S. Li, C-S. Lee. Achieving high singlet-oxygen generation by applying the heavy-atom effect to thermally activated delayed fluorescent materials. *Chem. Commun.* 2021,**57**, 4902-4905. DOI: 10.1039/D0CC08323B

[72] G. Farias, C. A. M. Salla, M. Aydemir, L. Sturm, P. Dechambenoit, F. Durola, B. de Souza, H. Bock, A. P. Monkman, I. H. Bechtold. *Chem. Sci.* 2021,**12**, 15116-15127. DOI: 10.1039/d1sc04936d *Chem. Mater.* 2020, **32**, 2583-2592. DOI: 10.1021/acs.chemmater.0c00078

[73] D. R. Lee, K. H. Lee, W. Shao, C. L. Kim, J. Kim, J. Y. Lee. Heavy Atom Effect of Selenium for Metal-Free Phosphorescent Light-Emitting Diodes. *Chem. Mater.* 2020, **32**, 2583–2592. DOI: 10.1021/acs.chemmater.0c00078

[74] S. Goto, Y. Nitta, N. O. Decarli, L. E. de Sousa, P. Stachelek, N. Tohnai, S. Minakata, P. de Silva, P. Data, Y. Takeda. Revealing the internal heavy chalcogen atom effect on the photophysics of the dibenzo[a,j]phenazine-cored donor–acceptor–donor triad. *J. Mater. Chem. C*, 2021,**9**, 13942-13953. DOI: 10.1039/D1TC02635F

[75] G. Pan, Z. Yang, H. Li, Y. Wen, X. Zhang, Y. Shen, C. Zhou, S-T. Zhang, B. Yang. Folding-Induced Spin–Orbit Coupling Enhancement for Efficient Pure Organic Room-Temperature Phosphorescence. *J. Phys. Chem. Lett.* 2022, **13**, 1563–1570. DOI: 10.1021/acs.jpclett.1c04180

[76] Y. Wang, J. Yang, M. Fang, Y. Gong, J. Ren, L. Tu, B. Z. Tang, Z. Li. New Phenothiazine Derivatives That Exhibit Photoinduced Room-Temperature Phosphorescence. *Adv. Funct. Mater.* 2021, **31**, 2101719. DOI: 10.1002/adfm.202101719

[77] Y. Li, L. Jiang, W. Liu, S. Xu, T-Y. Li, F. Fries, O. Zeika, Y. Zou, C. Ramanan, S. Lenk, R. Scholz, D. Andrienko, X. Feng, K. Leo, S. Reineke. Reduced Intrinsic Non-Radiative Losses Allow Room-Temperature Triplet Emission from Purely Organic Emitters. *Adv. Mater.* 2021, **33**, 2101844. DOI: 10.1002/adma.202101844

[78] S. Karmakar, S. Dey, M. Upadhyay, D. Ray. Phenoxazine–Quinoline Conjugates: Impact of Halogenation on Charge Transfer Triplet Energy Harvesting via Aggregate Induced Phosphorescence. *ACS Omega* 2022, **7**, 116827–16836. DOI: 10.1021/acsomega.2c01909

[79] D. Zhang, C. Jiang, Z. Wen, X. Feng, K. Li. Influence of Sulfur Atoms on TADF Properties from Through-Space Charge Transfer Excited States. *Eur. J. Chem.* 2022, e202202305. DOI: 10.1002/chem.202202305

[80] K. Matsuo, T. Yasuda. Blue thermally activated delayed fluorescence emitters incorporating acridan analogues with heavy group 14 elements for high-efficiency doped and non-doped OLEDs. *Chem. Sci.* 2019,**10**, 10687-10697. DOI: 10.1039/c9sc04492b

[81] P. Xu, Q. Qiu, X. Ye, M. Wei, W. Xi, H. Feng, Z. Qian. Halogenated tetraphenylethene with enhanced aggregation-induced emission: an anomalous anti-heavy-atom effect and self-reversible mechanochromism. *Chem. Commun*. 2019,**55**, 14938-14941. DOI: 10.1039/c9cc07045a

[82] S. Gan, S. Hu, X-L. Li, J. Zeng, D. Zhang, T. Huang. W. Luo, Z. Zhao, L. Duan, S-J. Su, B. Z. Tang. Heavy Atom Effect of Bromine Significantly Enhances Exciton Utilization of Delayed Fluorescence Luminogens. *ACS Appl. Mater. Interfaces* 2018, **10**, 17327–17334. DOI: 10.1021/acsami.8b05389

[83] Strickler, S. J.; Berg, R. A. Relationship between absorption intensity and fluorescence lifetime of molecules. *J. Chem. Phys.* 1962, **37**, 814–822. DOI: 10.1063/1.1733166

[84] Mohanty, J.; Na, W. M. Refractive index effects on the oscillator strength and radiative decay rate of 2,3-diazabicyclo[2.2.2]oct-2-ene. *Photochem. Photobiol. Sci*. 2004, **3**, 1026–1031. DOI: https://doi.org/10.1039/B412936A

[85] R. Furue, K. Matsuo, Y. Ashikari, H. Ooka, N. Amanokura, T. Yasuda. Highly Efficient Red–Orange Delayed Fluorescence Emitters Based on Strong π-Accepting Dibenzophenazine and Dibenzoquinoxaline Cores: toward a Rational Pure-Red OLED Design. *Adv. Opt. Mater.* 2018, **6**, 1701147. DOI: 10.1002/adom.201701147

# Publikacje

## [P1]

M. Mońka, I. E. Serdiuk, A. Kubicki, P. Bojarski.

Not only AIE: Light-sensitivity of 4-dimethylamino-2′-hydroxychalcones beneficial to highly efficient photochemical synthesis of 4′-dimethylaminoflavanones.

# Not only AIE: Light-sensitivity of 4-dimethylamino-2′-hydroxychalcones beneficial to highly efficient photochemical synthesis of 4′-dimethylaminoflavanones

Michal Mońka, Aleksander Kubicki, Piotr Bojarski, Illia E. Serdiuk *

*Faculty of Mathematics, Physics and Informatics, University of Gdańsk, Wita Stwosza 57, 80-308 Gdańsk, Poland*

## ABSTRACT

4-dimethylamino-2′-hydroxychalcone in crystals is well known for its aggregation induced emission (AIE) in the red region of spectrum. We however observe that in liquid solutions this dye and its analogues undergo reversible wavelength-dependent light-induced cyclization to the flavanone derivatives. Special care thus should be taken when this compound is used for optoelectronic applications requiring high purity, especially via solution-processed methods. The discussed intramolecular cyclization proceeds faster in nonpolar medium and is quenched completely in the presence of protic solvents or via formation of aggregates in crystal phase. In spite of that quantum yield of a single photoinduced transformation does not exceed 1%, continuous irradiation affords 92% of product which makes it the most efficient preparation route for 4′-dimethylminoflavanone and its derivatives among the ones reported before. According to the DFT and TDDFT calculations supported by the experimentally investigated spectral features, the mechanism of photoinduced formation of a 4′-dimethylaminoflavanone involves several transformations: excited state intramolecular proton transfer (ESIPT), excited and ground state rotational isomerization from *s-trans* to *s-cis* isomer, cyclization and enol-keto tautomerization via proton transfer in the ground state.

© 2020 Elsevier B.V. All rights reserved.

## 1. Introduction

Chalcones are important components of human diet abundant in plants possessing various medicinal features [1,2]. Some of chalcone derivatives such as 4-dimethylamino-2′-hydroxychalcone (**1**, Chart 1) have been recently reported to exhibit strong emission in solid crystal phase attributed to aggregation induced emission (AIE), which makes them also attractive for applications in organic optical electronics and lasers [3,4]. In the view of potential applicability of **1** for the latter purposes, its stability, especially in the electronically excited states, becomes an important issue. Here, we show that whilst stable in crystal phase, **1** should be handled with care in its liquid solutions due to sensitivity to light. From the point of view of applications which require highly pure **1**, this can cause certain difficulties.

On the other hand, our findings indicate that continuous irradiation of **1** with blue light converts it to the cyclization product 4′-dimethylaminoflavanone (**2**, Chart 1) with an excellent yield. This reaction also proceeds in **1** derivatives **1-Cl** and **1-Br**, and was previously reported for analogues (**3**) without dimethylamino group [5]. From the point of view of synthesis of biologically active compounds, this is one

of the most efficient preparation of flavanone derivatives. The latter compounds due to high affinity to different receptors in the human body [6] are well-known for their important medicinal features and high biological activity in general, namely anticancer, antitumor, antibacterial, antimicrobial, antioxidant, estrogenic and anti-estrogenic properties [7]. To the best of our knowledge, the described here photoinduced formation of 4′-dimethylaminoflavanone and its derivatives with a 92% of isolated yield is the most efficient preparation route as compared to the 18–48% yields usually reported for such compounds [8–10].

Understanding of the mechanism of **1** → **2** transformation is obviously a key for successful design of highly stable chalcone-based light emitting materials and development of efficient synthetic pathways for biologically active flavanones. Matsushima and coworkers investigated experimentally photocyclization of 2′-hydroxychalcones without amino groups to respective flavanones [11,12]. They found that the reaction proceeded faster in basic solvents like dioxane, and was negligibly affected by the presence of triplets scavengers. Moreover, the efficiency of side reactions is lower under irradiation by the long-wavelength light source (>360 nm). Authors first assumed a twophoton mechanism for the photocyclization with proton transfer and *s-cis–s-trans* isomerization in the excited state as key steps. Later however, they proposed a one-photon mechanism instead assuming an
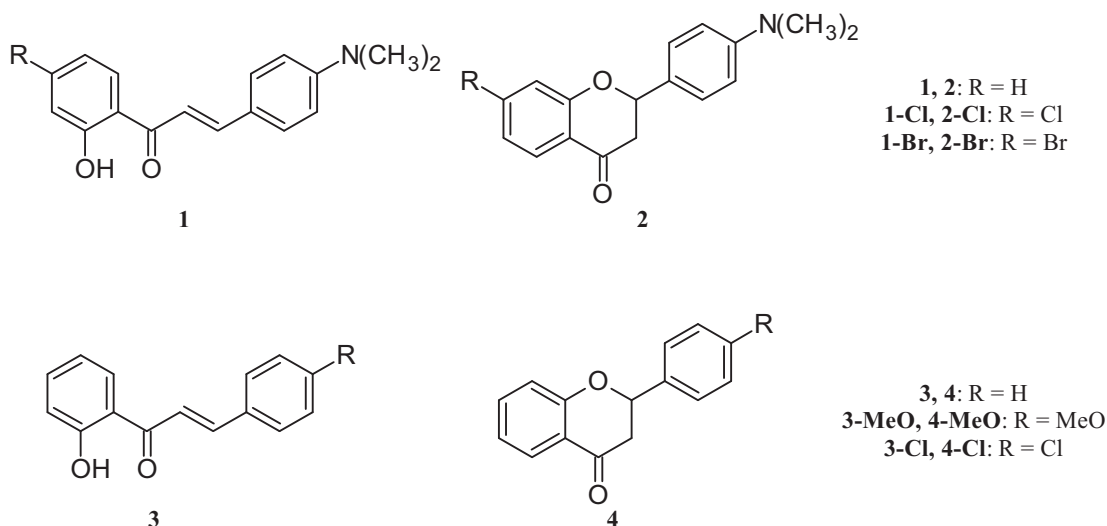
**Chart 1.** Structures of the investigated compounds.

equilibrium excited state intramolecular proton transfer (ESIPT). It was also suggested that the photocyclization is an acid self-catalyzed process [13]. Unfortunately, due to very limited abilities of computational methods at that time, mechanistic investigations of such multistep dark transformations were very complicated. Until now, no clear mechanistic model for the 2′-hydroxychalcone–flavanone photocyclization has been proposed.

On the basis of DFT and TDDFT calculations and spectral features of **1** in various media, we conduct a step-by-step analysis of formation of **2**. Our results evidence that the most probable route involves ultrafast ESIPT after excitation, deactivation of the excited state via conical intersection, and then ground state *s-cis–s-trans* isomerization, cyclization and enol-keto tautomerization.

## 2. Experimental and theoretical methods

### 2.1. Reagents and compounds

All reagents and solvents of relevant grade for syntheses and spectroscopy were purchased from commercial sources and used without further purification. 2′-hydroxychalcone was purchased from TCI. Thin layer chromatography (TLC) was performed on Merck silica gel plates 60 254F.

### 2.2. Synthesis

Chalcones **1**, **1-Cl**, **1-Br**, **3-MeO**, and **3-Cl** were synthesized from commercially available acetophenone and benzaldehyde derivatives through the base-catalyzed Claisen-Schmidt condensation. For synthetic procedures and results of analyses see Supporting Information (SI).

### 2.3. Sample preparation and photochemical experiments

Cyclohexane (CH) and dichloromethane (DCM) solutions of chalcones for photochemical investigations were prepared for concentrations $c = 7.5 \cdot 10^{-6}$ M to eliminate any aggregation effects and provide detectable optical density during absorption measurements; cells of 1 cm length optical path were used. Crystals of **1**, **1-Cl**, and **1-Br** were obtained via slow evaporation of acetone solutions. All photochemical experiments were performed in aerated solutions at room temperature under continuous stirring. Progress of photodegradation

was controlled by absorption spectroscopy and TLC. Detailed procedures for determination of rate constants and quantum yields of photo-induced transformation **1 → 2** are presented in the SI.

### 2.4. Apparatus and measurements

The identity of synthetized compounds was confirmed by $^1$H NMR (Bruker AVANCE III 500 MHz) and $^{13}$C NMR (250 MHz) spectroscopy with trimethylsilane as a reference. Purity of compounds was controlled by TLC. HRMS spectra were measured on Agilent 6550 iFunnel Q-TOF LC/MS system.

Absorption spectra were recorded on a UV-1900 Shimadzu spectrophotometer. Steady-state fluorescence spectra were recorded on a Cary Eclipse spectrofluorometer (Varian Inc., Australia) using right-angle "L-shaped" geometry for solutions and front face geometry for crystals. Fluorescence spectra were corrected for the instrumental sensitivity. Photoluminescence quantum yields ($\varphi_{fl}$) were measured relatively to rhodamine 6G in MeOH as a reference ($\varphi_{fl} = 0.94$) [14] and corrected for refractive indices of the solvents used. Decomposition of fluorescence emission spectra into individual bands was performed using the Siano-Metzler functions [15].

For photochemical experiments samples were irradiated with the laser heads LDH-D-C-405, LDH-D-C-440, and LDH-D-C-470 (PicoQuant, Germany) operating at 30 mW CW mode and 254 nm UV lamp LF-206. LS (UVITEC, England). LaserCheck (Coherent Inc., USA) laser power meter was used. For irradiation of a 20 mg sample of **1** in DCM, 130W U-HGLGPS High Pressure Mercury Lamp (Olympus, Japan) was used with a band-pass filter BP460-495.

### 2.5. Quantum chemical calculations

Geometry optimizations of tautomeric and isomeric forms of **1** and **2** in the ground ($S_0$), excited singlet ($S_1$) and triplet ($T_1$) electronic states were performed at DFT/TD DFT level of theory [16] with the B3LYP [17] hybrid functional with the cc-pVDZ basis set using the GAUSSIAN 16 program package [18]. Unspecific solvent effect (CH and DCM) was included at the level of the Polarized Continuum Model (PCM) [19]. After completion of each optimization, the Hessian matrix was calculated to find out whether the obtained structures were stationary. Potential energy surfaces for various transformations were obtained by constrained geometry optimizations via scan of respective bond length and/or dihedral angle values.

# 3. Results and discussion

## 3.1. Spectroscopic investigations

We started our experiment with testing photostability of **1**. Its solutions in cyclohexane (CH) and dichloromethane (DCM) were irradiated with laser light at 440 nm and 470 nm, respectively. These wavelengths are close to the 0-0 transition of the $S_0$-$S_1$ absorption band and thus correspond to the minimal energy needed to excite **1** under such media polarity. During irradiation, the yellow color of solution bleached. As shown in Fig. 1, the absorption spectra changed drastically: the band of **1** centered at 415–450 nm disappeared and the one at 310 nm became more intensive.

Weak dual fluorescence of **1** also disappeared (Fig. S1, SI). TLC of the irradiated sample confirmed formation of a new compound (Fig. S2, SI). This compound was isolated from the irradiated solution by column chromatography. Its structure was identified by means of the ^{1}H NMR spectroscopy, which revealed three doublet of doublets peaks at 2.88, 3.18 and 5.42 ppm in CDCl$_3$ corresponding to three neighboring aliphatic hydrogen atoms absent in **1** (Fig. 2). The ^{1}H NMR spectrum perfectly matched the one of 4′-dimethylaminoflavanone **2** reported before [8]; and the HRMS analysis of the same sample confirmed no mass change during the investigated photoinduced transformation (for details see part LCMS analyses in SI). All these findings allowed us to conclude that under light irradiation **1** undergoes intramolecular cyclisation to **2**.

Analysis of the **1** ⟶ **2** transformation kinetics reveals its first order (Fig. 3, Table 1). Its rate depends on the solvent polarity, being nearly twice higher in CH than in DCM. The quantum yield of photoreaction, calculated from the decreasing long-wavelength absorption band of **1** equals 0.38% and 0.19%, respectively. In spite of such a low yield of a single photoinduced transformation, continuous irradiation of concentrated solutions of **1** enabled its 92% conversion to **2** on the 20 mg scale.

Surprisingly, very small additions of methanol dramatically increase photostability of **1**, as no decrease of absorption was observed under the applied conditions. It is known that **1** undergoes ultrafast ESIPT, and protic solvents can interfere its rate and efficiency due to the external hydrogen bonding [20]. To find out if the above mentioned increased photostability is due to blocked ESIPT, the fluorescence spectra were analyzed. In dry DCM, the ratio of N* (initial tautomeric form) and T* (ESIPT tautometic form) emission bands is 1:2.4 (Fig. 4). After addition of 1% of methanol, this value changes to 1:1.1. Therefore, even though specific interaction of **1** with aprotic solvents is obvious, ESIPT is not quenched completely and the mechanism of increased photostability

must involve other steps of the investigated photoinduced transformation.

On the other hand, in the crystal phase, **1** shows even higher photostability and no signs of formation of **2** were observed during irradiation for 5 h. According to the absorption spectra shown on Fig. S3 in SI, **1** forms aggregates in the ground state: absorption maximum in crystals shows a drastic 4600 cm$^{-1}$ red-shift to 560 nm as compared to that at 445 nm in DCM solution (Table 2). Formation of aggregates $N_{agg}$ thus provides large stabilization of **1** in the ground state. On the other hand, crystals exhibit only one-band fluorescence with a small Stokes shift below 2500 cm$^{-1}$, which indicates very limited relaxation of the emitting species after excitation. Moreover, comparison of the latter value with those for the N* (3400 cm$^{-1}$) and T* (6160 cm$^{-1}$) bands in DCM solutions strongly evidences lack of ESIPT in crystals (Fig. S3, SI). Such an aggregated induced emission (AIE) thus originates from the directly excited aggregated species $N_{agg}^*$, being the most stable species in the excited state.

**2** readily transforms back to **1** when irradiated at its long-wavelength absorption. Fig. S4 in SI represents the absorption spectra in DCM recorded before and after irradiation at 440 nm, and then after irradiation at 254 nm. Comparison of the absorbance at 410 nm indicates, that **1** is recovered in 87% in such a cycle. Under similar conditions, decyclization of the unsubstituted flavanone (**4**) to 2′-hydroxychalcone (**3**) was reported to proceed in 20% yield, and was followed by formation of numerous by-products [21].

In the above mentioned **1** → **2** → **1** cycle, we observed only one main by-product, which on the basis of the comparative TLC analysis and strong blue fluorescence was identified as 4′-dimethylaminoflavone [22]. Unfortunately, due to the low yield of formation and low stability under the conditions applied in chromatographical purification, other kinds of analyses were unavailable for this compound.

To gain more information on the investigated transformation we checked derivatives of **1**. First, we checked the role of intersystem crossing in the investigated mechanism. The 4-dimethyamino-2′-hydroxychalcones bearing chlorine and bromine atoms at positions 4′ were investigated (**1-Cl** and **1-Br**, Chart 1). As compared to **1**, its chloro derivative **1-Cl** transforms to a flavanone with a higher quantum yield of 1.2% (Table 2). However, in spite of >4 times higher spin orbit coupling constant of bromine than chlorine [23], **1-Br** shows the decrease of quantum yield down to 1.0%. Higher values for **1-Cl** and **1-Br** as compared to **1** can be thus rather caused by the electronic effects of halogens, which modulate the energy levels of species before (N*) and after (T*) ESIPT, This is supported by the changes of emission bands maxima (Table 2).
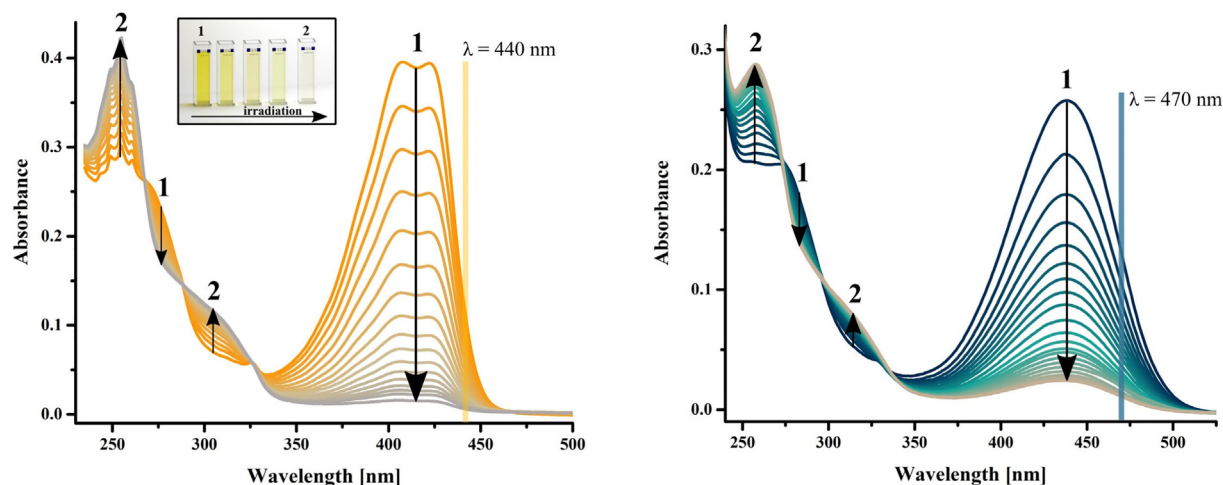


**Fig. 1.** Absorption spectra of **1** in CH (left) and DCM (right) solutions under irradiation; yellow and blue bars indicate irradiation wavelengths.
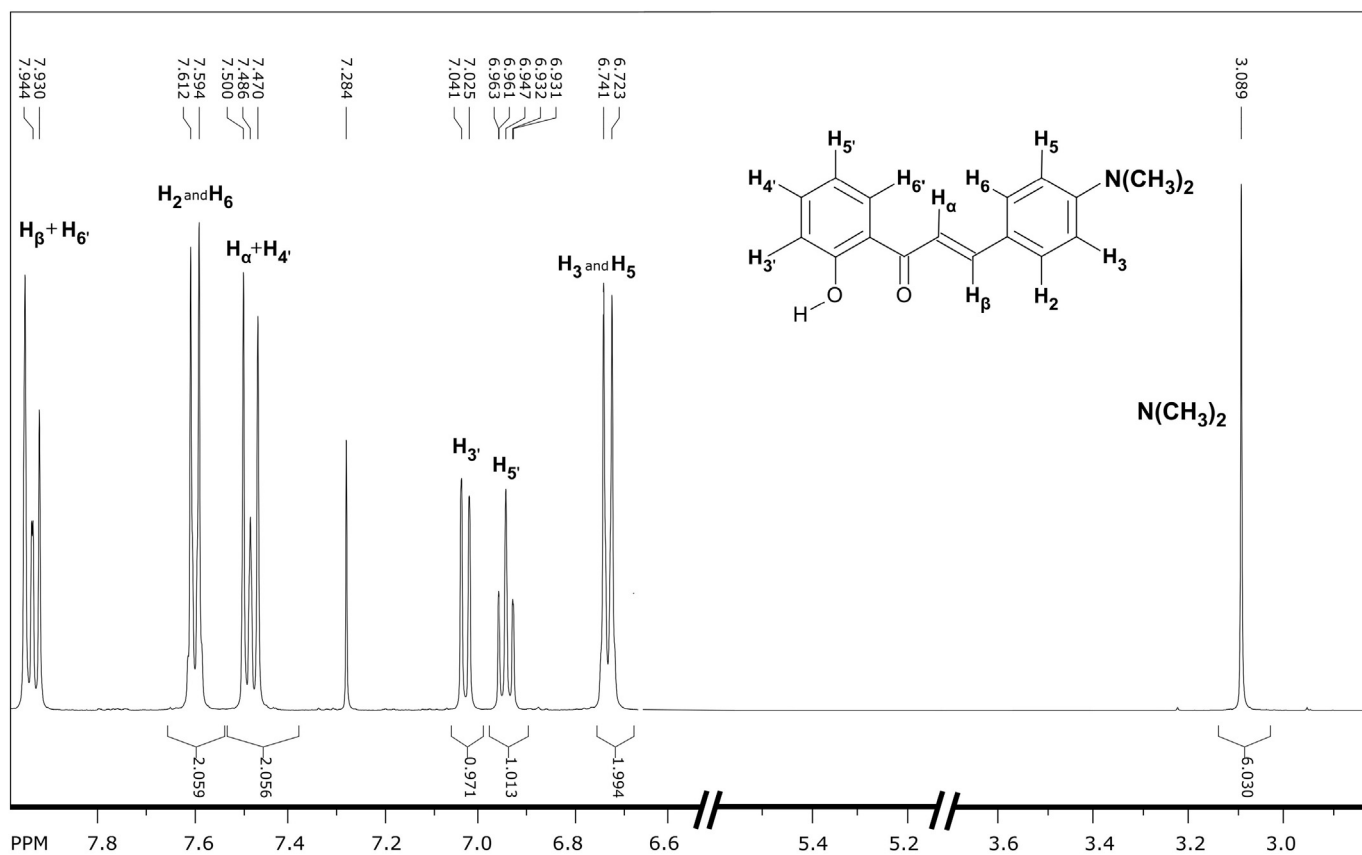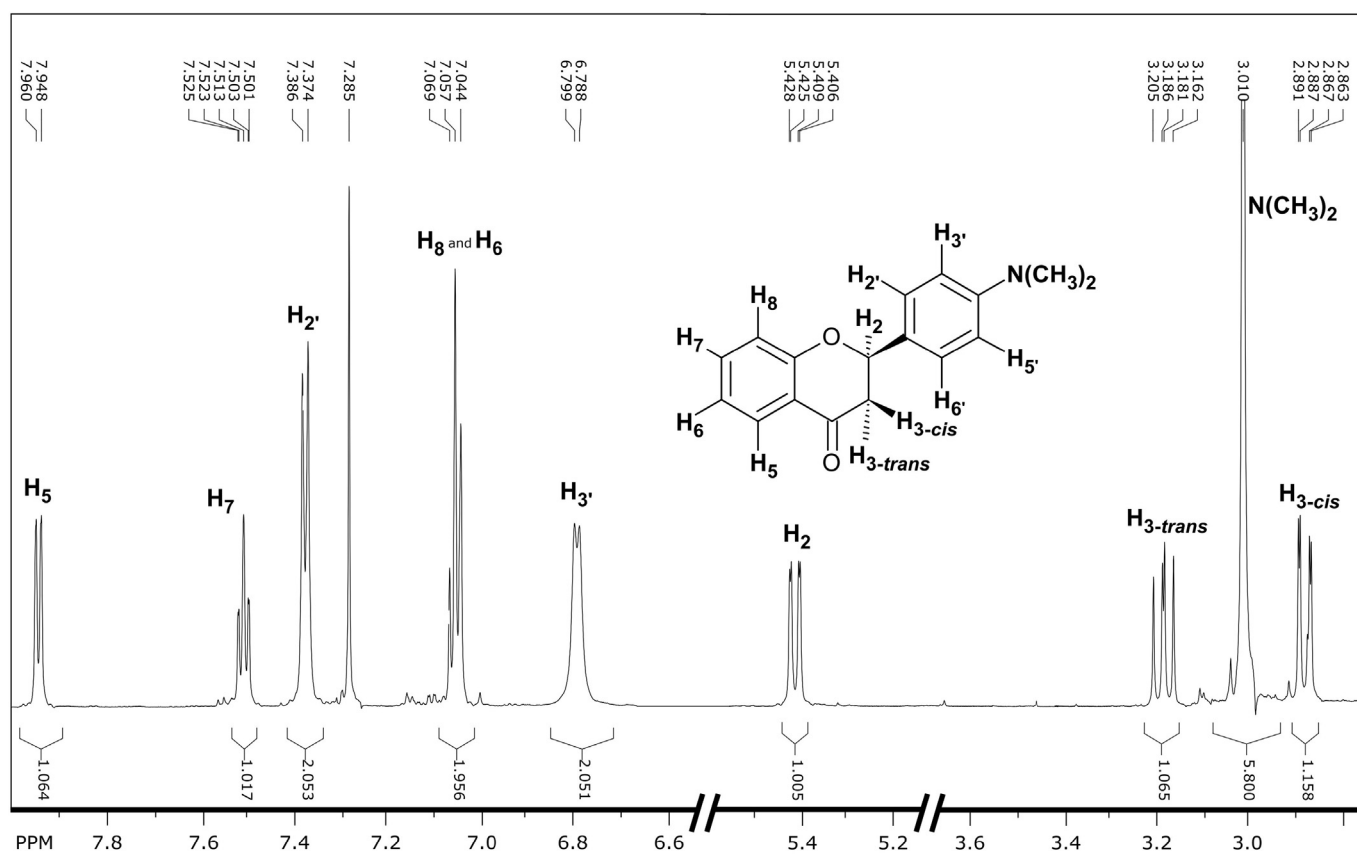
**Fig. 2.** $^1$H NMR spectrum of **1** and isolated product **2** before and after irradiation.
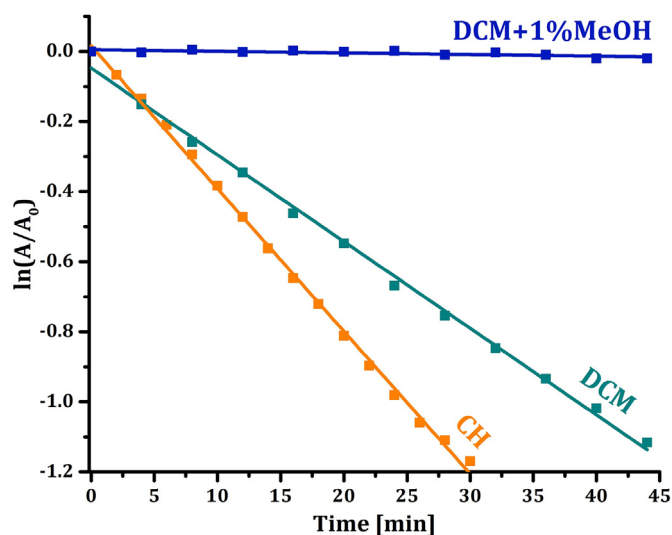
**Fig. 3.** Dependence of the relative absorbance logarithm at long-wavelength maximum of **1** on the time of irradiation in various solutions.

**Table 1**
Photodegradation rate constants of **1** in various media corrected by the $\varepsilon_\lambda$ values (see SI).

| Medium | $k_{corr}$ [$10^8$] |
|---|---|
| CH | 3.8 |
| DCM | 2.0 |
| 1% MeOH in DCM | <0.01 |

**Table 2**
Spectral parameters of chalcones and photoreaction yields of transformation to flavanones.[a]

| Cmpd | Medium | Band | $\lambda_{abs}$ [nm] | $\lambda_{fl}$ [nm] | $\varphi_{fl}$ [%] | $\varphi_{1\to2}$ [%] |
|---|---|---|---|---|---|---|
| 1 | CH | N | 420 | | <0.1 | 0.38 |
| | | T | | 568 | | |
| | DCM | N | 445 | 524 | 0.3 | 0.19 |
| | | T | | 613 | | |
| | 1% MeOH in DCM | N | 445 | 551 | 0.9 | N.A. |
| | | T | | 623 | | |
| | Crystal | $N_{agg}$ | 560 | 651 | 32 [25] | N.A. |
| 1-Cl | CH | N | 425 | | 0.3 | 1.2 |
| | | T | | 578 | | |
| | DCM | N | 447 | 526 | 2.6 | 0.44 |
| | | T | | 597 | | |
| | Crystal | $N_{agg}$ | 551 | 657 | 15 | N.A. |
| 1-Br | CH | N | 427 | | 0.2 | 1.04 |
| | | T | | 579 | | |
| | DCM | N | 448 | 528 | 3.1 | 0.22 |
| | | T | | 597 | | |
| | Crystal | $N_{agg}$ | 558 | 674 | 10 | N.A. |
| 3 | CH | N | 313 | Non-fluorescent | | 0.13 |
| | | T | | | | |
| | DCM | N | 318 | | | 0.09 |
| | | T | | | | |
| 3-Cl | CH | N | 318 | Non-fluorescent | | 0.06 |
| | | T | | | | |
| | DCM | N | 328 | | | 0.04 |
| | | T | | | | |
| 3-MeO | CH | N | 350 | Non-fluorescent | | 0.04 |
| | | T | | | | |
| | DCM | N | 367 | | | 0.02 |
| | | T | | | | |

[a] $\varphi_{fl}$ – fluorescence quantum yield; $\varphi_{1\to2}$ – quantum yield of **1** → **2** transformation.

We further compared the reactivity of other 2′-hydroxychalcones without dimethylamino group in the discussed light-induced transformation to flavanones. 2′-hydroxychalcone (**3**) as well as its 4′-methoxy (**3-MeO**) and 4′-chloro (**3-Cl**) derivatives were irradiated at their red-edge of absorption spectra. Qualitatively, according to the LCMS analyses, all three compounds transformed to the respective flavanone derivatives **4** with high selectivity (see part LCMS analyses in SI). Quantitatively, from the point of view of the reaction quantum efficiency, reactivity of 2′-hydroxychalcones without dimethylamino group is nearly 3–10 times lower than that of **1**.

In the case of **3** and especially **3-Cl**, some trace amounts of 3-hydroxyflavone (flavonol) derivatives were detected by its distinctive

ESIPT fluorescence and TLC analysis. However, our experiments reveal that the main product is flavanone **4** and **4-Cl**, respectively, whilst the amount of formed flavonol should be below 5% of produced flavanone, which complicates its quantitative analysis. Formation of trace amounts of a flavonol derivative was previously reported for irradiated **1** solutions [24], but our experiments do not support this finding.

### 3.2. Investigations of the mechanism

To reveal the mechanism of photoinduced transformation of chalcones to flavanones we analyzed in detail features of **1** in the view of its promising applicative features and detectable emission of both its tautomeric forms N* and T*. Quantum chemical calculations were
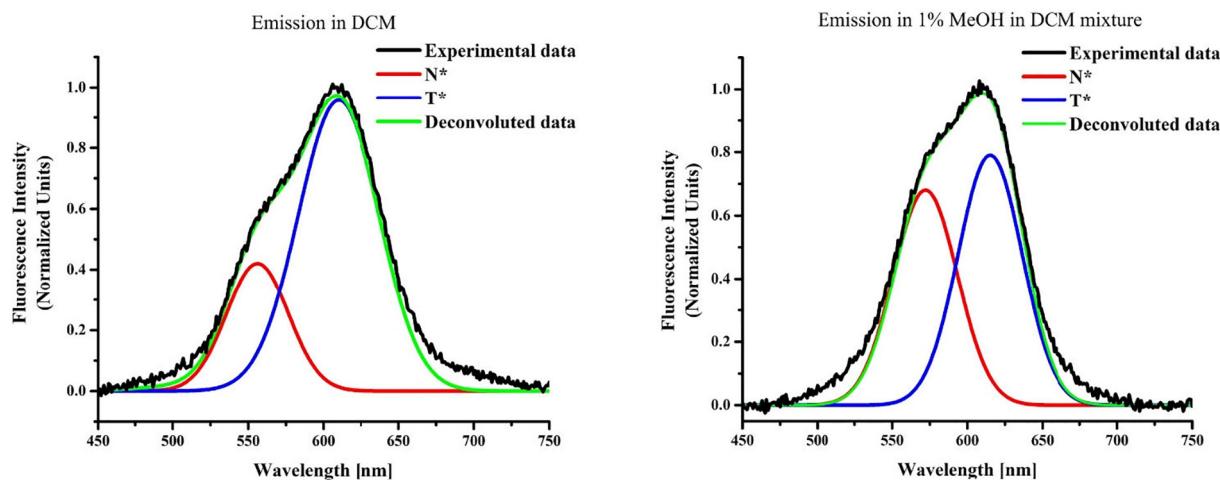


**Fig. 4.** Fluorescence spectrum of **1** in dry DCM (left) and 1% MeOH in DCM mixture (right).
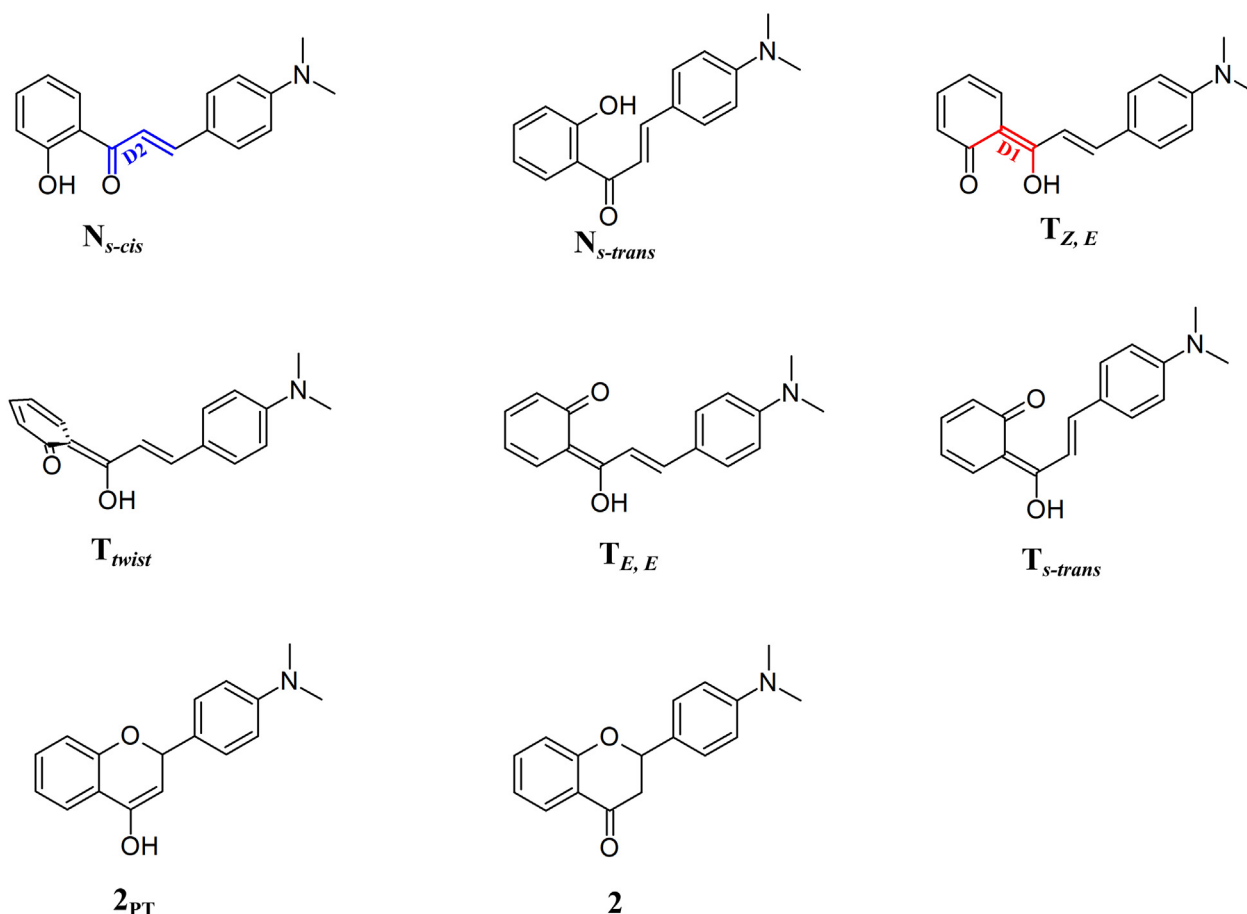
**Chart 2.** Canonic structures of tautomeric and isomeric forms of **1** and **2**.

performed on the DFT and TDDFT level of theory to explain the experimental findings.

In the absence of light in the ground state, **1** exists in the "enol" form with $E$ ($s$-$cis$) conformation (form $N_{s\text{-}cis}$, Chart 2), which has fully planar structure. After excitation, three non-radiative deactivation pathways of the excited $^1N_{s\text{-}cis}$ are possible: intersystem crossing (ISC), rotational isomerization, and ESIPT.

1) ISC can lead to the second triplet state ($T_2$) of $^1N_{s\text{-}cis}$, which has only 0.16 eV higher energy than $S_1$ (Scheme 1). According to the calculated frontier orbitals (Fig. S5, SI), $S_1$ and $T_2$ states have different nature and thus transition between them is partly allowed by the Al Sayed rules. However, on the basis of numerous examples of organic molecules with similar electronic parameters one can expect ISC rate close to $10^8$ s$^{-1}$. This is much slower than the ESIPT rate constant $1$–$0.75 \cdot 10^{12}$ s$^{-1}$ reported for **1** [26].

The ISC rate can be accelerated by introduction of a heavy atom. As was concluded above from the investigations of **1-Cl** and **1-Br**, no heavy-atom effect was observed. Together with much slower expected rate of ISC compared to ESIPT, this convinced us to insignificant population of the triplet $^3N_{s\text{-}cis}$ state and its role in the **1** → **2** transformation.

2) To undergo rotational isomerization involving propen-1-one fragment in the $S_1$ state, $^1N_{s\text{-}cis}$ should overcome some energetic barriers (Fig. S6). The lowest value among such barriers of $+10.2$ kJ/mol corresponds to the change of dihedral angle D2 (Chart 2). Even though this value can be readily overcome by thermal activation at room temperature, further transformation to $^1N_{s\text{-}trans}$ is endothermic (Scheme 1): $\Delta G = +23.7$ kJ/mol. Moreover, presence of the energetic barrier indicates that the $s$-$cis$–$s$-$trans$ isomerization in $^1N_{s\text{-}cis}$ to $^1N_{s\text{-}trans}$ is much slower than the barrierless ESIPT, as discussed below.

3) Calculations predict that ESIPT in $^1N_{s\text{-}cis}$ is irreversible ($\Delta G = -26.1$ kJ/mol); it is also barrierless (Fig. S7) and thus should be ultrafast. This is in good qualitative agreement with the reported experimental ESIPT rate in **1** [26]. It also explains the absence of N* band in emission spectra of **1** in CH solutions in spite of high value of the absorption extinction coefficient of $1.7 \cdot 10^4$ L·mol$^{-1}$·cm$^{-1}$, determined from the long-wavelength absorption band. Therefore ESIPT efficiently produces "keto" tautomeric form in the $Z$, $E$ conformation (form $^1T_{Z,\,E}$, Chart 2, Scheme 2).

Planar geometry of $^1T_{Z,E}$ in the $S_1$ state is unstable and it twists spontaneously so its semiquinone and 4′-dimethylaminocinnamoyl fragments become orthogonal (form $^1T_{twist}$, Chart 2 and Scheme 2). In nonpolar CH, such a rotation along dihedral angle D1 decreases the energy by $-53.9$ kJ/mol and has no barrier which predicts its very fast rate. This explains very low fluorescence quantum yield of T* fluorescence in solutions of **1** (Table 2).

In the $T_{twist}$ structure, surfaces of potential energies of $S_0$ and $S_1$ states become very close. The calculated energy difference between these states is only 7.1 kJ/mol and thus the $S_1$ state effectively deactivates due to conical intersection. Such an effective deactivation of the excited state seems to be the most likely scenario for the investigated **1** → **2** transformation. In fact, energies of $S_1$ and $T_1$ states of $^1N_{s\text{-}cis}$ and $^1T_{Z,E}$ species of **1** are much lower than those of **2** (Scheme 1), and thus intramolecular cyclization is thermodynamically unfavorable in the excited states.

In the ground state, the $T_{twist}$ species is unstable as twisted structure breaks conjugation of the molecular fragments. The molecule should thus planarize via change of the dihedral angle D1 and there are two possible ways for it. In the case of decrease of D1 (reverse rotation),
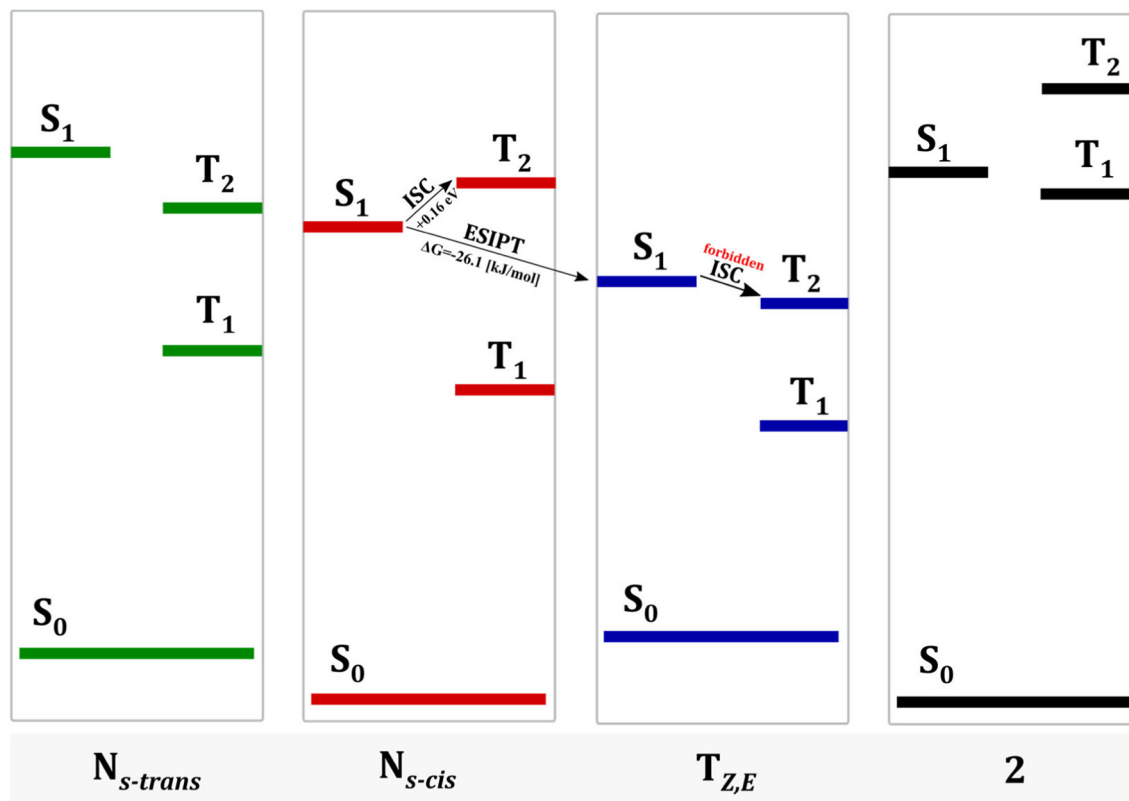
**Scheme 1.** Relative energies of the ground and excited singlet and triplet states of $N_{s\text{-}cis}$, $N_{s\text{-}trans}$, $T_{Z,\,E}$, and **2**.

the molecule returns to $T_{Z,E}$ geometry loosing −142.3 kJ/mol (Fig. 5). In the ground-state, "keto" tautomeric species are less stable than "enol" ones. $T_{Z,E}$ thus further transforms back to the starting point of

photocycle $N_{s\text{-}cis}$ via reverse proton transfer through intramolecular hydrogen bond. Change of the Gibbs free energy for the latter process is −46.1 kJ/ mol (Scheme 2).
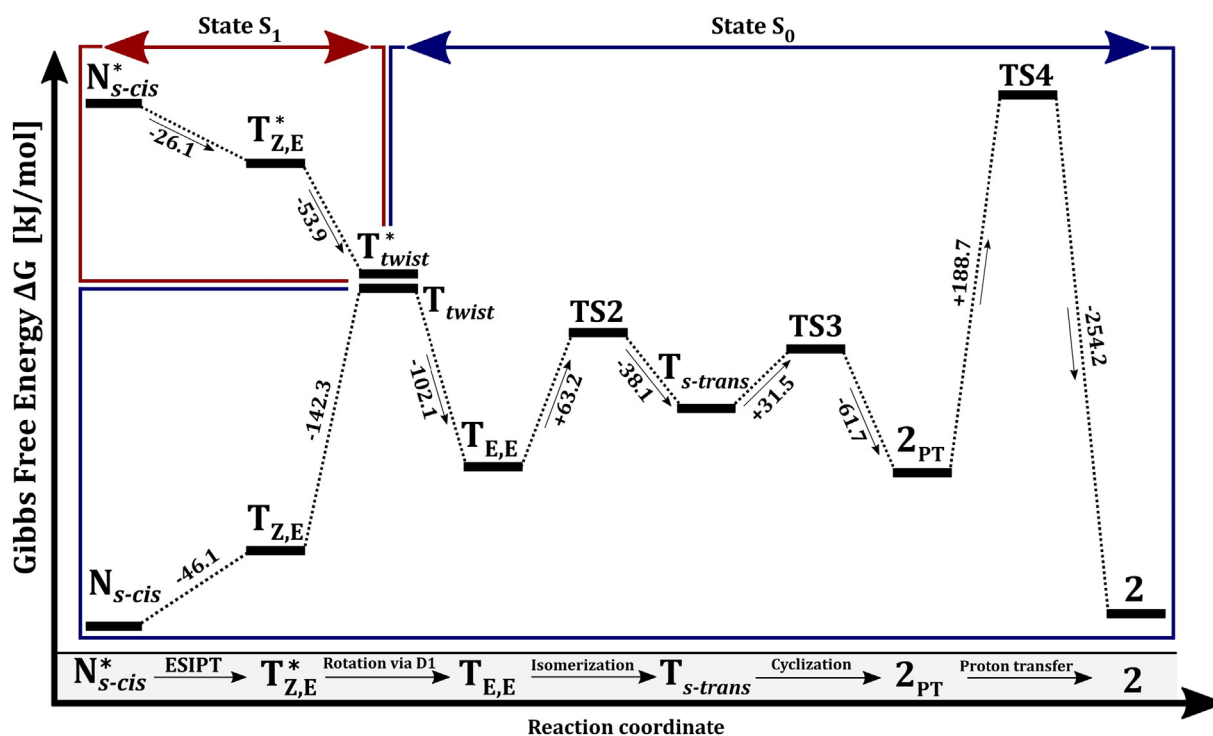


**Scheme 2.** Diagram representing stage-by-stage transformation of **1** ($N_{s\text{-}cis}$ form) to **2** in CH, TS denotes transition state.
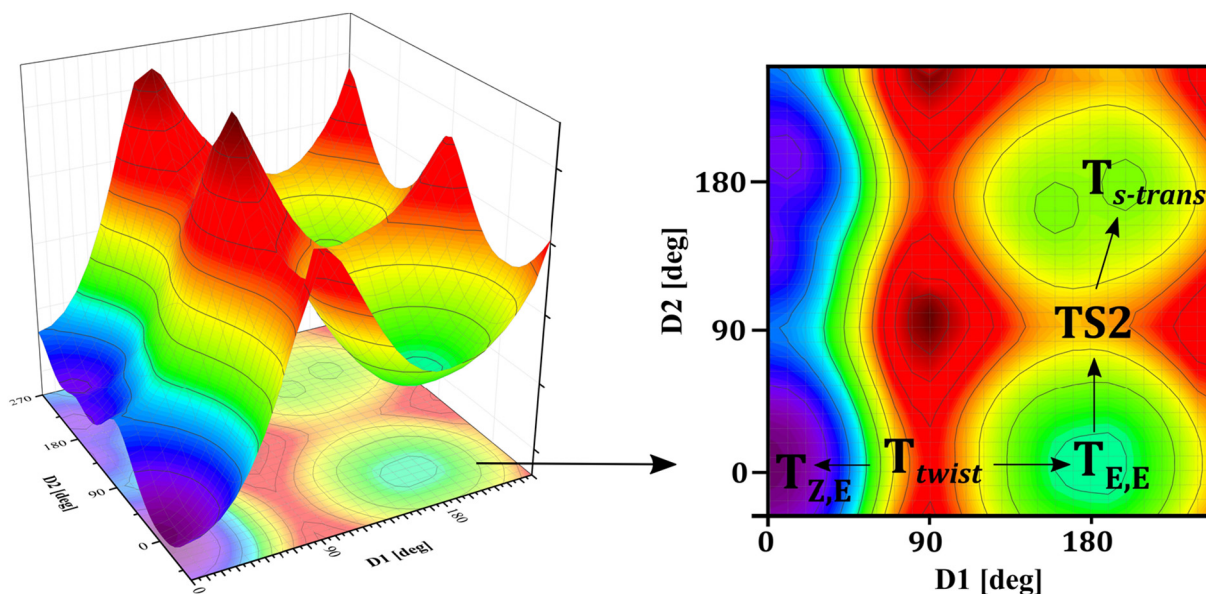
**Fig. 5.** Potential energy surface of the ground state isomers of **T** form as a function of dihedral angles D1 and D2.

If the above described transformations only took place, **1** would show high photostability. There is however another option of rotation of the ground-state **T**$_{twist}$ species: the increase of D1 angle, which results in the **T**$_{E,E}$ isomer (Chart 2, Scheme 2, and Fig. 5). The latter has 40.4 kJ/mol higher energy than the **T**$_{Z,E}$ one, because it lacks the intramolecular hydrogen bond. Nevertheless, according to the slopes of potential energy curves, both **T**$_{twist}$ → **T**$_{E,E}$ and **T**$_{twist}$ → **T**$_{Z,E}$ rotations are barrierless and thus should occur with a similar probability.

To enable cyclization, **T**$_{E,E}$ should first transform to its *s-trans* isomer **T**$_{s-trans}$ via rotation of the single bond in propen-2-ylidene fragment (dihedral angle D2, Chart 2). In this case, such a *s-cis–s-trans* isomerization is an endothermic process, but it is followed by an exothermic cyclization affording a 2*H*-chromen-4-ol derivative (**2**$_{PT}$, Chart 2 and Scheme 2). Thanks to this, total change of Gibbs free energy of the **T**$_{E,E}$ → **2**$_{PT}$ transformation is negative, −5.1 kJ/mol. With this value in mind and also taking into account similar $E_a$ values of *s-cis/s-trans* isomerization **T**$_{E,E}$ → **T**$_{s-trans}$ and decyclization **2**$_{PT}$ → **T**$_{trans}$ (Scheme 2) one can describe this system as a dynamic quasiequilibrium between **T**$_{E,E}$ and **2**$_{PT}$ species taking place on a millisecond time scale. The **T**$_{s-trans}$ species can be thus considered rather as one of the short-living transition states due to fast transformation to **T**$_{E,E}$ and **2**$_{PT}$ within tens of nanoseconds.

Finally, to accomplish transformation to the 65.5 kJ/mol more stable species **2**, its tautomeric "enol" form **2**$_{PT}$ should undergo intramolecular proton transfer from the hydroxyl group to the neighboring sp2 hybridized carbon atom. As there is no intramolecular hydrogen bonding, molecule should overcome the energetic barrier of 188.7 kJ/mol (Scheme 2 and Fig. 8, SI), which is inaccessible under the applied experimental conditions. However, in some structurally analogous compounds, including acetophenone derivatives, in spite of similarly high $E_a$ values of keto-enol tautomerism, proton transfer was reported to be much faster and occur on the 0.1 μs time scale [27]. This phenomenon together with substantial decrease of the proton transfer rate under deuterium exchange is explained by large impact of tunneling mechanism [28]. In the case of the **2**$_{PT}$ → **2** transformation, the tunneling distance calculated as a distance between the equilibrium hydrogen atom positions before and after PT is 2.27 Å, which is acceptable for efficient tunneling [28].

Within the mechanism described above, the increase of torsion angle D1 value to 90° in the excited $^1$**T**$_{Z,E}$ species ($^1$**T**$_{Z,E}$ → $^1$**T**$_{twist}$) and its further increase to 180° in the ground-state **T**$_{twist}$ species (**T**$_{twist}$ → **T**$_{E,E}$) are crucial stages in formation of **2**. Changes in the molecular environment can affect the rate and yield of these stages and thus the total

yield of **2**. In fact, according to the calculations conducted for polarity of DCM, the rotation $^1$**T**$_{Z,E}$ → $^1$**T**$_{twist}$ in polar medium is no longer barrierless as in CH (TS1 on Fig. S9). Appearance of such an energetic barrier which indicates increase of the $^1$**T**$_{Z,E}$ lifetime, excellently correlates with the increased quantum yield of fluorescence of T* band and decreased quantum yield of the **2** formation determined experimentally for DCM solutions (Table 2).

On the other hand, formation of hydrogen-bonding complexes of proton-transfer site with e.g. methanol molecules can limit sufficiently rotation along the dihedral angle D1. Calculations predict that in the excited $^1$**T**$_{twist}$ complex with methanol, the torsion angle D1 between semiquinone and 4′-dimethylaminocinnamoyl fragment is ca. 77°, which is closer to **T**$_{Z,E}$ than **T**$_{E,E}$ (Fig. 6). Such a geometry defines direction of further rotation of the **T**$_{twist}$ complex after conical intersection: back to **T**$_{Z,E}$ but not to **T**$_{E,E}$. This explains the discussed above drastic increase of photostability of **1** in the presence of small amounts of methanol.

Finally, according to the fluorescence measurements in crystals – the medium of the highest photostability of **1** – formation of aggregates of $^1$**N**$_{s-cis}$ is more favorable than ESIPT. According to the onsets of fluorescent bands, the excited state of N$_{agg}$* in crystals is >20 kJ/mol below that of T* species in DCM solutions (Fig. S3). Together with the restriction of rotations of large molecular fragments due to crystal packing, this results in high photostability, appearance of strong AIE features and absence of $^1$**T**$_{Z,E}$ emission.

## 4. Conclusions

4-Dimethylamino-2′-hydroxychalcone and its 4′-chloro and bromo derivatives undergo photoinduced intramolecular cyclization to respective 4′-dimethylaminoflavanone derivatives. In aprotic solvents under continuous irradiation, conversion yields exceed 90% on the 20 mg scale, representing highly efficient and selective synthetic method of 4′-dimethylaminoflavanones. This transformation can be, however, efficiently inhibited by addition of protic solvents in solutions or via formation of aggregates in the crystal phase.

DFT/TDDFT calculations reveal the following mechanism of this transformation. In the excited state, formation of 4′-dimethylaminoflavanone is thermodynamically unfavorable. Excited states thus serve as transition states enabling rotational isomerism. Photoexcitation induces ultrafast intramolecular proton transfer followed
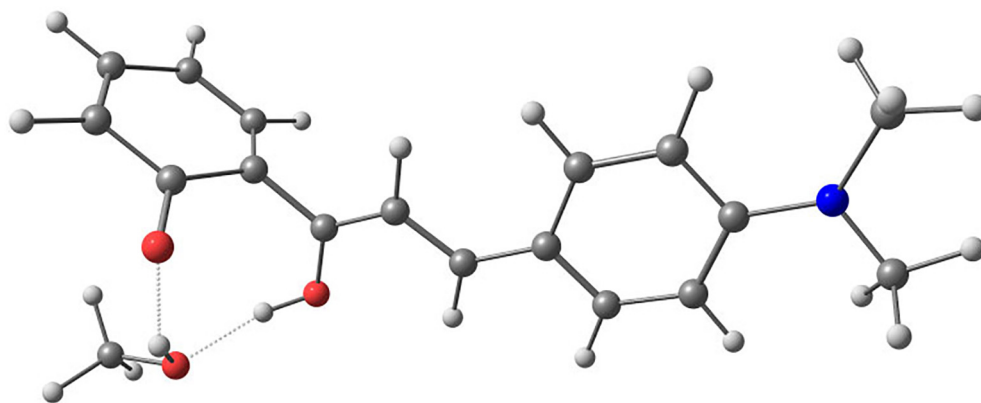
**Fig. 6.** Optimized structure of $^1\mathbf{T}_{twist}$ complex with methanol ($S_1$ state).

by molecular twist and transition to the ground state via conical intersection. In the ground state, two pathways are possible for the twisted species. The first one leads back to the initial state – 4-dimethylamino-2′-hydroxychalcone, whilst second one enables reversible *s-cis–s-trans* isomerization followed by intramolecular cyclization. The latter processes involve a relatively high barrier of ca. 60 kJ/mol for rotation of respective torsion angles. Cyclization is thus expected to occur on the millisecond time scale. Final stage enol-keto tautomerization via proton transfer provides 4′-dimethylaminoflavanone most likely through the tunneling mechanism as reported for similar compounds.

From the mechanism described above we conclude that in the crystal phase aggregation of 4-dimethylamino-2′-hydroxychalcone not only provides its applicatively promising AIE features, but also enables high photostability via blocking ESIPT – first stage of the photoinduced flavanone synthesis.

## CRediT authorship contribution statement

**Michal Mońka:**Conceptualization, Investigation, Validation, Data curation, Formal analysis, Visualization.**Aleksander Kubicki:**Resources, Funding acquisition.**Piotr Bojarski:**Writing - review & editing, Resources, Funding acquisition.**Illia E. Serdiuk:**Conceptualization, Methodology, Supervision, Writing - original draft.

## Acknowledgements

## Declaration of competing interest

The authors declare that they have no known competing financial interests or personal relationships that could have appeared to influence the work reported in this paper.

## Appendix A. Supplementary data

Supporting Information. Synthetic procedures and analyses; procedures for determination of quantum yield and rate constant of photoinduced transformations; results of DFT and TDDFT calculations: optimized structures and energies, potential energy surfaces; additional absorption and fluorescence spectra. Supplementary data to this article can be found online at doi: https://doi.org/10.1016/j.molliq.2020.113526.

## References

[1] S.H. Mah, Chalcones in diets, in: J. Xiao, S. Sarker, Y. Asakawa (Eds.), Handbook of Dietary Phytochemicals, Springer, Singapore, 2020.
[2] M. Schnekenburger, M. Diederich, Chapter 18. Nutritional epigenetic regulators in the field of cancer: new avenues for chemopreventive approaches, in: S.G. Gray (Ed.), Epigenetic Cancer Therapy, Academic Press, Boston 2015, pp. 393–425.
[3] M. Dommet, M. Riviera, R. Crespo-Otero, How inter- and intramolecular processes dictate aggregation induced emission in crystals undergoing excited-state proton transfer, J. Phys. Chem. Lett. 8 (2017) 6148–6153, https://doi.org/10.1021/acs.jpclett.7b02893.
[4] X. Cheng, K. Wang, S. Huang, H. Zhang, H. Zhang, Y. Wang, Organic crystals with near-infrared amplified spontaneous emissions based on 2′-hydroxychalcone derivatives: subtle structure modification but great property change, Angew. Chem. Int. Ed. 54 (2015) 8369–8373, https://doi.org/10.1002/anie.201503914.
[5] M. Sisa, S.L. Bonnet, D. Ferreira, J.H. Van der Westhuizen, Photochemistry of flavonoids, Molecules 15 (2010) 5196–5245, https://doi.org/10.3390/molecules15085196.
[6] B.E. Evans, K.E. Rittle, M.G. Bock, R.M. Dipardo, R.M. Freidinger, W.L. Whitter, G.F. Lundell, D.F. Veber, P.S. Anderson, R.S.L. Chang, V.J. Lotti, D.J. Cerino, T.B. Chen, P.J. Kling, K.A. Kunkel, J.P. Springer, J. Hirshfield, Methods for drug discovery: development of potent, selective, orally effective cholecystokinin antagonists, J. Med. Chem. 31 (1988) 2235–2246, https://doi.org/10.1021/jm00120a002.
[7] Ø.M. Andersen, K.R. Markham, Flavonoids: Chemistry, Biochemistry and Applications, CRC Taylor & Francis, Boca Raton, FL, 2006.
[8] N. Ahmed, N.K. Konduru, Naveen Kumar, Praveen, A. Kumar, Kamaluddin, Silica supported-double metal cyanides (DMCs): a green and highly efficient catalytic protocol for isomerisation of 2′-hydroxychalcones to flavanones, J. Mol. Catal. A Chem. 373 (2013) 135–141, https://doi.org/10.1016/j.molcata.2013.03.009.
[9] R. Mondal, A.D. Gupta, A.K. Mallik, Synthesis of flavanones by use of anhydrous potassium carbonate as an inexpensive, safe, and efficient basic catalyst, Tetrahedron Lett. 52 (2011) 5020–5024, https://doi.org/10.1016/j.tetlet.2011.07.072.
[10] T. Matsumura, T. Tsuchiya, T. Takeda, K. Imafuku, Synthesis of 6- and 8-phenyl-substituted flavonoids, Bull. Chem. Soc. Jpn. 56 (1983) 2037–2043, https://doi.org/10.1246/bcsj.56.2037.
[11] R. Matsushima, I. Hirao, Photocyclization of 2′-hydroxyflavones to 4-flavanones, Bull. Chem. Soc. Jpn. 53 (1980) 518–522, https://doi.org/10.1246/bcsj.53.518.
[12] R. Matsushima, H. Kageyama, Photochemical cyclization of 2′-hydroxychalcones, J. Chem. Soc., Perkin Trans. II (6) (1985) 743–748, https://doi.org/10.1039/P29850000743.
[13] F.R. Stermitz, J.A. Adamovic, J. Geigert, Synthesis and photoreactions of sorbophenones. A photochemical synthesis of flavone, Tetrahedron Lett. 37 (1975) 1593–1595, https://doi.org/10.1016/0040-4020(75)87018-9.
[14] A.M. Brouwer, Standards for photoluminescence quantum yield measurements in solution (IUPAC technical report), Pure Appl. Chem. 83 (2011) 2213–2228, https://doi.org/10.1351/PAC-REP-10-09-31.
[15] D.B. Siano, D.E. Metzler, Band shapes of the electronic spectra of complex molecules, J. Chem. Phys. 51 (1969) 1856–1861, https://doi.org/10.1063/1.1672270.
[16] J.K. Labanowski, in: J.W. Andzelm (Ed.), Density Functional Methods in Chemistry, Springer-Verlag, New York, 1991.
[17] A.D. Becke, A new mixing of Hartree-Fock and local-density-functional theories, J. Chem. Phys. 98 (1993) 1371–1377, https://doi.org/10.1063/1.464304.
[18] M.J. Frisch, G.W. Trucks, H.B. Schlegel, G.E. Scuseria, M.A. Robb, J.R. Cheeseman, G. Scalmani, V. Barone, G.A. Petersson, H. Nakatsuji, X. Li, M. Caricato, A.V. Marenich, J. Bloino, B.G. Janesko, R. Gomperts, B. Mennucci, H.P. Hratchian, J.V. Ortiz, A.F.

Izmaylov, J.L. Sonnenberg, D. Williams-Young, F. Ding, F. Lipparini, F. Egidi, J. Goings, B. Peng, A. Petrone, T. Henderson, D. Ranasinghe, V.G. Zakrzewski, J. Gao, N. Rega, G. Zheng, W. Liang, M. Hada, M. Ehara, K. Toyota, R. Fukuda, J. Hasegawa, M. Ishida, T. Nakajima, Y. Honda, O. Kitao, H. Nakai, T. Vreven, K. Throssell, J.A. Montgomery, J.E. Peralta Jr., F. Ogliaro, M.J. Bearpark, J.J. Heyd, E.N. Brothers, K.N. Kudin, V.N. Staroverov, T.A. Keith, R. Kobayashi, J. Normand, K. Raghavachari, A.P. Rendell, J.C. Burant, S.S. Iyengar, J. Tomasi, M. Cossi, J.M. Millam, M. Klene, C. Adamo, R. Cammi, J.W. Ochterski, R.L. Martin, K. Morokuma, O. Farkas, J.B. Foresman, D.J. Fox, Gaussian 16, Revision C.01, Gaussian, Inc, Wallingford CT, 2016.

[19] V. Barone, M. Cossi, J. Tomasi, A new definition of cavities for the computation of solvation free energies by the polarizable continuum model, J. Chem. Phys. 107 (1997) 3210–3221, https://doi.org/10.1063/1.474671.

[20] D. Ghosh, S. Batuta, N.A. Begum, D. Mandal, Unusually slow intramolecular proton transfer dynamics of 4′-N,N-dimethylamino-3-hydroxyflavone in high n-alcohols: involvement of solvent relaxation, Photochem. Photobiol. Sci. 15 (2016) 266–277, https://doi.org/10.1039/C5PP00377F.

[21] P.O. Mack, J.T. Pinhey, The photochemistry of flavanone, J. Chem. Soc. Chem. Commun. 8 (1972) 451–452, https://doi.org/10.1039/C39720000451.

[22] P. Wang, S. Wu, Study of the temperature-dependent luminescence behaviour of 4′-N,N-Dimethylaminoflavone derivatives, J. Photochem. Photobiol. A Chem. 76 (1993) 27–32, https://doi.org/10.1016/1010-6030(93)80169-A.

[23] M. Blume, R.E. Watson, Theory of spin-orbit coupling in atoms, II. Comparison of theory with experiment, Proc. R. Soc. A. 271 (1963) 565–578, https://doi.org/10.1098/rspa.1963.0036.

[24] T.L. Brack, S. Conti, C. Radu, N. Wachter-Jurcsak, Photochemical formation of 4′-N,N-dimethylamino-3-hydroxyflavone in hydrocarbon solutions of 4-N,N-dimethylamino-2′-hydroxychalcone, Tetrahedron Lett. 40 (1999) 3995–3998, https://doi.org/10.1016/S0040-4039(99)00662-0.

[25] N.I. Zahid, M.S. Mahmood, B. Subramanian, S. Said, O.K. Abou-Zied, New insight into the origin of the red/near-infrared intense fluorescence of a crystalline 2-hydroxychalcone derivative: a comprehensive picture from the excited-state femto-second dynamics, J. Phys. Chem. Lett. 8 (2017) 5603–5608, https://doi.org/10.1021/acs.jpclett.7b02601.

[26] H. Song, Z. Kuang, X. Wang, Y. Guo, Q. Guo, H. Zhang, A. Xia, Solvent polarity dependent excited state dynamics of 2′-hydroxychalcone derivatives, J. Phys. Chem. C 122 (2018) 15108–15117, https://doi.org/10.1021/acs.jpcc.8b03133.

[27] K.H. Grellmann, H. Weller, E. Tauer, Tunnel effect on the kinetics of hydrogen shifts. The enol-ketone transformation of 2′-methylacetophenone, Chem. Phys. Lett. 95 (1983) 195–199, https://doi.org/10.1016/0009-2614(83)87230-3.

[28] W. Siebrand, T.A. Wildman, M.Z. Zgierski, Golden rule treatment of hydrogen-transfer reactions. 2. Applications, J. Am. Chem. Soc. 106 (1984) 4089–4096, https://doi.org/10.1021/ja00327a004.

# Supporting Information

## Not Only AIE: Light-Sensitivity of 4-Dimethylamino-2'-hydroxychalcones Beneficial to Highly Efficient Photochemical Synthesis of 4'-Dimethylaminoflavanones

**Michal Mońka, Aleksander Kubicki, Piotr Bojarski, Illia E. Serdiuk\***

Faculty of Mathematics, Physics and Informatics, University of Gdańsk, Wita Stwosza 57, 80-308 Gdańsk, Poland

*Correspondence e-mail: illia.serdiuk@ug.edu.pl, illia.serdiuk@gmail.com

## Table of contents

# 1. Synthesis and identification of compounds

## 1.1 General procedure for 2'-hydroxychalcones.

Mixture of respective 2'-hydroxyacetophenone (1 mmol) and benzaldehyde derivatives (1.1 mmol), and NaOH (10 mmol) were dispersed in MeOH (1 mL) and vigorously stirred for 10-40h. After disappearance of 2'-hydroxyacetophenone monitored by TLC, mixture was neutralized by 0.1 M HCl and the resulting precipitate was collected. Pure compounds were obtained by recrystallization from appropriate solvents.
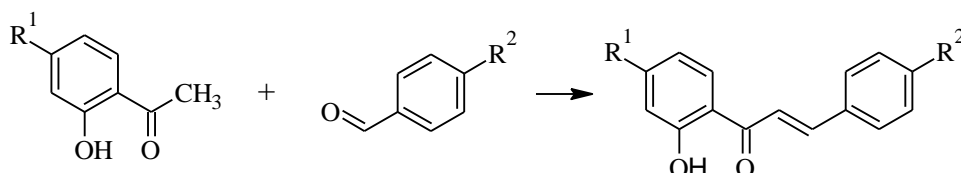


| # | $R^1$ | $R^2$ | compound |
|---|-------|-------|----------|
| 1. | H | $N(CH_3)_2$ | **1** |
| 2. | Cl | $N(CH_3)_2$ | **1-Cl** |
| 3. | Br | $N(CH_3)_2$ | **1-Br** |
| 4. | H | Cl | **3-Cl** |
| 5. | H | $OCH_3$ | **3-MeO** |

**2'-Hydroxy-4-dimethylaminochalcone (1).** Red powder, yield 68%. $^1H$ NMR (500 MHz, CDCl$_3$, $\delta$): 3.09 (s, 6H), 6.73 (d, 2H, $J$ =8.8 Hz), 6.94 (t, 1H, $J$ =7.7 Hz), 7.03 (d, 1H, $J$ = 8.0 Hz), 7.45-7.50 (m, 2H), 7.60 (2H, d, $J$ =8.8 Hz), 7.92-7.98 (m, 2H), 13.21 (s, 1H). $^{13}C$ NMR (250 MHz, CDCl$_3$, $\delta$): 193.5, 163.5, 152.3, 146.5, 135.7, 130.9, 129.4, 122.5, 120.4, 118.6, 118.5, 114.4, 111.9, 40.2. HRMS $m/z$: calculated for C$_{17}$H$_{17}$NO$_2$, 268.1332 [$M$+H]$^+$; found, 268.1336.

**4'-Chloro-2'-Hydroxy-4-dimethylaminochalcone (1-Cl).** Orange powder, yield 28%. $^1H$ NMR (500 MHz, CDCl$_3$, $\delta$): 3.09 (s, 6H), 6.71 (d, 2H, $J$ = 8.8 Hz), 6.91 (dd, 1H, $J$ = 8.7 Hz; $J$ = 2.0 Hz), 7.03 (d, 1H, $J$ = 2.0 Hz), 7.37 (d, 1H, $J$ = 15.2 Hz), 7.58 (d, 2H, $J$ = 8.8 Hz), 7.85 (d, 1H, $J$ = 8.7 Hz), 7.94 (d, 1H, $J$ = 15.2 Hz), 13.46 (s, 1H). $^{13}C$ NMR (250 MHz, CDCl$_3$, $\delta$): 192.6, 164.2, 152.5, 147.1, 141.2, 131.0, 130.3, 122.2, 119.2, 119.0, 118.5, 113.8, 111.8, 40.1. HRMS $m/z$: calcd for C$_{17}$H$_{16}$ClNO$_2$, 309.0942 [$M$+H]$^+$; found, 309.0942.

**4'-Bromo-2'-Hydroxy-4-dimethylaminochalcone (1-Br).** Orange powder, yield 28%. $^1H$ NMR (500 MHz, CDCl$_3$, $\delta$): 3.09 (s, 6H), 6.71 (d, 2H, $J$ = 8.8 Hz), 7.06 (dd, 1H, $J$ = 8.7 Hz, $J$ = 2.0 Hz), 7.21 (d, 1H, $J$ =2.0 Hz), 7. 37 (d, 1H, $J$ =15.2 Hz), 7. 58 (d, 2H, $J$ = 8.8 Hz), 7.77 (d, 1H, $J$ =8.6 Hz), 7.94 (d, 1H, $J$ = 15.2 Hz), 13.42 (s, 1H). $^{13}C$ NMR (250 MHz, CDCl$_3$, $\delta$): 192.8, 164.0, 152.5, 147.2, 131.0,

130.3, 129.8, 122.1, 121.7, 119.3, 113.7, 111.8, 40.1. HRMS *m/z*: calcd for $C_{17}H_{16}BrNO_2$, 346.0437 [*M*+H]$^+$; found, 346.0440.

**2'-Hydroxy-4-chlorochalcone (3-Cl).** Yellow powder, yield 78%. $^1$H NMR (500 MHz, CDCl$_3$, $\delta$): 6.86 (t, 1H, *J* = 7.6 Hz), 6.95 (d, 1H, *J* = 8.4 Hz), 7.32 (d, 2H, *J* = 8.5 Hz), 7.42 (t, 1H, *J* = 7.9 Hz), 7.50 (d, 2H, *J* =8.5 Hz), 7.53 (d, 1H, *J* =15.5 Hz), 7.77 (d, 1H, *J* = 15.4 Hz), 7.82 (dd, 1H, *J* =8.2 Hz, *J* = 1.3 Hz), 12.67 (s, 1H). $^{13}$C NMR (250 MHz, CDCl$_3$, $\delta$): 193.5, 163.6, 143.9, 136.9, 136.6, 133.1, 129.8, 129.6, 129.4, 120.6, 119.9, 118.9, 118.7. HRMS *m/z*: calcd for $C_{15}H_{11}ClO_2$, 259.0520 [*M*+H]$^+$; found, 259.0520.

**2'-Hydroxy-4-methoxychalcone (3-MeO).** Yellow powder, yield 93%. $^1$H NMR (500 MHz, CDCl$_3$, $\delta$): 3.89 (s, 3H), 6.94-7.00 (m, 3H), 7.05 (d, 1H, *J* = 8.4 Hz), 7.51 (t, 1H, *J* = 7.8 Hz), 7.56 (d, 1H, *J* = 15.2 Hz), 7.65 (d, 2H, *J* = 8.8 Hz), 7.93 (d, 1H, *J* = 15.2 Hz), 7.94 (dd, 1H, *J* = 8.1 Hz, *J* =1.3 Hz), 12.97 (s, 1H). $^{13}$C NMR (250 MHz, CDCl$_3$, $\delta$): 193.7, 163.6, 162.1, 145.4, 136.2, 130.6, 129.6, 127.4, 120.1, 118.8, 118.6, 117.6, 114.5, 55.5. HRMS *m/z*: calcd for $C_{16}H_{14}O_3$, 255.1016 [*M*+H]$^+$; found, 255.1020.

**1.2 General procedure for flavanones** (0.1 mg scale).

A 7.5·10$^{-6}$ M solution of a 2'-hydroxychalcone derivative in CH or DCM was irradiated by the light source of appropriate wavelength (see main text) for 2-5h at RT. Reaction progress was monitored by absorption spectra, TLC (eluent CHCl$_3$ or 1%MeOH in CHCl$_3$) and LCMS analyses (eluent MeOH).

**Procedure for 4'-dimethylaminoflavanone** (**2**, 20 mg scale). 20 mg of 2'-hydroxy-4-dimethylaminochalcone (**1**) was dissolved in DCM (100 mL) and irradiated by the >450 nm light source for 2 days under stirring at RT. Solvent was evaporated and the residue was purified by column chromatography. White powder, yield 92%. $^1$H NMR (700 MHz, CDCl$_3$, $\delta$): 2.87 (1H, dd, *J* =16.9 Hz, *J* = 2.6 Hz), 3.01 (6H, s), 3.18 (1H, dd, *J* = 16.8 Hz, *J* = 13.7 Hz), 5.42 (1H, dd, *J* = 13.5 Hz, *J* = 2.3 Hz), 6.79, (2H, d, *J* = 7.2 Hz), 7.02 − 7.08 (m, 2H), 7.38 (2H, d, *J* = 8.4 Hz), 7.51 (1H, t, *J* = 7.4 Hz), 7.95 (1H, dd, *J* = 7.9 Hz, *J* = 1.3 Hz). HRMS *m/z*: calculated for $C_{17}H_{17}NO_2$, 268.1332 [*M*+H]$^+$; found, 268.1335.

# ¹H-NMR analyses
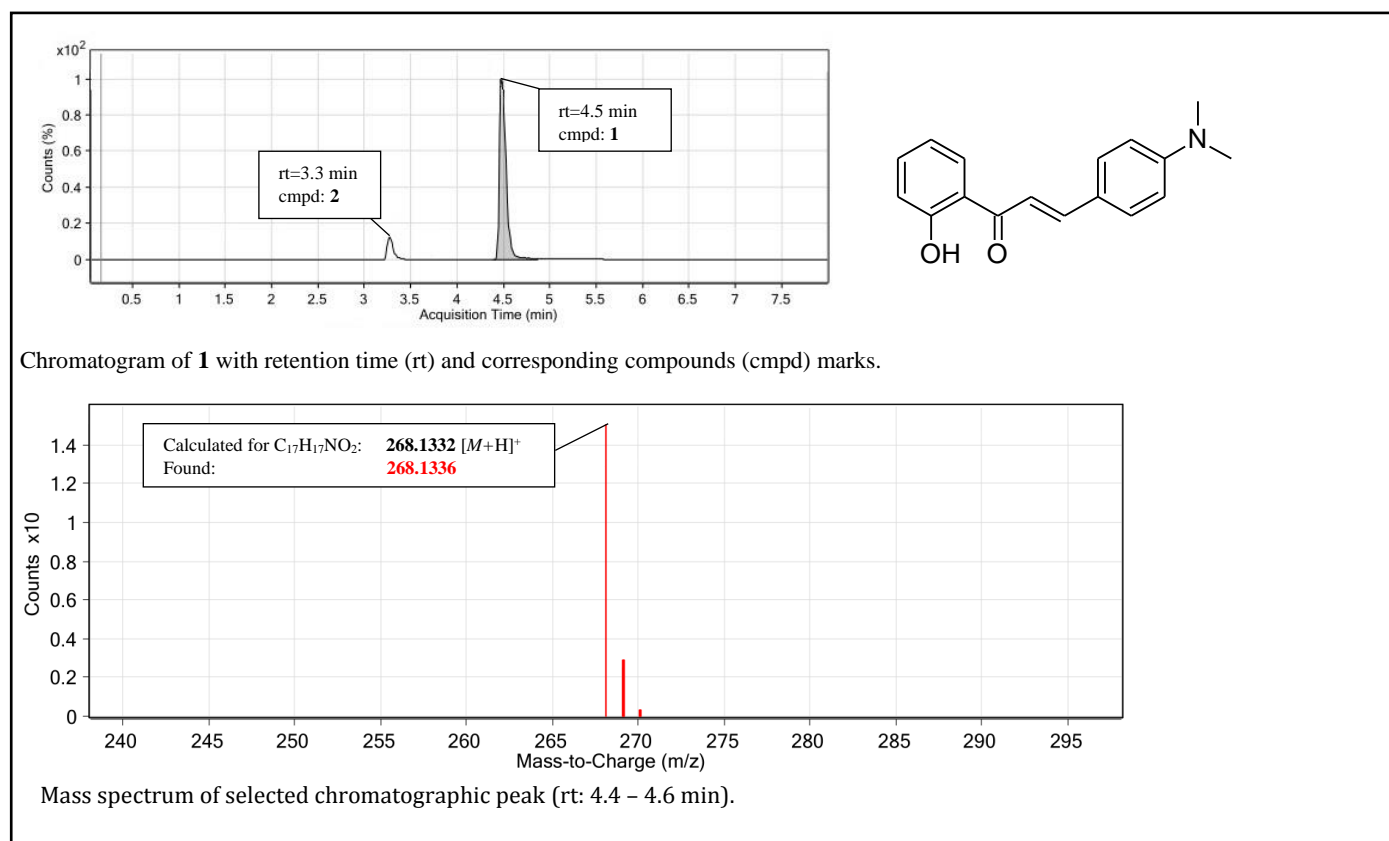
3-MeO
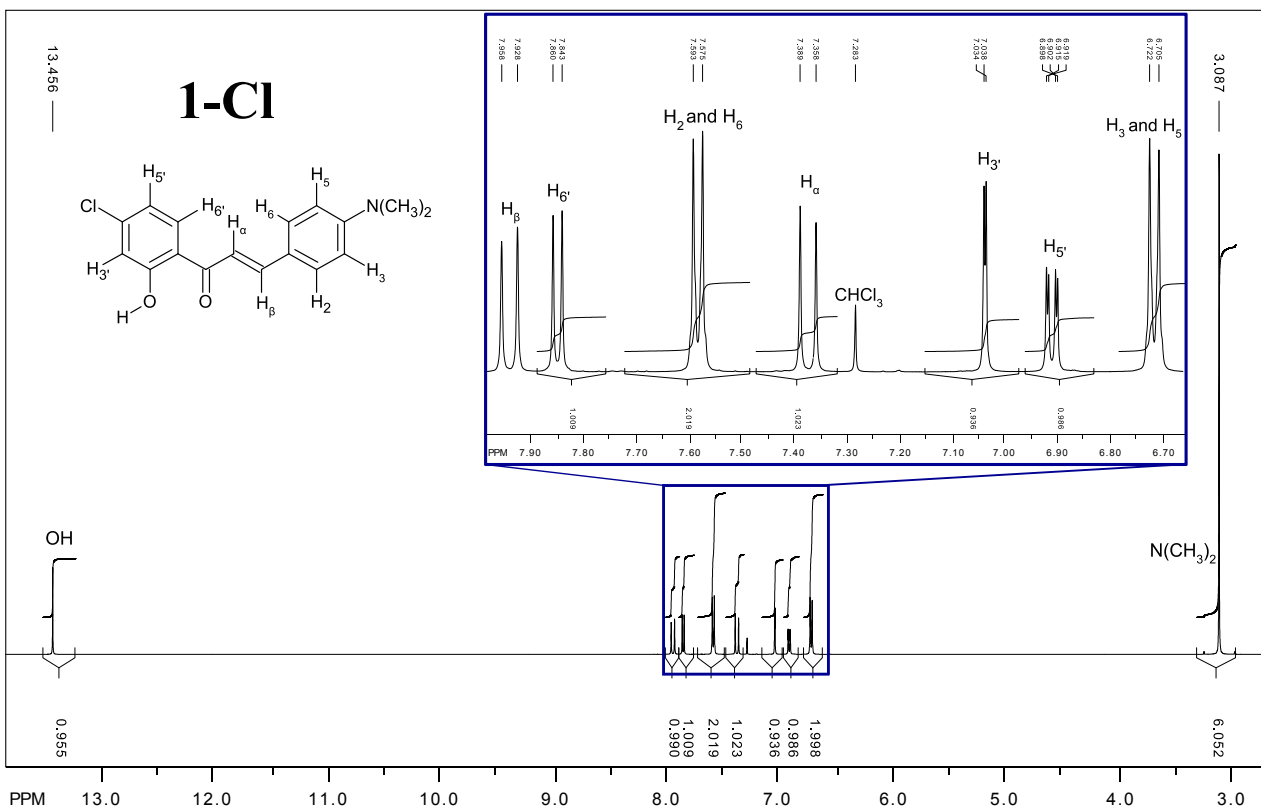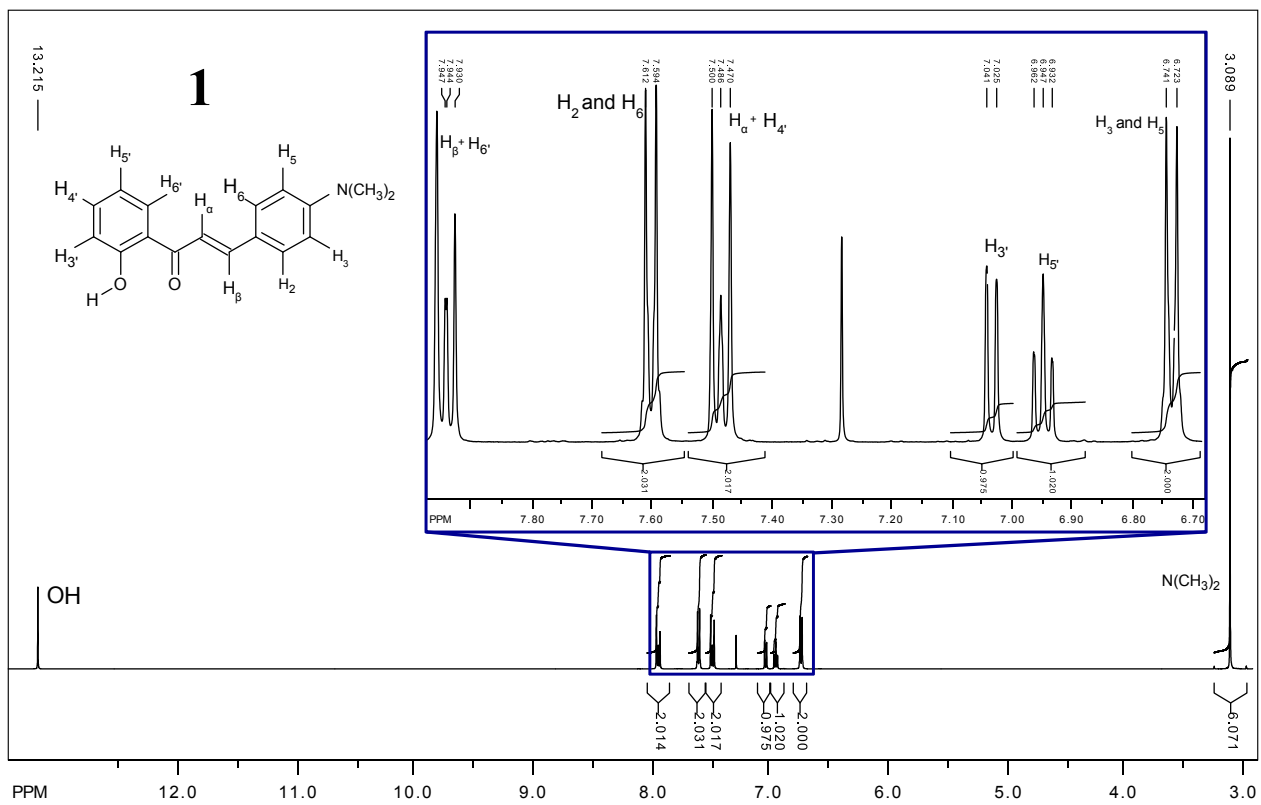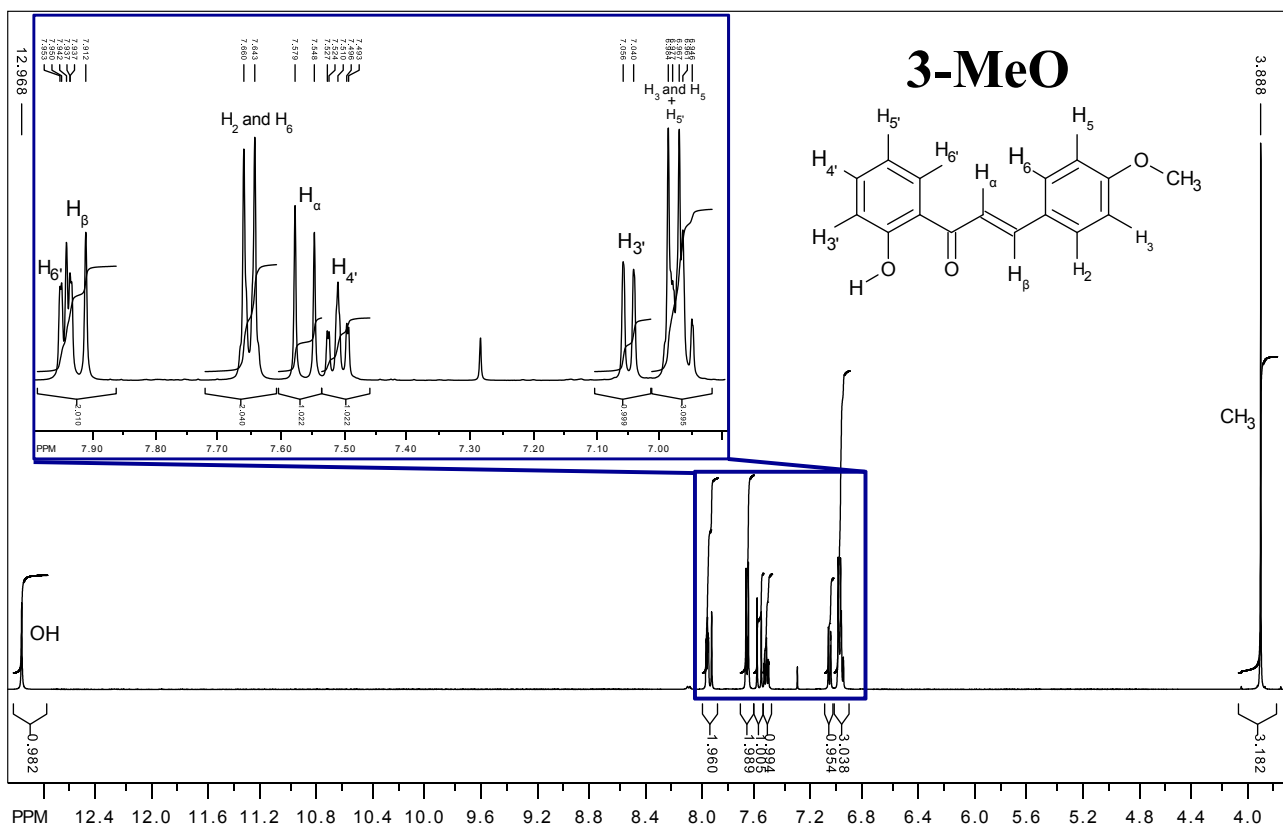
# LCMS analyses

## Sample preparation

**2'-Hydroxychalcones.** The solutions of respective 2'-hydroxychalcones were prepared for a few hours before experiment and were transferred to the LCMS analyses. Due to the discussed sensitivity to the visible light, trace amounts of respective flavanones are present in the chromatograms of 2'-hydroxychalcones.
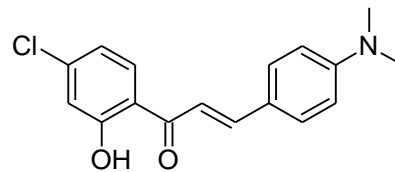
**Flavanones.** It should be noted that for detection of flavanones in the LCMS experiments, samples were irradiated for a limited amount of time. Due to the different rates of photoinduced cyclization, in some cases the conversion was not full. It does not however indicate that full conversion of a respective 2'-hydroxychalcone cannot be reached.

## 2'-Hydroxychalcones

## 2'-Hydroxy-4-dimethylaminochalcone (1)



Chromatogram of **1** with retention time (rt) and corresponding compounds (cmpd) marks.



Mass spectrum of selected chromatographic peak (rt: 4.4 – 4.6 min).

# 4'-Chloro-2'-hydroxy-4-dimethylaminochalcone (1-Cl).
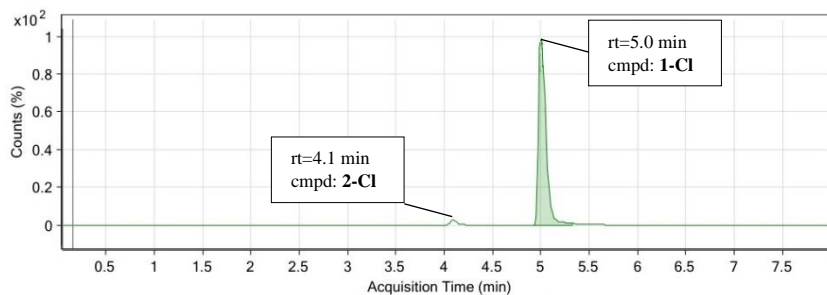


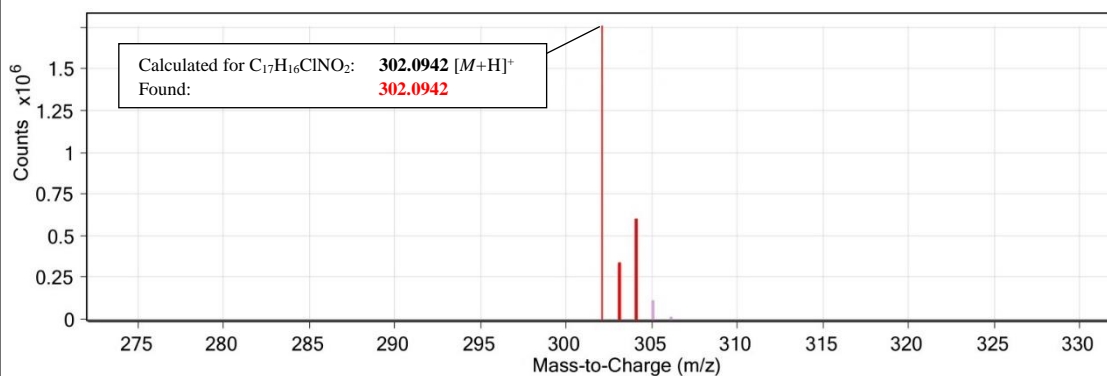Chromatogram of **1-Cl** with retention time (rt) and corresponding compounds (cmpd) marks.

| | |
|---|---|
| Calculated for $C_{17}H_{16}ClNO_2$: | **302.0942** $[M+H]^+$ |
| Found: | **302.0942** |

Mass spectrum of selected chromatographic peak (rt: 4.9 – 5.3 min).

# 4'-Bromo 2'-Hydroxy-4-dimethylaminochalcone (1-Br).
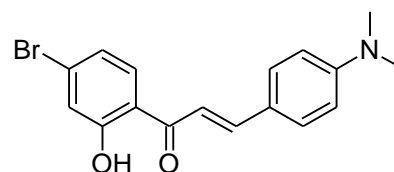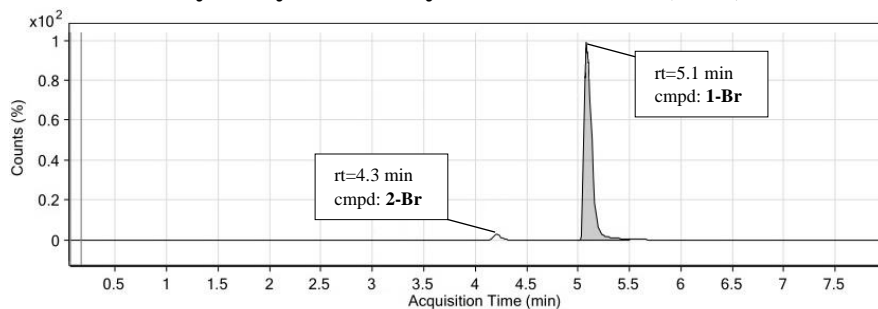


Chromatogram of **1-Br** with retention time (rt) and corresponding compounds (cmpd) marks.

| | |
|---|---|
| Calculated for $C_{17}H_{16}BrNO_2$: | **346.0437** $[M+H]^+$ |
| Found: | **346.0440** |

Mass spectrum of selected chromatographic peak (rt: 5.0-5.2 min).

## 2'-Hydroxy-4-chlorochalcone (3-Cl).
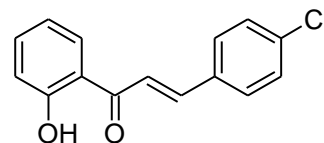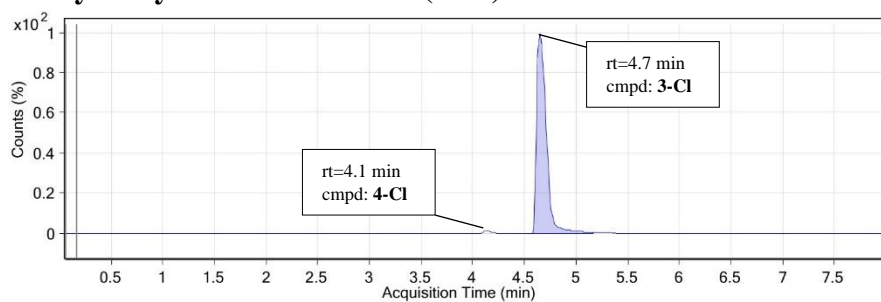


Chromatogram of **3-Cl** with retention time (rt) and corresponding compounds (cmpd) marks.

rt=4.7 min
cmpd: **3-Cl**

rt=4.1 min
cmpd: **4-Cl**



Calculated for $C_{15}H_{11}ClO_2$:    **259.0520** $[M+H]^+$
Found:    **259.0523**

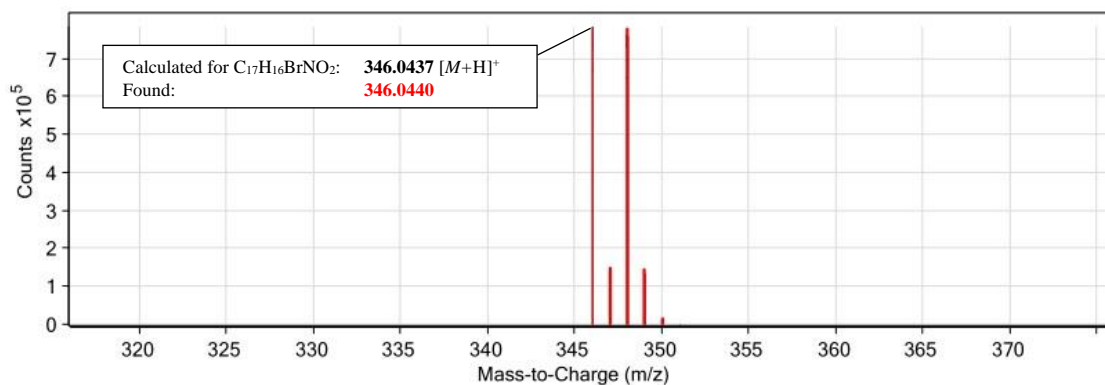Mass spectrum of selected chromatographic peak (rt: 4.6-4.9 min).

## 2'-Hydroxy-4-methoxychalcone (3-MeO)
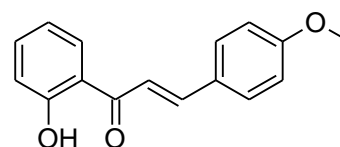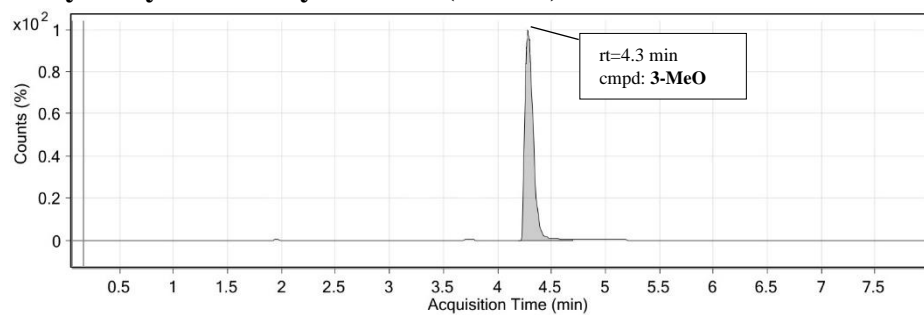


Chromatogram of **3-MeO** with retention time (rt) and corresponding compounds (cmpd) marks.

rt=4.3 min
cmpd: **3-MeO**



Calculated for $C_{16}H_{14}O_3$:    **255.1016** $[M+H]^+$
Found:    **255.1020**

Mass spectrum of selected chromatographic peak (rt: 4.3 – 4.4 min).

## 2'-Hydroxychalcone (3)
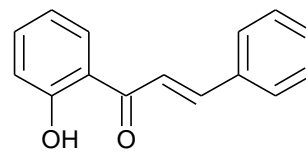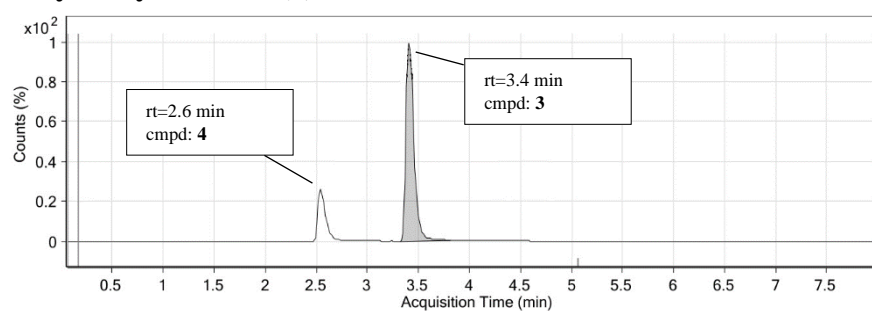


Chromatogram of **3** with retention time (rt) and corresponding compounds (cmpd) marks.



| Calculated for $C_{15}H_{12}O_2$: | **255.0910** $[M+H]^+$ |
| Found: | **255.0916** |

Mass spectrum of selected chromatographic peak (rt: 3.3 – 3.4 min).

## 4.2 Flavanones

### 4'-Dimethylaminoflavanone (2).



Chromatogram of **2** with retention time (rt) and corresponding compound (cmpd) marks.

rt=3.3 min
cmpd: **2**

rt=4.5 min
cmpd: **1**



| Calculated for $C_{17}H_{17}NO_2$: | **268.1332** $[M+H]^+$ |
| Found: | **268.1335** |

Mass spectrum of selected chromatographic peak (rt: 3.2 – 3.4 min).

### 4-Chloro-4'-Dimethylaminoflavanone (2-Cl).



Chromatogram of **2-Cl** with retention time (rt) and corresponding compound (cmpd) marks.

rt=4.1 min
cmpd: **2-Cl**

rt=5.0 min
cmpd: **1-Cl**



| Calculated for $C_{17}H_{16}ClO_2$: | **302.0942** $[M+H]^+$ |
| Found: | **302.0942** |

Mass spectrum of selected chromatographic peak (rt: 4.1 – 4.2 min).
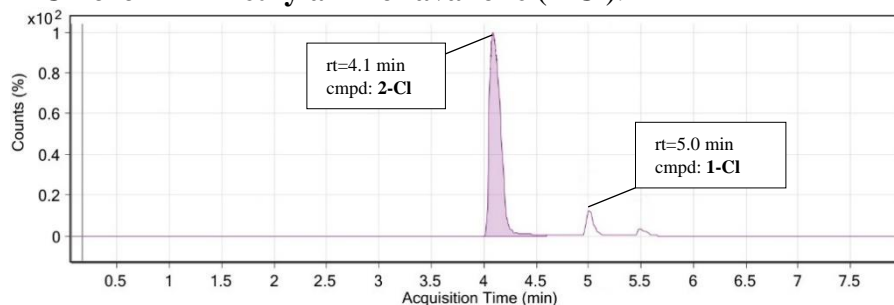
## 4'-Bromo-4-Dimethylaminoflavanone (2-Br)
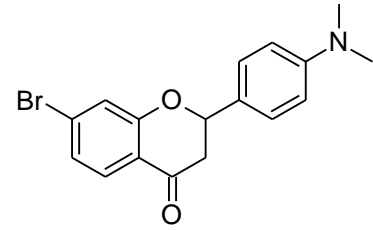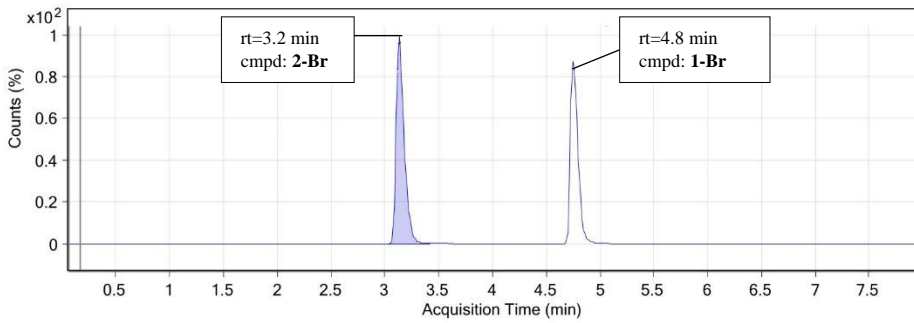


Chromatogram of **2-Br** with retention time (rt) and corresponding compound (cmpd) marks.



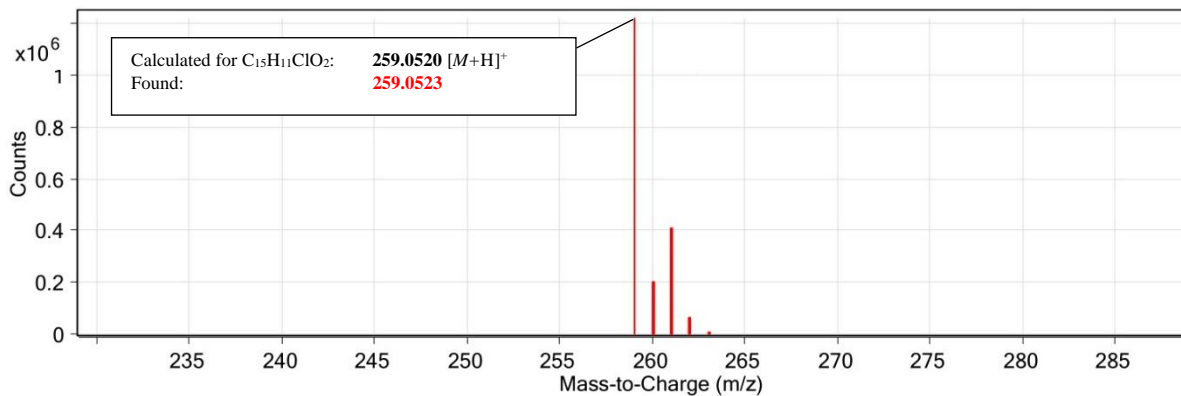Calculated for $C_{17}H_{16}BrNO_2$:   **346.0437** $[M+H]^+$
Found:                                 **346.0437**
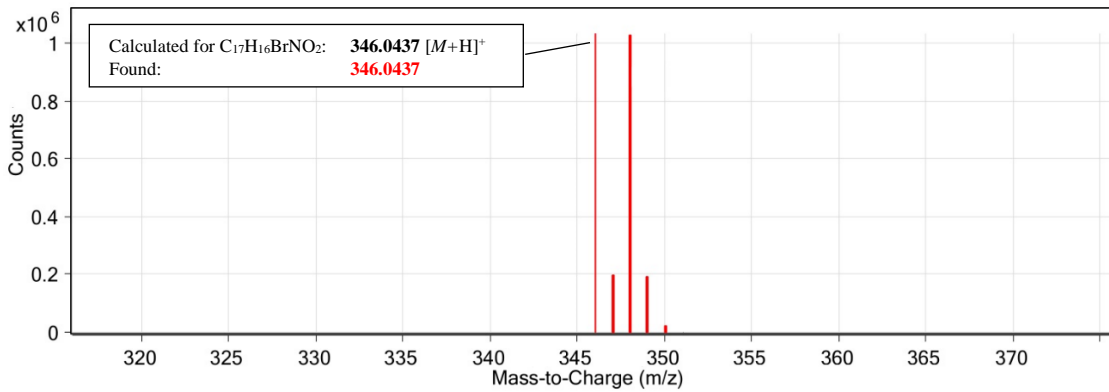
Mass spectrum of selected chromatographic peak (rt: 3.1 – 3.3 min).

## Flavanone (4)
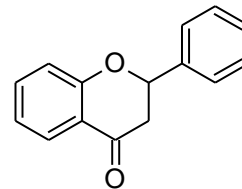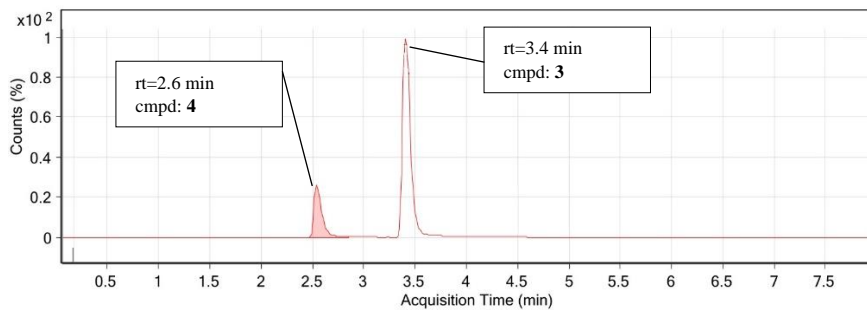


Chromatogram of **4** with retention time (rt) and corresponding compound (cmpd) marks.



Calculated for $C_{15}H_{12}O_2$:   **255.0910** $[M+H]^+$
Found:                              **255.0915**
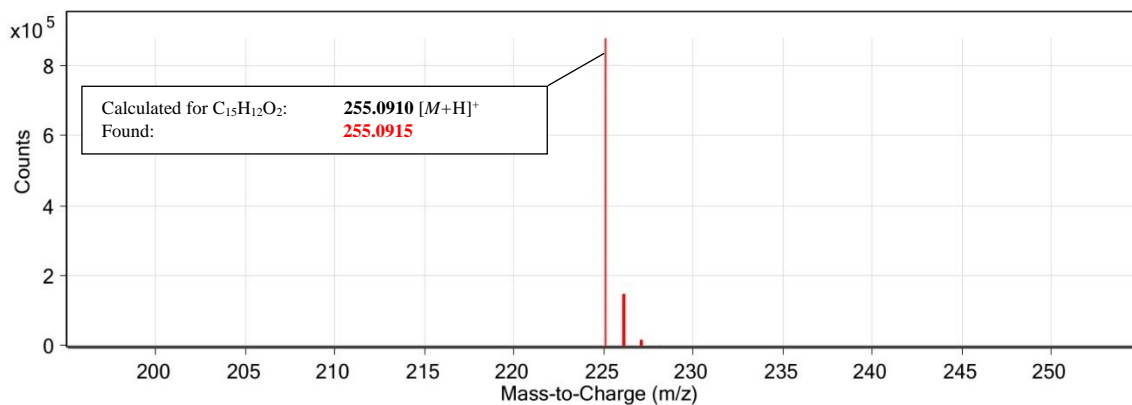
Mass spectrum of selected chromatographic peak (rt: 2.5 – 2.7 min).

## 4'-Chloroflavanone (4-Cl)
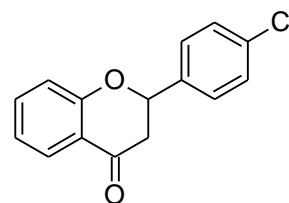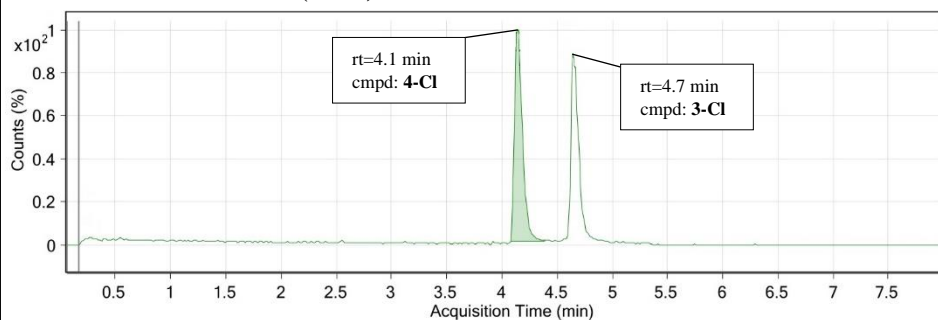


Chromatogram of **4-Cl** with retention time (rt) and corresponding compound (cmpd) marks.

rt=4.1 min
cmpd: **4-Cl**

rt=4.7 min
cmpd: **3-Cl**

Calculated for $C_{15}H_{11}ClO_2$:  **259.0520** $[M+H]^+$
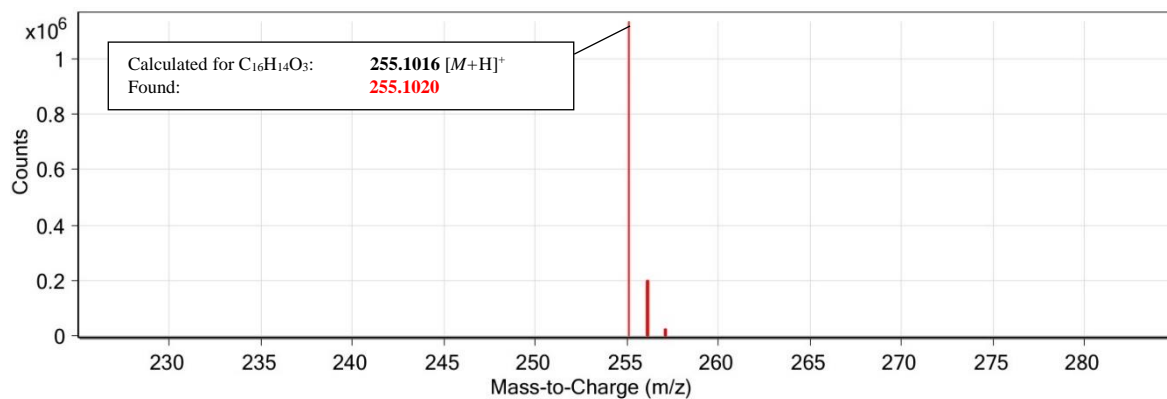Found:                                **259.0521**
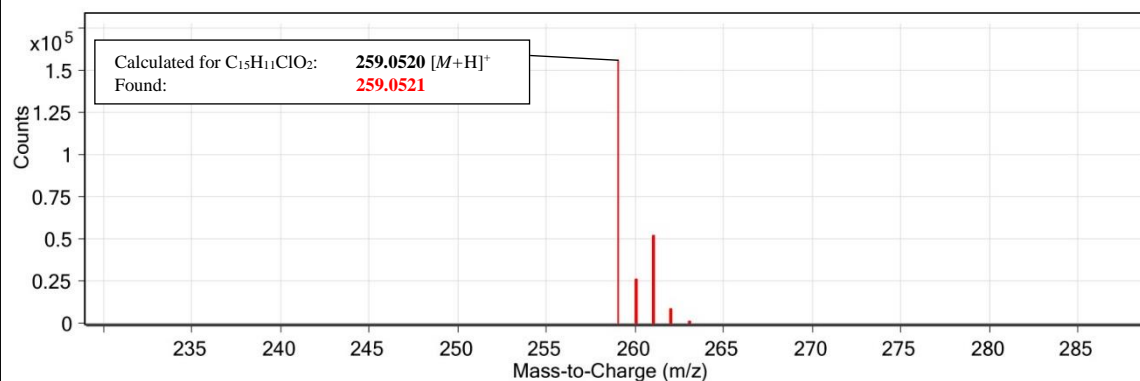


Mass spectrum of selected chromatographic peak (rt: 4.0 – 4.2 min).

## 4'-Methoxyflavanone (4-MeO)
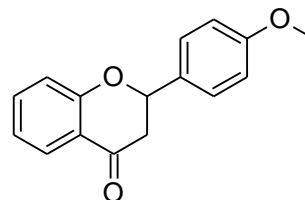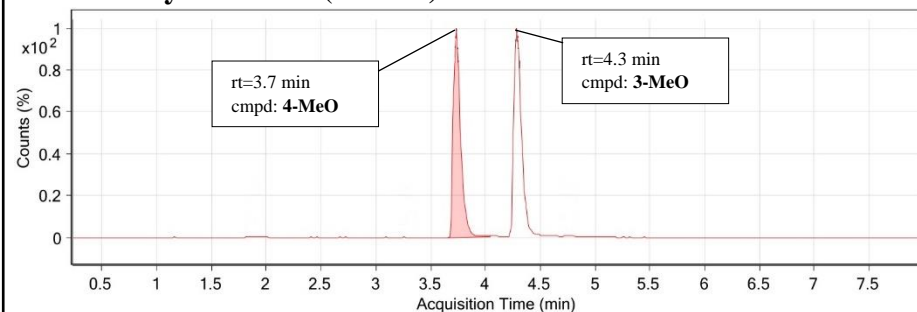


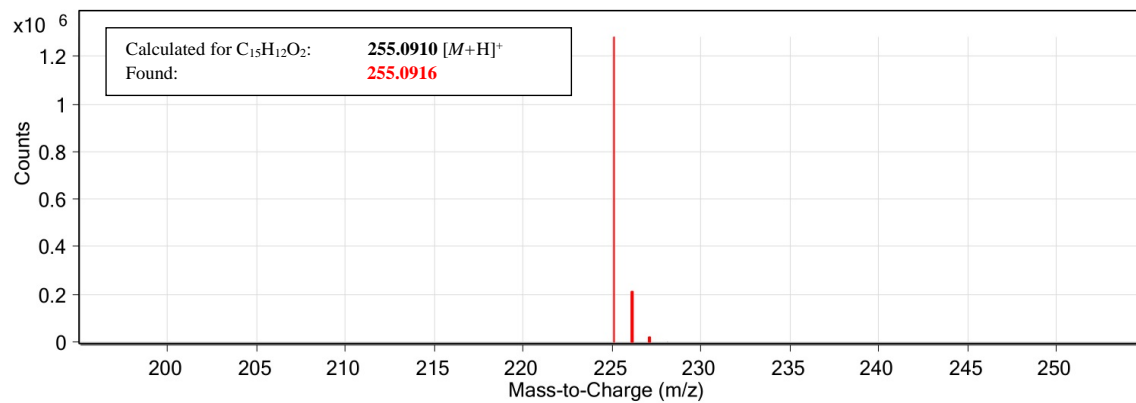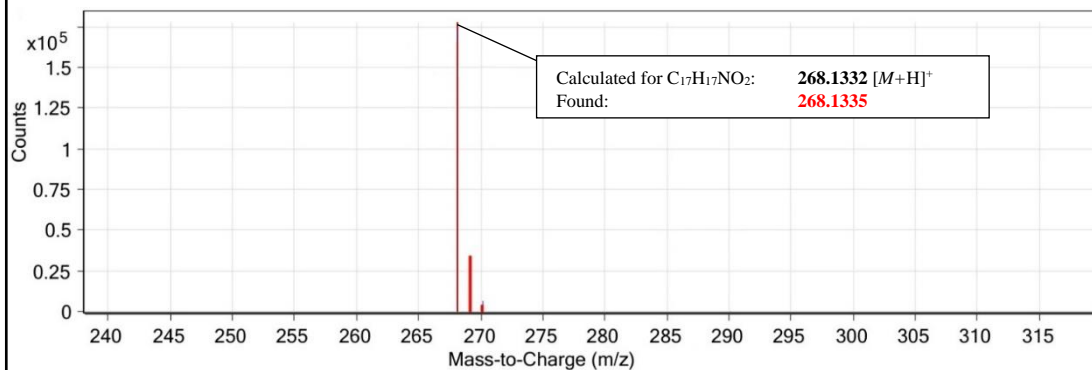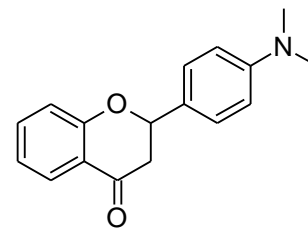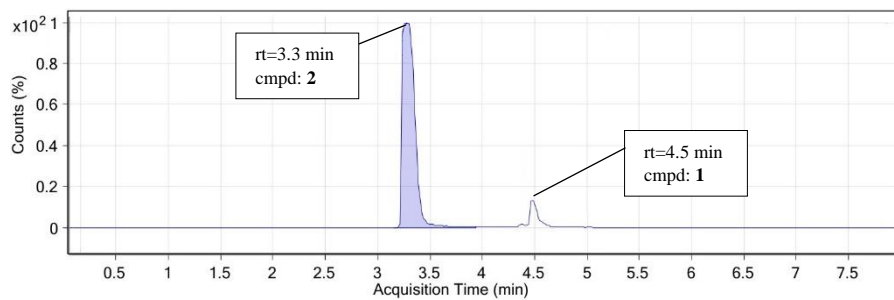Chromatogram of **4-MeO** with retention time (rt) and corresponding compound (cmpd) marks.

rt=3.7 min
cmpd: **4-MeO**

rt=4.3 min
cmpd: **3-MeO**

Calculated for $C_{16}H_{14}O_3$:  **259.0520** $[M+H]^+$
Found:                             **259.0521**
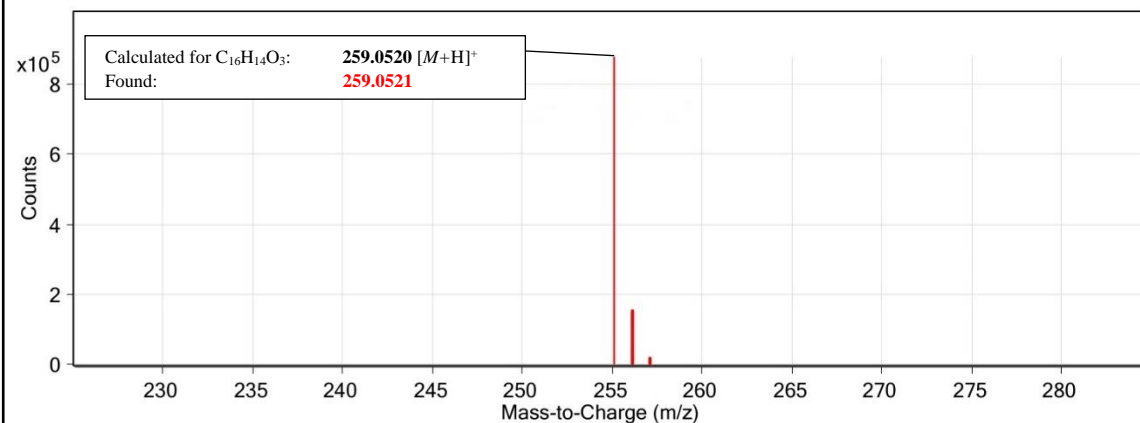


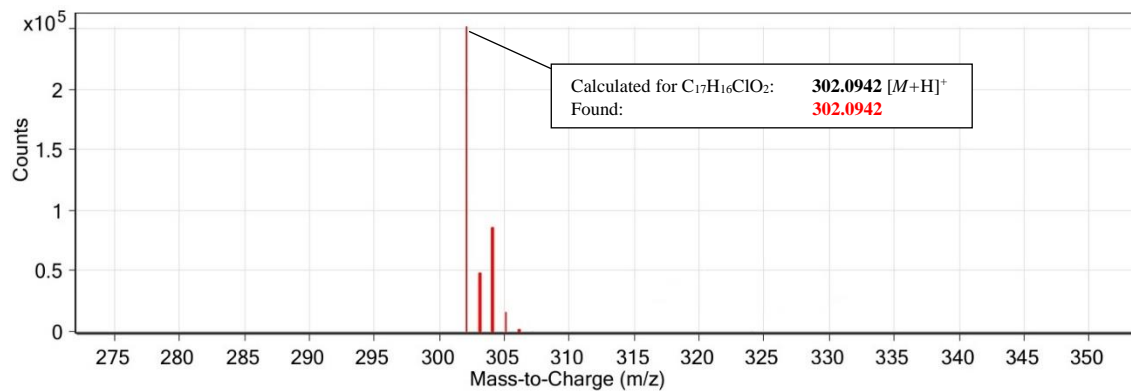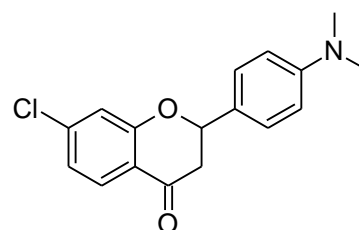Mass spectrum of selected chromatographic peak (rt: 3.6 – 3.8 min).

# 2. Photochemical investigations

## Procedure for determination of quantum yield of photoinduced transformation 1→2

Due to the lack of absorption of flavanones at the irradiation wavelengths all the photoreaction yields $\varphi_{1\to2}$ were determined using the decrease of the long-wavelength absorption of chalcones.

The quantum yield of photoinduced transformation $\varphi_{1\to2}$ can be expressed as follows:

$$\varphi_{1\to2} = \frac{N_{mol}}{N_{ph}} \cdot 100\%, \tag{1}$$

where:

- $N_{mol}$ is total number of reacted molecules,
- $N_{ph}$ is total number of absorbed photons.

To calculate $N_{ph}$ we used a following formula:

$$N_{ph} = N_0 - N, \tag{2}$$

where:

- $N_0$ is the total number of incident photons,
- $N$ is the total number the photons which have not been absorbed by the sample.

Figures **S0.1** and **S0.2** present to experimental setups for determination the $N_0$ and $N$ values.
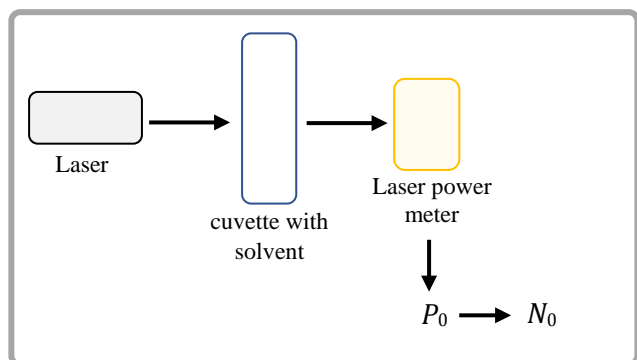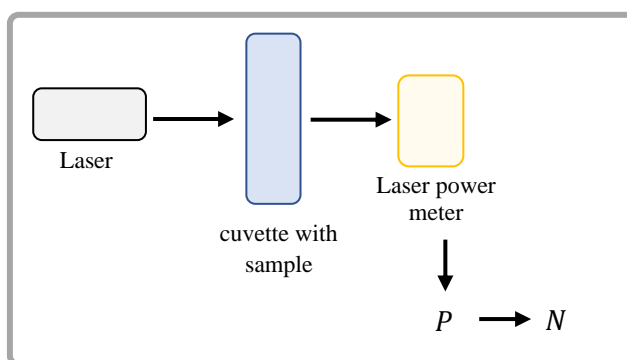


Figure **S0.1**          Figure **S0.2**

The value measured directly in the experiment is power of light $P$. Is is converted to $N$ as follows.

Total energy $E_{tot}$ of the photons within laser beam equals:

$$E_{tot} = P \cdot t, \tag{3}$$

where $t$ is the time of irradiation. Energy of a single photon $E_{sph}$:

$$E_{sph} = \frac{h \cdot c}{\lambda}, \tag{4}$$

where $h$ is the Planck constant, $c$ is the speed of light and $\lambda$ the wavelength of used light.

The number of photons $N_0$ and $N$ can be obtained from:

$$N = \frac{\text{Total energy within laser beam}}{\text{Energy of a single photon}} = \frac{E_{tot}}{E_{sph}}, \tag{5}$$

$$N = \frac{P \cdot t}{\frac{h \cdot c}{\lambda}}, \tag{6}$$

$$N_0 = \frac{P_0 \cdot t}{\frac{h \cdot c}{\lambda}}. \tag{7}$$

As concentration and thus absorption of **1** is decreasing under irradiation (figure **S0.3**), $P$ in equation (6) is a function of time $P(t)$. The number of photons $N$ per second will be expressed by the following formula:

$$\frac{N}{t} = \frac{P(t)}{\frac{h \cdot c}{\lambda}}, \tag{8}$$

$$\frac{N_0}{t} = \frac{P_0}{\frac{h \cdot c}{\lambda}}. \tag{9}$$

According to equation (2), expressions (8) and (9) can be merged as follows:

$$\frac{N_{ph}}{t} = \frac{N_0}{t} - \frac{N}{t} = \frac{P_0 - P(t)}{\frac{h \cdot c}{\lambda}}. \tag{10}$$

Finally, the number of total absorbed photons $N_{ph}$ during time interval $[t_0 : t_e]$ will be given by following integral:

$$N_{ph} = \int_{t_e}^{t_0} \frac{N_{ph}}{t} \, dt = \int_{t_e}^{t_0} \frac{P_0 - P(t)}{\frac{h \cdot c}{\lambda}} \, dt. \tag{11}$$

Equation (11) allows one to calculate total number of absorbed photons using calibrated laser light power meter.

The number of reacted molecules $N_{mol}$ is the difference between number of molecules before and after irradiation. It is determined from absorbance as:

$$N_{mol} = c_0 \cdot V \left(1 - \frac{A}{A_0}\right), \tag{12}$$

where $c_0$ is the concentration at $t_0$ time, $V$ is the volume of solution, $A$ and $A_0$ are the absorbances at $t_e$ and $t_0$ time, respectively.

## Representative calculation of $\varphi_{1 \to 2}$ for DCM solution.

Figure S0 shows changes in absorption spectra of $7.6 \cdot 10^{-6}$ M solution of **1** in DCM, during 28 minutes of irradiation. Eight absorption measurements and power light measurements were performed with a 4 minute interval. The collected experimental data are presented in Table S0. The $P_0$ value of 28.2 mW was obtained for pure DCM solvent.
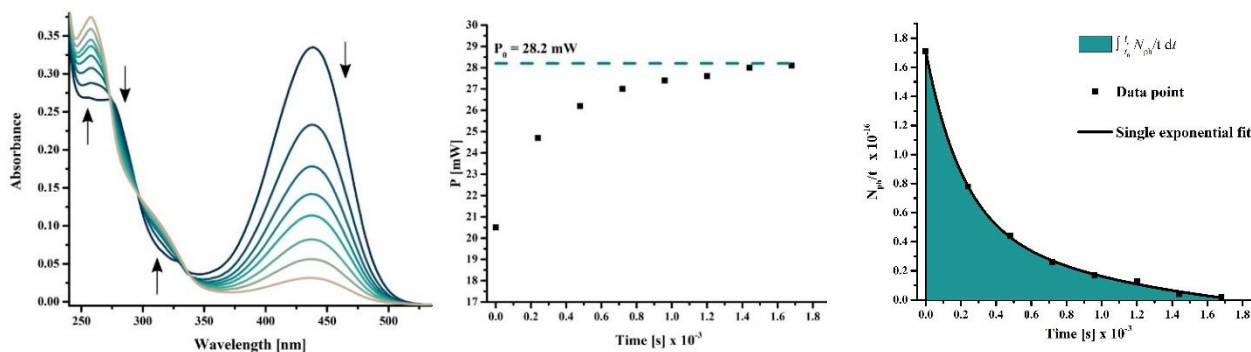


**Figure S0.** Changes in absorption spectra during 28 minutes of irradiation (left), the results of P measurements during irradiation (center) and the number of absorbed photons per second plotted vs time with integrated area (right).

**Table S0.** Experimental data collected during 28 minutes of irradiation **1** in DCM solution.

| # | $t$ [s] | $P(t)$ [mW] | $P_0 - P(t)$ [mW] | $\frac{N_{ph}}{t} \cdot 10^{16}$ [s$^{-1}$] |
|---|---|---|---|---|
| 1 | 0 | 20.5 | 7.7 | 1.71 |
| 2 | 240 | 24.7 | 3.5 | 0.78 |
| 3 | 480 | 26.2 | 2.0 | 0.44 |
| 4 | 720 | 27.0 | 1.2 | 0.26 |
| 5 | 960 | 27.4 | 0.8 | 0.17 |
| 6 | 1200 | 27.6 | 0.6 | 0.13 |
| 7 | 1440 | 28.0 | 0.2 | 0.04 |
| 8 | 1680 | 28.1 | 0.1 | 0.02 |

Finally, we obtain $N_{ph} = 6.61 \cdot 10^{18}$ and $N_{mol} = 1.22 \cdot 10^{16}$. According with (1):

$$\varphi_{1 \to 2} = \frac{N_{mol}}{N_{ph}} \cdot 100\% = \frac{1.22 \cdot 10^{16}}{6.61 \cdot 10^{18}} * 100\% = 0.19\%. \tag{13}$$

# Calculation of rate constant of photoinduced transformation 1→2

Rate constants $k$ were obtained using first order reaction kinetics equation:

$$ln\left(\frac{A}{A_0}\right) = -kt,$$

Where $A$ and $A_0$ are absorbances measured at the maximum of long-wavelength absorption bands (420nm for CH and 440nm for DCM solutions) at time $t$ and $t = 0$, respectively. Due to different molar extinction coefficients at irradiation wavelengths $\varepsilon_\lambda$ depending on the solvent polarity, the $k$ values evaluated for different media cannot be compared with each other. Therefore, following correction was done:

$$ln\left(\frac{A}{A_0}\right) = -\frac{k}{\varepsilon_\lambda}t = k_{corr}t.$$

Thus obtained $k_{corr}$ is independent of the amount of absorbed light per second and can be compared for various conditions used.
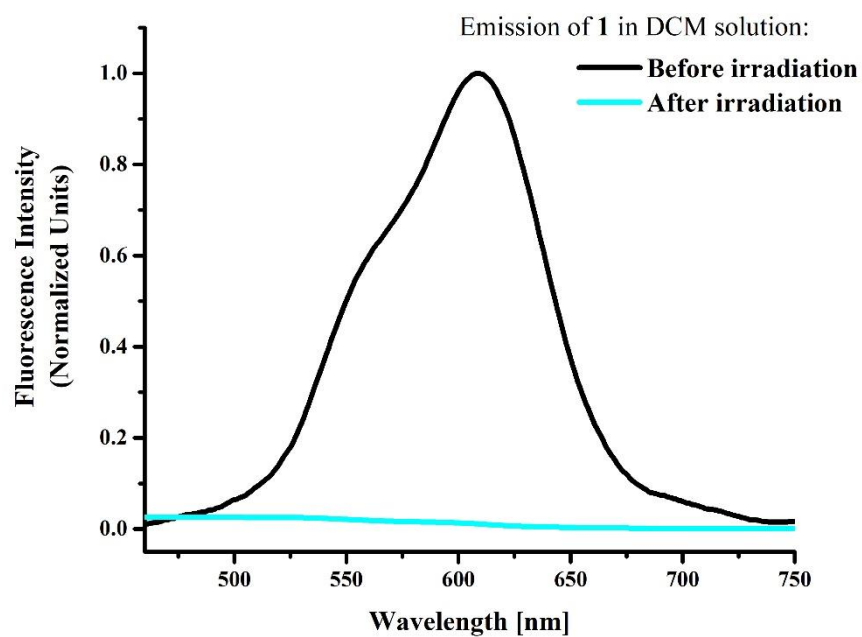
**Figure S1.** Fluorescence spectrum of **1** in DCM before irradiation (black) and after irradiation (cyan)
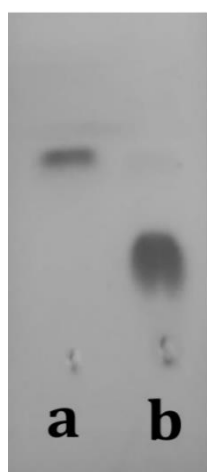


**Figure S2.** Representative TLC on the example of **1**→**2** reaction: before (a, **1**) and after (b, **2**) irradiation.
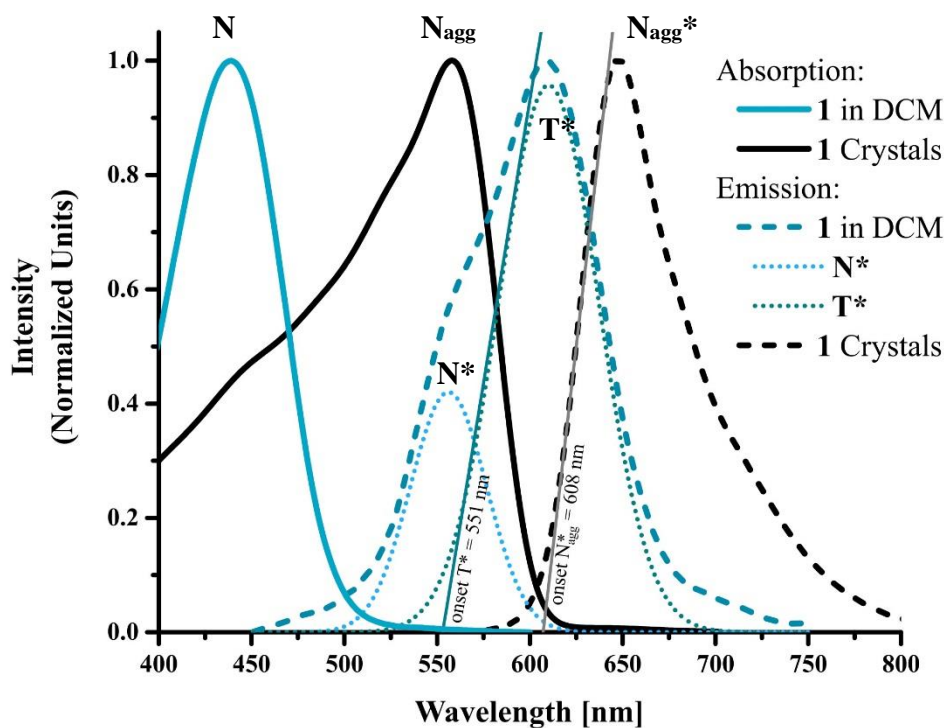
**Figure S3**. Comparison of absorption and fluorescence spectra of **1** in DCM solution and crystal phase. Lines indicate linear fit curves to determine onset values of T* state in DCM and $N_{agg}$* in crystal.
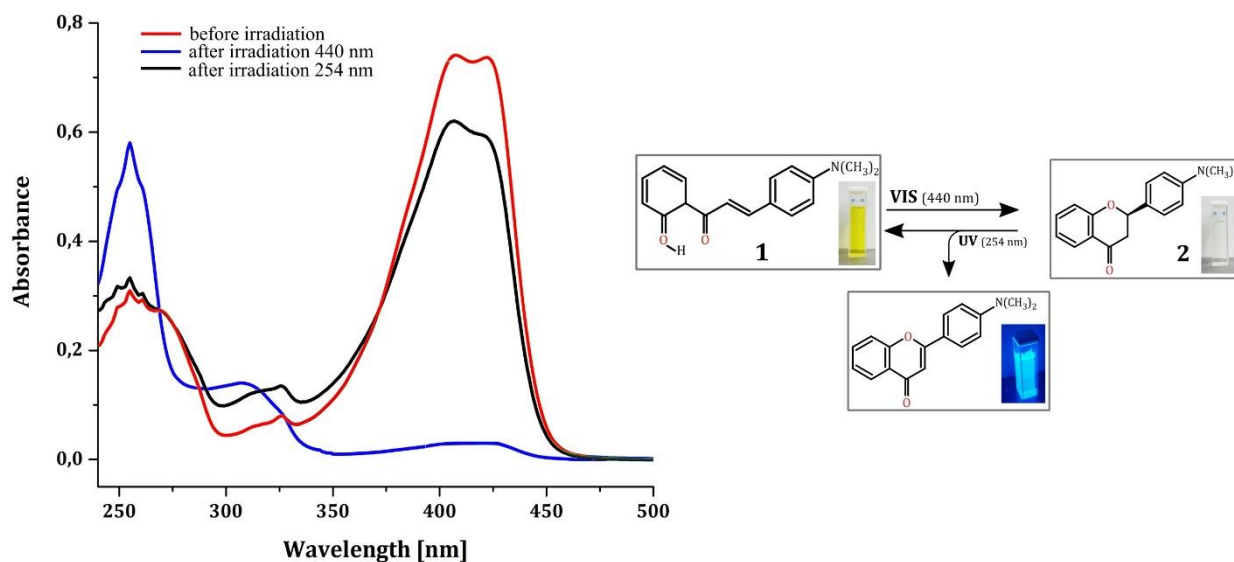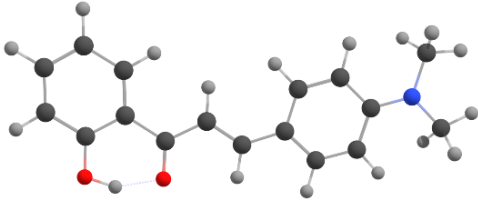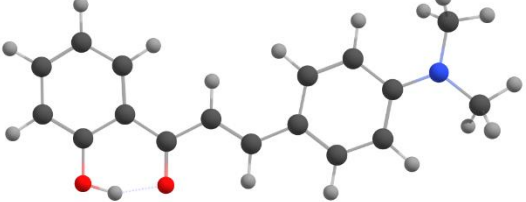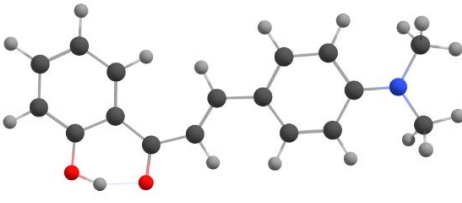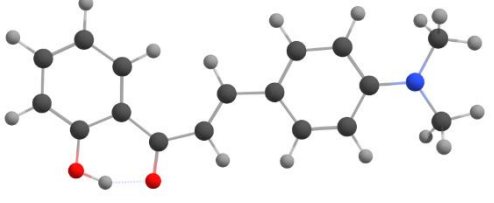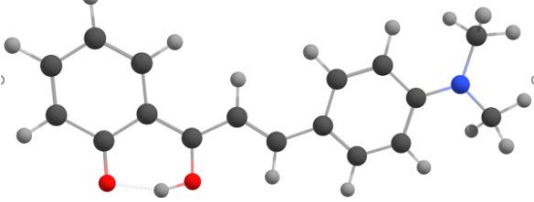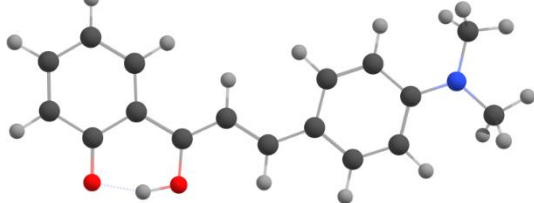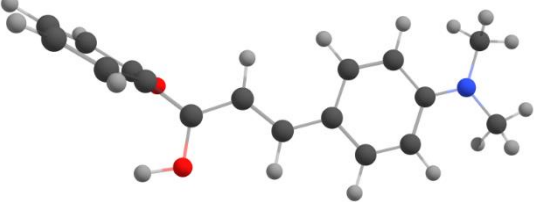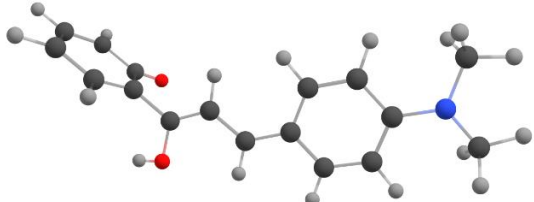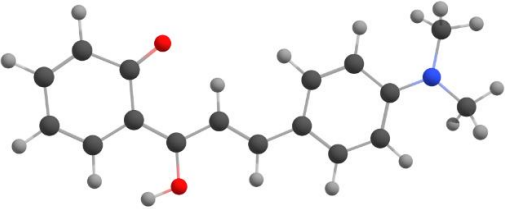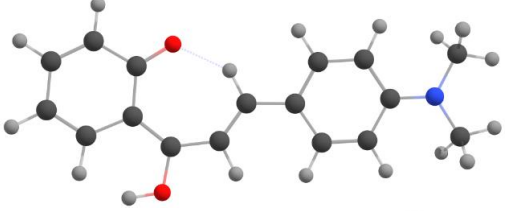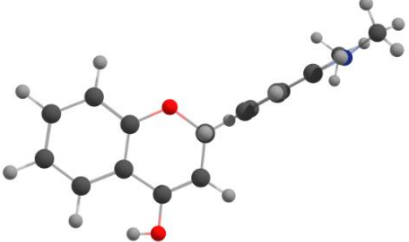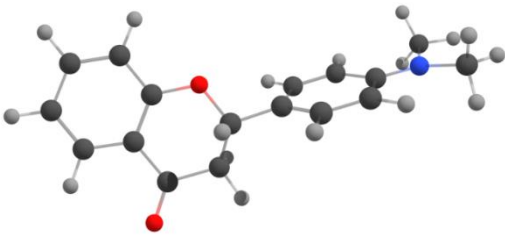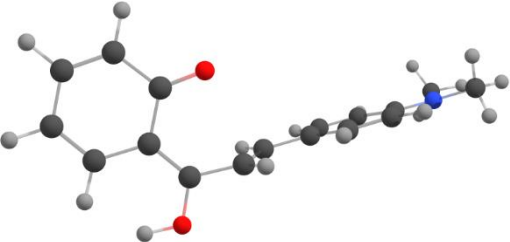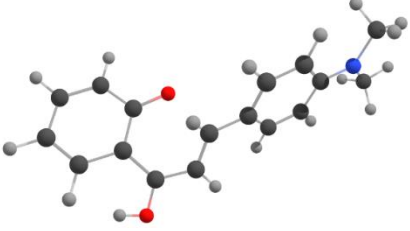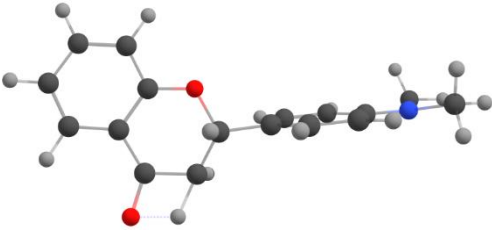


**Figure S4.** Absorption spectrum of **1** in **CH** before irradiation (red), after irradiation with 440nm (blue) and 254 nm (black).

# 3. Calculations

**Optimized structures and Gibbs energies of tautomeric and isomeric forms of 1 in ground and excited states.**

| Form | State | G, hartree | Optimized structure |
|---|---|---|---|
| $N_{s\text{-}cis}$ | $S_0$ | -863.047557 | |
| | $S_1$ | -862.942132 | |
| $N_{s\text{-}trans}$ | $S_0$ | -863.037151 | |
| | $S_1$ | -862.933106 | |
| $T_{Z,E}$ | $S_0$ | -863.029993 | |
| | $S_1$ | -862.952013 | |
| $T_{twist}$ | $S_0$ | -862.975776 | |
| | $S_1$ | -862.973114 | |

| | | | |
|---|---|---|---|
| $T_{E,E}$ | $S_0$ | -863.014538 |  |
| $T_{s\text{-}trans}$ | $S_0$ | -863.004632 |  |
| $2_{PT}$ | $S_0$ | -863.015806 |  |
| 2 | $S_0$ | -863.040714 |  |
| TS2 | $S_0$ | -862.990269 |  |
| TS3 | $S_0$ | -862.992556 |  |
| TS4 | $S_0$ | -862.942143 |  |

## $S_0 - S_1$ and $S_0 - T_1$ transitions



**HOMO**  **LUMO**

## $S_0 - T_2$ transition



**HOMO-1**  **LUMO**
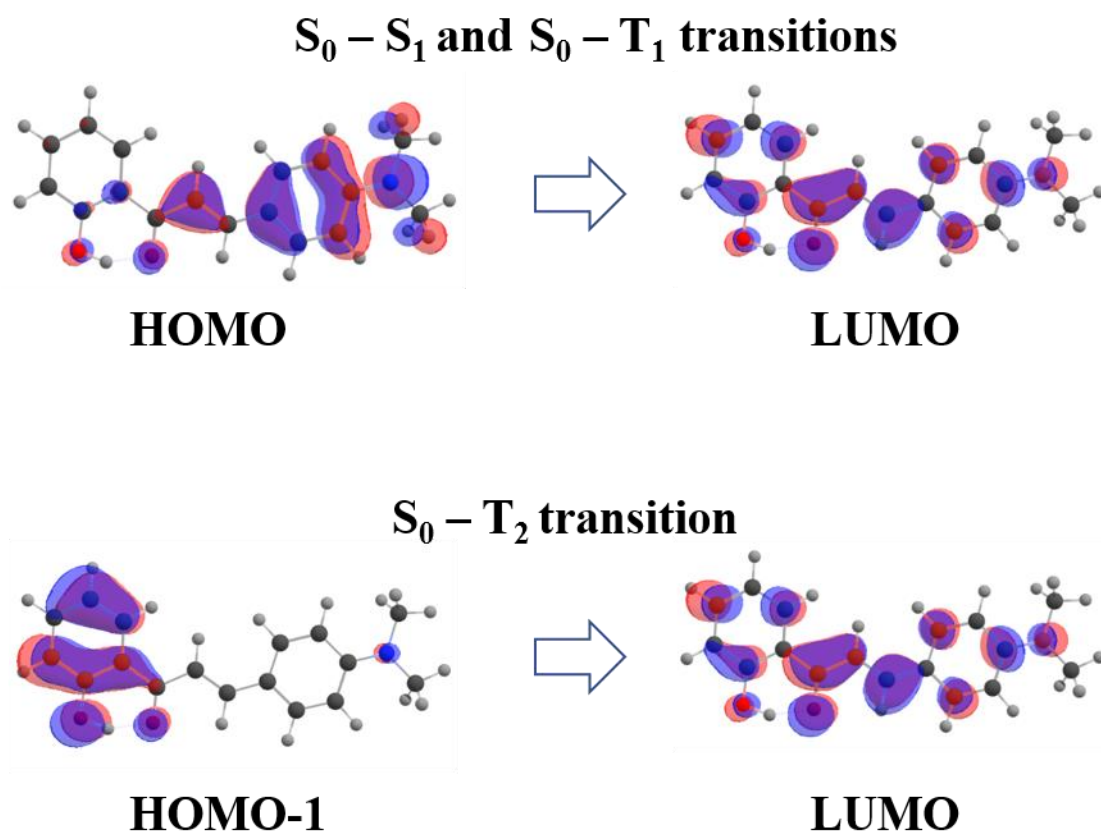
**Figure S5.** Molecular orbitals of $\mathbf{N}_{s\text{-}cis}$ involved in the $S_0$-$S_1$, $S_0$-$T_1$, and $S_0$-$T_2$ transitions
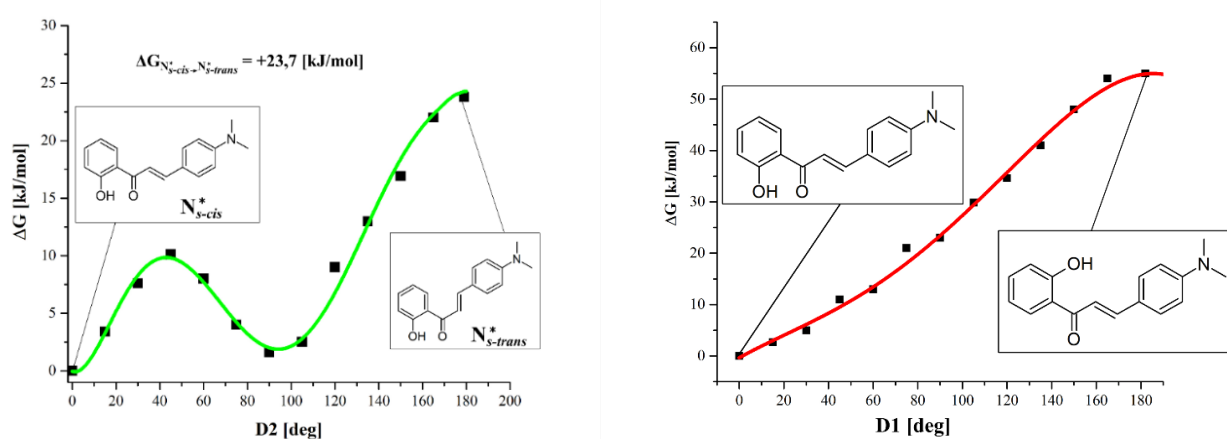


**Figure S6.** Energy scan of $\mathbf{N}_{s\text{-}cis}$ rotations along D1 and D2 dihedral angles in the excited state
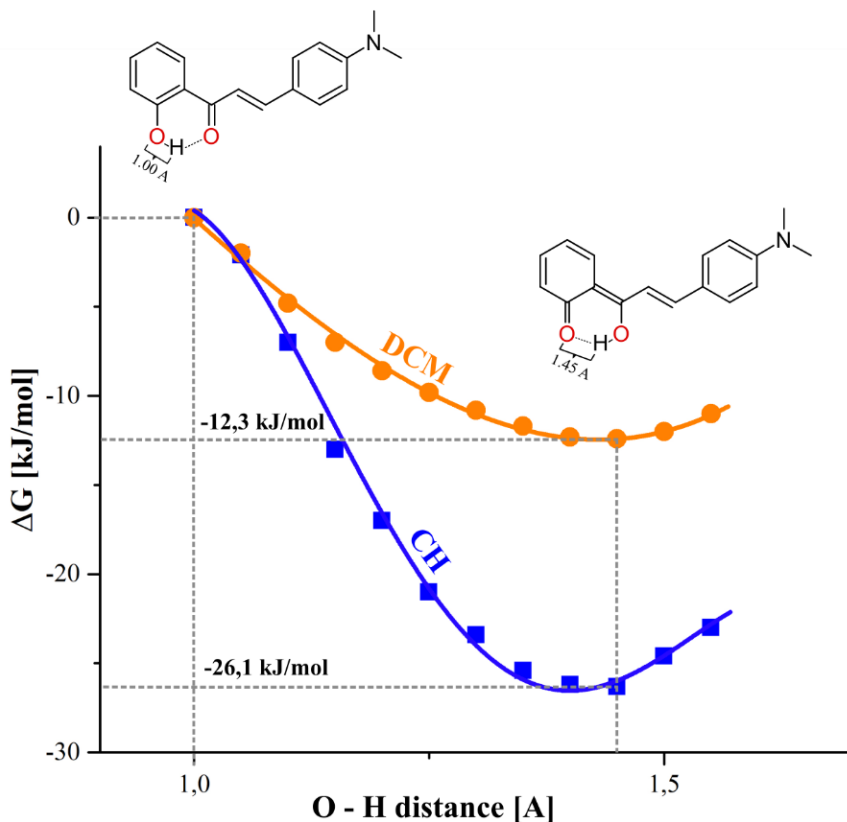
**Figure S7.** Energy change during ESIPT in **1** in cyclohexane (CH) and dichloromethane (DCM)
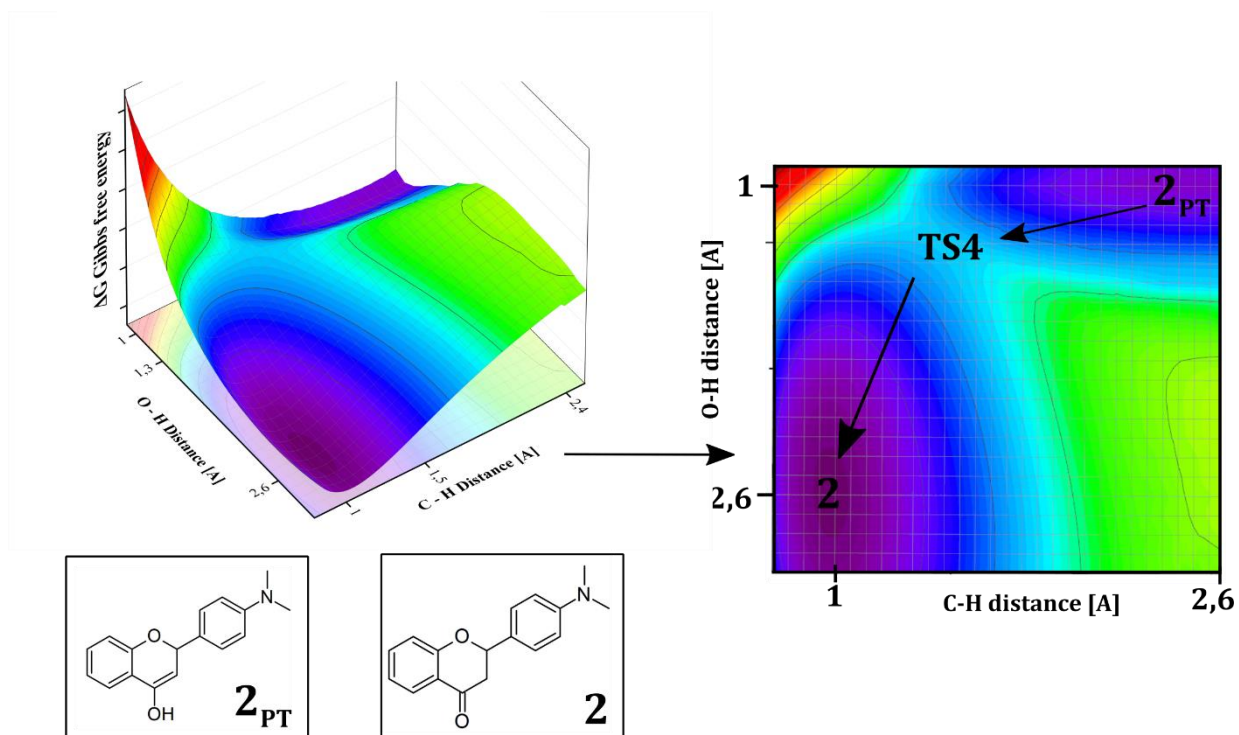


**Figure S8.** Potential energy scan for the ground state proton transfer ($2_{PT} \rightarrow 2$ transformation)
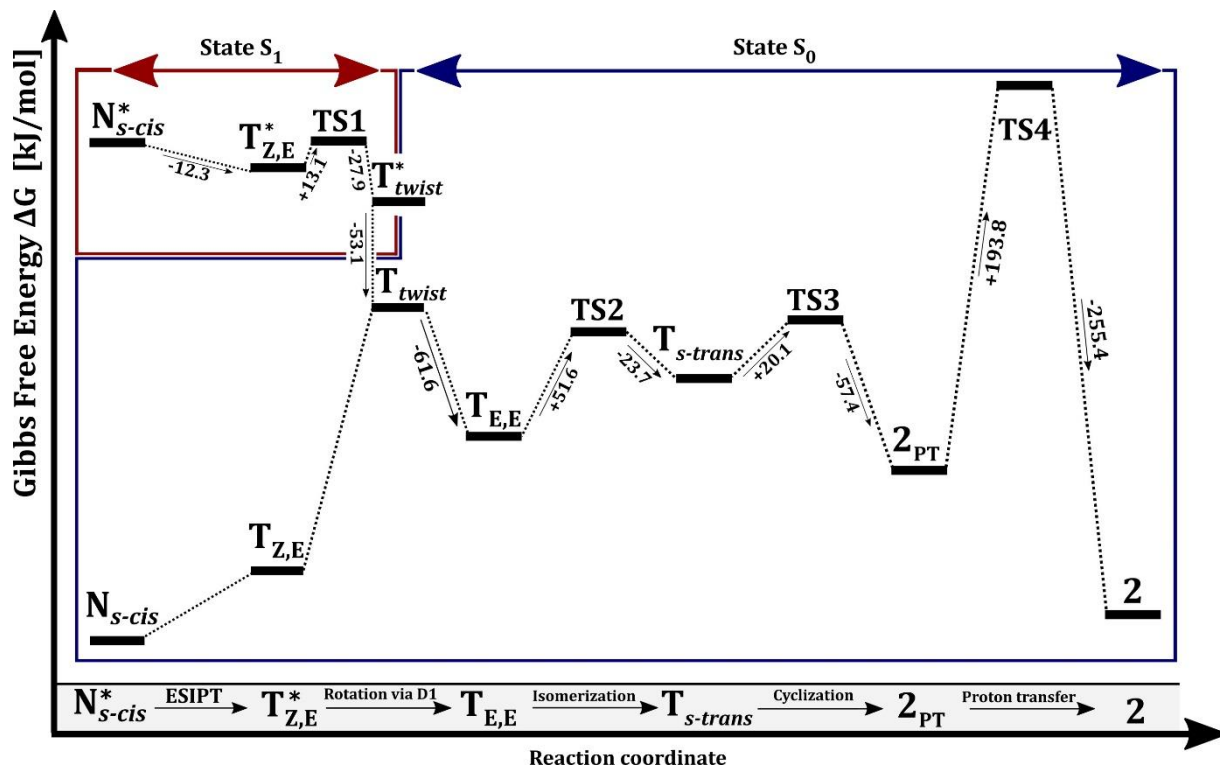
**Figure S9:** Diagram representing stage-by-stage transformation of **1** ($N_{s\text{-}cis}$ form) to **2** in DCM.

# 4. Additional spectra
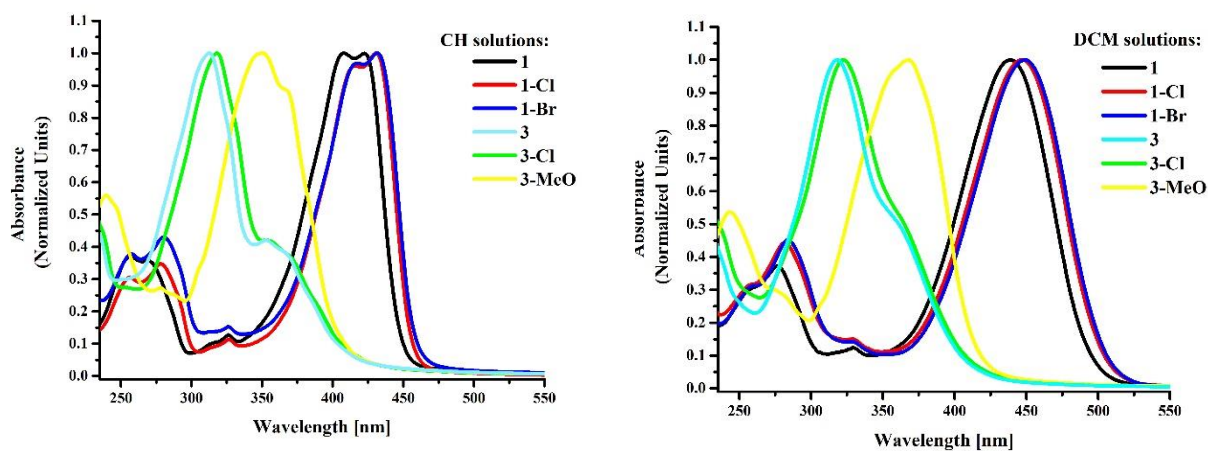


Absorption spectra of 2'-hydroxychalcones in CH and DCM solutions



Fluorescence spectra of 2'-hydroxychalcones in CH and DCM solutions

## [P2]

I. E. Serdiuk, M. Mońka, K. Kozakiewicz, B. Liberek, P. Bojarski, S. Y. Park.

Vibrationally Assisted Direct Intersystem Crossing between the Same Charge-Transfer States for Thermally Activated Delayed Fluorescence: Analysis by Marcus–Hush Theory Including Reorganization Energy.

Article

# Vibrationally Assisted Direct Intersystem Crossing between the Same Charge-Transfer States for Thermally Activated Delayed Fluorescence: Analysis by Marcus−Hush Theory Including Reorganization Energy

Illia E. Serdiuk,* Michał Mońka, Karol Kozakiewicz, Beata Liberek, Piotr Bojarski, and Soo Young Park

ACCESS | Metrics & More | Article Recommendations | Supporting Information

**ABSTRACT:** Thermally activated delayed fluorescence (TADF) has recently become an extensively investigated phenomenon due to its high potential for application in organic optoelectronics. Currently, there is still lack of a model describing correctly basic photophysical parameters of organic TADF emitters. This article presents such a photophysical model describing the rates of intersystem crossing (ISC), reverse ISC (rISC), and radiative deactivation in various media and emphasizing key importance of molecular vibrations on the example of a popular TADF dye 9,10-dihydro-9,9-dimethyl-10-(4-(4,6-diphenyl-1,3,5-triazin-2-yl)phenyl)-acridine (DMAC-TRZ). The presented experimental and theoretical investigations prove that ISC and rISC can occur efficiently between the singlet and triplet states of the same charge-transfer nature ($^1CT$ and $^3CT$, respectively). In emitters with the orthogonal donor and acceptor fragments, such spin-forbidden $^1CT \leftrightarrow {}^3CT$ transitions are activated by molecular vibrations. Namely, the change of dihedral angle between the donor and the acceptor affords reasonable spin−orbit coupling, which together with a small energy gap and reorganization energy enable $^1CT \leftrightarrow {}^3CT$ transition rates reaching $1 \times 10^7$ s$^{-1}$. Evidence of direct $^1CT \leftrightarrow {}^3CT$ spin-flip and negligible role of a second triplet state, widely believed as a key parameter in the design of (r)ISC materials, change significantly the current understanding of TADF mechanism. In authors' opinion, photophysics, and molecular design principles of TADF emitters should be revised considering the importance of vibrationally enhanced $^1CT \leftrightarrow {}^3CT$ transitions.
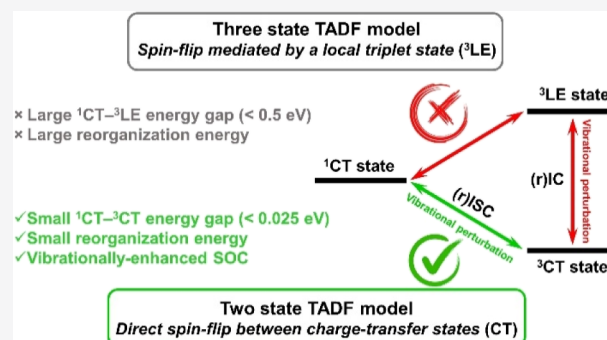
## INTRODUCTION

Over the last decade, fast development of all-organic optoelectronics with an increasing number of potential applications provided a plethora of experimental solutions on the (sub)molecular level. In one of the most promising applications of all-organic light-emitting diodes (OLEDs), these solutions are mainly focused on the problem of triplet harvesting. Due to spin statistics, recombination of charges in organic semiconductors leads to formation of singlet (25%) and triplet (75%) excitons. In heavy-atom free molecular systems, triplet excitons usually cannot ensure fast rates of light emission and should be converted to the singlet ones for high electroluminescence efficiency.

Currently, probably the best solution for triplet harvesting is the use of materials with fast reverse intersystem crossing (rISC). This can be realized either by emitters exhibiting thermally activated delayed fluorescence (TADF) dispersed in common OLED hosts[1] or by common fluorescent emitters dispersed in TADF emitters in the role of hosts, the so-called "hyperfluorescence" approach.[2] Numerous photo- and electro-luminescent investigations revealed strong dependence of

internal and external quantum efficiencies on the rISC rate. The importance of materials with fast rISC for further development of optoelectronics cannot be thus overestimated.

Up to the moment, there has been no general theoretical model which would correctly describe the basic photophysical parameters of TADF materials such as rates of intersystem crossing (ISC), rISC, and radiative deactivation in various media. Obviously, this impedes correct understanding of the mechanism and design principles of efficient TADF materials. In this article, we present such a model and on the example of one of the most popular TADF emitters explain how high rISC and ISC rates are achieved under various conditions. To date, all organic emitters with superior rISC rates are built of spatially separated strong electronic donor and acceptor
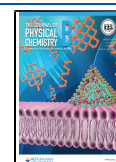
molecular fragments, which is the key principle of design strategy of TADF emitters. Such a structure enables formation of charge-transfer (CT) states, which represent the lowest excited singlet $^1$CT and triplet $^3$CT electronic states. Efficient separation of the donor and acceptor provides a negligible overlap of highest occupied molecular orbital (HOMO) and lowest unoccupied molecular orbital (LUMO), which decreases the exchange and energy gap ($\Delta E_{^1CT-^3CT}$) between the $^1$CT and $^3$CT states. All theoretical models developed before to describe the bases of TADF photophysics follow the selection rule stating that spin-flip between the $^1$CT and $^3$CT states is forbidden due to their identical nature. In fact, state-of-the-art methods of quantum chemistry predict a zero spin−orbit coupling constant (SOCME) for the $^1$CT and $^3$CT interaction. For this reason, TADF efficiency is believed to be strongly dependent on the presence of at least one additional triplet state with close energy to the $^1$CT and $^3$CT ones. This can be either a locally excited $^3$LE state localized on a donor or an acceptor[3] or another CT state formed via electronic transition on different molecular orbitals.[4] According to this, rISC is mediated by this third state because the transition between it and the $^1$CT state is more allowed due to their different nature. The presence of such a third state is believed as another key requirement in the design of TADF emitters.

Among the above-described cases, the one relying on the energetically close donor or acceptor $^3$LE state has been used to explain the majority of TADF examples including a triazine derivative 9,10-dihydro-9,9-dimethyl-10-(4-(4,6-diphenyl-1,3,5-triazin-2-yl)phenyl)-acridine (DMAC-TRZ) investigated here. It should be emphasized that such a three-state model predicts maximum rISC rate when $^3$LE and $^3$CT/$^1$CT states are energetically close. In terms of spectroscopic parameters measured experimentally, this means that the energy gap between $^1$CT and $^3$LE states ($\Delta E_{^1CT-^3LE}$) should be zero. More advanced variations of the three-state model specify an additional condition for maximal rISC: vibronic coupling between $^3$LE and $^3$CT states.[5] Similar criterion is found in another theoretical model, which assumes that the $T_1$ state of various *s*-triazine and benzonitrile emitters is not of pure CT-nature but contains various portions of LE nature.[6] Such a model thus suggests different nature of $S_1$ and $T_1$ states, which provides relatively high SOCME values and in such a way explains efficient rISC. The extent of LE contribution can be substantial in a non-polar medium, when CT energy is close to the triplet energy of a separate acceptor or donor, but it should decrease when CT is stabilized in high-polarity media. As follows from all these models, when the lowest CT states are stabilized and the $\Delta E_{^1CT-^3LE}$ energy gap increases by module, the rISC rate should decrease sharply. What is more, the same conclusion should be true for the forward ISC transition because it should also strongly depend on $\Delta E_{^1CT-^3LE}$. Here, we provide evidence that such conclusions on the dependence of ISC and rISC rates on the $\Delta E_{^1CT-^3LE}$ value are not supported by the experiment.

Some previous articles have already pointed at some discrepancies between the three-state model and the experimental behavior of TADF emitters. Namely, some of the investigations evidence the key role of molecular vibrations in TADF photophysics. For example, introduction of methyl groups at positions 1 and/or 9 of phenothiazine donor decreases drastically TADF rate and efficiency of phenothiazine-dibenzothiophene-*S,S*-dioxide emitters even in liquid solutions.[7] In this case, in spite of low $\Delta E_{^1CT-^3LE}$ value, the

restriction of some undetermined molecular vibrations by methyl groups was concluded to be extremely important for rISC: the more the vibrational freedom was restricted, the less TADF efficiency was observed. In the case of less flexible derivatives with more bulky isopropyl or *tert*-butyl groups, TADF was almost absent and the $T_1$ state deactivated mainly via room-temperature phosphorescence. Next, it was found that the explanation of the radiative rate of TADF emitters with orthogonal donor and acceptor fragments is not possible within "frozen" optimized geometry because of zero oscillator strength predicted by calculations.[8] It was proved that molecular vibrations should be taken into account for adequate prediction of oscillator strength and electronic transition moment. In another recent investigation, the behavior of DMAC-TRZ in solid solutions was explained by the inhomogeneity of its geometry caused by rotational isomerism and distribution of CT states.[9] Another recent theoretical model assumed that both spin−orbit coupling (SOC, $T_2/T_1 \rightarrow S_1$) and the so-called direct SOC ($T_1 \rightarrow S_1$) play important roles in rISC.[10] However, the direct $T_1 \rightarrow S_1$ transition was predicted to be efficient when the nature of $T_1$ and $S_1$ states is different: the presented calculations predicted 92% CT nature for the $S_1$ state and 95% LE nature for the $T_1$ state. The proposed model can thus also be valid only in the case of the proximity of $^1$CT and $^3$LE states. Despite the fact that the above-mentioned investigations were still explained by the three-state model, these experimental results question the primary importance of minimal $\Delta E_{^1CT-^3LE}$ value for a maximum rISC rate at $T > 0$ K where molecules exist in various excited vibronic states.

The importance of molecular vibrations for efficient TADF was also suggested for the carbene−heavy-metal complexes.[11] Fast rISC in such emitters was explained by the thermally activated rotation along the bond between the metal atom and the donor fragment, which decreased the $\Delta E_{^1CT-^3CT}$ value and facilitated direct $T_1 \rightarrow S_1$ transition. Together with the reasonable SOC values[12] due to heavy-atom effect, this resulted in high TADF rate constant (ca. $3 \times 10^6$ s$^{-1}$). Further investigations of similar compounds revealed that the energetic closeness of $^3$LE state itself does not reduce the activation energy of rISC but results in the undesired decrease of emissive rate of the $S_1-S_0$ transition.[13]

It should also be noticed that according to the three-state model, the differences between the $^1$CT and $^3$LE states should favor the interaction between them. However, different electronic structures lead to the differences in geometry. In terms of Marcus semiclassical electron-transfer theory,[6] this means the increase of reorganization energy of $^1$CT $\leftrightarrow$ $^3$LE transitions ($\lambda_{^1CT\leftrightarrow^3LE}$) and should not increase but rather decrease their rates. The investigations presented here prove that minimization of reorganization energy is as much important as small energy gap between singlet and triplet state ($\Delta E_{ST}$) value for achieving high rates of ISC and rISC. Substantial differences in the reorganization energies play the decisive role in favor of $^3$CT $\leftrightarrow$ $^1$CT transitions but not the $^1$CT $\leftrightarrow$ $^3$LE ones.

In this research, to check the widely accepted importance of $^3$LE state for spin-flip transitions, both $\Delta E_{^1CT-^3CT}$ and $\Delta E_{^1CT-^3LE}$ values were scanned experimentally. One of the most simple and basic but reliable spectroscopic experiments was conducted—solvatochromic measurements. The use of media of different polarities provides information on the effect of alignment of energy levels on all basic photophysical
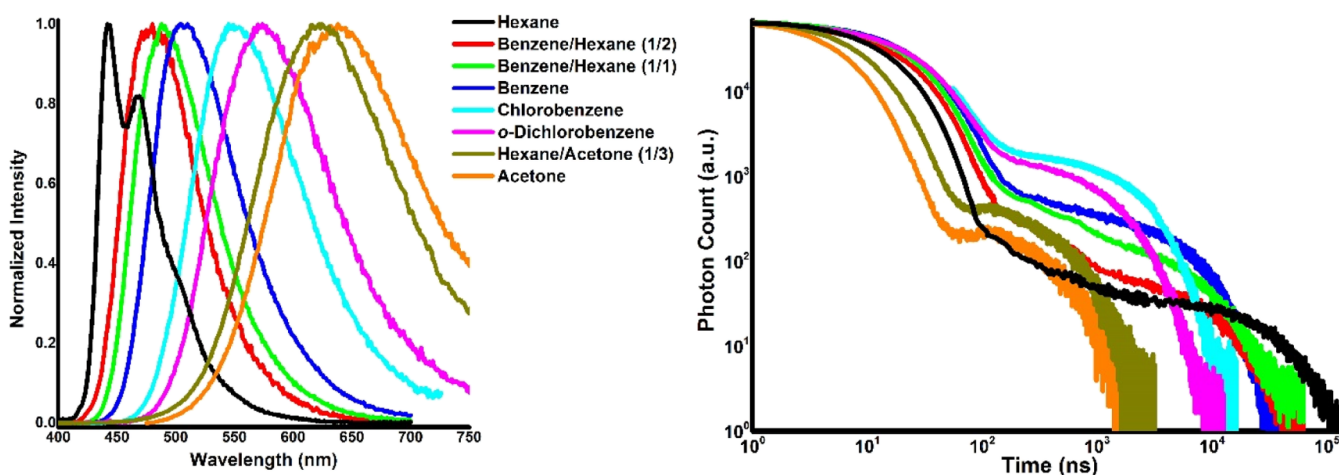
**Figure 1.** Intensity-normalized emission spectra and decays of DMAC-TRZ in various solutions.

parameters, which is especially valuable for understanding TADF photophysics. DMAC-TRZ emitter was selected, which together with its various derivatives exhibits one of the best photo- and electroluminescent characteristics extensively studied lately.[14,15] Due to the high transition dipole moment of the $^1$CT and $^3$CT states, their energies were effectively decreased with increasing medium polarity. Localized transitions are much less sensitive to the polarity of medium; therefore, the $^3$LE value is concerned as a constant. Thus, manipulation of solvent polarity, in a common notion meaning overall solvation capability, allowed us to tune $\Delta E_{^1CT-^3LE}$ from positive (low polarity, $E_{^1CT} > E_{^3LE}$) to negative (higher polarity, $E_{^1CT} < E_{^3LE}$) values. Importantly, evidence was found that the energy gap between $^1$CT and $^3$CT states also changes with polarity. In spite of experimental simplicity of solvatochromic experiment, it remains a challenging task for calculations using the methods of time-dependent density functional theory (TDDFT). For this reason, the results of calculations were treated here with special attention and analyzed only in the case of good correlation with experimental data.

## METHODS

DMAC-TRZ was synthesized as reported previously[16] and purified by sublimation in vacuum. Solvents for photophysical measurements were of spectroscopic grade or higher. All the photophysical measurements were conducted in the argon atmosphere.

Steady-state photoluminescence spectra were obtained with a PTI QuantaMaster 40 spectrofluorometer. All the emission spectra were corrected on the photodetector sensitivity. Photoluminescence quantum yields (PLQY) were obtained using 9,10-diphenylanthracene in cyclohexane (93%) as a reference.[17] Time-dependent emission measurements at room temperature were obtained using a FluoTime 300 fluorescence lifetime spectrometer equipped with a LDH-P-C-375 laser head. The parameters of photophysical processes were calculated using equations described in the literature;[18,19] for details, see the Supporting Information.

**Quantum-Chemical Calculations.** The unconstrained geometry optimizations of DMAC-TRZ were performed for the ground ($S_0$), excited singlet ($S_1$), and triplet ($T_1$, $T_2$, and $T_3$) electronic states at DFT/TDDFT level of theory[20] using the Gaussian 16 program package.[21] The B3LYP[22] hybrid functional was used with the cc-pVDZ basis set. Nature of

states (CT or LE) was established on the basis of analysis of molecular orbitals involved in each transition, for details, see the Supporting Information, Scheme S1. The energies of $^1$CT$-S_0$, $^1$CT$-^3$CT, and $^1$CT$-^3$LE transitions were obtained by single-point calculations using the optimized geometry of $^1$CT state ($S_1$); the respective values for the $^3$CT$-S_0$, $^3$CT$-^1$CT and $^3$LE$-S_0$, $^3$LE$-^1$CT transitions were obtained by single-point calculations using the optimized geometries of $^3$CT ($T_1$) and $^3$LE ($T_2$), respectively. Computational $\Delta E_{^1CT-^3CT}$ and $\Delta E_{^1CT-^3LE}$ values represent differences between minimal energies of respective states. The electronic energies and transition energies of rotational isomers in $^1$CT, $^3$CT, and $^3$LE states were calculated by single-point calculations via dihedral angle scan using the geometries of the respective states. The SOC constants were calculated within the ORCA program package,[23] using ZORA relativistic contraction of the TZVP basis set.

For each rotational isomer, the rate constants of ISC and rISC via $^1$CT $\rightarrow$ $^3$CT, $^1$CT $\rightarrow$ $^3$LE and $^3$CT $\rightarrow$ $^1$CT, $^3$LE $\rightarrow$ $^1$CT transitions were calculated using the Marcus–Hush equation

$$k = \frac{V^2}{\hbar} \sqrt{\frac{\pi}{k_B T \lambda}} \exp\left[-\frac{(\Delta E_{ST} + \lambda)^2}{4 k_B T \lambda}\right] \tag{1}$$

where $k$ is a rate constant, $V$ is the SOC constant, $\lambda$ is the sum of internal and external ($\lambda_{solv}$) reorganization energies for the respective transition, $\Delta E_{ST}$ is an energy gap between $^1$CT and the respective triplet state, $k_B$ is the Boltzmann constant, $\hbar$ is the reduced Planck's constant, and $T$ is the temperature (298.15 K). For detailed procedures and examples of calculations, see the Supporting Information.

## RESULTS AND DISCUSSION

Figure 1 shows the emission spectra and decays, respectively, of DMAC-TRZ in various liquid solutions. Strong positive solvatochromism evidenced energy decrease of the $^1$CT state with the increase of medium polarity. Taking into account the 440 nm onset of $^3$LE phosphorescence measured in frozen methylcyclohexane solution,[16] the $\Delta E_{^1CT-^3LE}$ values in these experiments varied from +0.1 eV in hexane to −0.4 eV in acetone. In further discussion, to analyze the medium effect and avoid fluctuations of composition of solvent mixtures
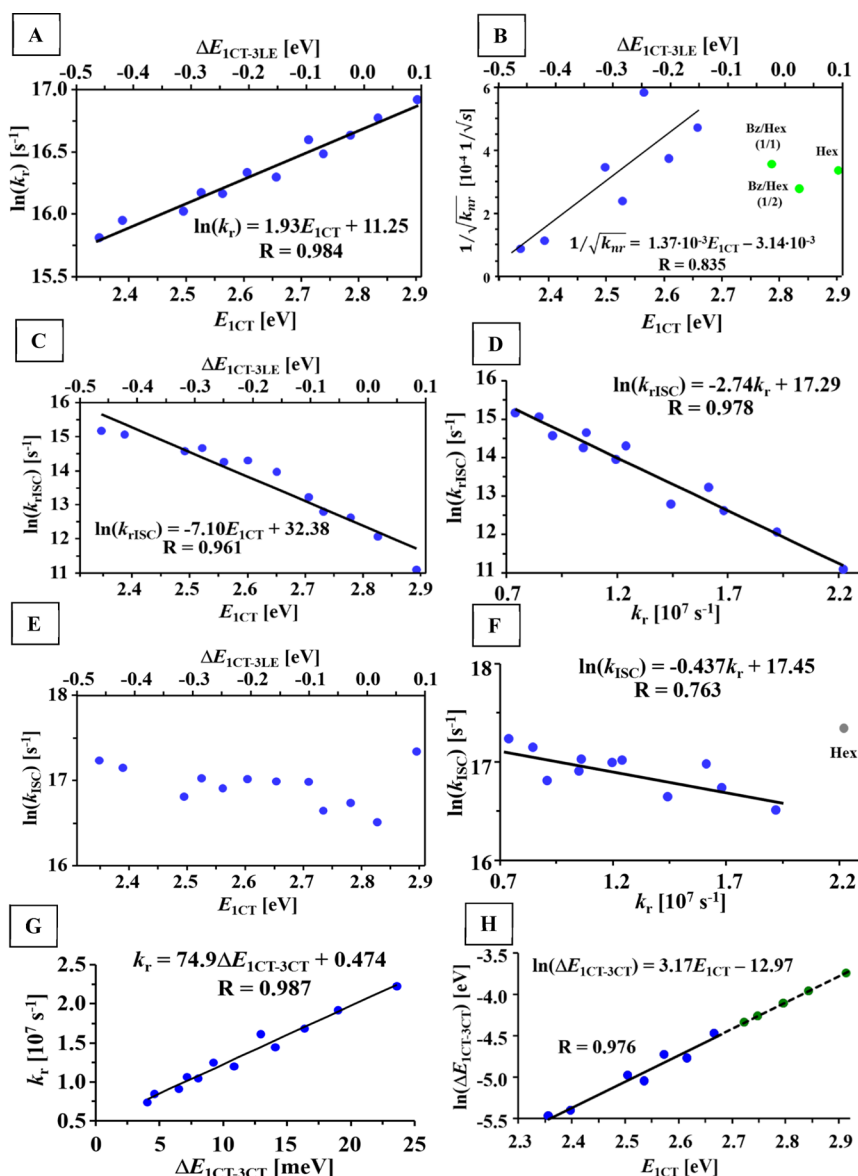
**Figure 2.** Dependencies of experimental rate constants of radiative (A) and nonradiative (B) deactivation, rISC (C) and ISC (E) on the energy of $^1$CT state and $\Delta E_{^1CT-^3LE}$ energy gap. Dependencies of experimental rate constants of rISC (D) and ISC (F) on radiative rate constant. Correlation between the experimental rate constant of radiative deactivation and reconstructed $^1$CT–$^3$CT energy gap (G). Logarithm of energy gap between $^1$CT and $^3$CT states as a function of $^1$CT-state energy (H, blue points obtained using experimental $k_{rISC}$ values, green ones calculated by extrapolation).

during the removal of oxygen, onset of fluorescence spectrum ($E_{^1CT}$) is used as an internal polarity parameter.

Rates and yields of photophysical processes are presented in Table S1 (Supporting Information). The rate constant of radiative deactivation ($k_r$) exhibited strong exponential dependence on $E_{^1CT}$ (Figure 2A). The highest $k_r$ value of 2.2 × 10$^7$ s$^{-1}$ was obtained for an $E_{^1CT}$ of 2.91 eV in non-polar hexane, while the lowest $k_r$ of 7.4 × 10$^6$ s$^{-1}$ was obtained for an $E_{^1CT}$ of 2.36 eV in polar acetone. Such a reduction of $k_r$ with the increase of polarity is well known for donor−acceptor molecular systems.[24] In current discussion, it should be noted that the observed dependence provides evidence that the increasing polarity and solvent-relaxation efficiency in the excited state favors more effective separation of frontier orbitals involved in the S$_1$−S$_0$ transition. On the one hand, this reduces oscillator strength and $k_r$. On the other hand, this

favors minimization of the exchange energy between S$_1$ and T$_1$ states of the same nature, which leads to the reduction of $\Delta E_{^1CT-^3CT}$ value. Within the same D−A chromophore, $k_r$ can thus be referred as a measure of $\Delta E_{^1CT-^3CT}$. This assumption is quite important because of the lack of reliable experimental methods for the estimation of $\Delta E_{^1CT-^3CT}$ and $^3$CT-state energy, especially in solutions and at room temperature. As will be discussed further, the determined $\Delta E_{^1CT-^3CT}$ in fact correlates perfectly with $k_r$.

Analysis of the emission decay profiles (Figure 1) leads to important conclusions on the polarity effect on nonradiative transitions. When polarity increases from hexane to o-dichlorobenzene, the time range in which emission occurs is shortened, but the intensity of the delayed component represented by the intensity of the second decay plateau is increased. This indicates the increase of rISC rate with

medium polarity. In more polar acetone and 75% acetone in hexane, the time range of emission shortens sharply, indicating strong increase of nonradiative deactivation. In terms of the determined parameters (Table S1, Supporting Information), in a low-polarity medium, the rate constant of nonradiative deactivation ($k_{nr}$) of $^1$CT state is minimal, when $\Delta E_{^1CT-^3LE}$ is close to zero. One can thus suggest that the energetic closeness of $^1$CT and $^3$LE states is important for high PLQY. In more polar solvents, lower $^1$CT level corresponds to faster nonradiative deactivation. Importantly, the increase of $k_{nr}$ is the key factor decreasing PLQY in polar media but not the changes in ISC or rISC rates. In polar media, the main nonradiative deactivation channel is most likely internal conversion, the rate constant of which is proportional to $1/\Delta E_{S_1-S_0}^2$.[25] In fact, $k_{nr}$ shows good correlation with $1/\Delta E_{S_1-S_0}^2$ in polar media (Figure 2B), but not in the low-polar one, indicating different mechanisms of nonradiative deactivation probably due to slow rISC.

**rISC Rate.** To present further evidence of $\Delta E_{^1CT-^3CT}$ dependence on polarity, rISC is discussed prior to ISC. The value of $k_{rISC}$ shows strong logarithmic dependence on polarity of medium, namely, $E_{^1CT}$ as a polarity parameter: the lower the $E_{^1CT}$, the higher the $\ln(k_{rISC})$ (Figure 2C). In terms of the $\Delta E_{^1CT-^3LE}$ energy gap, rISC reaches highest rate when $^1$CT is most separated from the $^3$LE state. In contrast to the three-state model, experimental data thus do not support maximal rISC rate at the point of energetic degeneracy of CT and locally excited states. When $E_{^1CT}$ decreases, the alignment of excited states changes (Figure 3): $^3$CT becomes the lowest triplet state and the fraction of excited molecules in the second triplet state ($^3$LE) decreases sharply. Despite that $\Delta E_{^1CT-^3LE}$ becomes negative increasing the driving force of $^3LE \rightarrow {}^1CT$ transition, decreased population of the $^3$LE state should result in $k_{rISC}$ decrease, which is not the case.

Figure 3 illustrates the significance of reorganization energy $\lambda^{^1CT\leftrightarrow^3LE}$ and driving force $\Delta E_{^1CT-^3LE}$ for the transitions between the $^1$CT and $^3$LE states of different geometries. Within the Marcus theory, the maximum rate of $^3LE \rightarrow {}^1CT$ transition is not predicted for the same energy of the $^1$CT and $^3$LE states because of the additional reorganization energy involved. If rISC occurs via the $^3LE \rightarrow {}^1CT$ transition, the dependence of $k_{rISC}$ on $E_{^1CT}$ should contain two regions. First is "normal region", where $-\Delta E_{^1CT-^3LE} < \lambda^{^1CT\leftrightarrow^3LE}$ (Figure 3, hexane and benzene). In this region, the rISC rate should increase, when $-\Delta E_{^1CT-^3LE}$ draws closer to $\lambda^{^1CT\leftrightarrow^3LE}$ and reach maximum, when these values are equal. In the second region, "inverted region", where $-\Delta E_{^1CT-^3LE} > \lambda^{^1CT\leftrightarrow^3LE}$, the rISC rate should decrease as the $-\Delta E_{^1CT-^3LE}$ value increases (Figure 3, o-dichlorobenzene). Clearly, these regions are not observed in the experimental $k_{rISC}$ on $E_{^1CT}$ dependence.

On the other hand, the experimental rISC rate shows strong exponential dependence on $k_r$ (Figure 2D), which as suggested above correlates with the energy gap between the CT states of different multiplicity. At this point, it is concluded that $k_{rISC}$ is strongly dependent on $\Delta E_{^1CT-^3CT}$ but not the $\Delta E_{^1CT-^3LE}$ value.

To explain the experimental dependences, the effect of specific molecular vibrations on the electronic features of DMAC-TRZ is analyzed. As was mentioned above, in the optimal geometries with ideally orthogonal DMAC and TRZ fragments, SOCME between $^3$CT and $^1$CT states is 0.00 cm$^{-1}$ which excludes the possibility of efficient spin-flip transition. It is however well known that at temperatures above 0 K,
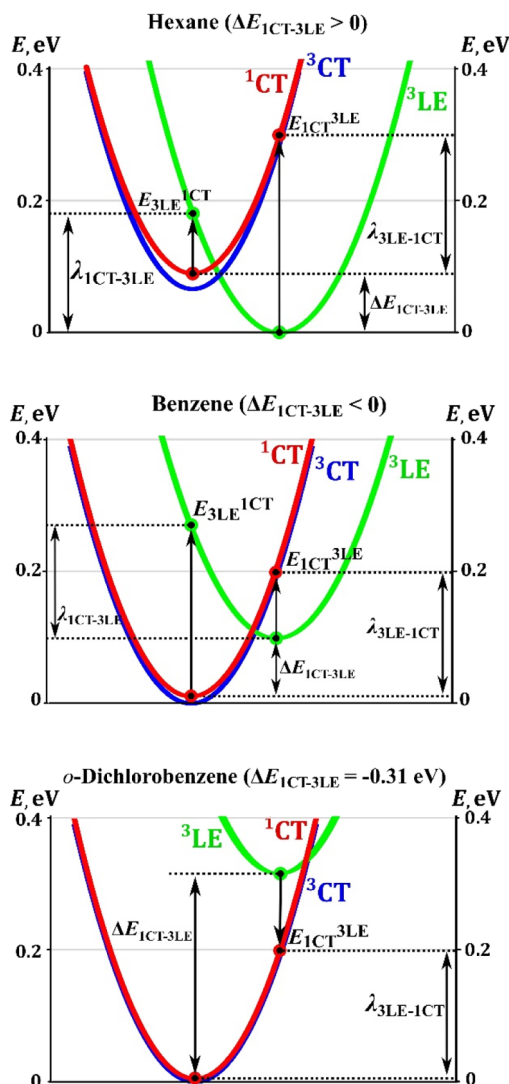


**Figure 3.** Potential energy curves of the lowest excited states in various media.

molecules exist in the excited vibronic states. Molecular vibrations are responsible for the violation of some selection rules such as symmetry forbidden and n−π* transitions.[26] Similarly, the transitions forbidden by the El-Sayed rule, based on the electronic nature of states, can occur due to vibrational coupling perturbations. Apparently, a theoretical model describing photophysics of TADF emitters should take into account the effect of molecular vibrations on geometry. In the first vibronic mode of DMAC-TRZ, the dihedral angle ($\theta$) between the donor and acceptor is changing (Figure 4A). Such molecular vibrations have immense influence on electronic properties, and therefore, the model presented below is based on these vibrations.

Importantly, SOC between the $^3$CT and $^1$CT states was found to be extremely sensitive to the dihedral angle $\theta$ (Figure 4B): SOCME is zero in optimal geometry with $\theta$ of 90°, rises up to 0.05 cm$^{-1}$ at 85°, and reaches 0.2 cm$^{-1}$ when $\theta$ is below 65°. The discussed vibrational mode has lower energy in the $^3$CT state (9.84 cm$^{-1}$) as compared to $^1$CT (13.20 cm$^{-1}$). Consequently, the energies (Figure 4C) and molar fractions (Figure 4D) of rotational isomers are also different in the $^1$CT and $^3$CT states. In the $^1$CT state, rotamer energy increases by
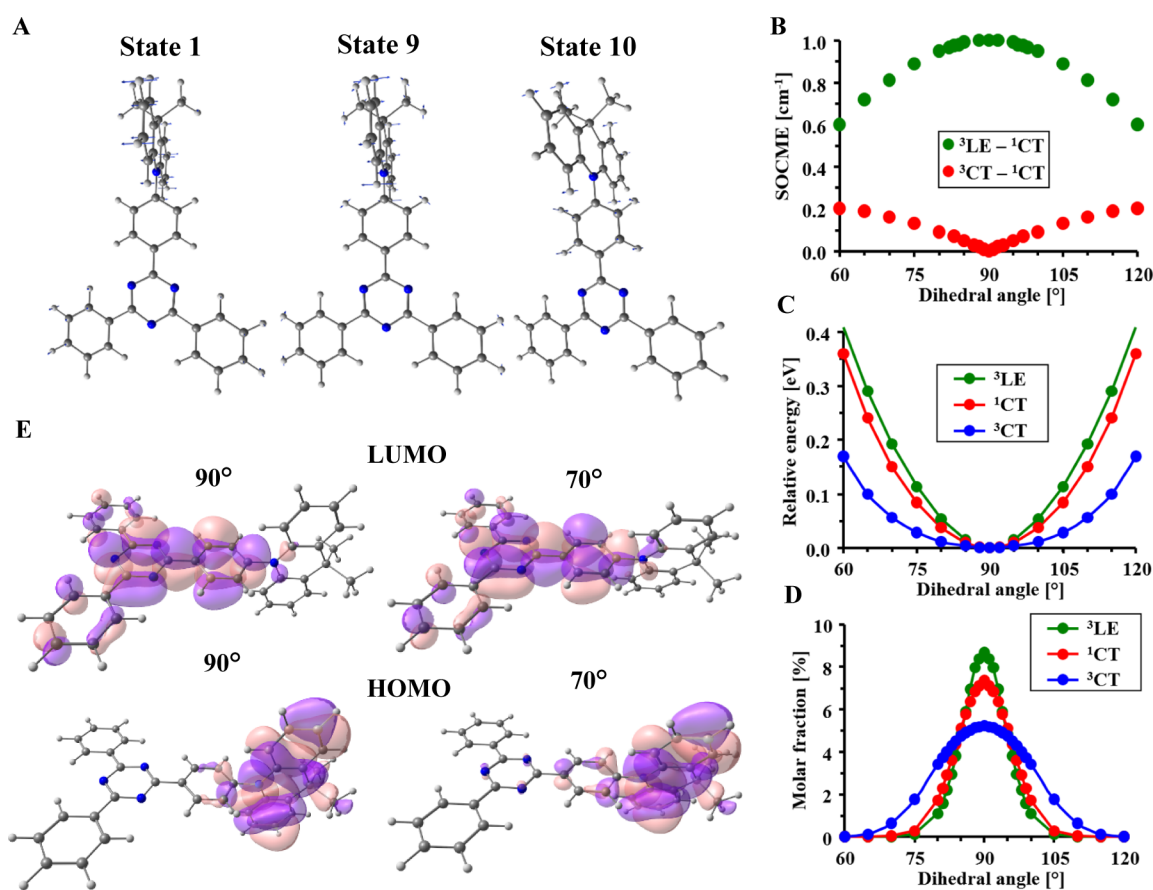
**Figure 4.** (A) Vectors of atomic movements in selected lowest vibrational states of the $^1$CT state. (B) Dependence of SOCME between $^3$LE−$^1$CT ($^3$LE geometry) and $^3$CT−$^1$CT (same for the $^3$CT and $^1$CT geometries) states on the dihedral angle between donor and acceptor fragments. (C) Dependence of the relative energy of excited state on the dihedral angle. (D) Dependence of the molar fractions of rotational isomers at room temperature. (E) HOMO and LUMO calculated for various torsion angles between DMAC and TRZ fragments (contour value 0.017, $^1$CT-state geometry).

0.2 eV when $\theta$ reaches 67 or 113°, while for the $^3$CT state, this value is 58° (122°). For this reason, mean SOCME values of 0.043 and 0.051 cm$^{-1}$ are obtained for the $^1$CT → $^3$CT and $^3$CT → $^1$CT transitions, respectively. The increase of SOC under deviation from orthogonality is explained by the increasing overlap of molecular orbitals involved in CT transitions, namely, increased contribution of the phenyl-$s$-triazine fragment in HOMO (Figure 4E).

The same analysis conducted for the $^3$LE → $^1$CT transition in the $^3$LE-state geometry revealed that the SOCME value between these two states is 1.0 cm$^{-1}$. This value is very close to most of other organic TADF systems explained so far via the three-state model.[5,6,10,14,15] The SOC of the $^3$LE → $^1$CT transition in DMAC-TRZ decreases when the torsional angle $\theta$ deviates from 90° (Figure 4B). Higher energy of the discussed rotation also results in lower contribution of the rotational isomers than in the case of CT state (Figure 4D).

Prior to the theoretical prediction of rISC rate using the Marcus−Hush equation (see Methods), the effect of dihedral angle $\theta$ on $\Delta E^1{}_{CT-^3CT}$ and reorganization energy should be analyzed. Expectedly, deviation from orthogonal geometry and increase of HOMO−LUMO overlap cause the increase of $\Delta E^1{}_{CT-^3CT}$. When $\theta$ = 90°, TD-DFT/B3LYP calculations predict the $\Delta E^1{}_{CT-^3CT}$ value of 6.6 meV, which rises up gradually to 0.20 eV at 60° (Figure S1, Supporting Information). Within the Marcus theory, internal (structural)

and external (solvent) reorganization energies are distinguished. For the $^3$CT → $^1$CT transition, calculations predict very low structural reorganization energy <0.5 meV, which is independent of $\theta$ within 90−65°. Due to a very similar geometry and electronic parameters of these two states, solvent reorganization energy ($\lambda_{solv}$) should also be low. One can expect that similar to $\Delta E^1{}_{CT-^3CT}$, the $\lambda_{solv}$ value should increase together with the growing difference between the electronic parameters of the $^3$CT and $^1$CT states. In further calculations, we thus assumed that the sum of reorganization energies for $^3$CT ↔ $^1$CT transitions ($\lambda^1{}_{CT-^3CT}$) is equal to $\Delta E^1{}_{CT-^3CT}$.

The rISC rate constant calculated as a statistical sum of the rate constants of $^3$CT → $^1$CT transition for various rotational isomers using the Marcus−Hush equation and calculated $\Delta E^1{}_{CT-^3CT}$ and SOCME values (Table S2, Supporting Information) gives a $k^3{}_{CT→^1CT}$ value of 2.26 × 10$^6$ s$^{-1}$. This value matches perfectly the experimental $k_{rISC}$ value of 2.1 × 10$^6$ s$^{-1}$ in $o$-dichlorobenzene. The predicted S$_1$−S$_0$ transition maximum of 611 nm is also in good correlation with the experimental emission maximum in $o$-dichlorobenzene at 570 nm.

Such a remarkable match of experimental and computational data leads to two main conclusions. First, the B3LYP calculations of D−A-type emitters correlate very well with the experiment in the medium of relatively high polarity. The most important conclusion is that the $^3$CT → $^1$CT transition
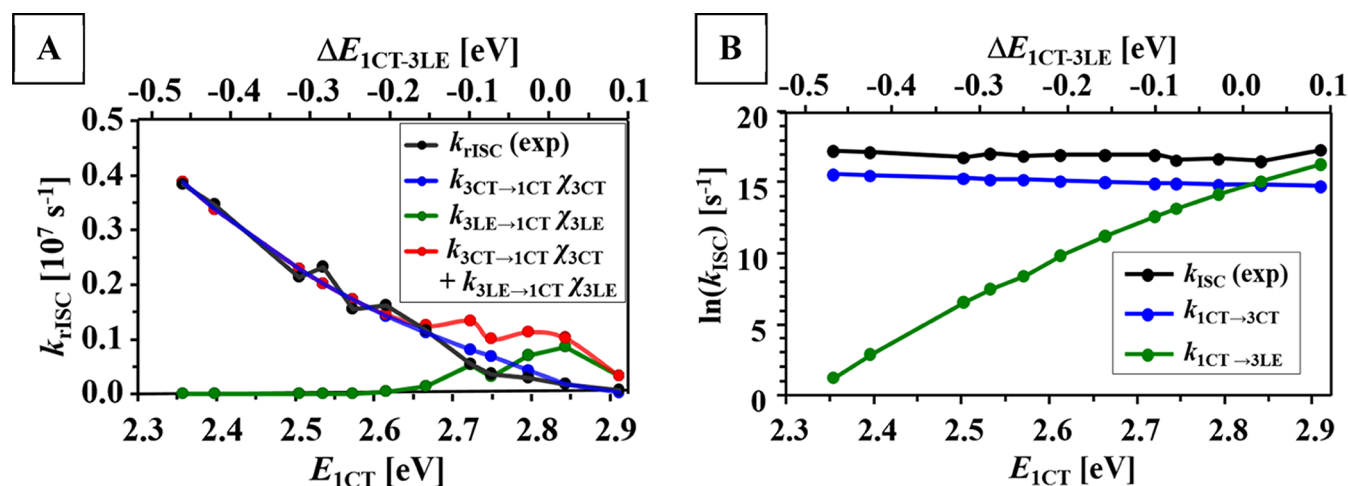
**Figure 5.** Comparison of calculated (Table S3) and experimental (Table S1) rates of triplet−singlet transitions (A) and singlet−triplet transitions in logarithmic scale (B) in a function of $^1$CT-state energy. The rate constants of $^3$LE $\leftrightarrow$ $^1$CT transitions were calculated using $\lambda_{solv}$ = 0.3 eV.

can solely afford high rISC rates due to molecular vibrations. High rate of $^3$CT $\rightarrow$ $^1$CT transition is a combination of couple of factors. First is vibrationally activated SOC between the same CT states of different multiplicities. Even though it is 10−20 times smaller than the SOC between the $^3$LE and $^1$CT states, the small $\Delta E_{^1CT-^3CT}$ energy gap together with almost identical geometry and thus comparably small reorganization energy enable fast $^3$CT $\rightarrow$ $^1$CT rate. As discussed further, the reorganization energy of $^3$LE $\rightarrow$ $^1$CT transition is much larger, which is a decisive factor in favor of $^3$CT $\rightarrow$ $^1$CT transition.

Similar analysis of the experimental $k_{rISC}$ in polar media ($E_{^1CT} \leq 2.67$ eV) was done. Under such conditions, according to the Boltzmann distribution, the population of $^3$LE state is below 0.2% and thus $^3$LE $\rightarrow$ $^1$CT transition cannot contribute considerably to rISC. The $^3$CT $\rightarrow$ $^1$CT transition is thus the only pathway of rISC and its parameters can be estimated. The $\Delta E_{^1CT-^3CT}$ values corresponding to experimental $k_{rISC}$ according to the Marcus−Hush equation are presented in Table S1 (Supporting Information). The thus-obtained $\Delta E_{^1CT-^3CT}$ values decrease with the rise of medium polarity, which supports perfectly the conclusions drawn above based on the experimental $k_r$ values (Figure 2G). The dependence of $\Delta E_{^1CT-^3CT}$ on $E_{^1CT}$ is best fitted by a logarithmic function (Figure 2H). Its extrapolation afforded the $\Delta E_{^1CT-^3CT}$ values in less polar media. Consequently, the lowest energy gap of 4.2 meV is obtained for the most polar acetone solution, while the highest value of 24 meV corresponds to the hexane solution.

The $k_{^3CT\rightarrow^1CT}$ values calculated using the reconstructed dependence of $\Delta E_{^1CT-^3CT}$ on $E_{^1CT}$ are compared with the experimental $k_{rISC}$ in Figure 5A. To take into account the medium-dependent population of species in $^3$CT and $^3$LE states, $k_{^3CT\rightarrow^1CT}$ is multiplied by the molar fraction of molecules in the $^3$CT state at 298 K ($\chi_{^3CT}$).

In the media of lower polarity with $E_{^1CT} \geq 2.72$ eV, the molar fractions of species in the $^3$LE state should be taken into account (Table S3, Supporting Information). To calculate the rate of $^3$LE $\rightarrow$ $^1$CT transition, the experimental $\Delta E_{^1CT-^3LE}$ and computationally predicted structural reorganization energies ($\lambda_{^3LE-^1CT}$, 0.209−0.226 eV) for various rotational isomers were used (for detailed procedure, see the Supporting Information). The thus-obtained $k_{^3LE\rightarrow^1CT}$ ($\lambda_{solv}$ = 0.3 eV) multiplied by the molar fraction of molecules in the $^3$LE state at 298 K ($\chi_{^3LE}$) are plotted in Figure 5A (for calculations using lower $\lambda_{solv}$, see the

Supporting Information). According to this, the $^3$LE $\rightarrow$ $^1$CT transition should have the key contribution to rISC in the region of low polarity with $E_{^1CT}$ close to 2.8 eV and $\Delta E_{^1CT-^3LE}$ close to zero. In this region, the three-state model predicts maximum rISC rate, which is well described by the dependence of calculated $k_{^3LE\rightarrow^1CT}$ on $E_{^1CT}$. This however completely contradicts our experimental data: $k_{rISC}$ do not reach any maximum at $\Delta E_{^1CT-^3LE} \approx 0$. In contrast, the experimental dependence of $k_{rISC}$ on $E_{^1CT}$ is almost perfectly described by the rates of $^3$CT $\rightarrow$ $^1$CT transition, but by neither the $^3$LE $\rightarrow$ $^1$CT one nor the sum of rates of these two transitions even in the low-polarity region (Figure 5A). Therefore, the data presented above unambiguously prove the decisive role of $^3$CT $\rightarrow$ $^1$CT transition, but not the $^3$LE $\rightarrow$ $^1$CT one in the rISC process in DMAC-TRZ.

**ISC Rate.** ISC is another important process representing forward transformation of singlet S$_1$ state to the triplet ones. ISC and rISC are closely connected; thus, any theoretical model which explains rISC but fails to describe correctly ISC cannot be regarded as satisfactory.

The experimental ISC rate shows complex dependence on the $^1$CT-state energy (Figure 2E). In hexane ($E_{^1CT}$ = 2.91 eV), an ISC rate constant ($k_{ISC}$) value of $3.4 \times 10^7$ s$^{-1}$ is the highest, but it decreases sharply to $1.5 \times 10^7$ s$^{-1}$ in the benzene−hexane (1:2, v/v) mixture, where the $E_{^1CT}$ value is 2.84 eV. A further decrease of $E_{^1CT}$ causes gradual increase of $k_{ISC}$ up to $3.1 \times 10^7$ s$^{-1}$ in acetone. According to the alignment of excited states, the decrease of $E_{^1CT}$ in polar media makes the $^1$CT $\rightarrow$ $^3$LE transition endothermic (Figure 3). Under such a distancing of $^1$CT and $^3$LE states, if the $^1$CT $\rightarrow$ $^3$LE transition was the main pathway of ISC, a sharp decrease of $k_{ISC}$ with the $\Delta E_{^1CT-^3LE}$ value would be observed, which is not the case.

In contrast, $k_{ISC}$ grows exponentially with the decrease of $k_r$ (Figure 2F), regarded as a measure of reduction of the $^1$CT−$^3$CT energy gap. These findings provide evidence that when the $^1$CT and $^3$CT states have lower energy than the $^3$LE one, ISC occurs mainly via the $^1$CT $\rightarrow$ $^3$CT channel in the nanosecond regime, even though it is forbidden by the El Sayed's rules.

Similar to rISC, two mechanisms of ISC in DMAC-TRZ can be suggested: $^1$CT $\rightarrow$ $^3$LE and $^1$CT $\rightarrow$ $^3$CT transitions. In hexane, the $^1$CT $\rightarrow$ $^3$LE transition rate calculated using the Marcus−Hush equation is close to experimental $k_{ISC}$. However,

in more polar media, $k^{1}_{CT \to {}^3LE}$ decreases sharply (Figure 5B) due to the increasing negative value of $\Delta E^{1}_{CT-{}^3LE}$ and thus growing endothermicity of this process. For example, in acetone and *o*-dichlorobenzene, $k^{1}_{CT \to {}^3LE}$ does not exceed 3 and $1 \times 10^{3}$ s$^{-1}$, respectively, and thus, its contribution to ISC is negligible. On the other hand, the rate constant of $^{1}CT \to$ $^{3}CT$ transition calculated as a statistical sum of $k^{1}_{CT \to {}^3CT}$ of various rotational isomers correlates well with the experimental $k_{ISC}$ in all the investigated media except for hexane: $k^{1}_{CT \to {}^3CT}$ increases with the decrease of $E^{1}_{CT}$ (Figure 5B). The reason of such a dependence is the above-mentioned decrease of $\Delta E^{1}_{CT-{}^3CT}$ with growing medium polarity. Therefore, in almost all experimental conditions, ISC proceeds via the $^{1}CT \to {}^3CT$ transition. Only in non-polar hexane, where the CT states are the least stabilized and $\Delta E^{1}_{CT-{}^3CT}$ reaches maximum, both pathways are realized and the $^{1}CT \to {}^3LE$ transition contributes noticeably to ISC.

In spite of perfect prediction of $k_{ISC}-E^{1}_{CT}$ dependence, the calculated $k^{1}_{CT \to {}^3CT}$ values are ca. 4−5 times lower than the experimental ones. Apparently, real SOCME values of the $^{1}CT \to {}^3CT$ transition are higher. Similarly, the radiative deactivation rate calculated as the statistical sum of various rotational isomers (described in detail in the Supporting Information) is 4.2 times underestimated as compared to the experimental value in *o*-dichlorobenzene (Table S4, Supporting Information). It should be noticed that the discussed approach is a simplified model based on the first-mode vibrations. Even though these vibrations have the key influence on the electronic properties of the CT states due to the change of dihedral angle $\theta$ between donor and acceptor planes, some other vibrations of higher energies also reduce the separation of HOMO and LUMO (Figure 4A). For example, vibrations of the ninth vibronic state also change $\theta$, and in the tenth state, the planarity of the donor is disrupted. These vibrations lead to further increase of SOC as well as oscillator strength and $k_r$. More correct description of each TADF emitter should take into account the influence of all vibrations characteristic for each compound on the CT state. It should be noticed that, in general, understanding of vibrational enhancement of SOC cannot be simplified to the conformational changes. We, however, believe that the simplified approach presented here can be successfully used for design and semiqualitative unified description of rates of ISC, rISC, and radiative deactivation of a large number of D−A-type emitters with an orthogonal structure.

**Connection with Other Investigations.** The analysis of experimental reports on other emitters proves that within similar molecular systems, the highest rISC and/or external quantum efficiency (EQE) is achieved when the CT states are most stabilized and thus, as concluded above, $\Delta E^{1}_{CT-{}^3CT}$ is minimized. This can be achieved in two ways. First is the change of medium or the host matrix. The reported experiments generally provide evidence that higher polarity favors faster rISC and, in the absence of nonradiative deactivation, higher photo- and electroluminescence efficiency. As an example, 2,7-bis(9,9-dimethyl-acridin-10-yl)-9,9-dimethylthioxanthene-*S,S*-dioxide (DDMA-TXO2) exhibited faster rISC in the DPEPO host than in Zeonex films,[27] OLED devices containing tBuCzDCNPy emitter showed more than 3 times higher EQE when the DPEPO host was used instead of less polar mCP,[28] as well as TTAZ and TXAZ emitters dispersed in the DPEPO host instead of the less polar medium, the mixture of mCP and TSPO1 (1:1) hosts.[29]

Almost all previous theoretical models were developed on the basis of experimental photophysical data in the media of low polarity such as OLED hosts (mCP, CBP, DPEPO, etc.) or polymer matrixes such as Zeonex, polystyrene, and PMMA. Within such media, the variation of $E^{1}_{CT}$ of a selected emitter usually does not exceed 0.15 eV, which is too small to study a case with large $\Delta E^{1}_{CT-{}^3LE}$. Another important remark: in TADF emitters bearing conjugated fragments such as phenothiazine, phenoxazine, phenyl-*s*-triazine, phenylpyrimidine, phenazine, benzophenone, naphthalimide, and so forth, as well as some carbazole derivatives and similar aromatic heterocycles, the $^{3}LE$ energies are relatively low and, in non-polar medium, represent the T$_1$ states. Numerous TADF emitters can serve as examples: PTZ-DBTO2,[30] DPTZ-DPTO2,[31] and their derivatives based on which the three-state model was mainly developed, numerous *s*-triazine derivatives,[14−16,29,32] DBT-BZ-DMAC,[33] NAI,[34] various indolo[3,2-*b*]indole derivatives,[35] POZ-DBPHZ,[36] and so on. When polarity increases, the CT states of such emitters are getting energetically closer to $^{3}LE$, but simultaneously, the energy difference between $^{1}CT$ and $^{3}CT$ states also decreases, which most likely plays the key role in TADF.

The second way to change the CT-state energies is chemical modification. According to the literature reports, within derivatives bearing similar donor and acceptor fragments, better TADF parameters are observed in the emitters with higher donor/acceptor strength. For example, in toluene, DMAC-TRZ[16] bearing strong *s*-triazine acceptor shows higher rISC rate ($7 \times 10^{5}$ s$^{-1}$) as compared to its weaker 2-pyrimidine (no TADF) and 4-pyrimidine analogues ($6 \times 10^{4}$ s$^{-1}$).[37] In the DPEPO host, despite a larger absolute $\Delta E^{1}_{CT-{}^3LE}$ value, CT states of DMAC-TRZ are more stabilized and afford EQE$_{max}$ of 25%, in contrast to the pyrimidine analogues not exceeding 8% and 12%, respectively. Similarly, the change of spiroacridine donor to a weaker phenazasiline one in combination with the same aryl-1,3,5-triazine acceptors led to destabilization of CT states, slower TADF, and lower EQE.[29]

The only one known example of a molecular emitter with an extremely small $\Delta E^{1}_{CT-{}^3CT}$ value of < 2 meV and a large $\Delta E^{1}_{CT-{}^3LE}$ value of 0.2 eV serves as an excellent proof for the key importance of energetic closeness of $^{3}CT$ and $^{1}CT$ (compound **2**, ref 38). Taking into account the very low $\Delta E^{1}_{CT-{}^3CT}$ value emphasized by authors, the experimental evidence of very fast ISC and rISC exceeding the rate of radiative deactivation supports the vibrationally enhanced $^{3}CT$ $\leftrightarrow {}^1CT$ SOC model presented here.

As concluded above, one of the factors of efficient $^{3}CT \leftrightarrow$ $^{1}CT$ transformation is the vibrationally enhanced SOC with an average value of 0.05 cm$^{-1}$. In one of the pioneering works, the phenomenon of hyperfine coupling between the $^{1}CT$ and $^{3}CT$ states was suggested as a main reason explaining fast population of T$_1$ state in TADF emitters in time-resoled EPR experiment.[39] According to this model, SOCME due to hyperfine interaction can however reach a maximum of 0.2 cm$^{-1}$, when $\Delta E^{1}_{CT-{}^3CT}$ is below 0.051−0.025 meV (0.4−0.2 cm$^{-1}$). This can be valid for radical pairs; however, in almost all known molecular TADF emitters, the $\Delta E^{1}_{CT-{}^3CT}$ value is hundred times higher. A conclusion on negligible impact of hyperfine coupling on the TADF photophysics was also made previously on the basis of theoretical modeling.[5]

Finally, the vibronically assisted ISC model was applied for the 2CzPN and 4CzIPN emitters to explain the electron spin resonance (ESP) experiments.[40] It should be mentioned that

donor and acceptor in these emitters are not completely orthogonal, which provides HOMO/LUMO overlap, differences in the $S_1$ and $T_1$ states' nature, and thus non-zero SOC with large $\Delta E_{ST}$ already in the optimal geometry.[41] However, the ESP results consistent with the vibronically assisted ISC model indicate that molecular vibrations play the key role in facilitating direct ISC and rISC via the $S_1 \leftrightarrow T_1$ in such compounds. Therefore, the model presented here should be valid not only for D−A emitters with orthogonal structure and well-separated frontier molecular orbitals but also for other kinds of CT TADF emitters with appropriate $\Delta E_{ST}$ values.

In DMAC-TRZ, substantial differences in geometries and dipole moments of $^1$CT and $^3$LE states lead to large internal and external reorganization energies for the $^1$CT $\leftrightarrow$ $^3$LE transitions. To summarize the key numerical data for DMAC-TRZ, the calculated internal reorganization energies $\lambda_{^1CT-^3LE}$ and $\lambda_{^3LE-^1CT}$ are 179.6 meV and 208.8, respectively, which are more than 350 times higher than the internal $\lambda_{^1CT-^3CT}$ value of 0.5 meV. The analysis of solvatochromic effect on the photophysical parameters revealed that the $^1$CT $\leftrightarrow$ $^3$LE transition with large reorganization energy do not explain the experimental growth of rISC and ISC rates with the polarity of medium. In various media from hexane to acetone solutions, the $\Delta E_{^1CT-^3LE}$ values estimated experimentally changed in the large range from +94 to −460 meV, whereas the $\Delta E_{^1CT-^3CT}$ values changed from 24 to 4.2 meV. The corresponding TD-DFT calculated values were 559 and 6.6 meV, respectively. In contrast to the $^1$CT $\leftrightarrow$ $^3$LE transitions, the $^1$CT $\leftrightarrow$ $^3$CT ones perfectly explained the experimental dependencies due to much smaller reorganization energy and energy gap as well as vibrationally enhanced SOC.

In D−A emitters, the role of $^3$LE state in spin-flip processes should thus be carefully analyzed using both $\Delta E_{^1CT-^3LE}$ and $\lambda_{^1CT-^3LE}$ values, namely, how the change of latter values correlate with the experimental rate constants. In our opinion, the evidence of fast ISC and rISC between the $^1$CT and $^3$CT states presented here significantly change the current understanding of TADF photophysics. Previous interpretation of the photophysical properties of TADF emitters based on the $\Delta E_{^1CT-^3LE}$ value as the key parameter and negligible rate of the $^3$CT $\leftrightarrow$ $^1$CT transitions should be reconsidered.

## CONCLUSIONS

The main conclusion of this research is that correct description of the basic photophysical parameters of TADF emitters such as rates of ISC, rISC, and radiative deactivation is not possible without taking into account molecular vibrations and deviation from the orthogonality of D−A planes. A relatively simple and illustrative model presented here brings further important consequences. The evidence of efficient interaction of the same CT states with different multiplicities changes significantly the current understanding of TADF. Photophysics of some emitters as well as molecular design principles should be revised with an accent on $\Delta E_{^1CT-^3CT}$.

Experimental investigations of DMAC-TRZ in solvents of large range of polarity provided evidence of the increase of rates of forward and rISC under the stabilization of CT states. Supported by the TDDFT calculations, the polarity dependence of ISC and rISC was explained by the growing efficiency of the $^1$CT $\leftrightarrow$ $^3$CT interaction, which is forbidden in "frozen" optimal excited-state geometry but is effectively activated by molecular vibrations and accelerated in polar media due to the reduction of the $^1$CT−$^3$CT energy gap.

To describe correctly the experimental data, a theoretical model was developed, which treats photophysical parameters as statistical sums of respective values for selected rotational isomers existing at room temperature. Molecular vibrations changing the dihedral angle between donor and acceptor fragments were found to increase the SOC sharply between the $^1$CT and $^3$CT states of the same nature. According to the theoretical and experimental results, ISC and rISC occur through the $^3$CT $\leftrightarrow$ $^1$CT channel exclusively. The exception is the medium of lowest polarity, hexane, where the $\Delta E_{^1CT-^3CT}$ value is the highest one and the ISC rate is abnormally high, indicating some influence of the $^3$LE state.

The main factors enabling effective $^1$CT $\leftrightarrow$ $^3$CT transitions are the vibrationally enhanced SOC, very small energy gap, and comparably small reorganization energy due to similar geometries in the $^1$CT and $^3$CT states. In contrast, much larger reorganization energy $\lambda_{^1CT-^3LE}$, growing $|\Delta E_{^1CT-^3LE}|$ value, and decreasing population of the $^3$LE state result in negligible contribution of $^3$LE $\leftrightarrow$ $^1$CT transition rate in media more polar than hexane.

Further development of high-precision theoretical TADF model at a given temperature should take into account numerous molecular vibrations and their impact on the electronic properties of lowest excited states. Moreover, special attention should be given to the effects of viscosity of medium on molecular vibrations, especially in the case of amorphous emitting layers in optoelectronic devices.

## ASSOCIATED CONTENT

### Supporting Information

The Supporting Information is available free of charge at https://pubs.acs.org/doi/10.1021/acs.jpcb.0c10605.

Experimental photophysical parameters and detailed procedure of their determination, results of DFT calculations, detailed procedures, and examples of calculations of ISC, rISC, and $k_r$ within the developed model (PDF)

## AUTHOR INFORMATION

### Corresponding Author

**Illia E. Serdiuk** − *Faculty of Mathematics, Physics and Informatics, University of Gdańsk, 80-308 Gdańsk, Poland;* orcid.org/0000-0002-4563-0773; Phone: +48 58 523 22 44; Email: illia.serdiuk@ug.edu.pl

### Authors

**Michał Mońka** − *Faculty of Mathematics, Physics and Informatics, University of Gdańsk, 80-308 Gdańsk, Poland*

**Karol Kozakiewicz** − *Faculty of Chemistry, University of Gdańsk, 80-308 Gdańsk, Poland*

**Beata Liberek** − *Faculty of Chemistry, University of Gdańsk, 80-308 Gdańsk, Poland*

**Piotr Bojarski** − *Faculty of Mathematics, Physics and Informatics, University of Gdańsk, 80-308 Gdańsk, Poland*

**Soo Young Park** − *Center for Supramolecular Optoelectronic Materials, Department of Materials Science and Engineering, Seoul National University, 151-744 Seoul, Republic of Korea;* orcid.org/0000-0002-2272-8524

Complete contact information is available at:
https://pubs.acs.org/10.1021/acs.jpcb.0c10605

## Notes

The authors declare no competing financial interest.

## ■ ACKNOWLEDGMENTS

## ■ REFERENCES

(1) Uoyama, H.; Goushi, K.; Shizu, K.; Nomura, H.; Adachi, C. Highly Efficient Organic Light-Emitting Diodes from Delayed Fluorescence. *Nature* **2012**, *492*, 234−240.

(2) Nakanotani, H.; Higuchi, T.; Furukawa, T.; Masui, K.; Morimoto, K.; Numata, M.; Tanaka, H.; Sagara, Y.; Yasuda, T.; Adachi, C. High-Efficiency Organic Light-Emitting Diodes with Fluorescent Emitters. *Nat. Commun.* **2014**, *5*, 4016.

(3) Dias, F. B.; Bourdakos, K. N.; Jankus, V.; Moss, K. C.; Kamtekar, K. T.; Bhalla, V.; Santos, J.; Bryce, M. R.; Monkman, A. P. Triplet Harvesting with 100% Efficiency by way of Thermally Activated Delayed Fluorescence in Charge Transfer OLED Emitters. *Adv. Mater.* **2013**, *25*, 3707−3714.

(4) Noda, H.; Chen, X.-K.; Nakanotani, H.; Hosokai, T.; Miyajima, M.; Notsuka, N.; Kashima, Y.; Brédas, J.-L.; Adachi, C. Critical Role of Intermediate Electronic States for Spin-Flip Processes in Charge-Transfer-Type Organic Molecules with Multiple Donors and Acceptors. *Nat. Mater.* **2019**, *18*, 1084−1090.

(5) Gibson, J.; Monkman, A. P.; Penfold, T. J. The Importance of Vibronic Coupling for Efficient Reverse Intersystem Crossing in Thermally Activated Delayed Fluorescence Molecules. *ChemPhysChem* **2016**, *17*, 2956−2961.

(6) Samanta, P. K.; Kim, D.; Coropceanu, V.; Brédas, J.-L. Up-Conversion Intersystem Crossing Rates in Organic Emitters for Thermally Activated Delayed Fluorescence: Impact of the Nature of Singlet vs Triplet Excited States. *J. Am. Chem. Soc.* **2017**, *139*, 4042−4051.

(7) Ward, J. S.; Nobuyasu, R. S.; Batsanov, A. S.; Data, P.; Monkman, A. P.; Dias, F. B.; Bryce, M. R. The Interplay of Thermally Activated Delayed Fluorescence (TADF) and Room Temperature Organic Phosphorescence in Sterically-Constrained Donor−Acceptor Charge-Transfer Molecules. *Chem. Commun.* **2016**, *52*, 2612−2615.

(8) Zeng, W.; Gong, S.; Zhong, C.; Yang, C. Prediction of Oscillator Strength and Transition Dipole Moments with the Nuclear Ensemble Approach for Thermally Activated Delayed Fluorescence Emitters. *J. Phys. Chem. C* **2019**, *123*, 10081−10086.

(9) Stavrou, K.; Franca, L. G.; Monkman, A. P. Photophysics of TADF Guest−Host Systems: Introducing the Idea of Hosting Potential. *ACS Appl. Electron. Mater.* **2020**, *2*, 2868−2881.

(10) Kim, I.; Jeon, S. O.; Jeong, D.; Choi, H.; Son, W.-J.; Kim, D.; Rhee, Y. M.; Lee, H. S. Spin−Vibronic Model for Quantitative Prediction of Reverse Intersystem Crossing Rate in Thermally Activated Delayed Fluorescence Systems. *J. Chem. Theory Comput.* **2020**, *16*, 621−632.

(11) Di, D.; Romanov, A. S.; Yang, L.; Richter, J. M.; Rivett, J. P. H.; Jones, S.; Thomas, T. H.; Abdi Jalebi, M.; Friend, R. H.; Linnolahti, M.; et al. High-Performance Light-Emitting Diodes Based on Carbene-Metal-Amides. *Science* **2017**, *356*, 159−163.

(12) Föller, J.; Marian, C. M. Rotationally Assisted Spin-State Inversion in Carbene−Metal− Amides Is an Artifact. *Phys. Chem. Lett.* **2017**, *8*, 5643−5647.

(13) Feng, J.; Reponen, A. P. M.; Romanov, A. S.; Linnolahti, M.; Bochmann, M.; Greenham, N. C.; Penfold, T.; Credgington, D. Influence of Heavy Atom Effect on the Photophysics of Coinage Metal Carbene-Metal-Amide Emitters. *Adv. Funct. Mater.* **2021**, *31*, 2005438.

(14) Cui, L.-S.; Gillett, A. J.; Zhang, S.-F.; Ye, H.; Liu, Y.; Chen, X.-K.; Lin, Z.-S.; Evans, E. W.; Myers, W. K.; Ronson, T. K.; et al. Fast Spin-Flip Enables Efficient and Stable Organic Electroluminescence From Charge-Transfer States. *Nat. Photon.* **2020**, *14*, 636−642.

(15) Wada, Y.; Nakagawa, H.; Matsumoto, S.; Wakisaka, Y.; Kaji, H. Organic Light Emitters Exhibiting Very Fast Reverse Intersystem Crossing. *Nat. Photon.* **2020**, *14*, 643−649.

(16) Serdiuk, I. E.; Ryoo, C. H.; Kozakiewicz, K.; Mońka, M.; Liberek, B.; Park, S. Y. Twisted Acceptors in the Design of Deep-Blue TADF Emitters: Crucial Role of the Excited-State Relaxation on the Photophysics of Methyl Substituted *s*-Triphenyltriazine Derivatives. *J. Mater. Chem. C* **2020**, *8*, 6052−6062.

(17) Meech, S. R.; Phillips, D. Photophysics of Some Common Fluorescence Standards. *J. Photochem.* **1983**, *23*, 193−217.

(18) Dias, F. B.; Penfold, T. J.; Monkman, A. P. Photophysics of Thermally Activated Delayed Fluorescence Molecules. *Methods Appl. Fluoresc.* **2017**, *5*, 012001.

(19) Tao, Y.; Yuan, K.; Chen, T.; Xu, P.; Li, H.; Chen, R.; Zheng, C.; Zhang, L.; Huang, W. Thermally Activated Delayed Fluorescence Materials Towards the Breakthrough of Organoelectronics. *Adv. Mater.* **2014**, *26*, 7931−7958.

(20) Labanowski, J. K. *Density Functional Methods in Chemistry*; Andzelm, J. W., Ed.; Springer-Verlag: New York, 1991.

(21) Frisch, M. J.; Trucks, G. W.; Schlegel, H. B.; Scuseria, G. E.; Robb, M. A.; Cheeseman, J. R.; Scalmani, G.; Barone, V.; Petersson, G. A.; Nakatsuji, H.; et al. *Gaussian 16*, Revision C.01; Gaussian, Inc.: Wallingford, CT, 2016.

(22) Becke, A. D. A New Mixing of Hartree−Fock and Local Density-Functional Theories. *J. Chem. Phys.* **1993**, *98*, 1372−1377.

(23) Neese, F. The ORCA Program System. *Wiley Interdiscip. Rev.: Comput. Mol. Sci.* **2012**, *2*, 73−78.

(24) Kapturkiewicz, A.; Herbich, J.; Karpiuk, J.; Nowacki, J. Intramolecular Radiative and Radiationless Charge Recombination Processes in Donor−Acceptor Carbazole Derivatives. *J. Phys. Chem. A* **1997**, *101*, 2332−2344.

(25) Shizu, K.; Noda, H.; Tanaka, H.; Taneda, M.; Uejima, M.; Sato, T.; Tanaka, K.; Kaji, H.; Adachi, C. Highly Efficient Blue Electroluminescence Using Delayed-Fluorescence Emitters with Large Overlap Density between Luminescent and Ground States. *J. Phys. Chem. C* **2015**, *119*, 26283−26289.

(26) Valeur, B. *Molecular Fluorescence: Principles and Applications*; Wiley-VCH Verlag GmbH, 2001; p 30.

(27) Dos Santos, P. L.; Ward, J. S.; Bryce, M. R.; Monkman, A. P. Using Guest−Host Interactions To Optimize the Efficiency of TADF OLEDs. *J. Phys. Chem. Lett.* **2016**, *7*, 3341−3346.

(28) Gan, L.; Gao, K.; Cai, X.; Chen, D.; Su, S.-J. Achieving Efficient Triplet Exciton Utilization with Large $\Delta E_{ST}$ and Nonobvious Delayed Fluorescence by Adjusting Excited State Energy Levels. *J. Phys. Chem. Lett.* **2018**, *9*, 4725−4731.

(29) Woo, S.-J.; Kim, Y.; Kwon, S.-K.; Kim, Y.-H.; Kim, J.-J. Phenazasiline/Spiroacridine Donor Combined with Methyl-Substituted Linkers for Efficient Deep Blue Thermally Activated Delayed Fluorescence Emitters. *ACS Appl. Mater. Interfaces* **2019**, *11*, 7199−7207.

(30) Nobuyasu, R. S.; Ren, Z.; Griffiths, G. C.; Batsanov, A. S.; Data, P.; Yan, S.; Monkman, A. P.; Bryce, M. R.; Dias, F. B. Rational Design of TADF Polymers Using a Donor−Acceptor Monomer with Enhanced TADF Efficiency Induced by the Energy Alignment of Charge Transfer and Local Triplet Excited States. *Adv. Optical Mater.* **2016**, *4*, 597−607.

(31) Etherington, M. K.; Gibson, J.; Higginbotham, H. F.; Penfold, T. J.; Monkman, A. P. Revealing the Spin−Vibronic Coupling Mechanism of Thermally Activated Delayed Fluorescence. *Nat. Commun.* **2016**, *7*, 13680.

(32) Tanaka, H.; Shizu, K.; Miyazaki, H.; Adachi, C. Efficient Green Thermally Activated Delayed Fluorescence (TADF) from a Phenoxazinetriphenyltriazine (PXZ-TRZ) Derivative. *Chem. Commun.* **2012**, *48*, 11392−11394.

(33) Guo, J.; Li, X.-L.; Nie, H.; Luo, W.; Gan, S.; Hu, S.; Hu, R.; Qin, A.; Zhao, Z.; Su, S.-J.; et al. Achieving High-Performance Nondoped OLEDs with Extremely Small Efficiency Roll-Off by Combining Aggregation-Induced Emission and Thermally Activated Delayed Fluorescence. *Adv. Funct. Mater.* **2017**, *27*, 1606458.

(34) Zeng, W.; Zhou, T.; Ning, W.; Zhong, C.; He, J.; Gong, S.; Xie, G.; Yang, C. Realizing 22.5% External Quantum Efficiency for Solution-Processed Thermally Activated Delayed-Fluorescence OLEDs with Red Emission at 622 nm via a Synergistic Strategy of Molecular Engineering and Host Selection. *Adv. Mater.* **2019**, *31*, No. e1901404.

(35) Ryoo, C. H.; Cho, I.; Han, J.; Yang, J.-h.; Kwon, J. E.; Kim, S.; Jeong, H.; Lee, C.; Park, S. Y. Structure−Property Correlation in Luminescent Indolo[3,2-b]indole (IDID) Derivatives: Unraveling the Mechanism of High Efficiency Thermally Activated Delayed Fluorescence (TADF). *ACS Appl. Mater. Interfaces* **2017**, *9*, 41413−41420.

(36) Data, P.; Pander, P.; Okazaki, M.; Takeda, Y.; Minakata, S.; Monkman, A. P. Dibenzo[a,j]phenazine-Cored Donor-Acceptor-Donor Compounds as Green-to-Red/NIR Thermally Activated Delayed Fluorescence Organic Light Emitters. *Angew. Chem., Int. Ed.* **2016**, *55*, 5739−5744.

(37) Ganesan, P.; Ranganathan, R.; Chi, Y.; Liu, X.-K.; Lee, C.-S.; Liu, S.-H.; Lee, G.-H.; Lin, T.-C.; Chen, Y.-T.; Chou, P.-T. Functional Pyrimidine-Based Thermally Activated Delay Fluorescence Emitters: Photophysics, Mechanochromism, and Fabrication of Organic Light-Emitting Diodes. *Chem. Eur. J.* **2017**, *23*, 2858−2866.

(38) Yersin, H.; Mataranga-Popa, L.; Czerwieniec, R.; Dovbii, Y. Design of a New Mechanism beyond Thermally Activated Delayed Fluorescence toward Fourth Generation Organic Light Emitting Diodes. *Chem. Mater.* **2019**, *31*, 6110−6116.

(39) Ogiwara, T.; Wakikawa, Y.; Ikoma, T. Mechanism of Intersystem Crossing of Thermally Activated Delayed Fluorescence Molecules. *J. Phys. Chem. A* **2015**, *119*, 3415−3418.

(40) Evans, E. W.; Olivier, Y.; Puttisong, Y.; Myers, W. K.; Hele, T. J. H.; Menke, S. M.; Thomas, T. H.; Credgington, D.; Beljonne, D.; Friend, R. H.; et al. Vibrationally Assisted Intersystem Crossing in Benchmark Thermally Activated Delayed Fluorescence Molecules. *J. Phys. Chem. Lett.* **2018**, *9*, 4053−4058.

(41) Hosokai, T.; Matsuzaki, H.; Nakanotani, H.; Tokumaru, K.; Tsutsui, T.; Furube, A.; Nasu, K.; Nomura, H.; Yahiro, M.; Adachi, C. Evidence and Mechanism of Efficient Thermally Activated Delayed Fluorescence Promoted by Delocalized Excited States. *Sci. Adv.* **2017**, *3*, No. e1603282.

SUPPLEMENTAL INFORMATION

**Vibrationally Assisted Direct Intersystem Crossing Between the Same Charge Transfer**

**States for Thermally Activated Delayed Fluorescence: Analysis by Marcus-Hush Theory**

**Including Reorganization Energy**

Illia E. Serdiuk,* Michał Mońka, Karol Kozakiewicz, Beata Liberek, Piotr Bojarski, Soo

Young Park

*Correspondence e-mail: illia.serdiuk@ug.edu.pl

**Table of contents**

## Determination of photophysical parameters

Intensity weighted mean lifetime values were used for polyexponential decays of prompt (PF) or delayed (DF) fluorescence. The ratio of DF and PF quantum yields ($\varphi_{DF}/\varphi_{PF}$) was determined as following:

$$\frac{\varphi_{DF}}{\varphi_{PF}} = \frac{A_{DF}\tau_{DF}}{A_{PF}\tau_{PF}}, \tag{S1}$$

where $A_{DF}$ and $A_{PF}$ are pre-exponential factors of prompt and delayed fluorescence lifetimes, respectively; $\tau_{PF}$ and $\tau_{DF}$ are lifetimes of prompt and delayed fluorescence, respectively. Rate constants of radiative ($k_r$) and nonradiative ($k_{nr}$) decay, and intersystem crossing ($k_{ISC}$) were given by equations:

$$k_r = \frac{\varphi_{PF}}{\tau_{PF}}, \tag{S2}$$

$$k_{ISC} = \frac{\varphi_{DF}}{\tau_{PF}\varphi}, \tag{S3}$$

$$k_{nr} = \frac{1}{\tau_{PF}} - (k_r + k_{ISC}), \tag{S4}$$

where $\varphi$ is PLQY ($\varphi_{DF} + \varphi_{PF}$).

Further, the quantum yields of ISC and rISC were calculated as

$$\varphi_{ISC} = k_{ISC}\tau_{PF}, \tag{S5}$$

$$\varphi_{rISC} = \frac{1 - \varphi_{PF}/\varphi}{\varphi_{ISC}}. \tag{S6}$$

And finally, rate constant of rISC ($k_{rISC}$) was calculated as

$$k_{rISC} = \frac{\varphi_{rISC}}{\tau_{DF}}(\varphi/\varphi_{PF}). \tag{S7}$$

Photophysical parameters are summarized below in Table S1.

**Table S1**. Photoluminescent and photophysical parameters in various media*

| Solvent | $PL_{max}$ [nm] | PLQY [%] | $E_{1CT}$ (PL$_{onset}$) [nm] | $E_{1CT}$ (PL$_{onset}$) [eV] | $E_{3CT}$ [eV] | $\Delta E_{1CT\text{-}3LE}$ [eV] | $\Delta E_{1CT\text{-}3CT}$ [eV] | $\varphi_{DF}/\varphi_{PF}$ | $\tau_{PF}$ [ns] | $\tau_{DF}$ [µs] | $k_r$ | $k_{nr}$ | $k_{ISC}$ | $k_{rISC}$ |
|---|---|---|---|---|---|---|---|---|---|---|---|---|---|---|
| | | | | | | | | | | | \[10^7 s^{-1}\] | | | |
| Hexane | 459 | 71 | 426 | 2.91 | 2.89 | 0.094 | 0.024[a] | 1.1 | 15.4 | 32.0 | 2.2 | 0.9 | 3.4 | 0.007 |
| Benzene-hexane (1/2) | 480 | 60 | 436 | 2.84 | 2.83 | 0.026 | 0.019[a] | 0.5 | 21.3 | 8.4 | 1.9 | 1.3 | 1.5 | 0.017 |
| Benzene-hexane (1/1) | 488 | 68 | 443 | 2.80 | 2.78 | -0.022 | 0.016[a] | 0.8 | 23.1 | 5.8 | 1.7 | 0.8 | 1.9 | 0.030 |
| 5% Acetone in hexane | 522 | 100 | 451 | 2.75 | 2.73 | -0.069 | 0.014[a] | 1.2 | 31.9 | 6.1 | 1.4 | 0.0 | 1.7 | 0.036 |
| Benzene | 507 | 100 | 455 | 2.72 | 2.71 | -0.095 | 0.013[a] | 1.5 | 25.1 | 4.5 | 1.6 | 0.0 | 2.4 | 0.055 |
| 10% Acetone in hexane | 543 | 73 | 465 | 2.67 | 2.66 | -0.15 | 0.0115[b] | 1.5 | 24.8 | 2.1 | 1.2 | 0.4 | 2.4 | 0.12 |
| 15% Acetone in hexane | 561 | 63 | 474 | 2.62 | 2.61 | -0.20 | 0.0084[b] | 1.3 | 22.7 | 1.4 | 1.2 | 0.7 | 2.5 | 0.16 |
| Chlorobenzene | 550 | 78 | 482 | 2.57 | 2.56 | -0.25 | 0.0088[b] | 1.6 | 28.3 | 1.7 | 1.0 | 0.3 | 2.2 | 0.16 |
| 25% Acetone in hexane | 578 | 38 | 489 | 2.54 | 2.53 | -0.28 | 0.0064[b] | 0.9 | 18.9 | 0.8 | 1.1 | 1.8 | 2.5 | 0.23 |
| o-Dichlorobenzene | 573 | 52 | 495 | 2.51 | 2.50 | -0.31 | 0.0066[c] | 1.1 | 26.7 | 1.0 | 0.91 | 0.8 | 2.0 | 0.21 |
| 75% Acetone in hexane | 619 | 9.8 | 517 | 2.40 | 2.39 | -0.42 | 0.0045[b] | 0.3 | 8.7 | 0.4 | 0.85 | 7.8 | 2.8 | 0.35 |
| Acetone | 638 | 5.2 | 526 | 2.36 | 2.35 | -0.46 | 0.0042[b] | 0.2 | 5.8 | 0.3 | 0.74 | 13.4 | 3.1 | 0.38 |

*$PL_{max}$ and PLQY – photoluminescence maximum and quantum yield, respectively;

$E_{1CT}$ – energy of the $^1$CT state obtained as onset of photoluminescence spectra;

$E_{3CT}$ – energy of the $^3$CT state calculated using $E_{1CT}$ and $\Delta E_{1CT\text{-}3CT}$;

$\Delta E_{1CT\text{-}3LE}$ – energy gap between $^1$CT and $^3$LE states obtained from the onsets of respective emissions; negative values indicate that $E_{1CT} < E_{3LE}$.

$\Delta E_{1CT\text{-}3CT}$ – energy gap between $^1$CT and $^3$CT states obtained from Marcus-Hush equation and experimental $k_{rISC}$ values corresponding to the dihedral angle of 90° (see text).

$\varphi_{DF}/\varphi_{PF}$ – ratio of quantum yields of delayed (DF) and prompt (PF) fluorescence;

$\tau_{PF}$, $\tau_{DF}$ – lifetimes of PF and DF, respectively;
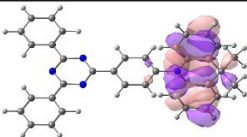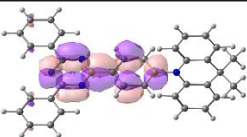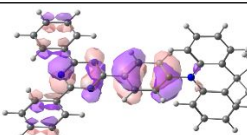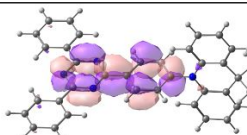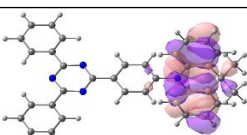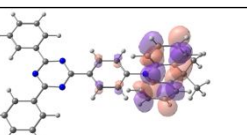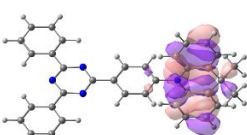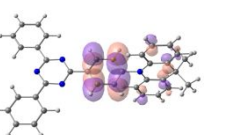
$k_{ISC}$, $k_{rISC}$, $k_r$, $k_{nr}$ – rates of intersystem crossing, reverse intersystem crossing, radiative and nonradiative deactivation, respectively.

[a] Values obtained by extrapolation of the $\Delta E_{1CT\text{-}3CT} – E_{1CT}$ dependence. [b] Values obtained using Marcus-Hush equation and experimental $k_{rISC}$ values. [c] Value predicted by TD-DFT calculations.

# Analysis of molecular orbitals and nature of electronically excited states

The nature of states was assigned based on the orbitals involved in respective transitions available from single-point calculations using optimal geometry in corresponding state. Thus, based on the optimized geometry of $T_1$-state, calculated highest occupied (HOMO) and lowest unoccupied molecular orbitals (LUMO) involved in the $T_1$-$S_0$ transition are localized on separate fragments: 9,9-dimethyl-9,10-dihydroacridine (DMAC) and phenyl-*s*-triazine, respectively (Scheme S1). The $T_1$ state was thus assigned as a $^3$CT state. The same conclusion was made for the $S_1$ state ($^1$CT).

Molecular orbitals, both HOMO and LUMO, involved in the $T_2$-$S_0$ transition calculated using the optimized geometry of $T_2$-state, are localized on the phenyl-*s*-triazine fragment (Scheme S1). Therefore, the $T_2$ state was assigned as a $^3$LE state. Molecular orbitals involved in the $T_3$-$S_0$ transition calculated using the optimized geometry of $T_3$-state, are localized on the *N*-phenyl-DMAC fragment. The $T_3$ state was thus assigned as a second $^3$LE state.

| Opt. geometry | Assigned | Orbitals involved | |
|---|---|---|---|
| | | **HOMO** | **LUMO** |
| $S_1$ and $T_1$* | CT |  100% |  |
| $T_2$ | $^3$LE |  >90% |  |
| $T_3$ | $^3$LE |  72% |  |
| | |  15% |  |

*geometries of the $^1$CT and $^3$CT states are almost identical so only the $^1$CT one is shown.

**Scheme S1.** Molecular orbitals involved in the electronic trasitions of DMAC-TRZ

Experimentally, the CT nature of $S_1$ state was confirmed by the strong positive solvatofluorochromism (Figure 1, the main text). As was reported previously,[1] at 78 K, the phosphorescence spectra of DMAC-TRZ and its derivatives are independent of solvent polarity in the range of low polarities. Such phosphorescence thus originates from the triplet state of LE nature. In DMAC-TRZ, its maximum near 484 nm correlates well with the TDDFT calculated $T_2$-$S_0$ transition energy involving orbitals localized on the phenyl-*s*-

etriazine fragment. Such [3]LE-state energy determined experimentally as onset of phosphorescence spectrum in methylcyclohexane equals 2.82 eV (440 nm). The $\Delta E_{1CT-3LE}$ values in various solvents were thus estimated using the $E_{1CT}$ values form the solvatofluorochromic measurements and the $E_{3LE}$ value mentioned above. The emission from [3]CT-state was not registered experimentally in these investigations.
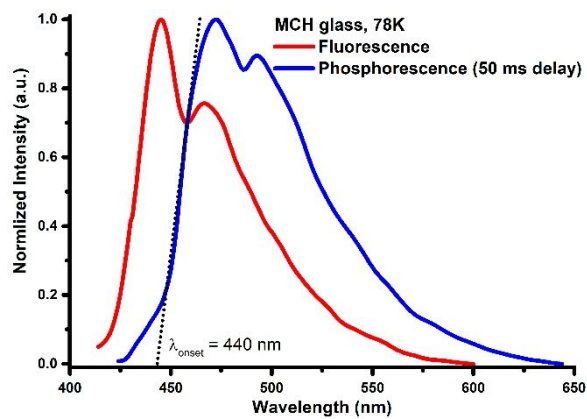
**Table S2**. Computational data for various rotational isomers is the $^3$CT-state geometry and rates of the $^3$CT→$^1$CT transition*

| Dihedral Angle [°] | $V_{3CT\text{-}1CT}$ [cm$^{-1}$] | $\Delta E_{1CT\text{-}3CT}$ [eV] | $\lambda_{1CT\text{-}3CT}$ [eV] | $k_{3CT\rightarrow1CT}$ [$10^7$ s$^{-1}$] | $\mu$ [%] | $\mu \cdot k_{3CT\rightarrow1CT}$ [$10^7$ s$^{-1}$] |
|---|---|---|---|---|---|---|
| 90 | 0.00 | 0.0066 | 0.0066 | 0.0000 | 5.20 | 0.0000 |
| 89 and 91 | 0.01 | 0.0068 | 0.0068 | 0.0224 | 10.39 | 0.0023 |
| 88 and 92 | 0.02 | 0.0076 | 0.0076 | 0.0824 | 10.25 | 0.0084 |
| 87 and 93 | 0.03 | 0.0089 | 0.0089 | 0.1631 | 10.07 | 0.0164 |
| 86 and 94 | 0.04 | 0.0107 | 0.0107 | 0.2459 | 9.80 | 0.0241 |
| 85 and 95 | 0.05 | 0.0130 | 0.0130 | 0.3186 | 9.46 | 0.0302 |
| 84 and 96 | 0.06 | 0.0159 | 0.0159 | 0.3723 | 9.05 | 0.0337 |
| 83 and 97 | 0.07 | 0.0192 | 0.0192 | 0.4042 | 8.56 | 0.0346 |
| 82 and 98 | 0.07 | 0.0230 | 0.0230 | 0.3187 | 8.02 | 0.0256 |
| 81 and 99 | 0.08 | 0.0273 | 0.0273 | 0.3231 | 7.42 | 0.0240 |
| 80 and 100 | 0.09 | 0.0320 | 0.0320 | 0.3143 | 6.79 | 0.0213 |
| 75 and 105 | 0.13 | 0.0621 | 0.0621 | 0.1458 | 3.55 | 0.0052 |
| 70 and 110 | 0.16 | 0.1012 | 0.1012 | 0.0378 | 1.22 | 0.0005 |
| 65 and 115 | 0.19 | 0.1467 | 0.1467 | 0.0075 | 0.21 | 0.0000 |
| **Sum** | | | | | | **0.226** |

*$V_{3CT\text{-}1CT}$ − SOCME value for the $^3$CT→$^1$CT transition; $\mu$ – statistical weight of a rotational isomer at room temperature calculated using relative energies of isomers in the $^3$CT state listed in Table S5.

**Table S3**. Rates of ISC and rISC as statistical sums for rotamers for all investigated media*

| Solvent | $\chi_{3CT}$ [%] | $\chi_{3LE}$ [%] | ISC [$10^7$ s$^{-1}$] | | | rISC [$10^7$ s$^{-1}$] | | | | |
|---|---|---|---|---|---|---|---|---|---|---|
| | | | $k_{1CT\to 3CT}$ | $k_{1CT\to 3LE}$ | $k_{1CT\to 3CT +}$ $k_{1CT\to 3LE}$ | $k_{3CT\to 1CT}$ | $k_{3LE\to 1CT}$ | $\chi_{3CT}k_{3CT\to 1CT}$ | $\chi_{3LE}k_{3LE\to 1CT}$ | $\chi_{3CT}k_{3CT\to 1CT} +$ $\chi_{3LE}k_{3LE\to 1CT}$ |
| Hexane | 5.6 | 94.4 | 0.26 | 1.27 | 1.53 | 0.023 | 0.034 | $1.3 \cdot 10^{-3}$ | 0.032 | 0.033 |
| Benzene-hexane (1/2) | 42.8 | 57.2 | 0.28 | 0.39 | 0.67 | 0.039 | 0.15 | 0.017 | 0.085 | 0.102 |
| Benzene-hexane (1/1) | 81.4 | 18.6 | 0.29 | 0.15 | 0.44 | 0.053 | 0.38 | 0.043 | 0.070 | 0.114 |
| Acetone-hexane (5%) | 96.3 | 3.7 | 0.31 | $5.6 \cdot 10^{-2}$ | 0.37 | 0.071 | 0.87 | 0.068 | 0.032 | 0.100 |
| Benzene | 98.6 | 1.4 | 0.32 | $3.1 \cdot 10^{-2}$ | 0.35 | 0.082 | 1.32 | 0.081 | 0.053 | 0.134 |
| Acetone-hexane (10%) | 99.8 | 0.18 | 0.35 | $7.9 \cdot 10^{-3}$ | 0.36 | 0.111 | 2.95 | 0.111 | 0.014 | 0.124 |
| Acetone-hexane (15%) | 100 | $2.8 \cdot 10^{-2}$ | 0.38 | $2.1 \cdot 10^{-3}$ | 0.38 | 0.142 | 5.55 | 0.142 | $3.7 \cdot 10^{-3}$ | 0.146 |
| Chlorobenzene | 100 | $5.1 \cdot 10^{-3}$ | 0.40 | $4.8 \cdot 10^{-4}$ | 0.40 | 0.172 | 9.49 | 0.172 | $1.1 \cdot 10^{-3}$ | 0.173 |
| Acetone-hexane (25%) | 100 | $1.3 \cdot 10^{-3}$ | 0.43 | $1.9 \cdot 10^{-4}$ | 0.43 | 0.202 | 12.5 | 0.202 | $3.3 \cdot 10^{-4}$ | 0.202 |
| o-Dichlorobenzene | 100 | $3.9 \cdot 10^{-4}$ | 0.46 | $7.4 \cdot 10^{-5}$ | 0.46 | 0.229 | 15.9 | 0.229 | $1.2 \cdot 10^{-4}$ | 0.229 |
| Acetone-hexane (75%) | 100 | $6.7 \cdot 10^{-6}$ | 0.56 | $1.8 \cdot 10^{-6}$ | 0.56 | 0.338 | 28.8 | 0.338 | $2.5 \cdot 10^{-6}$ | 0.338 |
| Acetone | 100 | $1.4 \cdot 10^{-6}$ | 0.58 | $3.6 \cdot 10^{-7}$ | 0.58 | 0.387 | 31.8 | 0.387 | $4.8 \cdot 10^{-7}$ | 0.387 |

*$\chi_{3CT}$ and $\chi_{3LE}$ − molar fractions of molecules coexisting in $^3$CT and $^3$LE states at 298.15 K, calculated using Boltzmann distribution law and energies of the respective triplet states listed in Table S1.

$k_{1CT\to 3LE}$ and $k_{3LE\to 1CT}$ calculated using $\lambda_{solv} = 0.3$ eV (Table S9 and S10)

*Prediction of the rate of radiative deactivation ($k_r$).* The rate of radiative deactivation was obtained as a statistical sum of respective values for each rotational isomer calculated using Strickler-Berg law:[2,3]

$$k_r = \sum_\theta \frac{0.668 \cdot f(\theta) \cdot n^2}{\lambda_{S1-S0}^2(\theta) \cdot 10^7}$$ 
(S8),

where $\lambda_{S1-S0}(\theta)$ and $f(\theta)$ are wavelength in nanometer and oscillator strength of $S_1$-$S_0$ transition for each rotational isomer, respectively; $n$ is refractive index of $o$-dichlorobenzene ($n = 1.551$).

**Table S4**. TD-DFT predicted energy ($\lambda_{S1-S0}$) and oscillator strengths ($f$) of $S_1$-$S_0$ transition, and calculated radiative deactivation constants ($k_r$) for various dihedral angles*

| Dihedral Angle $\theta$ [°] | $\lambda_{S1-S0}$ [nm] | $f$ | $k_r$ [$10^7$ s$^{-1}$] | $\mu$ [%] | $\mu \cdot k_r$ [$10^7$ s$^{-1}$] |
|---|---|---|---|---|---|
| 90 | 611.49 | 0.0000 | 0.000 | 7.37 | 0.0000 |
| 89 and 91 | 611.22 | 0.0002 | 0.009 | 14.2 | 0.0012 |
| 88 and 92 | 610.98 | 0.0008 | 0.034 | 13.6 | 0.0047 |
| 87 and 93 | 610.61 | 0.0018 | 0.078 | 12.7 | 0.0099 |
| 86 and 94 | 610.13 | 0.0031 | 0.134 | 11.5 | 0.0154 |
| 85 and 95 | 609.49 | 0.0049 | 0.212 | 10.2 | 0.0215 |
| 84 and 96 | 608.72 | 0.0070 | 0.304 | 8.70 | 0.0264 |
| 83 and 97 | 607.77 | 0.0096 | 0.418 | 7.23 | 0.0302 |
| 82 and 98 | 606.76 | 0.0125 | 0.546 | 5.84 | 0.0319 |
| 81 and 99 | 605.58 | 0.0158 | 0.692 | 4.57 | 0.0316 |
| 80 and 100 | 604.29 | 0.0194 | 0.854 | 3.48 | 0.0297 |
| 75 and 105 | 596.13 | 0.0428 | 1.935 | 0.56 | 0.0109 |
| 70 and 110 | 585.64 | 0.0740 | 3.467 | 0.04 | 0.0015 |
| 65 and 115 | 573.47 | 0.1124 | 5.492 | 0.001 | 0.0001 |
| **Sum** | | | | | **0.215** |

*$\mu$ – statistical weight of a rotational isomer in $^1$CT-state at room temperature calculated using relative energies of isomers listed in Table S5.
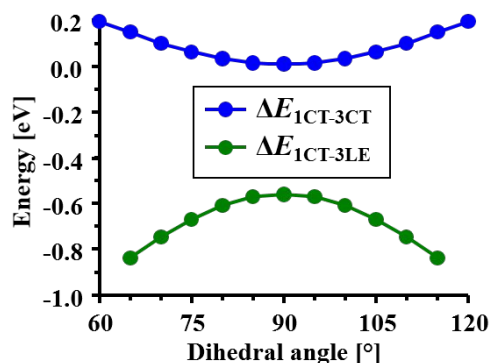


**Figure S1**. Dependence of the TD-DFT predicted energy gaps between singlet and triplet states on the dihedral angle between donor and acceptor fragments

**Theoretical model including rotational isomers and vibrationally-enhanced SOC**

*Corrections for various polarity.* Alignment of the potential curves of $^1$CT, $^3$CT, and $^3$LE states predicted on the TD-TDF/B3LYP level of theory is in excellent correlation with the experimental data in the media of relatively high polarity (like *o*-dichlorobenzene and 75% mixture of acetone in hexane). To mimic less and more polar medium, the energies of $^1$CT and $^3$CT states were corrected for each media according to the procedure below.

Unconstrained geometry optimizations of DMAC-TRZ were conducted for various excited states. The nature of each excited state was established by the analysis of molecular orbitals involved in respective transitions. The $\Delta E_{1CT-3CT}$ and $\Delta E_{1CT-3LE}$ values were calculated using electronic energies ($E$(TD-DFT)) of respective states in their energetic minima (Table S5), verified by the absence of imaginary (negative) vibrational frequencies. Next, starting with the optimized geometry in each excited state, the value of dihedral angle between DMAC and phenyl ring of acceptor fragment was scanned with a 1 degree step from 89° to 60°. Energies of respective states were calculated by single-point calculations. The $\Delta E_{1CT-3CT}$ and $\Delta E_{1CT-3LE}$ values for each rotational isomer were calculated using thus obtained energies.

**Table S5**. Energies of the excited states and gaps between them.

| | | | | | | Corrected for hexane | |
|---|---|---|---|---|---|---|---|
| Dihedral Angle [°] | $E_{1CT}{}^{1CT}$ [au] | $E_{3CT}{}^{3CT}$ [au] | $E_{3LE}{}^{3LE}$ [au] | $\Delta E_{1CT-3CT}$ [eV] | $\Delta E_{1CT-3LE}$ [eV] | $\Delta E_{1CT-3CT}$ [eV] | $\Delta E_{1CT-3LE}$ [eV] |
| 90 | -1607.76452079 | -1607.76476132 | -1607.74397545 | 0.0065 | -0.559 | 0.024 | 0.094 |
| 85 | -1607.76417036 | -1607.76467305 | -1607.74347908 | 0.0137 | -0.563 | 0.049 | 0.090 |
| 80 | -1607.76315795 | -1607.76435939 | -1607.74202884 | 0.0327 | -0.575 | 0.118 | 0.078 |
| 75 | -1607.76143695 | -1607.76374597 | -1607.73979476 | 0.0628 | -0.589 | 0.227 | 0.064 |
| 70 | -1607.75899058 | -1607.76273759 | -1607.73691709 | 0.1020 | -0.601 | 0.368 | 0.052 |
| 65 | -1607.75567303 | -1607.76121844 | -1607.73334284 | 0.1509 | -0.608 | 0.545 | 0.045 |

**Table S6.** Vertical transition energies of DMAC-TRZ calculated using PCM

| Medium | Vertical transition energy [nm] | |
|---|---|---|
| | $S_0$-$S_1$ | $S_1$-$S_0$ |
| Vacuum | 516 | 612 |
| Chloroform | 500 | 597 |
| Formamide | 496 | 593 |

DFT fails to predict medium polarity influence on the spectral properties of D-A emitters. Polarized continuum model, most extensively used for this purpose predicts incorrectly the solvent effect. (Table S6). To mimic medium of different polarity, minimum $^1$CT energy, energies of rotational isomers in $^1$CT state as well as all vertical transitions involving $^1$CT state were corrected by a correction factor $C$, obtained using experimental $\Delta E_{1CT\text{-}3LE}$ value (Table S1) for each medium:

$$C = E_{3LE}{}^{3LE} - E_{1CT}{}^{1CT} + \Delta E_{1CT\text{-}3LE} \tag{S9},$$

where $E_{3LE}{}^{3LE}$ and $E_{3LE}{}^{3LE}$ are the energies of respective states in their optimized geometries from Table S5 (dihedral angle 90°). Obtained $C$ values are listed below (Table S7):

**Table S7**. Correction factors for various media

| Solvent | $\Delta E_{1CT\text{-}3LE}$ [eV] | $C$ |
|---|---|---|
| Hexane | 0.094 | 0.65 |
| Benzene-hexane (1/2) | 0.026 | 0.58 |
| Benzene-hexane (1/1) | -0.022 | 0.54 |
| Acetone-hexane (5%) | -0.069 | 0.49 |
| Benzene | -0.095 | 0.46 |
| Acetone-hexane (10%) | -0.15 | 0.41 |
| Acetone-hexane (15%) | -0.20 | 0.36 |
| Chlorobenzene | -0.25 | 0.31 |
| Acetone-hexane (25%) | -0.28 | 0.28 |
| o-Dichlorobenzene | -0.31 | 0.25 |
| Acetone-hexane (75%) | -0.42 | 0.14 |
| Acetone | -0.46 | 0.10 |

For each medium, the $\Delta E_{1CT\text{-}3LE}$ values at various dihedral angles ($\theta$) were calculated as follows:

$$\text{"}\Delta E_{1CT\text{-}3LE}(\theta)\text{"} = (E_{1CT}{}^{1CT}(\theta) + C) - E_{3LE}{}^{3LE}(\theta)\text{"} \tag{S10},$$

The example of such calculations for hexane is listed in Table S5.

As the $\Delta E_{1CT\text{-}3CT}$ value changes also with the change of dihedral angle, for each medium, its value for each rotational isomer "$\Delta E_{1CT\text{-}3CT}{}^{Solvent}(\theta)$" was calculated proportional to that at 90°. In the example with hexane:

$$\text{"}\Delta E_{1CT\text{-}3CT}{}^{Hexane}(\theta)\text{"} = \text{"}\Delta E_{1CT\text{-}3CT}(\theta)\text{"} \cdot \text{"}\Delta E_{1CT\text{-}3CT}{}^{Hexane}\text{"} / \text{"}\Delta E_{1CT\text{-}3CT}\text{"} \tag{S11},$$

where

"$\Delta E_{1CT-3CT}(\theta)$" – computational value for respective dihedral angle from Table S5;

"$\Delta E_{1CT-3CT}$" – computational value for 90° dihedral angle from Table S5;

"$\Delta E_{1CT-3CT}^{Hexane}$" – experimental value listed for each medium in Table S1.

The example of such calculations for hexane is listed in Table S5.

Reorganization energies of the $^3LE \rightarrow ^1CT$ and $^1CT \rightarrow ^3LE$ transitions (Figure 3) were calculated as follows

$$\lambda_{3LE-1CT}(\theta) = E_{1CT}^{3LE}(\theta) - E_{1CT}^{1CT}(\theta) \tag{S12},$$

$$\lambda_{1CT-3LE}(\theta) = E_{3LE}^{1CT}(\theta) - E_{3LE}^{3LE}(\theta) \tag{S13},$$

where

$E_{1CT}^{3LE}(\theta)$ – TD-DFT energy of the $^1CT$ state at the $^3LE$ geometry at given dihedral angle value $\theta$; $E_{3LE}^{1CT}(\theta)$ – TD-DFT energy of the $^3LE$ state at the $^1CT$ geometry at given dihedral angle value $\theta$. These values are listed in Table S8.

**Table S8**. Energies of states in non-optimal geometries and reorganization energies

| Dihedral Angle [°] | $E_{1CT}^{3LE}$ [au] | $E_{3LE}^{1CT}$ [au] | $\lambda_{1CT-3LE}$ [eV] | $\lambda_{3LE-1CT}$ [eV] |
|---|---|---|---|---|
| 90 | -1607.756846 | -1607.737375 | 0.1796 | 0.2088 |
| 85 | -1607.756471 | -1607.736974 | 0.1770 | 0.2095 |
| 80 | -1607.755313 | -1607.735792 | 0.1697 | 0.2135 |
| 75 | -1607.753388 | -1607.733989 | 0.1580 | 0.2190 |
| 70 | -1607.750780 | -1607.731688 | 0.1423 | 0.2234 |
| 65 | -1607.747374 | -1607.728820 | 0.1231 | 0.2258 |

*Prediction of rISC rates. $^3CT \rightarrow ^1CT$ transition.*

Parameters for calculations of $^3CT \rightarrow ^1CT$ transition rate for various rotational isomers using Marcus-Hush equation and the B3LYP predicted $\Delta E_{1CT-3CT}$ values are presented in Table S2. For media with $E_{1CT} \leq 2.67$ eV, experimental $k_{rISC}$ was used for calculation of $\Delta E_{1CT-3CT}$ using Marcus-Hush equation and assuming $\Delta E_{1CT-3CT} = \lambda_{1CT-3CT}$. For less polar media, $\Delta E_{1CT-3CT}$ were obtained by extrapolation (Figure 2H in the main text). Reconstructed $k_{rISC}$ values for all media are shown in Table S3.

*Prediction of rISC rates. $^3LE \rightarrow ^1CT$ transition.* Examples of calculations of $^3LE \rightarrow ^1CT$ transition rates for various rotational isomers using Marcus-Hush equation are presented in Table S9.

**Table S9.** Calculation of the $^3LE \rightarrow ^1CT$ transition parameters*

Hexane, $\Delta E_{\text{1CT-3LE}} = 0.094$ eV.

| Dihedral Angle [°] | $\Delta E_{\text{1CT-3LE}}$ [eV] | $\lambda_{\text{3LE-1CT}}$ [eV] | $\mu$ [%] | $\lambda_{\text{solv}} = 0.2$ eV | | $\lambda_{\text{solv}} = 0.3$ eV | |
|---|---|---|---|---|---|---|---|
| | | | | $k_{\text{3LE}\rightarrow\text{1CT}}$ [$10^7$ s$^{-1}$] | $\mu \cdot k_{\text{3LE}\rightarrow\text{1CT}}$ [$10^7$ s$^{-1}$] | $k_{\text{3LE}\rightarrow\text{1CT}}$ [$10^7$ s$^{-1}$] | $\mu \cdot k_{\text{3LE}\rightarrow\text{1CT}}$ [$10^7$ s$^{-1}$] |
| 90 | 0.094 | 0.2088 | 40.6 | 0.092 | 0.037 | 0.032 | 0.013 |
| 85 and 95 | 0.090 | 0.2095 | 48.0 | 0.098 | 0.047 | 0.035 | 0.017 |
| 80 and 100 | 0.078 | 0.2135 | 10.3 | 0.115 | 0.012 | 0.040 | 0.004 |
| 75 and 105 | 0.064 | 0.2190 | 1.0 | 0.131 | 0.001 | 0.045 | 0.000 |
| 70 and 110 | 0.052 | 0.2234 | 0.0 | 0.134 | 0.000 | 0.046 | 0.000 |
| 65 and 115 | 0.045 | 0.2258 | 0.0 | 0.120 | 0.000 | 0.041 | 0.000 |
| | | | | | **0.098** | | **0.034** |

Benzene-hexane (1:2), $\Delta E_{\text{1CT-3LE}} = 0.026$ eV.

| Dihedral Angle [°] | $\Delta E_{\text{1CT-3LE}}$ [eV] | $\lambda_{\text{3LE-1CT}}$ [eV] | $\mu$ [%] | $\lambda_{\text{solv}} = 0.2$ eV | | $\lambda_{\text{solv}} = 0.3$ eV | |
|---|---|---|---|---|---|---|---|
| | | | | $k_{\text{3LE}\rightarrow\text{1CT}}$ [$10^7$ s$^{-1}$] | $\mu \cdot k_{\text{3LE}\rightarrow\text{1CT}}$ [$10^7$ s$^{-1}$] | $k_{\text{3LE}\rightarrow\text{1CT}}$ [$10^7$ s$^{-1}$] | $\mu \cdot k_{\text{3LE}\rightarrow\text{1CT}}$ [$10^7$ s$^{-1}$] |
| 90 | 0.026 | 0.2088 | 40.6 | 0.419 | 0.170 | 0.142 | 0.058 |
| 85 and 95 | 0.022 | 0.2095 | 48.0 | 0.443 | 0.213 | 0.150 | 0.072 |
| 80 and 100 | 0.010 | 0.2135 | 10.3 | 0.497 | 0.051 | 0.169 | 0.017 |
| 75 and 105 | -0.004 | 0.2190 | 1.0 | 0.540 | 0.005 | 0.183 | 0.002 |
| 70 and 110 | -0.016 | 0.2234 | 0.0 | 0.533 | 0.000 | 0.181 | 0.000 |
| 65 and 115 | -0.023 | 0.2258 | 0.0 | 0.467 | 0.000 | 0.159 | 0.000 |
| **Sum** | | | | | **0.440** | | **0.149** |

Benzene-hexane (1:1) mixture, $\Delta E_{\text{1CT-3LE}} = -0.022$ eV.

| Dihedral Angle [°] | $\Delta E_{\text{1CT-3LE}}$ [eV] | $\lambda_{\text{3LE-1CT}}$ [eV] | $\mu$ [%] | $\lambda_{\text{solv}} = 0.2$ eV | | $\lambda_{\text{solv}} = 0.3$ eV | |
|---|---|---|---|---|---|---|---|
| | | | | $k_{\text{3LE}\rightarrow\text{1CT}}$ [$10^7$ s$^{-1}$] | $\mu \cdot k_{\text{3LE}\rightarrow\text{1CT}}$ [$10^7$ s$^{-1}$] | $k_{\text{3LE}\rightarrow\text{1CT}}$ [$10^7$ s$^{-1}$] | $\mu \cdot k_{\text{3LE}\rightarrow\text{1CT}}$ [$10^7$ s$^{-1}$] |
| 90 | -0.022 | 0.2088 | 40.6 | 1.073 | 0.436 | 0.364 | 0.148 |
| 85 and 95 | -0.026 | 0.2095 | 48.0 | 1.123 | 0.539 | 0.381 | 0.183 |
| 80 and 100 | -0.038 | 0.2135 | 10.3 | 1.226 | 0.127 | 0.418 | 0.043 |
| 75 and 105 | -0.052 | 0.2190 | 1.0 | 1.292 | 0.013 | 0.444 | 0.004 |
| 70 and 110 | -0.064 | 0.2234 | 0.0 | 1.243 | 0.001 | 0.430 | 0.000 |
| 65 and 115 | -0.071 | 0.2258 | 0.0 | 1.074 | 0.000 | 0.373 | 0.000 |
| **Sum** | | | | | **1.115** | | **0.379** |

**Table S9** continued.

Benzene, $\Delta E_{\text{1CT-3LE}} = -0.095$ eV.

| Dihedral Angle [°] | $\Delta E_{\text{1CT-3LE}}$ [eV] | $\lambda_{\text{3LE-1CT}}$ [eV] | $\mu$ [%] | $\lambda_{\text{solv}} = 0.2$ eV | | $\lambda_{\text{solv}} = 0.3$ eV | |
|---|---|---|---|---|---|---|---|
| | | | | $k_{\text{3LE}\rightarrow\text{1CT}}$ [$10^7$ s$^{-1}$] | $\mu \cdot k_{\text{3LE}\rightarrow\text{1CT}}$ [$10^7$ s$^{-1}$] | $k_{\text{3LE}\rightarrow\text{1CT}}$ [$10^7$ s$^{-1}$] | $\mu \cdot k_{\text{3LE}\rightarrow\text{1CT}}$ [$10^7$ s$^{-1}$] |
| 90 | -0.095 | 0.2088 | 40.6 | 3.627 | 1.474 | 1.281 | 0.520 |
| 85 and 95 | -0.099 | 0.2095 | 48.0 | 3.745 | 1.798 | 1.327 | 0.637 |
| 80 and 100 | -0.111 | 0.2135 | 10.3 | 3.934 | 0.407 | 1.411 | 0.146 |
| 75 and 105 | -0.125 | 0.2190 | 1.0 | 3.966 | 0.038 | 1.443 | 0.014 |
| 70 and 110 | -0.137 | 0.2234 | 0.0 | 3.681 | 0.002 | 1.357 | 0.001 |
| 65 and 115 | -0.144 | 0.2258 | 0.0 | 3.112 | 0.000 | 1.157 | 0.000 |
| **Sum** | | | | | **3.719** | | **1.318** |

Acetone, $\Delta E_{\text{1CT-3LE}} = -0.46$ eV.

| Dihedral Angle [°] | $\Delta E_{\text{1CT-3LE}}$ [eV] | $\lambda_{\text{3LE-1CT}}$ [eV] | $\mu$ [%] | $\lambda_{\text{solv}} = 0.2$ eV | | $\lambda_{\text{solv}} = 0.3$ eV | |
|---|---|---|---|---|---|---|---|
| | | | | $k_{\text{3LE}\rightarrow\text{1CT}}$ [$10^7$ s$^{-1}$] | $\mu \cdot k_{\text{3LE}\rightarrow\text{1CT}}$ [$10^7$ s$^{-1}$] | $k_{\text{3LE}\rightarrow\text{1CT}}$ [$10^7$ s$^{-1}$] | $\mu \cdot k_{\text{3LE}\rightarrow\text{1CT}}$ [$10^7$ s$^{-1}$] |
| 90 | -0.460 | 0.2088 | 40.6 | 35.56 | 14.44 | 32.42 | 13.17 |
| 85 and 95 | -0.464 | 0.2095 | 48.0 | 34.54 | 16.59 | 31.94 | 15.34 |
| 80 and 100 | -0.476 | 0.2135 | 10.3 | 30.99 | 3.20 | 29.68 | 3.07 |
| 75 and 105 | -0.490 | 0.2190 | 1.0 | 26.35 | 0.26 | 26.19 | 0.25 |
| 70 and 110 | -0.502 | 0.2234 | 0.0 | 21.20 | 0.01 | 21.75 | 0.01 |
| 65 and 115 | -0.509 | 0.2258 | 0.0 | 16.44 | 0.00 | 17.21 | 0.00 |
| **Sum** | | | | | **34.50** | | **31.84** |

\* $\mu$ – statistical weight of a rotational isomer in $^3$LE-state at room temperature calculated using relative energies of isomers listed in Table S5.

*Prediction of ISC rates. $^1CT \rightarrow {}^3CT$ transition.* Rates of the $^1CT \rightarrow {}^3CT$ transition in various media were calculated as statistical sums for various rotational isomers using Marcus-Hush equation. The used $\Delta E_{1CT\text{-}3CT}$ values were calculated using equation S11 and are listed in Table S1. SOCME values are listed in Table S2. The $\lambda_{1CT\text{-}3CT}$ values were assumed equal to the $\Delta E_{1CT\text{-}3CT}$ ones. Thus obtained $k_{1CT\rightarrow 3CT}$ values for all media are listed in Table S3.

*Prediction of ISC rates. $^1CT \rightarrow {}^3LE$ transition.*

Examples of calculations of the $^1CT \rightarrow {}^3LE$ transition rates for various rotational isomers using Marcus-Hush equation are presented in Table S10.

**Table S10**. Calculation of the $^1CT \rightarrow {}^3LE$ transition parameters*

Hexane, $\Delta E_{1CT\text{-}3LE} = 0.094$ eV.

| Dihedral Angle [°] | $\Delta E_{3LE\text{-}1CT}$ [eV] | $\lambda_{1CT\text{-}3LE}$ [eV] | $\mu$ [%] | $\lambda_{solv} = 0.2$ eV | | $\lambda_{solv} = 0.3$ eV | |
|---|---|---|---|---|---|---|---|
| | | | | $k_{1CT\rightarrow 3LE}$ [$10^7$ s$^{-1}$] | $\mu \cdot k_{1CT\rightarrow 3LE}$ [$10^7$ s$^{-1}$] | $k_{1CT\rightarrow 3LE}$ [$10^7$ s$^{-1}$] | $\mu \cdot k_{1CT\rightarrow 3LE}$ [$10^7$ s$^{-1}$] |
| 90 | -0.094 | 0.1796 | 34.1 | 3.67 | 1.25 | 1.29 | 0.441 |
| 85 and 95 | -0.090 | 0.1731 | 47.0 | 3.71 | 1.74 | 1.30 | 0.612 |
| 80 and 100 | -0.078 | 0.1538 | 16.1 | 3.30 | 0.53 | 1.14 | 0.184 |
| 75 and 105 | -0.064 | 0.1281 | 2.6 | 3.42 | 0.089 | 1.16 | 0.030 |
| 70 and 110 | -0.052 | 0.1007 | 0.2 | 3.37 | $6.6 \cdot 10^{-3}$ | 1.13 | $2.2 \cdot 10^{-3}$ |
| 65 and 115 | -0.045 | 0.0746 | 0.0 | 3.32 | $1.9 \cdot 10^{-4}$ | 1.09 | $6.4 \cdot 10^{-5}$ |
| **Sum** | | | | | **3.62** | | **1.27** |

Benzene, $\Delta E_{1CT\text{-}3LE} = -0.095$ eV.

| Dihedral Angle [°] | $\Delta E_{3LE\text{-}1CT}$ [eV] | $\lambda_{1CT\text{-}3LE}$ [eV] | $\mu$ [%] | $\lambda_{solv} = 0.2$ eV | | $\lambda_{solv} = 0.3$ eV | |
|---|---|---|---|---|---|---|---|
| | | | | $k_{1CT\rightarrow 3LE}$ [$10^7$ s$^{-1}$] | $\mu \cdot k_{1CT\rightarrow 3LE}$ [$10^7$ s$^{-1}$] | $k_{1CT\rightarrow 3LE}$ [$10^7$ s$^{-1}$] | $\mu \cdot k_{1CT\rightarrow 3LE}$ [$10^7$ s$^{-1}$] |
| 90 | 0.095 | 0.1796 | 34.1 | 0.092 | 0.0314 | 0.032 | 0.0111 |
| 85 and 95 | 0.099 | 0.1731 | 47.0 | 0.089 | 0.0421 | 0.032 | 0.0149 |
| 80 and 100 | 0.111 | 0.1538 | 16.1 | 0.070 | 0.0113 | 0.025 | $4.1 \cdot 10^{-3}$ |
| 75 and 105 | 0.125 | 0.1281 | 2.6 | 0.061 | $1.6 \cdot 10^{-3}$ | 0.023 | $5.9 \cdot 10^{-4}$ |
| 70 and 110 | 0.137 | 0.1007 | 0.2 | 0.051 | $9.9 \cdot 10^{-5}$ | 0.019 | $3.8 \cdot 10^{-5}$ |
| 65 and 115 | 0.144 | 0.0746 | 0.0 | 0.043 | $2.5 \cdot 10^{-6}$ | 0.017 | $9.9 \cdot 10^{-7}$ |
| **Sum** | | | | | **0.086** | | **0.031** |

**Table S10** continued

Acetone, $\Delta E_{1CT-3LE} = -0.46$ eV.

| Dihedral Angle [°] | $\Delta E_{3LE-1CT}$ [eV] | $\lambda_{1CT-3LE}$ [eV] | $\mu$ [%] | $\lambda_{solv} = 0.2$ eV | | $\lambda_{solv} = 0.3$ eV | |
|---|---|---|---|---|---|---|---|
| | | | | $k_{1CT \to 3LE}$ [$10^7$ s$^{-1}$] | $\mu \cdot k_{1CT \to 3LE}$ [$10^7$ s$^{-1}$] | $k_{1CT \to 3LE}$ [$10^7$ s$^{-1}$] | $\mu \cdot k_{1CT \to 3LE}$ [$10^7$ s$^{-1}$] |
| 90 | 0.460 | 0.1796 | 34.1 | $4.2 \cdot 10^{-7}$ | $1.4 \cdot 10^{-7}$ | $4.4 \cdot 10^{-7}$ | $1.5 \cdot 10^{-7}$ |
| 85 and 95 | 0.464 | 0.1731 | 47.0 | $3.4 \cdot 10^{-7}$ | $1.6 \cdot 10^{-7}$ | $3.8 \cdot 10^{-7}$ | $1.8 \cdot 10^{-7}$ |
| 80 and 100 | 0.476 | 0.1538 | 16.1 | $1.6 \cdot 10^{-7}$ | $2.5 \cdot 10^{-8}$ | $2.1 \cdot 10^{-7}$ | $3.4 \cdot 10^{-8}$ |
| 75 and 105 | 0.490 | 0.1281 | 2.6 | $6.5 \cdot 10^{-8}$ | $1.7 \cdot 10^{-9}$ | $1.1 \cdot 10^{-7}$ | $2.9 \cdot 10^{-9}$ |
| 70 and 110 | 0.502 | 0.1007 | 0.2 | $2.2 \cdot 10^{-8}$ | $4.3 \cdot 10^{-11}$ | $5.5 \cdot 10^{-8}$ | $1.1 \cdot 10^{-10}$ |
| 65 and 115 | 0.509 | 0.0746 | 0.0 | $7.7 \cdot 10^{-9}$ | $4.5 \cdot 10^{-13}$ | $2.9 \cdot 10^{-8}$ | $1.7 \cdot 10^{-12}$ |
| **Sum** | | | | | **$3.3 \cdot 10^{-7}$** | | **$3.6 \cdot 10^{-7}$** |

\* $\mu$ – statistical weight of a rotational isomer in $^1$CT-state at room temperature calculated using relative energies of isomers listed in Table S5.

Summary of the ISC and rISC rates as statistical sums for rotamers calculated according to the Marcus-Hush equation is presented in Table S3.

**References**

[1] Serdiuk, I. E.; Ryoo, C. H.; Kozakiewicz, K.; Mońka, M.; Liberek, B.; Park, S. Y. Twisted Acceptors in the Design of Deep-Blue TADF Emitters: Crucial Role of the Excited-State Relaxation on the Photophysics of Methyl Substituted *s*-Triphenyltriazine Derivatives. *J. Mater. Chem. C* **2020**, *8*, 6052-6062.

[2] Strickler, S. J.; Berg, R. A.. Relationship between absorption intensity and fluorescence lifetime of molecules. *J. Chem. Phys.* **1962**, *37*, 814–822.

[3] Mohanty, J.; Na, W. M. Refractive index effects on the oscillator strength and radiative decay rate of 2,3-diazabicyclo[2.2.2]oct-2-ene. *Photochem. Photobiol. Sci.* **2004**, *3*, 1026–1031.

## [P3]

M. Mońka, I. E. Serdiuk, K. Kozakiewicz, E. Hoffman, J. Szumilas, A. Kubicki, S. Y. Park, P. Bojarski.

Understanding the internal heavy-atom effect on thermally activated delayed fluorescence: application of Arrhenius and Marcus theories for spin–orbit coupling analysis.

## PAPER

Check for updates

# Understanding the internal heavy-atom effect on thermally activated delayed fluorescence: application of Arrhenius and Marcus theories for spin−orbit coupling analysis†

Michał Mońka,[a] Illia E. Serdiuk, ✶[a] Karol Kozakiewicz,[b] Estera Hoffman,[a] Jan Szumilas,[a] Aleksander Kubicki,[a] Soo Young Park [c] and Piotr Bojarski[a]

Hybrid organic emitters containing abundant heavy atoms (HAs) are of rapidly growing interest for organic light emitting diodes (OLEDs) based on thermally activated delayed fluorescence (TADF). As substitutes of expensive and toxic heavy-metals, HAs can accelerate reverse intersystem crossing (rISC), whose low rate is specifically troublesome in blue all-organic TADF materials. Unfortunately, due to complex photophysics even qualitative predictions of the HA effect on organic emitters and hence molecular design are currently very challenging. Here, we report a photoluminescence data analysis approach for investigations of the TADF mechanism based on empirical spin−orbit coupling constants. Using this approach, heavy-halogen derivatives of a popular blue TADF emitter are investigated to understand the mechanism of the HA effect and molecular design fundamentals of high-efficiency TADF materials bearing HAs. Different HA effects on direct and reverse ISC were revealed. We thus conclude that to improve TADF in organic emitters (i) HA should participate in low-energy molecular vibrations which activate rISC between the lowest excited triplet and singlet states of the charge-transfer (CT) character and (ii) ISC should be minimized through a large energy gap between the $^1$CT-state and HA-affected locally-excited ($^3$LE) triplet state.

## Introduction

Pure organic materials with thermally activated delayed fluorescence (TADF) have been extensively investigated recently with an aim to replace heavy-metal complexes in organic light emitting diodes (OLEDs). The tempting prospect of minimization of the use of expensive and toxic rare-earth metals stimulates numerous efforts to develop highly efficient all-organic TADF materials which meet the specific demands of OLED technology.

[a] *Faculty of Mathematics, Physics and Informatics, University of Gdańsk, Wita Stwosza 57, 80-308 Gdańsk, Poland. E-mail: illia.serdiuk@ug.edu.pl; Tel: +48 58 523 22 44*

[b] *Faculty of Chemistry, University of Gdańsk, Wita Stwosza 63, 80-308 Gdańsk, Poland*

[c] *Center for Supramolecular Optoelectronic Materials, Department of Materials Science and Engineering, Seoul National University, 1 Gwanak-ro, Gwanak-gu, Seoul 151-744, Republic of Korea*

† Electronic supplementary information (ESI) available: Synthetic procedures and results of analyzes, description of methods used and procedure for the determination of photophysical parameters; detailed discussion on spectral properties; details of the analysis approach based on Arrhenius and Marcus theories; computational details and theoretical prediction of ISC and rISC rate constants within rotational, vibrational, and rotational-vibronic models; animation file for the key molecular vibrations. See DOI: https://doi.org/10.1039/d2tc00476c

The most demanded here remains the efficient transformation of triplet excitons dominating under electric excitation to the light emission. Since the emission from the triplet state is conditioned by the change of spin, a spin-forbidden process, the rate and efficiency of such emission are usually low, which makes triplet harvesting a challenging task for organic materials.[1,2] Thanks to stable emission color, TADF is regarded as one of the best triplet harvesting approaches. Triplet excitons are converted to the singlet ones *via* reverse intersystem crossing (rISC) and thus light emission always occurs from the $S_1$ state of the emitter (Fig. 1A). Due to the spin-forbidden nature of the $T_1$–$S_1$ transition, the main limitation of TADF is the rISC rate, which depends on the strength of the spin–orbit coupling (SOC). After almost a decade of successful implementation of the first general molecular design strategy of TADF materials for OLEDs,[3] achieving fast rISC in the nanosecond domain as demanded by the OLED technology remains the most challenging issue, especially for the deep-blue emitters. Obviously, our scarce knowledge about the origin, mechanisms and ways of manipulation of SOC in TADF emitters is a serious barrier for further progress in this field.

In light-atom organic materials, SOC is too low to enable fast rISC.[4] The introduction of cheap and abundant heavy atoms

This journal is © The Royal Society of Chemistry 2022

*J. Mater. Chem. C*, 2022, **10**, 7925–7934 | 7925

**Fig. 1** (A) General diagram of triplet exciton utilization *via* rISC, (B) structures of the investigated TADF emitters, (C) steady-state PL of the investigated compounds in ZNX and PMMA, (D) PL decays of investigated compounds, excitation wavelength $\lambda_{exc}$ = 370 nm, (E) PL intensity decay of **H** with evolution of PL onset indicated, and (F) calculated dependence of the $^1$CT-state energy on the dihedral angle $\theta$.

(HAs) into organic TADF emitters seems to be the most obvious and promising way to increase SOC,[5–8] and accelerate rISC, generally referred to as a "heavy-atom effect".[9] Undoubtedly, modification of organic emitters with the heavy atoms of groups 14–17 opens new prospects in the engineering of heavy-metal-free materials for optoelectronics. Unfortunately, at the current state of knowledge, even qualitative prediction of the HA effect on organic TADF emitters is extremely challenging. The attachment of HA at different positions of the emitter can have a different effect on intersystem crossing (ISC), rISC, and other processes, intermolecular interactions and eventually TADF efficiency.

From the point of view of the molecular design of TADF emitters, the idea of introducing HA into organic emitters can be controversial. On the one hand, HA can accelerate rISC and thus help to convert triplet states into excited singlet ones, which is favorable for TADF emitters. On the other hand, HA can accelerate ISC thus leading to the conversion of the emissive $S_1$ state to triplet ones. This is highly undesired for a TADF emitter, as it decreases the amount of singlet excitons in an OLED device which could be deactivated radiatively. The rapidly growing number of publications focusing on such hybrid organic emitters with nonmetallic HAs indicates their complex and non-intuitive effect on TADF.[10–17] On the one

hand, the reports on the increase in rISC rate constant $(k_{rISC})$[10] and even achievement of its record high value of $6 \times 10^7$ s$^{-1}$,[11] shortened lifetimes of delayed fluorescence (DF)[12] and excellent OLED performance with suppressed efficiency roll-off[13] indicate the beneficial role of the HA effect. Some other articles however, indicate its complex nature. For example, several articles report on a strong ISC enhancement and a weaker one for rISC[14] or *vice versa*;[15] some reports conclude negligible HA effect on rISC.[16] Even more surprising is the observation that a TADF emitter with a silicon atom can show an rISC twice as fast as its germanium analogue.[17] Such investigations indicate that HA presence itself does not necessarily warrant rISC acceleration, whilst the demanded selective enhancement of rISC instead of ISC is very challenging.[18] Obviously, none of the literature reports confirm the HA effect in organic emitters to a quantum physical relation derived for atoms: $V \sim Z^4$, where $V$ is a spin–orbit coupling constant and $Z$ is the atomic number.

Taking the above mentioned into account, in this study we aimed to reveal the ways of selective rISC acceleration and define the main principles of molecular design to enable them. To shed light on the complex processes covered by the term "heavy-atom effect", we performed thorough analysis of the electronic properties and spin–flip mechanisms in a series of (deep)-blue TADF emitters. Chlorine and bromine derivatives of

**7926** | *J. Mater. Chem. C*, 2022, **10**, 7925–7934

This journal is © The Royal Society of Chemistry 2022

a widely studied emitter 9,10-dihydro-9,9-dimethyl-10-(4-(4,6-diphenyl-1,3,5-triazin-2-yl)phenyl)-acridine (DMAC-TRZ, Fig. 1B) were selected after explanation of its photophysics.[19] To focus on the internal HA effect and distinguish it from the external one, methyl groups were introduced to the side rings of an acceptor fragment which minimized the emitter-emitter intermolecular interactions.[20] Temperature and polarity dependent photophysical investigations analyzed within Arrhenius and Marcus theories enabled estimation of SOC, energy gaps and reorganization energies using experimental data. It was found that due to different mechanisms of ISC and rISC, the HA effect manifests in different ways. Whilst ISC is accelerated up to 8 times due to the enhanced SOC between the states of different nature, rISC can be accelerated less than 3 times via vibronic activation of SOC between the states of the same nature. The presented results reveal that introduction of HA can improve TADF in the case of (i) effective activation of specific molecular vibrations involved in rISC and (ii) lack of ISC acceleration to localized triplet states.

# Experimental section

## Materials

Zeonex® (ZNX, Zeonex480R, density = 1.01 g cm$^{-3}$) or poly-methyl methacrylate (PMMA, 120000 Mw, density = 1.18 g cm$^{-3}$) were purchased from Zeon Europe GmbH and Sigma-Aldrich, respectively. Solvents for the synthesis and spectroscopic measurements were of corresponding grades and were used as supplied.

## Synthesis of emitters, isolated donor, and acceptor molecules

10-(4-(4,6-Bis(2-methylphenyl)-1,3,5-triazin-2-yl)phenyl)-9,9-dimethyl-9,10-dihydroacridine (**H**) was synthesized as described previously.[20]

## Typical halogenation procedure

0.1 mmol of **H** or 9,9-dimethyl-10-phenyl-9,10-dihydroacridine and 0.22 mmol N-chlorosuccinimide (for **diCl** and **diCl-DMAC**) or N-bromosuccinimide (for **diBr** and **diBr-DMAC**) were dissolved in 0.5 mL of chloroform and stirred at 55 °C for 12 h in the dark. $\frac{3}{4}$ of the solvent was evaporated and the residue was treated with methanol. The resulting precipitate was collected and purified using column chromatography on SiO$_2$ with appropriate hexane-chloroform mixtures as eluents.

## 10-(4-(4,6-Bis(2-methylphenyl)-1,3,5-triazin-2-yl)phenyl)-2,7-dichloro-9,9-dimethyl-9,10-dihydro-acridine (diCl)

Pale yellow powder, yield 87%. $^1$H NMR (500 MHz, CDCl$_3$, δ): 1.67 (s, 6H) 2.87 (s, 6H), 6.28 (d, J = 8.80 Hz, 2H), 6.94 (d, J = 8.07 Hz, 2H), 7.34–7.64 (m, 10H), 8.31–8.34 (m, 2H), 8.94 (d, J = 7.70 Hz, 2H). $^{13}$C NMR (250 MHz, CDCl$_3$, δ): 174.47, 170.01, 139.09, 139.05, 135.87, 131.98, 131.79, 131.38, 131.33, 131.26, 131.20, 126.49, 126.20, 126.18, 125.32, 115.45, 36.43, 30.86, 22.48. MALDI-TOF m/z: calcd for C$_{38}$H$_{30}$Cl$_2$N$_4$, 613.2 [M + H]$^+$; found, 613.4. For $^1$H and $^{13}$C NMR spectra see the ESI† (Fig. S1 and S2).

## 10-(4-(4,6-Bis(2-methylphenyl)-1,3,5-triazin-2-yl)phenyl)-2,7-dibromo-9,9-dimethyl-9,10-dihydro-acridine (diBr)

Pale yellow powder, yield 91%. $^1$H NMR (500 MHz, CDCl$_3$, δ): 1.67 (s, 6H), 2.87 (s, 6H), 6.22 (d, J = 8.69 Hz, 2H), 7.08 (dd, J = 8.69, 2.27 Hz, 2H), 7.40 (t, J = 7.55 Hz, 4H), 7.44–7.51 (m, 4H), 7.53 (d, J = 2.27 Hz, 2H), 8.29–8.35 (m, 2H), 8.94 (d, J = 8.69 Hz, 2H). $^{13}$C NMR (250 MHz, CDCl$_3$, δ): 174.47, 169.99, 144.35, 139.44, 139.09, 136.73, 135.86, 131.97, 131.85, 131.80, 131.33, 131.23, 131.20, 129.41, 128.19, 126.18, 115.91, 113.67, 36.35, 30.94, 22.47. MALDI-TOF m/z: calcd for C$_{38}$H$_{30}$Br$_2$N$_4$, 701.1 [M + H]$^+$; found, 701.2. For $^1$H and $^{13}$C NMR spectra see the ESI† (Fig. S3 and S4).

## 2,7-Dichloro-9,9-dimethyl-10-phenyl-9,10-dihydroacridine (diCl-DMAC)

White powder, yield 69%. $^1$H NMR (500 MHz, CDCl$_3$, δ): 1.67 (s, 6H) 6.21 (d, J = 8.79 Hz, 2H) 6.94 (dd, J = 8.92, 2.06 Hz, 2H) 7.31 (d, J = 7.14 Hz, 2H) 7.40 (d, J = 2.20 Hz, 2H) 7.53–7.58 (m, 1H) 7.64–7.68 (m, 2H) MALDI-TOF m/z: calcd for C$_{21}$H$_{17}$Cl$_2$N, 338.0 [M-CH$_3$]$^+$; found, 338.2.

## 2,7-Dibromo-9,9-dimethyl-10-(4-methylphenyl)-9,10-dihydroacridine (diBr-DMAC)

White powder, yield 78%. $^1$H NMR (500 MHz, CDCl$_3$, δ): 1.66 (s, 6H) 2.50 (s, 3H) 6.18 (d, J = 8.79 Hz, 2H) 7.07 (dd, J = 8.92, 2.33 Hz, 2H) 7.17 (d, J = 8.24 Hz, 2H) 7.44 (d, J = 7.96 Hz, 2H) 7.51 (d, J = 2.20 Hz, 2H) MALDI-TOF m/z: calcd for C$_{22}$H$_{19}$Br$_2$N, 442.2 [M-CH$_3$]$^+$; found, 442.0.

## 9,9-Dimethyl-10-phenyl-9,10-dihydroacridine

A mixture of 9,9-dimethyl-9,10-dihydroacridine (1 mmol, 209 mg), iodobenzene (1 mmol, 204 mg), tris(dibenzylideneacetone) dipalladium(0) (0.05 mmol, 46 mg) and tri-tert-butylphosphonium tetrafluoroborate (0.1 mmol, 29 mg) was dissolved in 15 ml of dry toluene under an argon atmosphere. Potassium tert-butoxide (1.5 mmol, 168 mg) was added and the mixture was stirred at 100 °C overnight. The solvent was removed under vacuum, and the dry residue was dissolved in dichloromethane and washed with water. Crude compound was purified by column chromatography using a mixture of dichloromethane and hexane (1 : 9). White powder, yield 72%. $^1$H NMR (500 MHz, CDCl$_3$, δ): 1.72 (s, 6H), 6.28 (d, J = 7.96 Hz, 2H), 6.93–7.01 (m, 4H), 7.36 (d, J = 7.41 Hz, 2H), 7.48 (d, J = 7.41 Hz, 2H), 7.51–7.55 (m, 1H), 7.62–7.67 (m, 2H). MALDI-TOF m/z: calcd for C$_{21}$H$_{19}$N, 270.3 [M-CH$_3$]$^+$; found, 270.1.

## 9,9-Dimethyl-10-(4-methylphenyl)-9,10-dihydroacridine

Was synthesized using 4-iodotoluene using the same protocol as for 9,9-dimethyl-10-phenyl-9,10-dihydroacridine. White crystalline powder, yield 88%. $^1$H NMR (500 MHz, CDCl$_3$, δ): 1.68 (s, 6H), 2.48 (s, 3H), 6.28 (d, J = 8.24 Hz, 2H), 6.87–6.93 (m, 2H), 6.95 (dt, J = 8.39, 1.45 Hz, 2H), 7.20 (dd, J = 8.09, 1.37 Hz, 2H), 7.39–7.46 (m, 4H). MALDI-TOF m/z: calcd for C$_{22}$H$_{21}$N, 300.4 [M + H]$^+$; found, 300.2.

## 2,4-Bis(2-methylphenyl)-6-phenyl-1,3,5-triazine

2-Methylbenzamidine hydrochloride (11 mmol) and potassium tert-butoxide (10.8 mmol) were mixed in DMSO and stirred at

This journal is © The Royal Society of Chemistry 2022

J. Mater. Chem. C, 2022, **10**, 7925–7934 | **7927**

RT for 30 min. Benzaldehyde (5 mmol) was added and the mixture was stirred at 100 °C for 12h. After cooling to RT, 2,3-dichloro-5,6-dicyano-p-benzoquinone (5 mmol) was added and the mixture was stirred at 50 °C for another hour. 50% aqueous methanol was added and the precipitate was collected by filtration. Column chromatography using 50% CHCl$_3$ in hexane afforded the pure title compound. White powder, yield 75%. $^1$H-NMR (300 MHz, CDCl$_3$, $\delta$): 2.84 (s, 6H), 7.35–7.41 (m, 4H), 7.42–7.47 (m, 2H), 7.53–7.57 (m, 2H), 7.58–7.61 (m, 1H), 8.28 (d, $J$ = 7.63 Hz, 2H), 8.68 (s, 2H). MALDI-TOF $m/z$: calcd for C$_{38}$H$_{30}$Cl$_2$N$_4$, 338.2 [M + H]$^+$; found, 338.2.

### Sample preparation for photophysical measurements

Stock solutions of **H**, **diCl** and **diBr** in dichloromethane were added to Zeonex or PMMA solutions in toluene and dichloromethane solutions to obtain homogeneous mixtures, which were used for film preparation. The films were prepared by drop cast deposition on warm quartz plates, and left in the dark for 5h to enable evaporation of solvents. The final mass fraction of emitters dispersed in polymers was *ca.* 1%.

### Photoluminescence measurements

UV-Vis absorption spectra were recorded using a Shimadzu UV-1900 spectrophotometer. Steady-state photoluminescence spectra were recorded using a Varian Cary Eclipse spectrofluorometer using front-face excitation geometry. The PL quantum yield (PLQY) was measured using an integrating sphere (Quantaurus C11347-11, Hamamatsu). Time-resolved measurements were performed at different temperatures using a customized system[21] consisting of a pulsed YAG:Nd laser (PL2251A, EKSPLA) coupled with an optical parametric generator (PG 401/SH) as an excitation light source and 2501S grating spectrometer (Bruker Optics) combined with the streak camera system (C4334-01 Hamamatsu) as a detection unit. The system was equipped with a double-stage high vacuum pump (T-Station 85 Edwards) coupled with a closed-cycle helium cryostat (APD DE-202) and a temperature controller (LakeShore 336). To reduce scattering, reflections and secondary order artifacts, a set of various high performance optical bandpass (BP) and longpass (LP) filters were used: in the excitation path 325/50BP or 375/50BP (CWL/FWHM), depending on the selected excitation wavelength, together with LP filters: 375LP or 350LP (Edmund Optics). In order to build PL intensity decay profiles, streak camera images were integrated over a constant wavelength interval (460–490 nm for ZNX and 475–515 nm for PMMA samples).

### Quantum chemical calculations

Quantum chemical calculations were conducted at the DFT/TD-DFT level of theory using the Gaussian 16 program package.[22] The B3LYP functional[23] was used with the LAN2LDZ basis set. Firstly, for each compound, unconstrained geometry optimizations were performed for the ground (S$_0$), excited singlet (S$_1$) and excited triplet electronic states (T$_1$, T$_2$, T$_3$). Convergence of all geometry optimizations was verified by the vibrational analysis: no negative frequencies were observed, therefore calculated

minima correspond to the "true" stationary points. The nature of the electronic excited states was determined by the analysis of molecular orbitals. Spin–orbit coupling constants were computed using the ORCA 4.2 software[24] package with the B3LYP functional, and the DEF2-TZVP basis set with included relativistic zero-order regular approximaion (ZORA).

## Results and discussion

### Synthesis

**diCl** and **diBr** were synthesized *via* efficient and simple halogenation of **H** using *N*-chlorosuccinimide and *N*-bromosuccinimide, respectively, as shown in Scheme 1. The isolation yields were close to 90%.

### Photoluminescence and excited-state alignment

The investigations of the TADF mechanism start with the analysis of the spectral features of the compounds and alignment of their lowest excited-states. The absorption spectra of the investigated compounds measured in solutions are very similar (Fig. S5, ESI†). Minor changes can be noticed at the long-wavelength band corresponding to the CT transition. The blue shift of the absorption maximum from 379 nm (**H**) to 373 nm is observed for **diCl** and to 375 nm for **diBr**. All compounds show deep-blue and sky-blue photoluminescence (PL) in nonpolar Zeonex® (ZNX) and more polar PMMA films, respectively (Table 1, Fig. 1C and Fig. S6, ESI†). Positive solvatochromism evidences a large change in the dipole moment during the S$_1$–S$_0$ transition and charge-transfer (CT) character of the S$_1$-state, like in DMAC-TRZ and other TADF emitters of D–A structure. The blue-shifted emission of **diCl** relative to **H** is the result of the negative inductive effect of chlorine atoms which decreases the donor strength and thus increases the $^1$CT energy. Interestingly, in **diBr** this effect is almost negligible. Taking into account a similar trend in the absorption spectra, one can conclude that in such large π-systems, the electronic effect of bromine on the S$_0$–$^1$CT transition is lower than that of chlorine. The PL quantum yields (PLQYs) are the highest for **H** (99%) and **diCl** (85%) in PMMA, whereas the respective value for **diBr** is lower (Table 1).

Time-resolved emission spectra (TRES) reveal that the "$^1$CT-state" is a continuous energy band rather than a single-energy level (Fig. 1D and Fig. S7–S11, ESI†). In PMMA films, broadened steady-state emission spectra are the result of spectral shifts at different time delays due to coexistence of various
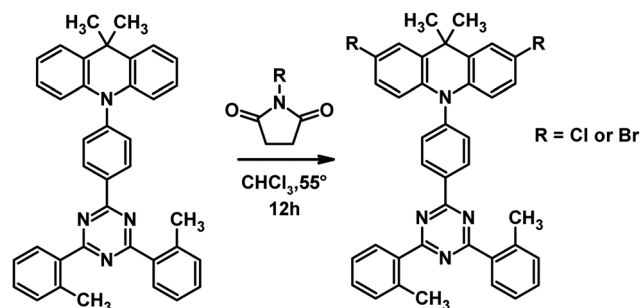


**Scheme 1** Synthesis of **diCl** and **diBr** emitters.

**7928** | *J. Mater. Chem. C*, 2022, **10**, 7925–7934

This journal is © The Royal Society of Chemistry 2022

**Table 1** Steady-state and kinetic PL parameters of the investigated TADF compounds

| Cmpd | Medium | PLQY[a] [%] | PL[b] $\lambda_{max}$ [nm] | $\Delta E_{1CT-3LE(A)}$[c] [meV] | $\Delta E_{1CT-3CT}$[c] [meV] | $\Delta E_{1CT-3LE(D)}$[c] [meV] | $\tau_{PF}$[d] [ns] | $\tau_{DF}$[d] [μs] | $k_{ISC}$[d] [s$^{-1}$ 10$^7$] | $k_{rISC}$[d] [s$^{-1}$ 10$^4$] |
|------|--------|-------|-------|-------|-------|-------|-------|-------|-------|-------|
| **H** | ZNX | 60 | 465 | 94 | — | −230 | 15.3 | 171 | 5.1 | 1.03 |
| **diCl** | | 75 | 462 | 133 | — | −55 | 13.1 | 333 | 6.1 | 0.87 |
| **diBr** | | 12 | 467 | 114 | — | −55 | 2.2 | 104 | 38.5 | 1.74 |
| **H** | PMMA | 99 | 498 | 46 | 85 | −278 | 17.1 | 96 | 3.8 | 2.92 |
| **diCl** | | 85 | 492 | 72 | 95 | −116 | 16.0 | 139 | 4.1 | 1.85 |
| **diBr** | | 21 | 499 | 60 | 86 | −109 | 2.8 | 38 | 30.8 | 8.23 |

[a] Values measured using integrating sphere and corrected for vacuum conditions (for the details see the ESI – Table S1). [b] Determined from steady-state photoluminescence measurement at 298 K (Fig. S6 and Table S1, ESI). [c] Determined from the difference of respective onsets of PL spectra, according to the general equation: $\Delta E_{1-2} = (1240/\lambda_{onset1} - 1240/\lambda_{onset2})$, onset values presented in Table S1 (ESI). [d] All of presented photophysical parameters ($\tau_{PF}$, $\tau_{DF}$, $k_{ISC}$ and $k_{rISC}$) were calculated from the PL intensity decay profiles (Fig. S8A and S9A, ESI) measured at 298 K under a vacuum. A detailed procedure of the calculations of photophysical parameters is included in the ESI – Section S3).

rotameric species with different dihedral angles between donor and acceptor units ($\theta$, Fig. 1B). Such rotamers play a key role in the TADF photophysics,[19,25–28] as the $^1$CT-state energy and $^3$CT–$^1$CT energy gap ($\Delta E_{1CT-3CT}$) are dependent on the $\theta$ value. Such $\theta$-rotamers with high deviation from the optimal 90° value and high $^1$CT-energy emit in the blue region in the very early prompt

fluorescence (PF) region and late DF, whereas $\theta$-rotamers close to 90° correspond to low $^1$CT-energy, late-PF and early-DF emissions (Fig. 1E). The $^1$CT energy thus deviates from 2.96 to 2.81 eV (**H**) (Fig. 1F and Table S1, ESI†) and 2.98 to 2.82 eV (**diCl, diBr**). Similar, but less pronounced dependences are observed for ZNX films (discussed in the ESI† – Section S2).
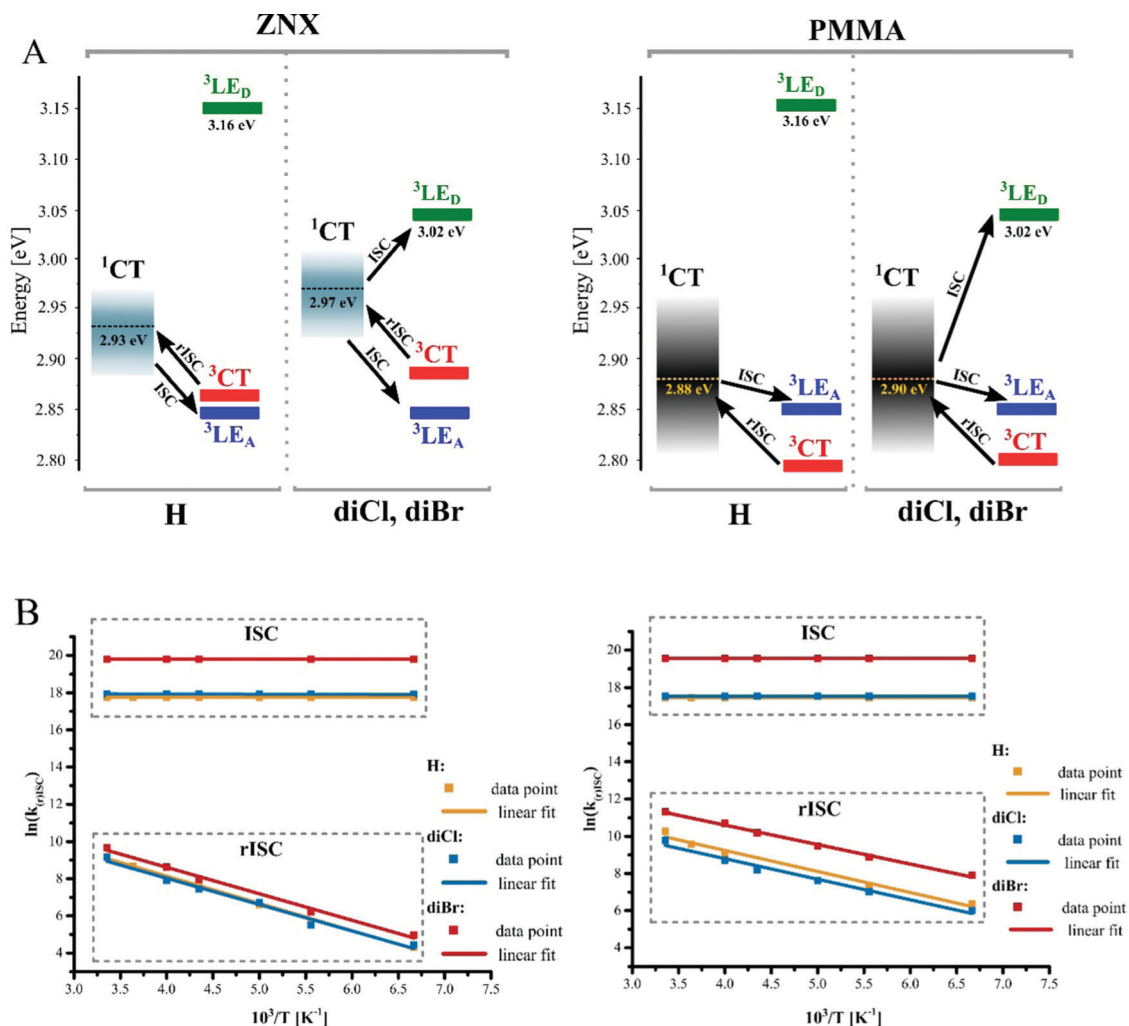


**Fig. 2** (A) The excited-state alignment and dominating spin–flip pathways. (B) Arrhenius plots derived from temperature-dependent time-resolved measurements in ZNX (left) and PMMA (right) taken in the 298–150 K range.

Thorough analysis of TRES at low temperatures reveals that different triplet states are responsible for the phosphorescence in different media. In ZNX, the vibronic structure of the phosphorescence spectrum differs from that of fluorescence, but matches perfectly the phosphorescence of an isolated acceptor (Fig. S6G, ESI†).[29] This suggests that the $T_1$ state is localized on the acceptor fragment, the $^3$LE(A)-state. Its estimated energy is 2.84 eV, similar to that in **DMAC-TRZ**.[27] In PMMA, the phosphorescence is different from the $^3$LE(A) one, but similar to fluorescence, and thus $^3$CT becomes the lowest triplet state (Fig. S6D–F, ESI†). In contrast to $^1$CT, the $^3$CT-emission onset is relatively constant, thus $^3$CT is a single-energy level of 2.80 eV (**H**) and 2.81 eV (**diCl**, **diBr**, see the phosphorescence spectra depicted in Fig. S6D–F and S11A–C, ESI†). The energy of the third triplet state localized on the donor fragment ($^3$LE(D)) was estimated from the phosphorescence of free donor molecules (Fig. S6H, ESI†). Thus the estimated $^3$LE(D)-energy is affected by halogen atoms, decreasing from 3.16 eV (**H**) to 3.02 and 3.01 eV in **diCl** and **diBr**, respectively.

The alignment of the excited states presented in Fig. 2A summarizes the discussion of spectral properties. In view of the TADF mechanism and HA effect, singlet–triplet energy gaps ($\Delta E_{1CT-Ti}$) are discussed further. Minimal, maximal, and statistical mean energy gaps (Tables S2, S3 and Fig. S10, S11, ESI†) reveal the macroscopic diversity of molecular electronic systems due to the distribution of $^1$CT-state energies. As the $^3$LE(A)-state is negligibly affected by the halogens, $\Delta E_{1CT-3LE(A)}$ varies similarly for all the emitters: in ZNX, from +0.06 to +0.15 eV with a mean value of *ca.* +0.10 eV; and in PMMA, from slightly negative to +0.14 eV with a mean value of *ca.* +0.05 eV (Table 1). The $^1$CT–$^3$CT energy difference estimated for the PMMA medium is also very similar for **H** and **diBr**, varying from 6.3 meV to 0.16 eV with the mean value of 85 meV; in **diCl** bearing the weakest donor fragment, the CT states are slightly more distanced (Table 1 and Table S1, ESI†). Therefore, the alignment of $S_1$, $T_1$, and $T_2$ states is generally similar for studied compounds. The distinguished electronic feature of halogenated emitters is the $^3$LE(D)-state being closer to $^1$CT. The lowest mean $\Delta E_{1CT-3LE(D)}$ values are in the ZNX films: −0.23 eV (**H**) and −0.055 eV (**diCl**, **diBr**); in PMMA, they increase to −0.28 eV and −0.11, respectively.

**Photoluminescence decays**

The kinetics of emission decay and its strong temperature dependence unambiguously proves the TADF property of the investigated emitters, as discussed in detail in the ESI.† Well-distinguished time domains of PF and DF decays exhibit different sensitivity to the HA effect (Fig. 1D, and Fig. S8A, S9A, ESI†). Introduction of chlorine and especially bromine atoms leads to the shortening of PF lifetime, because the ISC rate constant ($k_{ISC}$) increases up to 1.2 and 8.1 times, respectively (Table 1). The situation is more complex in the case of the DF lifetime, as it is almost twice longer in **diCl**, but three times shorter in **diBr** compared to **H**. The rISC rate constant ($k_{rISC}$) thus decreases in **diCl**, but increases almost three times in **diBr** in the PMMA films. At this point one can notice that only bromine accelerates both types of intersystem crossing transitions,

however it affects ISC more than rISC. This versatile effect of HA is analyzed further using experimental and computational approaches.

**Arrhenius and Marcus theories applied to the SOC analysis**

Looking for the analysis approach which could help to reveal the TADF mechanism in emitters with complex photophysics, we found that the combination Arrhenius law[30] (1) and Marcus–Hush eqn (2) can be a powerful tool for investigations of spin-flip processes.[31] Transformation of (1) and (2) provides valuable relationships (3, 4):

$$k_{(r)ISC} = A \cdot \exp\left(-\frac{E_a}{k_B T}\right), \tag{1}$$

$$k_{(r)ISC} = \frac{V^2}{\hbar}\sqrt{\frac{\pi}{k_B T \lambda}}\exp\left[-\frac{(\Delta E_{ST} + \lambda)^2}{4k_B T \lambda}\right], \tag{2}$$

$$A = \frac{V^2}{\hbar}\sqrt{\frac{\pi}{k_B T \lambda}}, \tag{3}$$

$$E_a = \frac{(\Delta E_{ST} + \lambda)^2}{4\lambda}, \tag{4}$$

where $A$ is the preexponential factor, $E_a$ is the activation energy, $V$ is the SOC constant, $\hbar$ is the reduced Planck constant, $\lambda$ is the sum of internal and external ($\lambda_{solv}$) reorganization energies for the respective transition, and $\Delta E_{ST}$ is the energy gap between singlet $^1$CT and the respective triplet state. First, the $k_{ISC}(1/T)$ and $k_{rISC}(1/T)$ dependencies are analyzed according to the Arrhenius law (Fig. 2B, and Section S4, Fig. S13–S15, Tables S5 and S6, ESI†). This enables two types of experimental data: (i) A from which SOC constants $V$ can be extracted and (ii) $E_a$ comprised of $\Delta E_{ST}$ and $\lambda$. Importantly, thus obtained $V$ values can be compared to those computed for various spin-flip channels and reveal the TADF mechanism. Within such an approach we discuss ISC and rISC separately and analyze the HA effect on each process.

**ISC**

In the investigated compounds, ISC is a barrierless process ($E_a = 0$), which indicates that (i) according to eqn (4), the $S_1$–$T_1$ reorganization energy is equal to the energy gap and (ii) according to eqn (2), $k_{ISC}$ is defined by the SOC constant. $V_{ISC}$ increases from 0.29 (**H**) and 0.31 (**diCl**) to 0.76 cm$^{-1}$ (**diBr**) (Table 2). Such an order of magnitude indicates that ISC occurs *via* a transition or a couple of transitions, so-called as "allowed by El-Sayed rules".[32] The ISC mechanism should thus involve excited states of different nature: $^1$CT and $^3$LE. In **H**, the key ISC channel is the $^1$CT → $^3$LE(A) transition due to the close energy of the respective states and well-matching computed $V_{1CT\to3LE(A)}$ and experimental $V_{ISC}$ values (Table 2 and Table S7, ESI†). In the halogenated derivatives, the rates of $^1$CT → $^3$LE(A) transition remain similar because of an identical $\Delta E_{1CT-3LE(A)}$. In fact, the calculations indicate the absence of the HA effect on this transition as neither Cl nor Br increase its SOC (see the ESI† – Section 5, Table S7).

**7930** | *J. Mater. Chem. C*, 2022, **10**, 7925–7934

This journal is © The Royal Society of Chemistry 2022

**Table 2** Photophysical parameters of the investigated TADF compounds derived from Arrhenius and Marcus–Hush equations

| Cmpd | Process | Arrhenius eqn (1) | | | Marcus–Hush eqn (2) | | | | |
|---|---|---|---|---|---|---|---|---|---|
| | | $A$ [s$^{-1}$ 10$^7$] | $E_a$ [meV] | $\sqrt{A_{hal}/A_H}$ | $\Delta E_{ST}$ [meV] | $\lambda$ [meV] | $E_a$ [meV] | $V$ [cm$^{-1}$] | $V_{hal}/V_H$ |
| **ZNX** | | | | | | | | | |
| **H** | ISC | 5.09 | 0 | | −122 | 122 | 0 | 0.29 | |
| **diCl** | | 6.12 | 0 | 1.1 | −127 | 127 | 0 | 0.31 | 1.0 |
| **diBr** | | 38.43 | 0 | 2.9 | −125 | 125 | 0 | 0.76 | 2.6 |
| **H** | rISC | 0.12 | 124 | | 122 | 122 | 122 | 0.05 | |
| **diCl** | | 0.09 | 127 | 0.9 | 127 | 127 | 127 | 0.04 | 0.8 |
| **diBr** | | 0.16 | 126 | 1.2 | 125 | 125 | 125 | 0.05 | 1.1 |
| **PMMA** | | | | | | | | | |
| **H** | ISC | 3.83 | 0 | | −93 | 93 | 0 | 0.29 | |
| **diCl** | | 4.11 | 0 | 1.0 | −97 | 97 | 0 | 0.30 | 1.0 |
| **diBr** | | 30.85 | 0 | 2.8 | −94 | 94 | 0 | 0.76 | 2.5 |
| **H** | rISC | 0.09 | 98 | | 93 | 93 | 93 | 0.05 | |
| **diCl** | | 0.06 | 95 | 0.8 | 97 | 97 | 97 | 0.04 | 0.8 |
| **diBr** | | 0.26 | 92 | 1.7 | 94 | 94 | 94 | 0.07 | 1.5 |

The observed strong HA effect on ISC correlates with the $^1$CT–$^3$LE(D) energy gaps. As compared to PMMA, the decrease of $|\Delta E_{1CT-3LE(D)}|$ in ZNX films leads to the increase of $k_{ISC}$. Theoretical calculations support this conclusion: the predicted SOC constants and rates of the $^1$CT → $^3$LE(D) transition evidence its sufficient role in **diCl** and **diBr** (Table S8, ESI†). For example, in PMMA films, the mean $k_{1CT-3LE(D)}$ increases drastically from $2.5 \times 10^3$ s$^{-1}$ (**H**) to $1.8 \times 10^6$ s$^{-1}$ (**diCl**) and $1.8 \times 10^7$ s$^{-1}$ (**diBr**). Regarding the $^1$CT-energy distribution, in **diBr** species with minimal $\Delta E_{1CT-3LE(D)}$, the maximal $k_{1CT-3LE(D)}$ value exceeds $1.5 \times 10^8$ s$^{-1}$ (Table S8, ESI†). The HA effect on ISC is thus realized mainly via $^3$LE(D)-state influenced directly by the heavy halogens (Table S9, ESI†). From the point of view of TADF efficiency, one can conclude the energetic closeness of the HA-affected $^3$LE state to the $^1$CT one and it is a negative factor, as it leads to strong acceleration of ISC.

**rISC**

A similar approach applied for rISC reveals that for all three compounds, thermal activation $E_a$ is roughly constant (Table 2). According to eqn (4), this indicates that neither Cl nor Br change the energy gap or reorganization energy for rISC. As compared to ZNX, in PMMA films, $E_a$ decreases by 30 meV from ca. 125 to 95 meV (Table 2). The SOC constant $V_{rISC}$ is significantly lower than that for ISC: in **diBr**, the HA effect is more than 2 times higher for ISC than for rISC ($V_{hal}/V_H$, Table 2). Together with unexpected $V_{rISC}$ decrease in **diCl**, these observations indicate different mechanisms for ISC and rISC.

In **H**, $V_{rISC}$ does not exceed 0.05 cm$^{-1}$ evidencing a dominating role of the "forbidden" channel: the $^3$CT → $^1$CT transition. Similarly the low $V_{rISC}$ of the halogenated derivatives indicate that neither the $^3$LE(D) nor $^3$LE(A) state contribute significantly to rISC. Despite the strong HA effect on the calculated $V_{3LE(D)-1CT}$, in ZNX, where $^3$LE(D) is closer to $^1$CT (Table 1 and Table S1, ESI†), **diBr** exhibits a lower experimental $V_{rISC}$ value than in PMMA. This indicates the insignificant role of the $^3$LE(D)-state in rISC due to its almost negligible population (Fig. 2A, Fig. S16 and Tables S10 and S11, ESI†). Neither the $^3$LE(A) → $^1$CT transition contributes noticeably, because the calculated rate constants and SOC of the

$^3$LE(A) → $^1$CT transition decrease in the row **diCl** – **H** ≈ **diBr** (Table S11, ESI†), which is not the case for $V_{rISC}$. Moreover, due to the large reorganization energies, $k_{3LE(A)→1CT}$ should exhibit much sharper temperature dependence than the experimental one (Fig. S14 and S15, ESI†).

The above-mentioned analysis indicates that rISC occurs mainly via the $^3$CT → $^1$CT transition. The analysis of molecular vibrations and inhomogeneity reveals why the effect of heavy halogens on the $^3$CT → $^1$CT spin–flip is so peculiar. Within our previously developed TADF model, in DMAC-TRZ,[19] the $^3$CT → $^1$CT transition is efficient in rotamers with various $\theta$-deviation due to non-zero SOC, low energy gap and reorganization energy. Surprisingly, in $\theta$-rotamers, the increase in the atomic number of the substituent results in the decrease of SOC (Fig. 3C). As a consequence, the rotational model predicts that the statistical sum of the $^3$CT → $^1$CT transition rate constants ($k_{3CT→1CT}$) for all $\theta$-rotamers decreases in the row **H–diCl–diBr** (see the ESI† – Section S6, Fig. 3B, 4 and Fig. S17–S19, Tables S12–S14). Interestingly, this correlates with the observed rISC inhibition in **diCl**, but contradicts the rISC acceleration in **diBr**.

The analysis of vibrational modes explains this discrepancy. In the case of the most stable 90°-rotamer, the $k_{3CT-1CT}$ values calculated taking into account eight lowest vibrational modes ($\omega_1$–$\omega_8$, see the ESI† – Section S7, Fig. 3A and Fig. S20–S25, Tables S15–S18, and the supporting animation file) follow the experimental trend of $k_{rISC}$ (Fig. 4). Thus the calculated rISC rates are underestimated, because other rotamers are not taken into account. The complete TADF model should thus combine rotational and vibronic models via vibrational SOC analysis for all $\theta$-rotamers, which unfortunately requires expensive and time-consuming computations. Assuming that vibrational SOC enhancement in all rotamers is similar to the 90°-rotamer, the rotational model was completed by the correction on vibrations (see the ESI† – Section S8). Thus the obtained corrected $k_{3CT-1CT}$ values better matched the experimental ones (Fig. 4 and Table S19).

Positive verification of such a rotational-vibronic model enables the analysis of key vibronic modes for rISC. In **H**, the $\omega_1$ mode leading to the $\theta$-deviation is almost exclusive $^3$CT → $^1$CT channel (Fig. 3A). This supports our previous findings, that
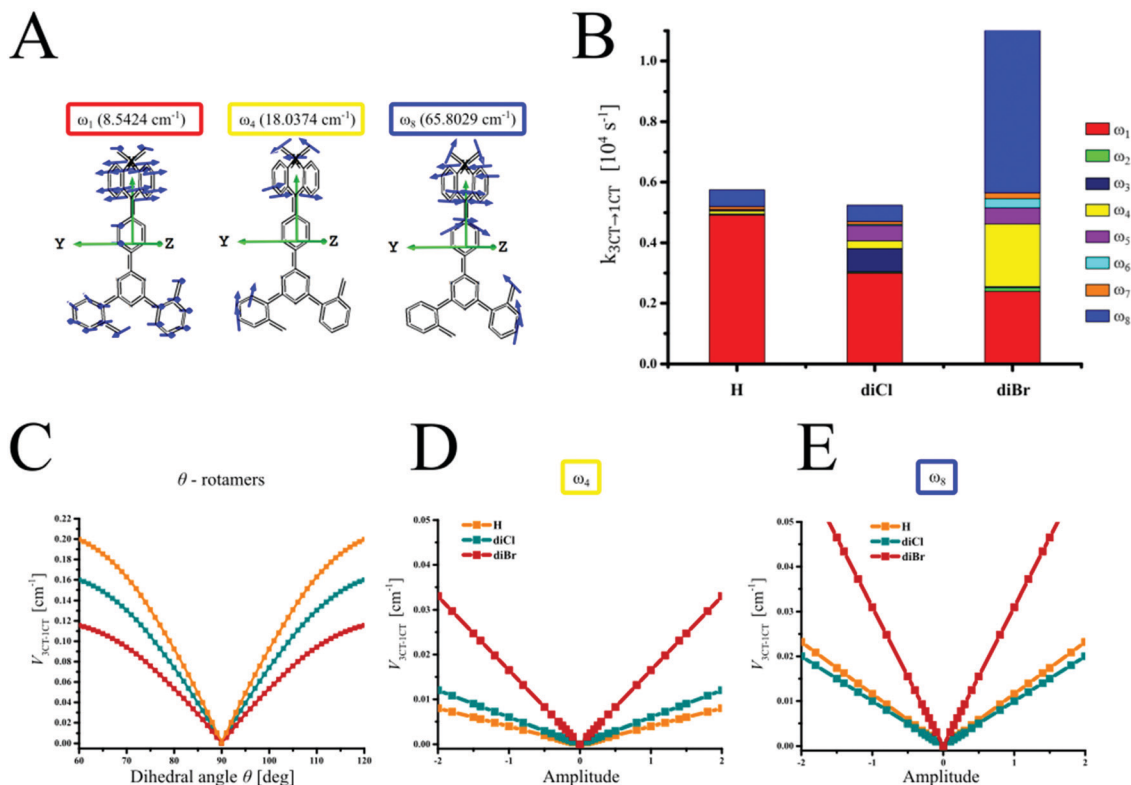
Fig. 3  The most important vibrational modes for SOC enhancement (A), contributions of low-energy vibrational modes to rISC (B), and dependence of $^3CT \rightarrow {}^1CT$ SOC constants on their amplitudes (C–E).
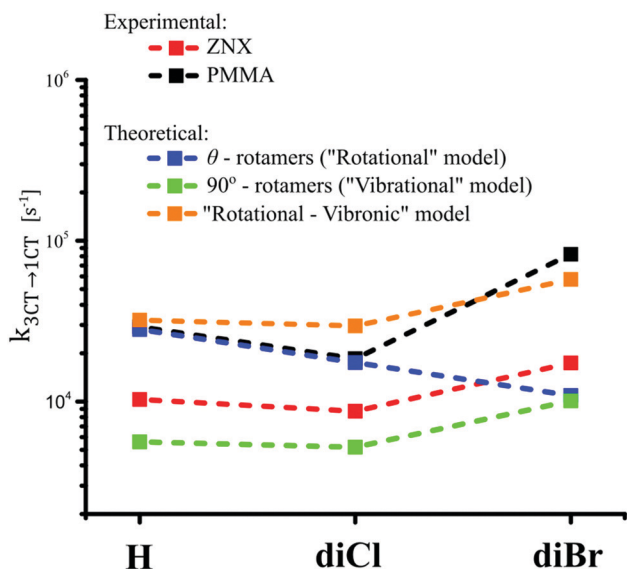


Fig. 4  Comparison of the experimental and model rISC values (see Table S19, ESI†).

in the orthogonal TADF emitters without heavy atoms, rISC *via* $^3CT \rightarrow {}^1CT$ transition is correctly predicted by the $\theta$-rotamer model which takes into account only relative rotations of the D and A fragments.[19] In **diCl** and **diBr**, however, $k_{3CT \rightarrow 1CT}$ realized *via* the $\omega_1$ mode decreases down to 1.6 and 2.0 times,

respectively (Fig. 3B). In **diBr**, the enhanced rISC is due to the activated $\omega_4$ and $\omega_8$ channels of the $^3CT \rightarrow {}^1CT$ transition. The $\omega_4$ and $\omega_8$ modes distort the planarity of the donor, causing motions of bromine atoms and SOC enhancement up to three times (Fig. 3A–E). As a result, **diBr** gains a four-fold increase of $k_{3CT \rightarrow 1CT}$ initially activated by $\omega_1$. For **diCl**, the $\omega_{3-5}$ and $\omega_8$ modes also activate SOC but their contribution to $k_{3CT \rightarrow 1CT}$ is only 40%.

The activation of $\omega_4$ and $\omega_8$ vibronic rISC channels in **diBr** indicate the importance of the position of HA in the emitter. Obviously, HA should be involved in the low-energy vibrations to increase $V_{3CT \rightarrow 1CT}$. On the other hand, **diCl** serves as an example of an unfortunate decrease of SOC *via* $\omega_1$ and weak compensation from other vibrations resulting in the rISC inhibition.

## Conclusions

In summary, using heavy-halogen derivatives of the DMAC-TRZ emitter, we verified an approach for the photoluminescence data analysis within Arrhenius and Marcus theories to explain the heavy-atom effect on blue TADF materials. Such an approach provides experimental electronic data on spin–flip transitions, among which spin–orbit coupling constants are especially helpful for the analysis of the TADF mechanism.

Triplet states of the LE character play an important role in the ISC process, especially in blue emitters like **diCl** and **diBr**.

The introduction of such halogens into the donor fragment decreases the energy of the donor-localized $T_3$-state in such a manner that it becomes close to the $^1$CT state of the blue emitters and thus decreases the $S_1$–$T_3$ energy gap. Together with the heavy atom effect which enhances SOC of the $^1$CT → $^3$LE(A) transition, this results in strong acceleration of ISC. From the point of view of potential application in OLED, the ISC rate should, however, be low to avoid competition with the radiative deactivation of singlet excitons. The first criterion of the molecular design of HA-containing emitters can thus be formulated as: avoid energetic closeness of singlet and triplet states of different nature directly affected by HA.

For the studied emitters, rISC is realized *via* the $^3$CT → $^1$CT transition, proving the appropriateness of the two-level model described in ref. 19 In the light-atom emitter **H**, the $^3$CT → $^1$CT SOC is enhanced by $\theta$-rotations. For rISC modelling in heavy-atom emitters, the two-level model should take into account molecular vibrations involving HAs. In contrast to the commonly used three-level model, our results evidence the negligible role of local $^3$LE states in rISC.

Heavy atoms in the donor unit inhibit spin–orbit coupling of the $^3$CT → $^1$CT transition *via* the $\theta$-rotational channel. However, SOC and rISC are activated by the low-energy vibrations which cause HA motions. Whilst in **diCl**, the former effect dominates causing rISC inhibition, in **diBr**, the latter effect is strong enough to accelerate rISC up to three times. Our second criterion of molecular design of TADF materials with HA is: the heavy atom should be involved in low-energy molecular vibrations to enhance the $^3$CT → $^1$CT transition.

## Conflicts of interest

There are no conflicts to declare.

## Acknowledgements

## References

1 F. B. Dias, T. J. Penfold and A. P. Monkman, *Methods Appl. Fluoresc.*, 2017, **5**, 012001.

2 P. K. Samanta, D. Kim, V. Coropceanu and J.-L. Bredas, *J. Am. Chem. Soc.*, 2017, **139**, 4042–4051.

3 H. Uoyama, K. Goushi, K. Shizu, H. Nomura and C. Adachi, *Nature*, 2012, **492**, 234–238.

4 T. J. Penfold, E. Gindensperger, C. Daniel and C. M. Marian, *Chem. Rev.*, 2018, **118**, 6975–7025.

5 Y.-F. Xiao, J.-X. Chen, W.-C. Chen, X. Zheng, C. Cao, J. Tan, X. Cui, Z. Yuan, S. Ji, G. Lu, W. Liu, P. Wang, S. Li and C.-S. Lee, *Chem. Commun.*, 2021, **57**, 4902–4905.

6 D. R. Lee, K. H. Lee, W. Shao, C. L. Kim, J. Kim and J. Y. Lee, *Chem. Mater.*, 2020, **32**, 2583–2592.

7 C. E. Housecroft and E. C. Constable, *J. Mater. Chem. C*, 2022, **10**, 4456–4482.

8 C. Sun, L. Llanos, P. Arce, A. Oliver, R. Wannemacher, J. Cabanillas-Gonzalez, L. Lemus and D. Aravena, *Chem. Mater.*, 2021, **33**, 6383–6393.

9 IUPAC. Compendium of Chemical Terminology, 2nd ed. (the ''Gold Book''). Compiled by A. D. McNaught and A. Wilkinson. Blackwell Scientific Publications, Oxford (1997). Online version (2019-) created by S. J. Chalk. ISBN 0-9678550-9-8. 10.1351/goldbook.

10 T. Huang, X. Song, M. Cai, D. Zhang and L. Duan, *Mater. Today Energy.*, 2021, **21**, 100705.

11 Y. Ren, Y. Wada, K. Suzuki, Y. Kusakabe, J. Geldsetzer and H. Kaji, *Appl. Phys. Express*, 2021, **14**, 071003.

12 D. Song, Y. Yu, L. Yue, D. Zhong, Y. Zhang, X. Yang, Y. Sun, G. Zhou and Z. Wu, *J. Mater. Chem. C*, 2019, **7**, 11953.

13 T. Hua, L. Zhan, N. Li, Z. Huang, X. Cao, Z. Xiao, S. Gong, C. Zhou, C. Zhong and C. Yang, *Chem. Eng. Sci.*, 2021, **426**, 131169.

14 S. Gan, S. Hu, X.-L. Li, J. Zeng, D. Zhang, T. Huang, W. Luo, Z. Zhao, L. Duan, S.-J. Su and B. Z. Tang, *ACS Appl. Mater. Interfaces*, 2018, **10**, 17327–17334.

15 Y. Xiang, Y. Zhao, N. Xu, S. Gong, F. Ni, K. Wu, J. Luo, G. Xie, Z.-H. Lu and C. Yang, *J. Mater. Chem. C*, 2017, **5**, 12204–12210.

16 D. Pereira, D. R. Lee, N. A. Kukhta, K. H. Lee, C. L. Kim, A. S. Batsanov, J. Y. Lee and A. P. Monkman, *J. Mater. Chem. C*, 2019, **7**, 10481–10490.

17 K. Matsuo and T. Yasuda, *Chem. Sci.*, 2019, **10**, 10687–10697.

18 I. S. Park, K. Matsuo, N. Aizawa and T. Yasuda, *Adv. Funct. Mater.*, 2018, **28**, 1802031.

19 I. E. Serdiuk, M. Mońka, K. Kozakiewicz, B. Liberek, P. Bojarski and S. Y. Park, *J. Phys. Chem. B*, 2021, **125**, 2696–2706.

20 I. E. Serdiuk, C. H. Ryoo, K. Kozakiewicz, M. Mońka, B. Liberek and S. Y. Park, *J. Mater. Chem. C*, 2020, **8**, 6052–6062.

21 A. A. Kubicki, P. Bojarski, M. Grinberg, M. Sadownik and B. Kukliński, *Opt. Commun.*, 2006, **269**, 275–280.

22 M. J. Frisch, G. W. Trucks, H. B. Schlegel, G. E. Scuseria, M. A. Robb, J. R. Cheeseman, G. Scalmani, V. Barone, G. A. Petersson, H. Nakatsuji, *et al.*, *Gaussian 16*, Revision C.01 Gaussian, Inc., Wallingford, CT, 2016.

23 A. D. Becke, *J. Chem. Phys.*, 1993, **98**, 1372–1377.

24 F. Neese, *Wiley Interdiscip. Rev.: Comput. Mol. Sci.*, 2012, **2**, 73–78.

This journal is © The Royal Society of Chemistry 2022

*J. Mater. Chem. C*, 2022, **10**, 7925–7934 | **7933**

25 S.-J. Woo, Y.-H. Kim and J.-J. Kim, *Chem. Mater.*, 2021, **33**, 5618–5630.

26 M. Hempe, N. A. Kukhta, A. Danos, M. A. Fox, A. S. Batsanov, A. P. Monkman and M. R. Bryce, *Chem. Mater.*, 2021, **33**, 3066–3080.

27 K. Stavrou, L. G. Franca and A. P. Monkman, *ASC Appl. Electron. Mater.*, 2020, **2**, 2868–2881.

28 L. G. Franca, A. Danos and A. Monkman, *J. Mater. Chem. C*, 2022, **10**, 1313–1325.

29 L.-S. Cui, H. Nomura, Y. Geng, J. U. Kim, H. Nakatomani and C. Adachi, *Angew. Chem.*, 2016, **56**, 1571–1575.

30 F. B. Dias, K. N. Bourdakos, V. Jankus, K. C. Moss, K. T. Kametekar, V. Bhalla, J. Santos, M. R. Bryce and A. P. Monkman, *Adv. Mater.*, 2013, **25**, 3707–3714.

31 J. Gibson and T. J. Penfold, *Phys. Chem. Chem. Phys.*, 2017, **19**, 8428–8434.

32 M. A. El Sayed, *J. Chem. Phys.*, 1963, **38**, 2834–2838.

**7934** | *J. Mater. Chem. C*, 2022, **10**, 7925–7934

This journal is © The Royal Society of Chemistry 2022

# Supporting information

**UNDERSTANDING THE INTERNAL HEAVY-ATOM EFFECT ON THERMALLY ACTIVATED DELAYED FLUORESCENCE: APPLICATION OF ARRHENIUS AND MARCUS THEORIES FOR SPIN-ORBIT COUPLING ANALYSIS**

Michał Mońka,[1] Illia E. Serdiuk[1],* Karol Kozakiewicz,[2] Estera Hoffman-Rusin,[1] Jan Szumilas,[1] Aleksander Kubicki,[1] Soo Young Park,[3] Piotr Bojarski[1]

[1] Faculty of Mathematics, Physics and Informatics, University of Gdańsk, Wita Stwosza 57, 80-308 Gdańsk, Poland

[2] Faculty of Chemistry, University of Gdańsk, Wita Stwosza 63, 80-308 Gdańsk, Poland

[3] Center for Supramolecular Optoelectronic Materials, Department of Materials Science and Engineering, Seoul National University, 1 Gwanak-ro, Gwanak-gu, Seoul 151-744, Republic of Korea

*Corresponding author. E-mail: illia.serdiuk@ug.edu.pl, phone + 48 58 523 22 44

# Table of contents

# Section S1. NMR spectra of target emitters



**Figure S1.** $^1$H NMR spectrum of **diCl**



**Figure S2.** $^{13}$C NMR spectrum of **diCl**
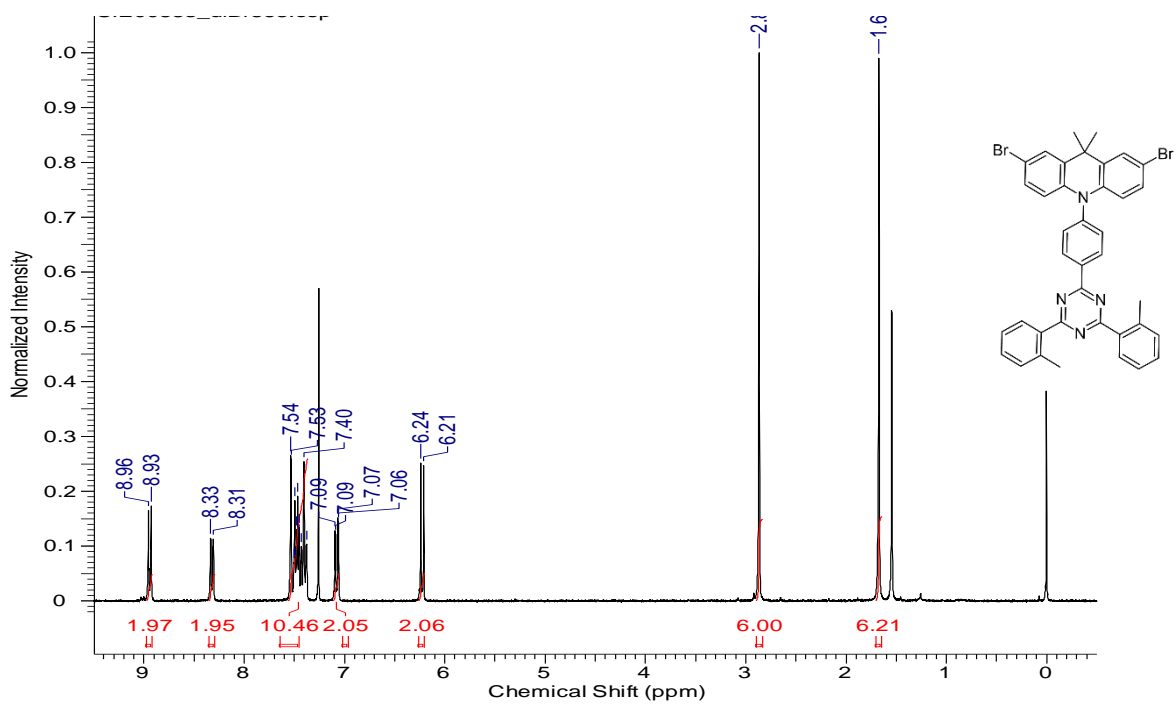
**Figure S3.** $^1$H NMR spectrum of **diBr**
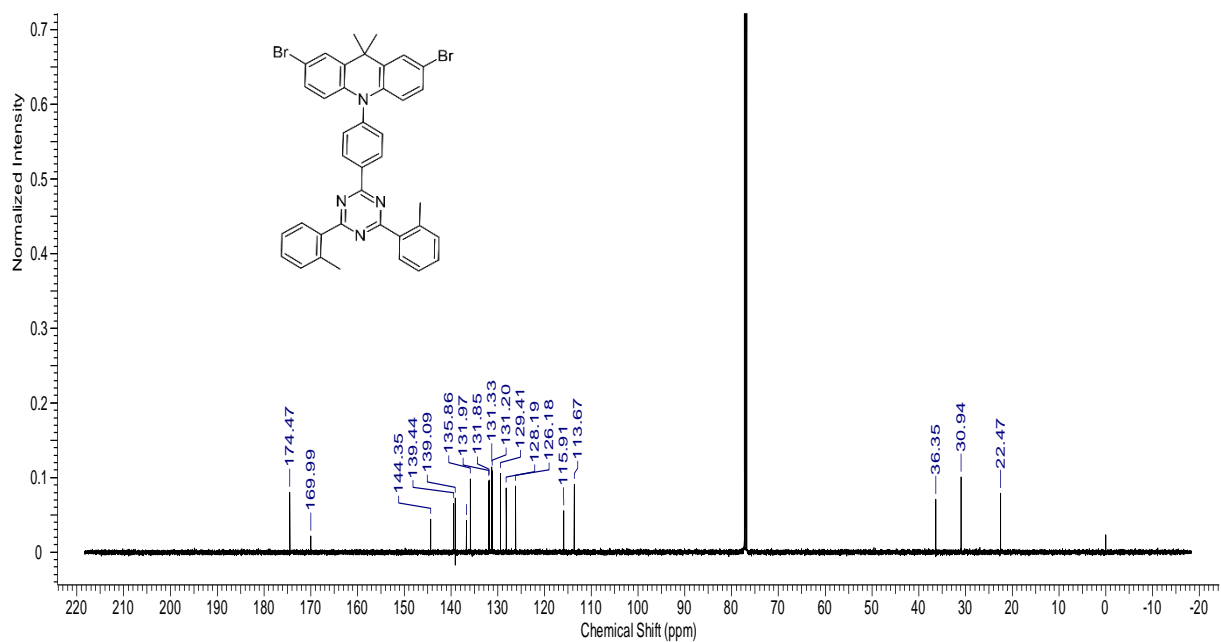


**Figure S4.** $^{13}$C NMR spectrum of **diBr**

## Section S2. Detailed discussion on spectral properties

*Analysis of the nature of lowest excited electronic states on the basis of steady-state measurements*. In nonpolar ZNX films at room temperature (RT), all three emitters (**H**, **diCl**, **diBr**) show vibronically-structured emission band with a maximum localized at 465–467 nm (**Figure 1C**). The onsets of fluorescence spectra ($\lambda_{onset}$, **Figures S6A-C**) were determined to be around 423, 418 and 421 nm for **H**, **diCl**, and **diBr**, respectively, which gives the $S_1$-state energies of 2.93, 2.97 and 2.95 eV, respectively (**Table S1**). In more polar PMMA, the emission becomes broad and structureless, and shifts to 492–499 nm range. The onsets of fluorescence in PMMA were estimated to be around $\lambda_{onset}$ = 430, 427 and 428 nm for **H**, **diCl**, and **diBr** respectively (**Figures S6D-F**), which gives the energy levels of $^1$CT states at 2.88, 2.90 and 2.89 eV. Such positive solvatofluorochromism typical for most of TADF emitters arises from the charge transfer (CT) character of the $S_1$-state [S1].

To reveal the nature and the energy of the lowest triplet excited states the phosphorescence measurements at low temperature were performed. As shown in **Figures S6A-C**, the phosphorescence spectrum of **H** in ZNX is red-shifted and has different shape as compared to that of fluorescence, with onset around $\lambda_{onset}$ = 437 nm, which gives the energy level at 2.84 eV. The presented phosphorescence spectrum profile perfectly matches the shape of emission of the isolated acceptor fragment that was measured separately, as depicted in **Figure S6G**. Taking into account the previous studies of similar compound **DMAC-TRZ** [S2] our results indicate that the lowest triplet excited state of **H** in ZNX is of the localized nature ($^3$LE$_A$) originating from the acceptor fragment. The same conclusion was made for the **diCl** and **diBr** derivatives, as no significant differences in the phosphorescence spectra of **diCl** and **diBr** in ZNX were observed. In fact, as the halogens were introduced into donor fragment, they were not expected to affect the acceptor-localized $^3$LE$_A$ state. With respect to this, the energy gap $\Delta E_{1CT-3LE}$ between lowest excited singlet ($^1$CT) and triplet ($^3$LE$_A$) states in ZNX was estimated to be of 94, 133 and 114 meV for **H**, **diCl** and **diBr**, respectively (**Table S1**).

In more polar PMMA films, the phosphorescence spectrum of **H** broadens, becomes structureless and red-shifted as compared to the one measured in ZNX (**Figure S6D**). It should be noted, that in PMMA at 10K, to distinguish phosphorescence from the $^1$CT-fluorescence, careful

S4

analysis of TRES was conducted. As mentioned above, the specific feature of the $^1$CT-fluorescence in DF region is its gradual blue-shift with the delay time. In PMMA films at 10K, the emission does not shift after the 50µs delay time (**Figure S8**). Its onset value in **H** falls around 443 nm, which is 0.04 eV below the $^3$LE$_A$ state. Such observation indicates, that in PMMA phosphorescence occurs from the triplet charge-transfer ($^3$CT) state, energy of which is estimated around 2.80 eV. Similar observations for **diCl** and **diBr** gave the $^3$CT levels of 2.81 eV (onset at 441 nm, **Figures S6E** and **S1F**). Taking into account these energies, the values of energy gap between lowest $^1$CT and $^3$CT states ($\Delta E_{1CT\text{-}3CT}$) were estimated as 85, 95 and 86 meV, as summarized in **Table 1.** Such relatively high values of $\Delta E_{1CT\text{-}3CT}$ are explained further.
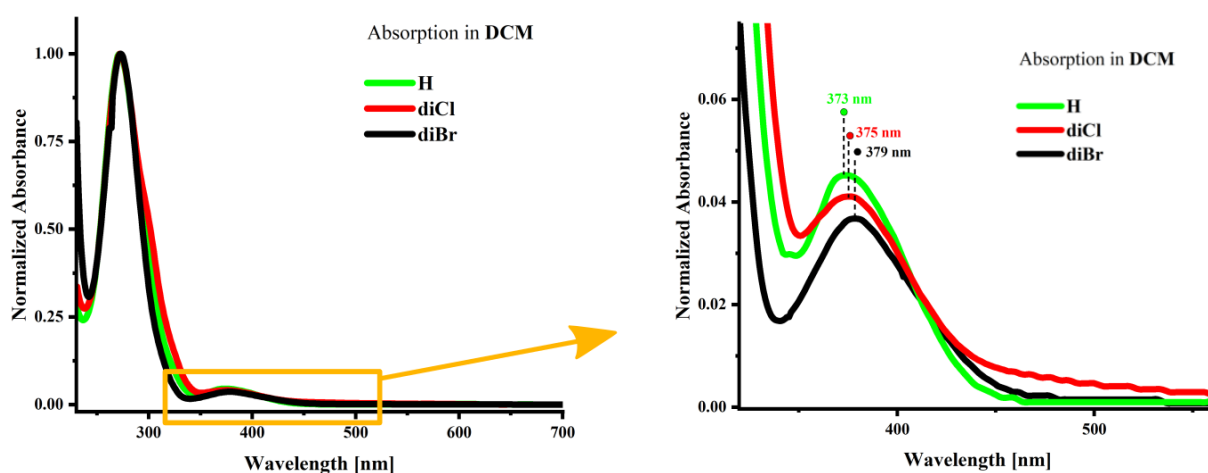


**Figure S5**. The absorption spectra of the investigated compounds measured in dichloromethane (DCM) solutions.
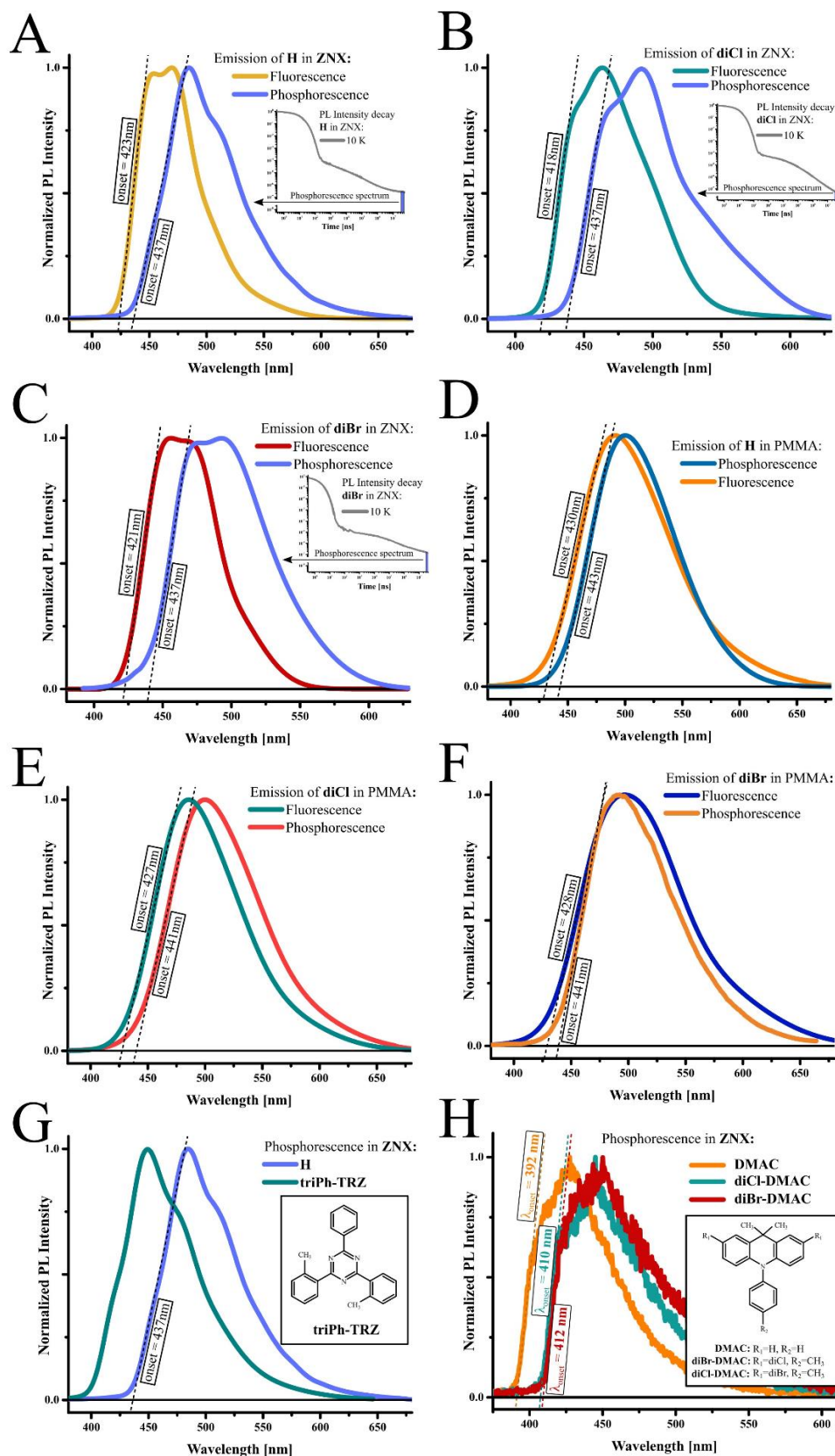
**Figure S6**. Steady-state fluorescence and phosphorescence spectra of **H**, **diCl** and **diBr** in ZNX (A, B, C, respectively) and in PMMA (D, E, F) with determined onsets. Fluorescence spectra were measured at room temperature in aerated conditions upon excitation $\lambda_{exc}$=370 nm. Phosphorescence spectra of isolated fragments: acceptor (G) and donors of **H**, **diCl** and **diBr** (H) were measured at 10 K with 30ms time delay under excitation $\lambda_{exc}$=320 nm.

**Table S1.** Photophysical parameters.

| cmpd | medium | PLQY[a] | Fluorescence ${}^1$CT | | | Phosphorescence ${}^3$LE(A) | | | Phosphorescence ${}^3$CT | | | Phosphorescence ${}^3$LE(D) | | | $\Delta E_{1CT-3LE(A)}$[e] | $\Delta E_{1CT-3CT}$[e] | $\Delta E_{1CT-3LE(D)}$[e] |
|---|---|---|---|---|---|---|---|---|---|---|---|---|---|---|---|---|---|
| | | [%] | $\lambda_{onset}$[b] [nm] | Energy[c] [eV] | $\lambda_{max}$[d] [nm] | $\lambda_{onset}$[b] [nm] | Energy[c] [eV] | $\lambda_{max}$[d] [nm] | $\lambda_{onset}$[b] [nm] | Energy[c] [eV] | $\lambda_{max}$[d] [nm] | $\lambda_{onset}$[b] [nm] | Energy[c] [eV] | $\lambda_{max}$[d] [nm] | [meV] | [meV] | [meV] |
| **H** | ZNX | 60 | 423 | 2.93 | 465 | 437 | 2.84 | 487 | - | - | - | 392 | 3.16 | 426 | 94 | - | -230 |
| **diCl** | | 75 | 418 | 2.97 | 462 | 437 | 2.84 | 489 | - | - | - | 410 | 3.02 | 447 | 133 | - | -55 |
| **diBr** | | 12 | 421 | 2.95 | 467 | 437 | 2.84 | 490 | - | - | - | 412 | 3.01 | 448 | 114 | - | -55 |
| **H** | PMMA | 99 | 430 | 2.88 | 498 | - | - | - | 443 | 2.80 | 498 | - | - | - | 46 | 85 | -278 |
| **diCl** | | 85 | 427 | 2.90 | 492 | - | - | - | 441 | 2.81 | 494 | - | - | - | 72 | 95 | -116 |
| **diBr** | | 21 | 428 | 2.89 | 499 | - | - | - | 441 | 2.81 | 500 | - | - | - | 60 | 86 | -109 |

[a] - PLQY was measured at 298K using integrating sphere under oxygen atmosphere. The values presented in the table are corrected for vacuum conditions according to proportional relationship: $PLQY = PLQY_{air} \times (DecArea_{vac}/DecArea_{air})$, where $PLQY_{air}$ is value obtained under oxygen atmosphere, $DecArea_{vac}$ and $DecArea_{air}$ are total areas under PL intensity decays measured in vacuum and under oxygen atmosphere, respectively (**Figure S7A-F**);

[b] - onsets determined experimentally from PL spectra (see **Figure S6A-F** for ${}^1$CT, **Figures S6A-C** and **S6G** for ${}^3$LE(A), **Figure S6H** for ${}^3$LE(D) and **Figure S6D-F** for ${}^3$CT-state);

[c] - energies of respective excited states calculated from relation: $E = 1240/\lambda_{onset}$;

[d] – photoluminescence maxima (see **Figure S6** for ${}^1$CT and ${}^3$LE(A), **Figures S6H** for ${}^3$LE(D) and **Figures S6D-F** for ${}^3$CT-state);

[e] - energy gap determined from the difference of respective onsets of PL spectra: $\Delta E_{1-2} = (1240/\lambda_{onset1} - 1240/\lambda_{onset2})$.

*Time-resolved emission spectra and emission decays*

As can be seen in **Figure S7**, the PL decay for each of studied emitters contains two well-separated areas in nano- and microsecond regimes corresponding to the prompt and delayed emission. The PL intensity decay profiles measured in the presence of oxygen differ from those recorded in the vacuum due to quenching by molecular oxygen, which confirms that TADF is mediated by triplet state(s).
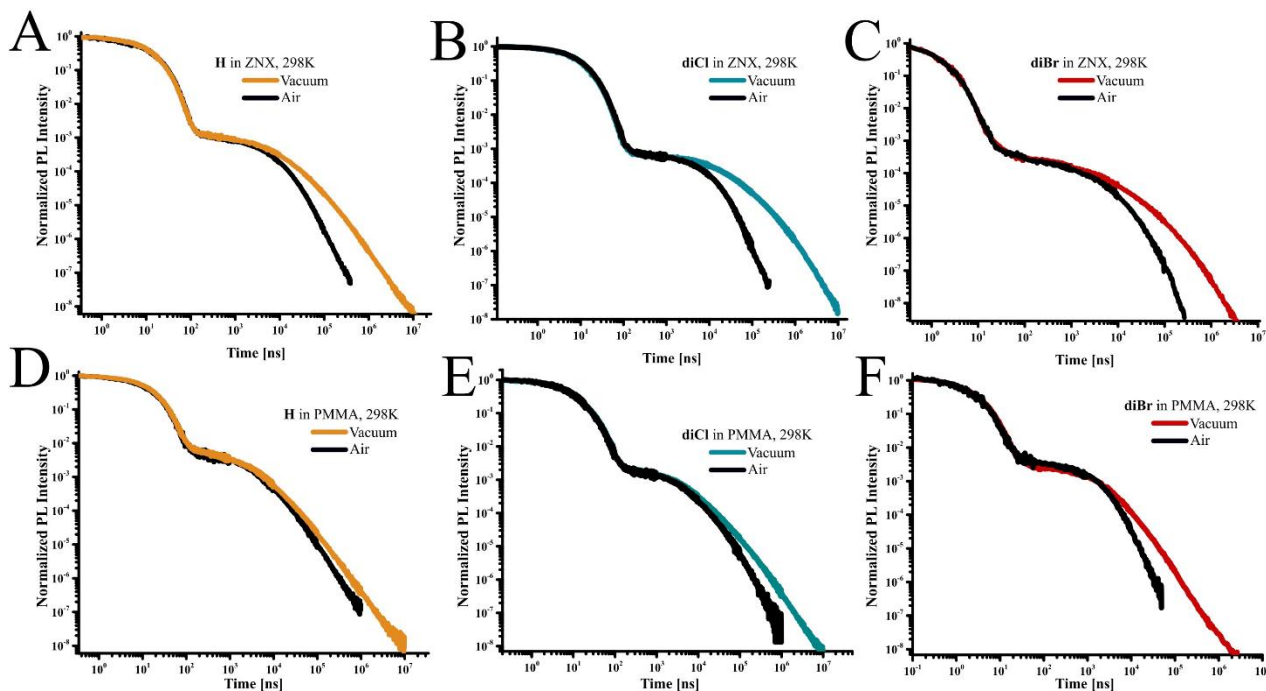


**Figure S7**. Time-resolved PL measurements of studied compounds dispersed in ZNX (A-C) and PMMA (D-F) in the presence of oxygen and in vacuum at 298 K. Excitation wavelength $\lambda_{exc}$=370 nm.

To verify whether the delayed emission originates from the $^1$CT-state, detailed time-dependent analysis of PL spectra was carried out (**Figures S8A** and **S9A**). Through the entire timescale of PL spectra of each emitter, all the collected spectra have roughly similar shape and maximum (**Figures S8B-D**, **S9B-D**). Therefore, the fast component can be identified as prompt fluorescence (PF), occurring from the directly excited $^1$CT-state, whilst the slow one is due to the delayed fluorescence (DF), where emission from the $^1$CT-state is preceded by ISC and rISC.

For time-resolved emission spectra (TRES) in PF region over the first 100 ns, the emission maximum red-shifts from 452 to 463 nm in ZNX and 473 to 497 nm in PMMA (**Figures S8-S11**). In

the DF regime starting from 1 µs, TRES undergo the red shift from 455 nm to 481 nm. Such spectral behavior can be explained by the distribution of $^1$CT states due to the coexistence of different emitter conformations. As suggested in previous reports[S2, S3], the most crucial conformers differ by the dihedral angle between donor and acceptor units ($\theta$, **Figures 1B** and **1D**, main text). At the very early stages of PF, the blue-shifted fluorescence spectrum originates from the conformers with the most deviated $\theta$-value from the optimal 90°. The deviation from orthogonality leads to the increased overlap of molecular orbitals (MOs) involved in the CT transition, and thus better conjugation of donor and acceptor fragments. For this reason, such conformers have higher energies of $^1$CT states and higher value of $S_1$-$S_0$ oscillator strength, which enables relatively fast emission. As $\theta$ approaches to orthogonal, the $^1$CT state becomes more stabilized due to decreased conjugation between D and A, which leads to red-shift of emission and lower $S_1$-$S_0$ oscillator strengths. Such conformers emit at the late PF. The opposite behavior is observed for the DF region. The red-shifted emission is responsible for the early-DF, whilst in the late-DF blue shift is observed. As the most orthogonal conformers have the smallest energy gap between singlet and triplet state $\Delta E_{ST}$, which according to Marcus-Hush equation (eq. 2 in main text) leads to the highest rISC rates, their red-shifted DF appears first. Consequently, as the $\theta$-deviation increases, $\Delta E_{ST}$ increases too, rISC becomes slower and the DF spectrum gradually shifts to shorter wavelengths.

The distribution of $^1$CT-state energy and relatively constant energy of the $^3$CT-state (**Figure S12A-C**), explains relatively high values of $\Delta E_{1CT-3CT}$ mentioned above.

**Figure S8.** PL intensity decay profiles of **H**, **diCl**, and **diBr** in ZNX (A) with PL spectra taken at different time delays (B-D). Excitation wavelength $\lambda_{exc}$=370 nm.

**Figure S9**. PL intensity decay profiles of **H**, **diCl**, and **diBr** in PMMA (A) with PL spectra taken at different time delays (B-D). Excitation wavelength $\lambda_{exc}$=370 nm.
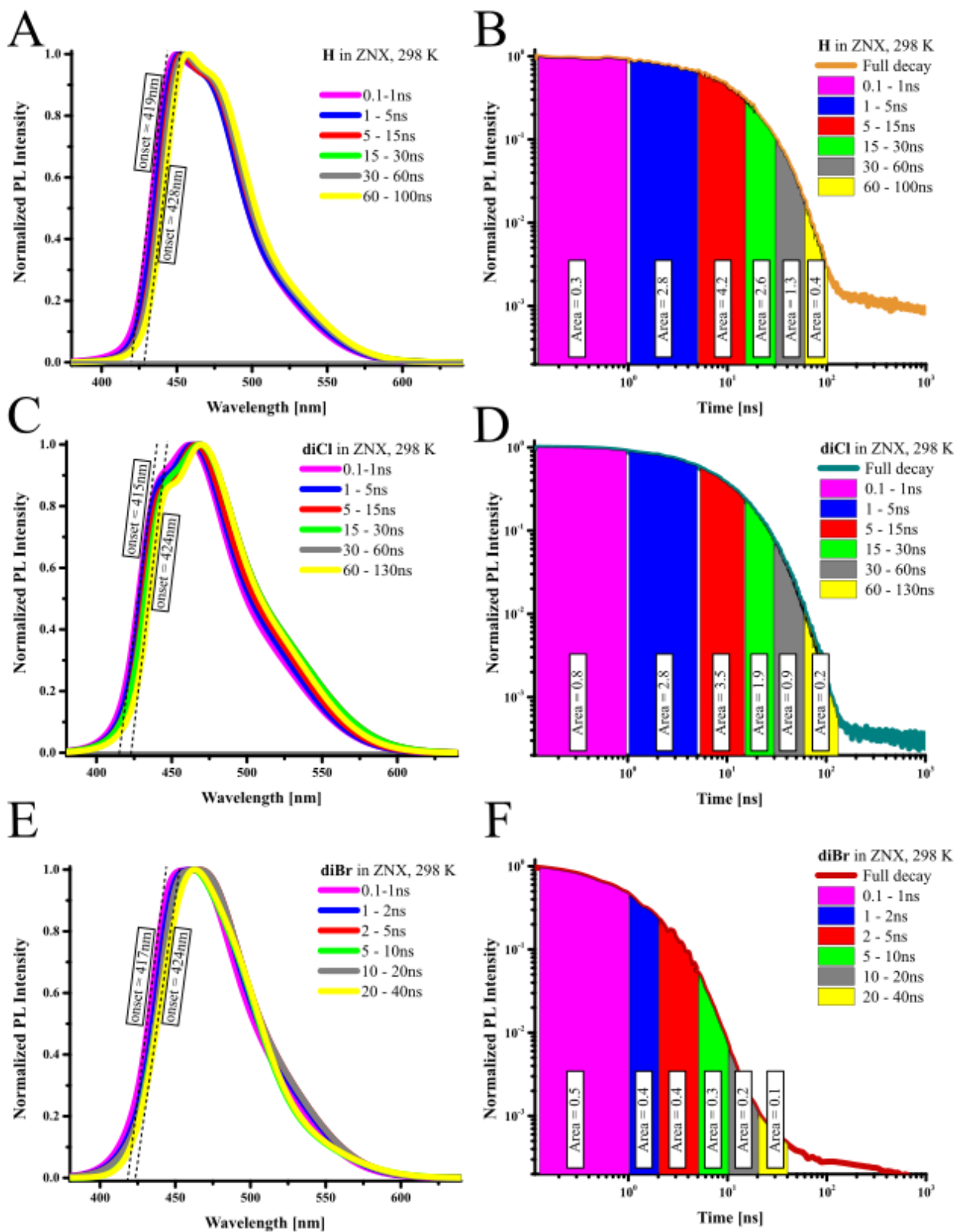
**Figure S10**. Time evolution of PL spectra within PF of **H, diCl** and **diBr** (A, C, E) with corresponding time frames (B, D, F) in ZNX measured at 298 K in vacuum. Excitation wavelength λ$_{exc}$=370 nm.
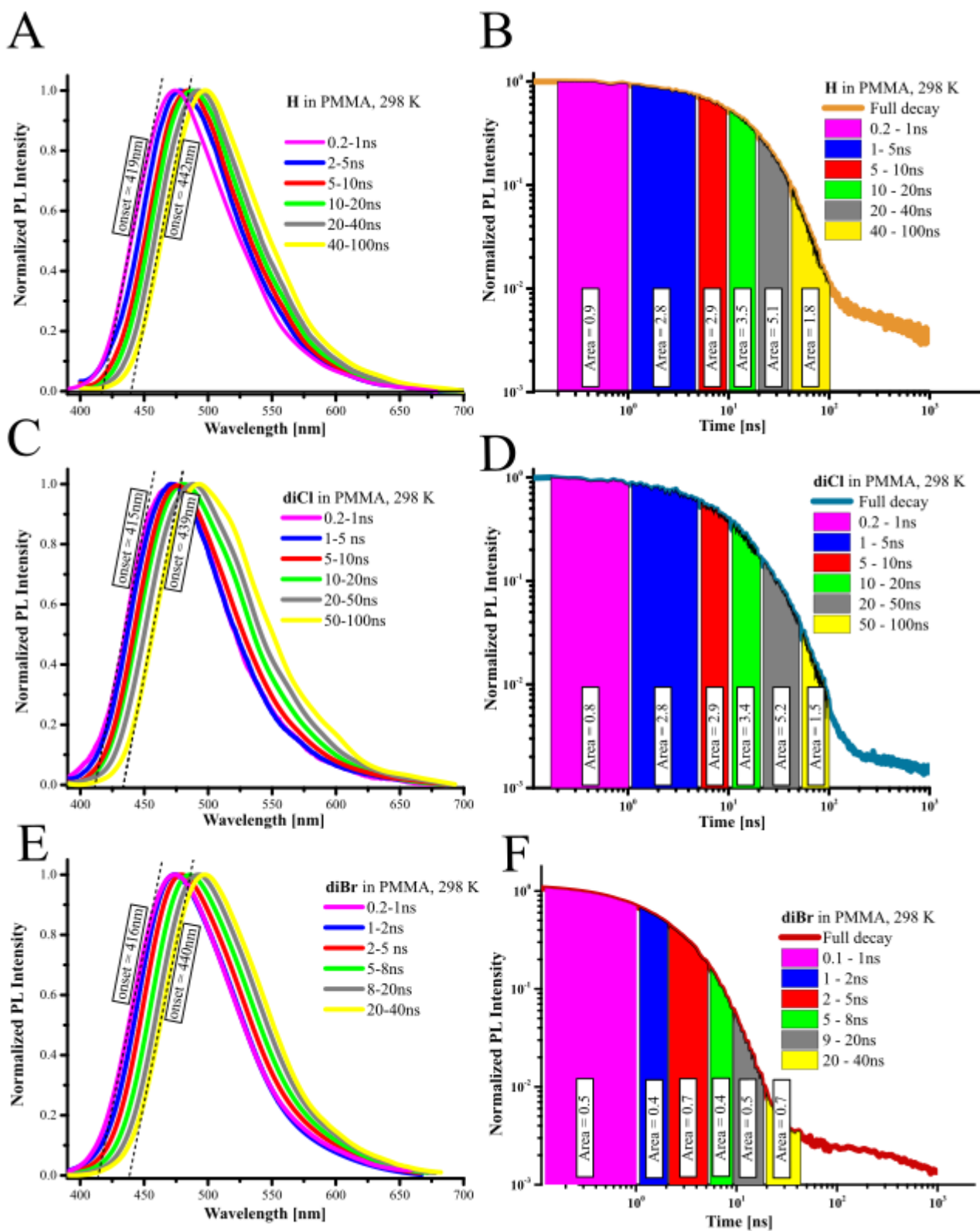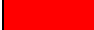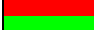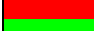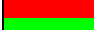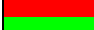
**Figure S11**. Time evolution of PL spectra within PF region of **H, diCl** and **diBr** (A, C, E) with corresponding time frames (B, D, F) in PMMA measured at 298 K in vacuum. Excitation wavelength $\lambda_{exc}$=370 nm.

**Table S2**. Experimental determination of minimal, maximal and statistically mean $^1$CT-onset values

| cmpd | Figures[a] | medium | | Time [ns] | Onset [nm] | Energy [eV][b] | Area[c] | Contribution [%] |
|---|---|---|---|---|---|---|---|---|
| **H** | **S10A, S10B** | ZNX | (magenta) | 0.2-1 | 419 | 2.96 | 0.7 | 5.8 |
| | | | (blue) | 1-5 | 420 | 2.95 | 2.8 | 23.2 |
| | | | (red) | 5-15 | 423 | 2.93 | 4.2 | 35.0 |
| | | | (green) | 15-30 | 424 | 2.92 | 2.6 | 21.7 |
| | | | (grey) | 30-60 | 427 | 2.90 | 1.3 | 11.0 |
| | | | (yellow) | 60-100 | 428 | 2.90 | 0.4 | 3.4 |
| | | | | **Weighted average** | **423** | **2.93** | | |
| **diCl** | **S10C, S10D** | ZNX | (magenta) | 0.2-1 | 415 | 2.96 | 0.8 | 7.9 |
| | | | (blue) | 1-5 | 416 | 2.95 | 2.8 | 27.8 |
| | | | (red) | 5-15 | 418 | 2.93 | 3.5 | 34.0 |
| | | | (green) | 15-30 | 420 | 2.92 | 1.9 | 19.1 |
| | | | (grey) | 30-60 | 422 | 2.90 | 0.9 | 9.1 |
| | | | (yellow) | 60-100 | 424 | 2.90 | 0.2 | 2.0 |
| | | | | **Weighted average** | **418** | **2.97** | | |
| **diBr** | **S10E, S10F** | ZNX | (magenta) | 0.1-1 | 417 | 2.97 | 0.5 | 26.1 |
| | | | (blue) | 1-2 | 420 | 2.95 | 0.4 | 21.6 |
| | | | (red) | 2-5 | 421 | 2.95 | 0.4 | 21.0 |
| | | | (green) | 5-10 | 422 | 2.94 | 0.3 | 15.9 |
| | | | (grey) | 10-20 | 423 | 2.93 | 0.3 | 10.6 |
| | | | (yellow) | 20-40 | 424 | 2.92 | 0.1 | 5.3 |
| | | | | **Weighted average** | **421** | **2.95** | | |
| **H** | **S11A, S11B** | PMMA | (magenta) | 0.2-1 | 419 | 2.96 | 0.9 | 5.1 |
| | | | (blue) | 2-5 | 421 | 2.95 | 2.8 | 16.1 |
| | | | (red) | 5-10 | 424 | 2.92 | 2.9 | 16.8 |
| | | | (green) | 10-20 | 428 | 2.90 | 3.5 | 20.5 |
| | | | (grey) | 20-40 | 437 | 2.84 | 5.1 | 30.5 |
| | | | (yellow) | 40-100 | 442 | 2.81 | 1.8 | 10.9 |
| | | | | **Weighted average** | **430** | **2.88** | | |
| **diCl** | **S11C, S11D** | PMMA | (magenta) | 0.2-1 | 415 | 2.99 | 0.8 | 4.9 |
| | | | (blue) | 1-5 | 417 | 2.97 | 2.8 | 17.3 |
| | | | (red) | 5-10 | 420 | 2.95 | 2.9 | 17.8 |
| | | | (green) | 10-20 | 427 | 2.90 | 3.4 | 20.5 |
| | | | (grey) | 20-50 | 433 | 2.86 | 5.2 | 30.9 |
| | | | (yellow) | 40-100 | 439 | 2.82 | 1.5 | 8.8 |
| | | | | **Weighted average** | **427** | **2.91** | | |
| **diBr** | **S11E, S11F** | PMMA | (magenta) | 0.2-1 | 416 | 2.98 | 0.5 | 15.2 |
| | | | (blue) | 1-2 | 419 | 2.96 | 0.4 | 12.3 |
| | | | (red) | 2-5 | 422 | 2.94 | 0.7 | 21.5 |
| | | | (green) | 5-8 | 429 | 2.89 | 0.4 | 12.5 |
| | | | (grey) | 8-20 | 438 | 2.83 | 0.5 | 16.0 |
| | | | (yellow) | 20-40 | 440 | 2.82 | 0.7 | 22.4 |
| | | | | **Weighted average** | **428** | **2.90** | | |

[a] – Figures demonstrating integration ranges and corresponding PL spectra;

[b] – Energy calculated from relation: $E = 1240/\lambda_{onset}$;

[c] – Area obtained by integration of PL decay curve over specified time interval, as depicted in respective figures[a].

**Table S3**. Minimal, maximal, and statistically mean values of energy gaps.

| | | $\Delta E_{1CT-3CT}$ [meV] | | | $\Delta E_{1CT-3LE(A)}$ [meV] | | | $\Delta E_{1CT-3LE(D)}$ [meV] | | |
| --- | --- | --- | --- | --- | --- | --- | --- | --- | --- | --- |
| | | Min | Mean | Max | Min | Mean | Max | Min | Mean | Max |
| **H** | PMMA | 6 | 85 | 160 | -32 | 46 | 121 | -203 | -278 | -357 |
| **diCl** | PMMA | 13 | 95 | 176 | -10 | 72 | 153 | -35 | -116 | -198 |
| **diBr** | PMMA | 6 | 86 | 169 | -20 | 60 | 143 | -24 | -109 | -189 |
| | | | | | | | | | | |
| **H** | ZNX | | | | 59 | 94 | 121 | -203 | -230 | -265 |
| **diCl** | ZNX | | | | 90 | 133 | 153 | -35 | -55 | -99 |
| **diBr** | ZNX | | | | 86 | 114 | 143 | -27 | -55 | -83 |

Energy gaps were determined from the difference of respective onsets of PL spectra, according to general equation: $\Delta E_{1-2} = (1240/\lambda_{onset1} - 1240/\lambda_{onset2})$.
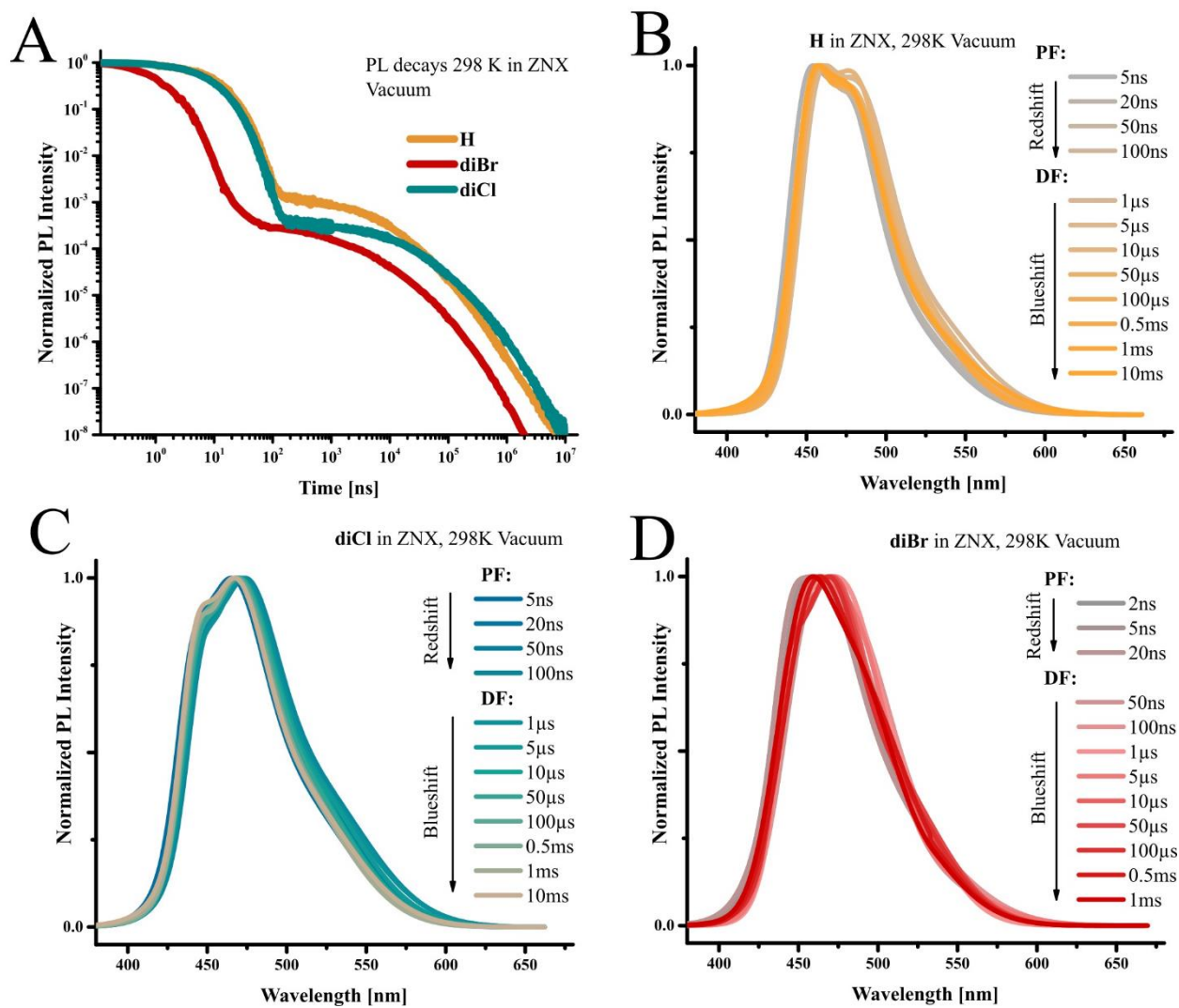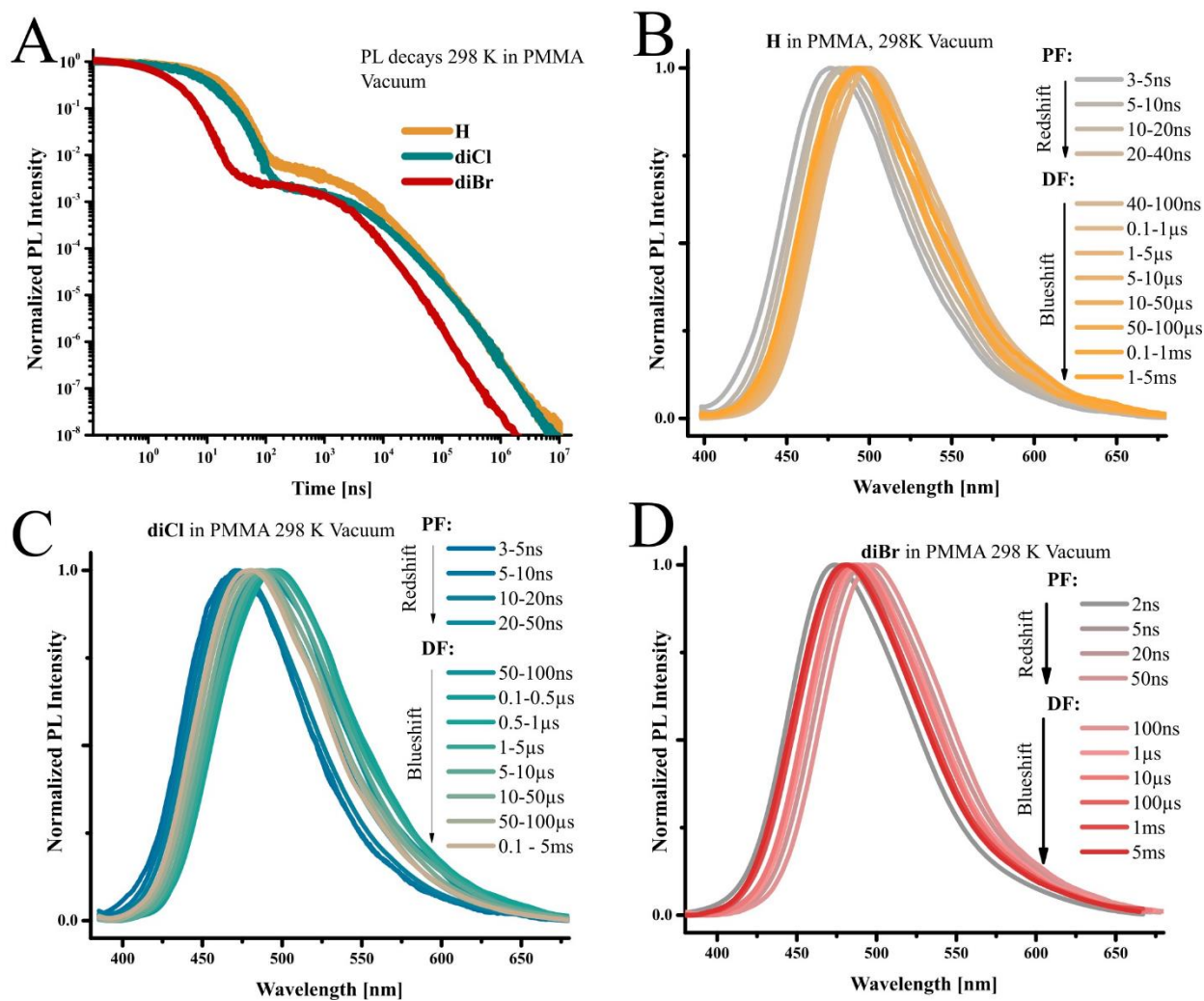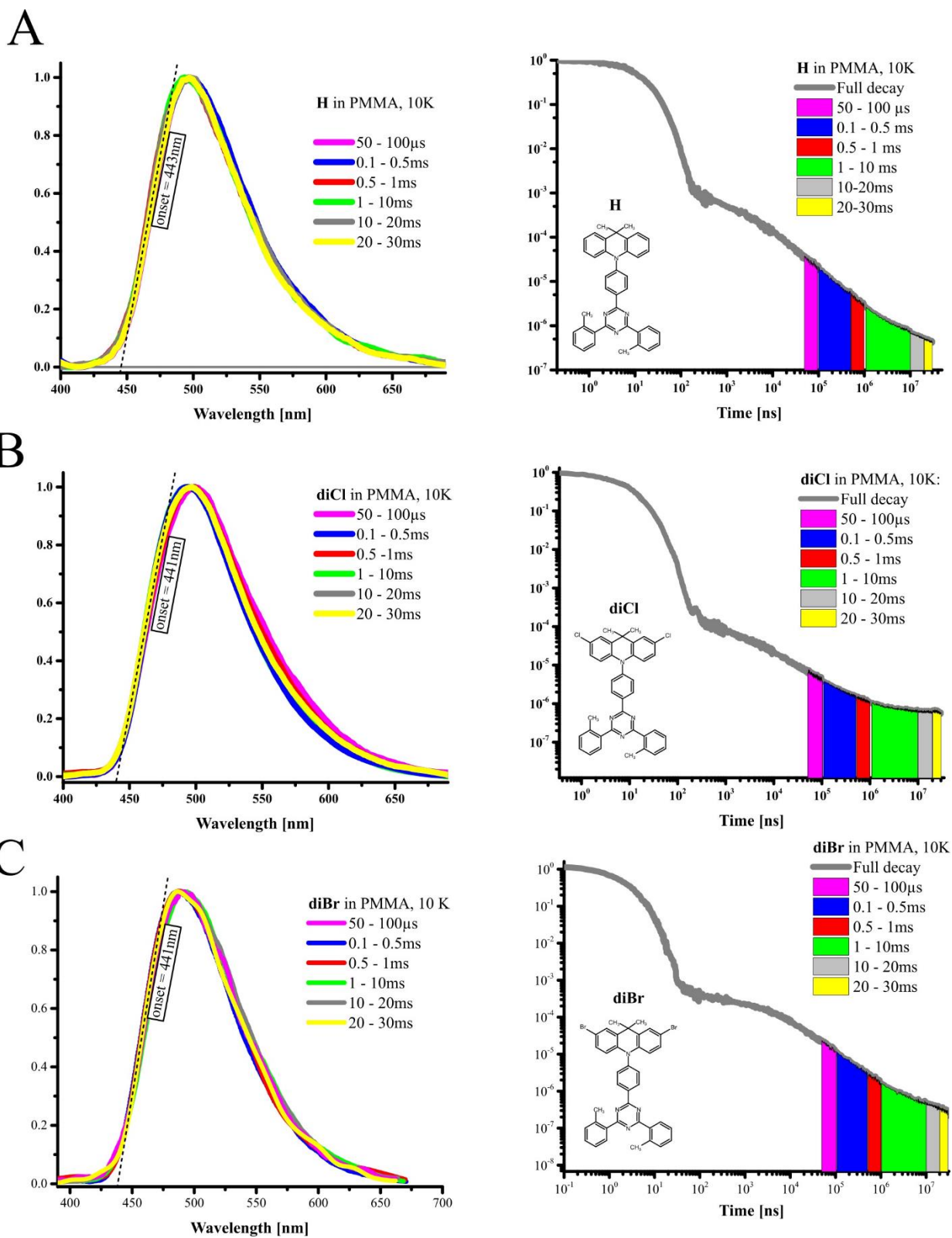
**Figure S12**. PL intensity decay profiles of **H**, **diCl**, and **diBr** in PMMA with PL spectra taken at different time delays measured at 10 K. Excitation wavelength $\lambda_{exc}$=370 nm.

## Section S3: Determination of photophysical parameters

PL decay curves (presented in **Figures S8A, S9A** and **S13**) were fitted with the multiexponential equation:

$$I(t) = A_0 + \sum_{i=1}^{n} A_i \exp\left(- {}^t/_{\tau_i}\right) \tag{S1}$$

where $A_i$ is the pre-exponential factor, $\tau_i$ is the decay time and $I(t)$ is emission intensity. Average lifetimes of prompt ($\tau_{PF}$) and delayed fluorescence ($\tau_{DF}$) were determined using the following formula:

$$\tau_{PF}, \tau_{DF} = \sum_{i=1}^{n} f_i \tau_i, \tag{S2}$$

where $f_i$ is fractional contribution of $i$-th component expressed as:

$$f_i = \frac{A_i \tau_i}{\sum_{i=1}^{n} A_i \tau_i} \tag{S3}$$

The ratio of DF and PF quantum yields $\varphi_{DF}/\varphi_{PF}$ was determined as follows [S4]:

$$\frac{\varphi_{DF}}{\varphi_{PF}} = \frac{\sum_{i=1}^{n} \tau_{DF(i)} A_{DF(i)}}{\sum_{j=1}^{n} \tau_{PF(j)} A_{PF(j)}} \tag{S4}$$

where $A_{DF(i)}$ and $A_{PF(j)}$ is the pre-exponential factor of delayed and prompt fluorescence component, respectively; $\tau_{DF(i)}$ and $\tau_{PF(j)}$ is the lifetime of delayed and prompt fluorescence component, respectively. The rate constants of radiative ($k_r$) and nonradiative ($k_{nr}$) decay and intersystem crossing ($k_{ISC}$) are given by equations:

$$k_r = \frac{\varphi_{PF}}{\tau_{PF}}, \tag{S5}$$

$$k_{ISC} = \frac{\varphi_{DF}}{\varphi \, \tau_{PF}}, \tag{S6}$$

$$k_{nr} = \frac{1}{\tau_{PF}} - (k_r + k_{ISC}). \tag{S7}$$

where $\varphi$ is PLQY ($\varphi_{DF} + \varphi_{PF}$). Further, the quantum yields for ISC and rISC were calculated as

$$\varphi_{ISC} = k_{ISC} \tau_{PF}, \tag{S8}$$

$$\varphi_{rISC} = \frac{1 - \varphi_{PF}/\varphi}{\varphi_{ISC}}. \tag{S9}$$

Finally, the rate constant of rISC ($k_{rISC}$) was calculated as

$$k_{rISC} = \frac{\varphi_{rISC}}{\tau_{DF}}\left(\frac{\varphi}{\varphi_{PF}}\right). \tag{S10}$$

Photophysical parameters are presented in **Tables 1** (main text) and **S4**.

**Table S4**. Experimentally determined photophysical parameters.

| Cmpd | medium | $\varphi_{PF}$ | $\varphi_{DF}$ | $\varphi_{DF}/\varphi_{PF}$ | $\tau_{PF}$ | $\tau_{DF}$ | $k_r$ | $k_{ISC}$ | $k_{rISC}$ |
|------|--------|------|------|------|------|------|------|------|------|
| | | [%] | [%] | | [ns] | [µs] | [s$^{-1}$ 10$^7$] | [s$^{-1}$ 10$^7$] | [s$^{-1}$ 10$^4$] |
| **H** | ZNX | 22.1 | 27.9 | 1.3 | 15.3 | 171 | 1.5 | 5.1 | 1.03 |
| **diCl** | | 21.6 | 53.2 | 2.5 | 13.1 | 333 | 1.8 | 6.1 | 0.87 |
| **diBr** | | 4.5 | 6.5 | 1.4 | 2.2 | 104 | 2.0 | 38.5 | 1.74 |
| **H** | PMMA | 33.4 | 63.3 | 1.8 | 17.1 | 96 | 2.1 | 3.8 | 2.92 |
| **diCl** | | 32.4 | 53.1 | 1.6 | 16.0 | 139 | 2.0 | 4.1 | 1.85 |
| **diBr** | | 5.7 | 15.1 | 2.7 | 2.8 | 38 | 2.0 | 30.8 | 8.23 |

# Section S4: Temperature-dependent time-resolved analysis based on Arrhenius and Marcus theories

Time-resolved PL measurements were conducted within the temperature range of 298–10 K (**Figure S13**). The PL decays in the 298 – 150 K range contained only prompt and delayed fluorescence, thus phosphorescence did not interfered. The latter temperature range was thus used for further investigations. The PL decay analysis as described in section S3 enabled $k_{ISC}$ and $k_{rISC}$ constant rates at various temperatures (**Tables S5, S6**). To determine the energy barriers $E_a$ for ISC and rISC, the Arrhenius law equation was applied:

$$k_{(r)ISC} = A \cdot \exp\left(-\frac{E_a}{k_B T}\right), \tag{S11}$$

where $k_B$ stands for Boltzmann constant, and $A$ is pre-exponential constant (**Table 2,** main text).
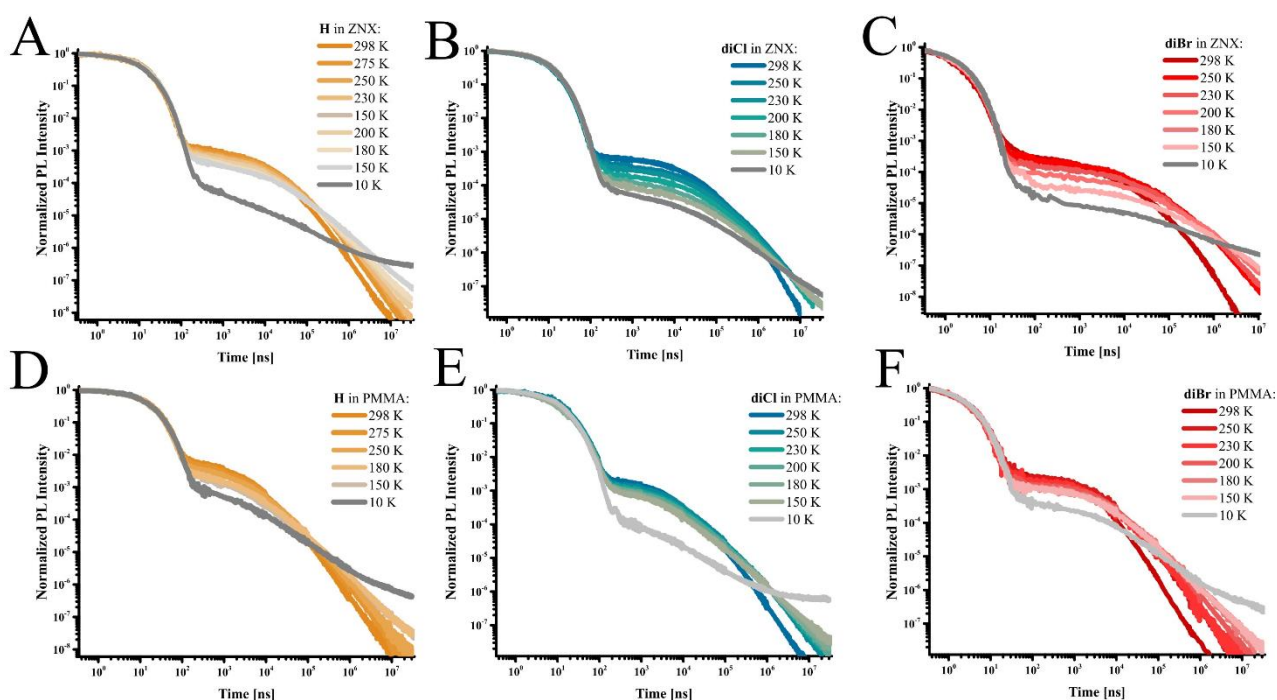


**Figure S13**. PL intensity decay profiles of **H**, **diCl**, and **diBr** in ZNX (A-C) and PMMA (D-F) conducted in various temperatures within 298-10 K. Excitation wavelength $\lambda_{exc}$=370 nm.

**Table S5**. Photophysical parameters in ZNX at various temperatures with corresponding linear regression parameters.

| | T [K] | $\tau_{PF}^b$ [ns] | $\tau_{DF}^b$ [μs] | $k_r$ $10^7$ [s$^{-1}$] | $k_{ISC}$ $10^7$ [s$^{-1}$] | $k_{nr}$ $10^7$ [s$^{-1}$] | $k_{rISC}$ $10^4$ [s$^{-1}$] | ln($k_{ISC}$) | ln($k_{rISC}$) |
|---|---|---|---|---|---|---|---|---|---|
| | | | | | | **ZNX** | | | |
| **H** | 298 | 15.3 | 171 | 1.5 | 5.1 | 0.0 | 1.03 | 17.7 | 9.16 |
| | 275 | 15.3 | 376 | 1.5 | 5.1 | 0.0 | 0.58 | 17.7 | 8.67 |
| | 250 | 15.3 | 724 | 1.5 | 5.1 | 0.0 | 0.30 | 17.7 | 7.98 |
| | 230 | 15.3 | 806 | 1.5 | 5.1 | 0.0 | 0.24 | 17.7 | 7.78 |
| | 200 | 15.3 | 2328 | 1.5 | 5.1 | 0.0 | 0.08 | 17.7 | 6.71 |
| | 180 | 15.3 | 6799 | 1.5 | 5.1 | 0.0 | 0.03 | 17.7 | 5.67 |
| | 150 | 15.3 | 30855 | 1.5 | 5.1 | 0.0 | 0.01 | 17.7 | 4.31 |

Parameters of linear regression for rISC derived from (S11):

| | |
|---|---|
| Slope | 1447 |
| Intercept | 14.02 |
| $E_a$ [meV] | 124 |
| $A$ [s$^{-1}$ $10^7$] | 0.12 |

| | T [K] | $\tau_{PF}^b$ [ns] | $\tau_{DF}^b$ [μs] | $k_r$ $10^7$ [s$^{-1}$] | $k_{ISC}$ $10^7$ [s$^{-1}$] | $k_{nr}$ $10^7$ [s$^{-1}$] | $k_{rISC}$ $10^4$ [s$^{-1}$] | ln($k_{ISC}$) | ln($k_{rISC}$) |
|---|---|---|---|---|---|---|---|---|---|
| **diCl** | 298 | 12.9 | 333 | 1.7 | 6.1 | 0.0 | 0.87 | 17.9 | 9.1 |
| | 250 | 12.8 | 1167 | 1.7 | 6.1 | 0.0 | 0.27 | 17.9 | 7.9 |
| | 230 | 12.9 | 1547 | 1.7 | 6.1 | 0.0 | 0.17 | 17.9 | 7.4 |
| | 200 | 12.9 | 3013 | 1.7 | 6.1 | 0.0 | 0.08 | 17.9 | 6.7 |
| | 180 | 12.9 | 6658 | 1.7 | 6.1 | 0.0 | 0.02 | 17.9 | 5.5 |
| | 150 | 13.0 | 17755 | 1.7 | 6.1 | 0.0 | 0.01 | 17.9 | 4.5 |

Parameters of linear regression for rISC derived from (S11):

| | |
|---|---|
| Slope | 1475 |
| Intercept | 13.71 |
| $E_a$ [meV] | 127 |
| $A$ [s$^{-1}$ $10^7$] | 0.09 |

| | T [K] | $\tau_{PF}^b$ [ns] | $\tau_{DF}^b$ [μs] | $k_r$ $10^7$ [s$^{-1}$] | $k_{ISC}$ $10^7$ [s$^{-1}$] | $k_{nr}$ $10^7$ [s$^{-1}$] | $k_{rISC}$ $10^4$ [s$^{-1}$] | ln($k_{ISC}$) | ln($k_{rISC}$) |
|---|---|---|---|---|---|---|---|---|---|
| **diBr** | 298 | 2.2 | 104 | 2.0 | 38.5 | 3.8 | 1.74 | 19.7 | 9.7 |
| | 250 | 2.2 | 816 | 2.0 | 38.5 | 1.8 | 0.56 | 19.7 | 8.6 |
| | 230 | 2.3 | 1435 | 2.0 | 38.5 | 1.7 | 0.29 | 19.7 | 7.9 |
| | 180 | 2.3 | 9272 | 2.0 | 38.5 | 1.2 | 0.05 | 19.7 | 6.2 |
| | 150 | 2.3 | 32595 | 2.0 | 38.5 | 0.4 | 0.01 | 19.7 | 4.9 |

Parameters of linear regression for rISC derived from (S11):

| | |
|---|---|
| Slope | 1443 |
| Intercept | 14.31 |
| $E_a$ [meV] | 125 |
| $A$ [s$^{-1}$ $10^7$] | 0.16 |
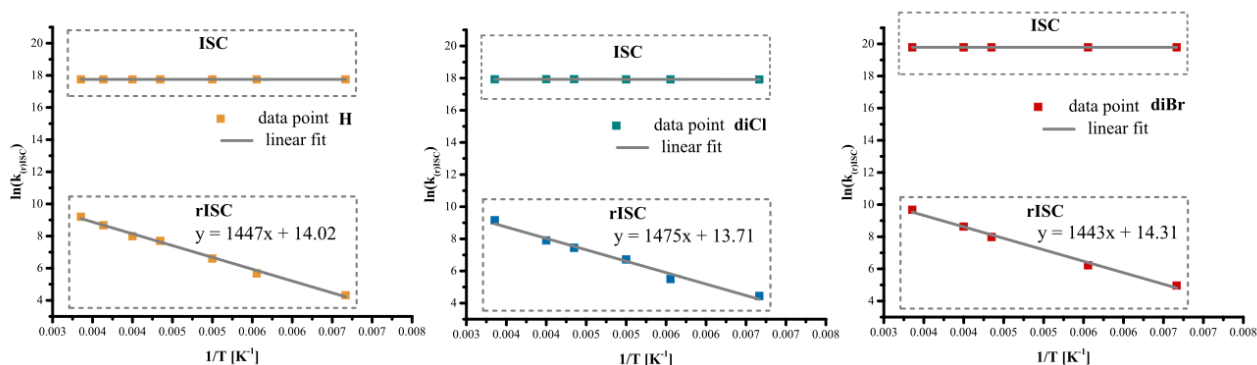


**Figure S14**. Arrhenius plots for emitters dispersed in ZNX.

**Table S6**. Photophysical parameters in PMMA at various temperatures with corresponding linear regression parameters.

| | T [K] | $\tau_{PF}{}^{b}$ [ns] | $\tau_{DF}{}^{b}$ [µs] | $k_r$ $10^7$ [s$^{-1}$] | $k_{ISC}$ $10^7$ [s$^{-1}$] | $k_{nr}$ $10^7$ [s$^{-1}$] | $k_{rISC}$ $10^4$ [s$^{-1}$] | ln($k_{ISC}$) | ln($k_{rISC}$) |
|---|---|---|---|---|---|---|---|---|---|
| | | | | | **PMMA** | | | | |
| **H** | 298 | 17.2 | 96 | 2.0 | 3.8 | 0.04 | 2.92 | 17.4 | 10.1 |
| | 275 | 17.1 | 188 | 2.1 | 3.8 | 0.03 | 1.45 | 17.4 | 9.6 |
| | 250 | 17.1 | 328 | 2.1 | 3.8 | 0.02 | 0.82 | 17.4 | 9.0 |
| | 180 | 17.2 | 1773 | 2.0 | 3.8 | 0.01 | 0.15 | 17.4 | 7.3 |
| | 150 | 17.1 | 4357 | 2.1 | 3.8 | 0.00 | 0.06 | 17.4 | 6.4 |

Parameters of linear regression for rISC derived from (S11):

| | |
|---|---|
| Slope | 1137 |
| Intercept | 13.71 |
| $E_a$ [meV] | 98 |
| $A$ [s$^{-1}$ $10^7$] | 0.09 |

| | T [K] | $\tau_{PF}{}^{b}$ [ns] | $\tau_{DF}{}^{b}$ [µs] | $k_r$ $10^7$ [s$^{-1}$] | $k_{ISC}$ $10^7$ [s$^{-1}$] | $k_{nr}$ $10^7$ [s$^{-1}$] | $k_{rISC}$ $10^4$ [s$^{-1}$] | ln($k_{ISC}$) | ln($k_{rISC}$) |
|---|---|---|---|---|---|---|---|---|---|
| **diCl** | 298 | 16.0 | 139 | 2.1 | 4.1 | 0.11 | 1.85 | 17.5 | 9.8 |
| | 250 | 16.0 | 431 | 2.1 | 4.1 | 0.10 | 0.67 | 17.5 | 8.7 |
| | 230 | 16.0 | 701 | 2.1 | 4.1 | 0.08 | 0.36 | 17.5 | 8.2 |
| | 200 | 15.9 | 1165 | 2.2 | 4.1 | 0.06 | 0.20 | 17.5 | 7.6 |
| | 180 | 16.1 | 2050 | 2.1 | 4.1 | 0.03 | 0.11 | 17.5 | 7.0 |
| | 150 | 16.1 | 5392 | 2.1 | 4.1 | 0.01 | 0.04 | 17.5 | 6.0 |

Parameters of linear regression for rISC derived from (S11):

| | |
|---|---|
| Slope | 1098 |
| Intercept | 13.23 |
| $E_a$ [meV] | 95 |
| $A$ [s$^{-1}$ $10^7$] | 0.06 |

| | T [K] | $\tau_{PF}{}^{b}$ [ns] | $\tau_{DF}{}^{b}$ [µs] | $k_r$ $10^7$ [s$^{-1}$] | $k_{ISC}$ $10^7$ [s$^{-1}$] | $k_{nr}$ $10^7$ [s$^{-1}$] | $k_{rISC}$ $10^4$ [s$^{-1}$] | ln($k_{ISC}$) | ln($k_{rISC}$) |
|---|---|---|---|---|---|---|---|---|---|
| **diBr** | 298 | 2.6 | 38 | 2.1 | 30.8 | 3.1 | 8.23 | 19.5 | 11.2 |
| | 250 | 2.6 | 110 | 2.1 | 30.8 | 2.9 | 4.43 | 19.5 | 10.7 |
| | 230 | 2.6 | 179 | 2.0 | 30.8 | 2.8 | 2.26 | 19.5 | 10.1 |
| | 200 | 2.6 | 386 | 2.1 | 30.8 | 2.0 | 1.30 | 19.5 | 9.5 |
| | 180 | 2.8 | 672 | 2.0 | 30.8 | 1.8 | 0.72 | 19.5 | 8.9 |
| | 150 | 2.8 | 1738 | 2.0 | 30.8 | 1.5 | 0.27 | 19.5 | 7.9 |

Parameters of linear regression for rISC derived from (S11):

| | |
|---|---|
| Slope | 1071 |
| Intercept | 14.77 |
| $E_a$ [meV] | 92 |
| $A$ [s$^{-1}$ $10^7$] | 0.26 |



**Figure S15**. Arrhenius plots for emitters dispersed in PMMA.

More detailed information can be derived using the Marcus-Hush equation:

$$k_{(r)ISC} = \frac{V^2}{\hbar} \sqrt{\frac{\pi}{k_B T \lambda}} \exp\left[-\frac{(\Delta E_{ST} + \lambda)^2}{4 k_B T \lambda}\right], \qquad \text{(S12)}$$

where $V$ is SOC constant, $\hbar$ is reduced Planck's constant, $\lambda$ is sum of internal and external ($\lambda_{solv}$) reorganization energies for respective transition, $\Delta E_{ST}$ is the energy gap between singlet $^1$CT and respective triplet state. This semiclassical expression, commonly used to predict constant rates for non-radiative transitions in D-A structure of TADF compounds can be connected with the Arrhenius equation (S11) by the following relations:

$$A = \frac{V^2}{\hbar} \sqrt{\frac{\pi}{k_B T \lambda}}, \qquad \text{(S13)}$$

$$E_a = \frac{(\Delta E_{ST} + \lambda)^2}{4\lambda}. \qquad \text{(S14)}$$

Consequently, by matching the $\Delta E_{ST}$ and $\lambda$ parameters to satisfy both relations, where $E_a$ and $A$ are derived from Arrhenius plot, it is possible to estimate empirical SOC values $V$ for each transition, as it is presented in **Table 2** (main text).

As discussed in main text, because ISC transition does not require thermal activation under all conditions investigated ($E_a = 0$), the relation (S14) predicts the same values of $\Delta E_{ST}$ and $\lambda$:

$$\Delta E_{ST} = \lambda. \qquad \text{(S15)}$$

Assuming equal values of $\Delta E_{ST}$ for both ISC and rISC (S6):

$$\Delta E_{ST}(\text{ISC}) = -\Delta E_{ST}(\text{rISC}), \qquad \text{(S16)}$$

the $\Delta E_{ST}$ and $\lambda$ values can be obtained from eq. (S14) and $E_a$ (**Table 2**). The $V_{ISC}$ and $V_{rISC}$ parameters are then available from eq. (S14) and $A$ (**Table 2**):

$$\text{(S17)}$$

$$A_{ISC} = \frac{V_{ISC}^2}{\hbar} \sqrt{\frac{\pi}{k_B T \lambda}},$$

$$A_{rISC} = \frac{V_{rISC}^2}{\hbar} \sqrt{\frac{\pi}{k_B T \lambda}}. \tag{S18}$$

The assumption (S16) seems to be valid because regardless of the ISC and rISC mechanism, the $\Delta E_{1CT-3CT}$ and $\Delta E_{1CT-3LE(A)}$ values were determined to be similar (**Table 1**). On the other hand, the changes in the obtained $V_{ISC}$ and $V_{rISC}$ values are much greater than those in $\Delta E_{ST}$. Therefore, the assumption (S16) introduces minor uncertainty and does not affect the most important conclusions made for ISC and rISC mechanisms.

*Test for the comparability of the investigated emitters.* In an ideal case, to compare different emitters under the conditions of isomeric inhomogeneity, same kinds of their rotational and vibrational isomers should be taken into account in the similar amounts. To check if this criterion is fulfilled the analysis of Arrhenius plot can be performed. In the current example, despite the fact that the $k_{nr}$ values are different under various temperatures, their change does not affect the dependence of $k_{rISC}$ on 1/T: 1) the $k_{rISC}$(1/T) dependence remains linear for all the investigated temperature range; 2) the slope of the $k_{rISC}$(1/T) dependence is almost identical for all three compounds (Figures S14 and S15). This means that all kinds of the rotational and vibrational isomers are represented under various temperatures and in all three compounds. None of the rotational and vibrational isomers are added or eliminated under the change of temperature. In other words, the investigated molecular systems are totally comparable but represent with different emission intensity due to different PLQY.

Strong temperature dependence of $k_{nr}$ in both **diCl** and **diBr**, evidence that main nonradiative deactivation channel can be activated by the molecular vibrations involving heavy atom(s). However, good photochemical stability of the investigated samples under experimental conditions, i.e. irradiation with 10 mJ laser beam, indicates the breakage of neither C–Br nor C–Cl bond is responsible for the non-radiative deactivation.

## Section S5: Theoretical prediction of ISC and rISC rate constants for the ¹CT-³LE transitions

**Calculations for ISC rate constants.** Theoretical rate constants of ISC and rISC were calculated using Marcus-Hush equation (S12). According to the IUPAC definition, [S5] term reorganization energy $\lambda$ corresponds to the energy that is dissipated by molecule that underwent vertical excitation, when relaxing to the equilibrium state for its new charge distribution. Commonly, total $\lambda$ is a sum of inner ($\lambda_{in}$) and outer ($\lambda_{out}$) reorganization energies:

$$\lambda = \lambda_{in} + \lambda_{out}. \tag{S19}$$

By performing single-point TD-DFT calculations for **H**, **diCl** and **diBr**, we determined the values of inner reorganization energies $\lambda_{in}$ for each ISC transition, namely:

- $^1CT \rightarrow {}^3LE(A)$: $\lambda_{in} = \lambda_{1CT \rightarrow 3LE(A)}$

- $^1CT \rightarrow {}^3LE(D)$: $\lambda_{in} = \lambda_{1CT \rightarrow 3LE(D)}$

using the following formulas:

$$\lambda_{1CT \rightarrow 3LE(A)} = E_{3LE(A)}^{1CT} - E_{3LE(A)}^{3LE(A)}, \tag{S20}$$

$$\lambda_{1CT \rightarrow 3LE(D)} = E_{3LE(D)}^{1CT} - E_{3LE(D)}^{3LE(D)}, \tag{S21}$$

where:

$E_{3LE(A)}^{1CT}$ - TD-DFT energy of $^3LE(A)$ excited state at the $^1CT$ optimized geometry

$E_{3LE(A)}^{3LE(A)}$ - TD-DFT energy of $^3LE(A)$ excited state at the $^3LE(A)$ optimized geometry

$E_{3LE(D)}^{1CT}$ - TD-DFT energy of $^3LE(D)$ excited state at the $^1CT$ optimized geometry,

$E_{3LE(D)}^{3LE(D)}$ - TD-DFT energy of $^3LE(D)$ excited state at the $^3LE(D)$ optimized geometry.

The $\lambda_{out}$ value of 0.05 eV was used for all calculations.

Since DFT fails to predict $\Delta E_{ST}$, the experimentally determined mean values of $\Delta E_{1CT-3LE(A)}$ and $\Delta E_{1CT-3LE(D)}$ were used (**Table 1**, main text).

Computed reorganization energies for respective ISC transitions:

| | $^1CT \to {}^3LE(A)$ | | | $^1CT \to {}^3LE(D):$ | | |
|---|---|---|---|---|---|---|
| | $E_{3LE(A)}^{1CT}$ | $E_{3LE(A)}^{3LE(A)}$ | $\lambda_{1CT\to3LE(A)}$ | $E_{3LE(D)}^{1CT}$ | $E_{3LE(D)}^{3LE(D)}$ | $\lambda_{1CT\to3LE(D)}$ |
| cmpd | [a. u] | [a. u] | [eV] | [a. u] | [a. u] | [eV] |
| **H** | -1607.3656182 | -1607.3715987 | 0.17 | -1607.3509293 | -1607.3594832 | 0.23 |
| **diCl** | -1636.0412315 | -1636.0470891 | 0.16 | -1636.0292145 | -1636.0381835 | 0.24 |
| **diBr** | -1632.4758713 | -1632.4840055 | 0.22 | -1632.4653425 | -1632.4757523 | 0.28 |

**Table S7.** Computational data for prediction ISC constant rate within $^1CT \to {}^3LE(A)$ transition

| | | $V_{1CT\to3LE(A)}{}^a$ | $\lambda_{1CT\to3LE(A)}{}^b$ | $\Delta E_{1CT\text{-}3LE(A)}{}^c$ | $k_{1CT\to3LE(A)}{}^d$ |
|---|---|---|---|---|---|
| | | [cm$^{-1}$] | [eV] | [eV] | $10^7$ [s$^{-1}$] |
| **H** | ZNX | 0.63 | 0.17 | -0.09 | 6.69 |
| **diCl** | | 0.49 | 0.16 | -0.13 | 6.45 |
| **diBr** | | 0.59 | 0.22 | -0.11 | 4.27 |
| | | | | | |
| **H** | PMMA | 0.63 | 0.17 | -0.05 | 3.41 |
| **diCl** | | 0.49 | 0.16 | -0.07 | 3.12 |
| **diBr** | | 0.59 | 0.22 | -0.06 | 1.98 |

[a] - SOC constant value for the $^1CT \to {}^3LE(A)$ transition calculated in optimized $^1CT$ – state geometry;

[b] - inner reorganization energy for $^1CT \to {}^3LE(A)$ transition ($\lambda_{out} = 0.05$ eV);

[c] - energy gap from **Table 1**;

[d] -predicted constant rate calculated using equation (S12).

**Table S8.** Computational data for prediction $^1CT \rightarrow {}^3LE(D)$ transition.

| $^1CT \rightarrow {}^3LE(D)$ | Mean $^1CT$ values | | | | | | | |
|---|---|---|---|---|---|---|---|---|
| | | $^1CT$ | | $^3LE(D)$ | | $V_{1CT \rightarrow 3LE(D)}{}^d$ | $\lambda_{1CT \rightarrow 3LE(D)}{}^e$ | $\Delta E_{1CT\text{-}3LE(D)}{}^f$ | $k_{1CT \rightarrow 3LE(D)}{}^i$ |
| | | $[nm]^a$ | $[eV]^b$ | $[nm]^c$ | $[eV]^b$ | $[cm^{-1}]$ | $[eV]$ | $[eV]$ | $10^7\ [s^{-1}]$ |
| **H** | ZNX | 423 | 2.93 | 392 | 3.16 | 0.70 | 0.23 | 0.23 | 0.016 |
| **diCl** | | 418 | 2.97 | 410 | 3.02 | 1.20 | 0.24 | 0.06 | 0.880 |
| **diBr** | | 421 | 2.95 | 412 | 3.01 | 3.30 | 0.28 | 0.06 | 6.122 |
| **H** | PMMA | 430 | 2.88 | 392 | 3.16 | 0.70 | 0.23 | 0.28 | 0.0003 |
| **diCl** | | 437 | 2.90 | 410 | 3.02 | 1.20 | 0.24 | 0.12 | 0.177 |
| **diBr** | | 428 | 2.89 | 412 | 3.01 | 3.30 | 0.28 | 0.11 | 1.810 |

| $^1CT \rightarrow {}^3LE(D)$ | Rotameric $^1CT$ species in PMMA | | | | | | | |
|---|---|---|---|---|---|---|---|---|
| | | $^1CT$ | | $^3LE(D)$ | | $V_{1CT \rightarrow 3LE(D)}{}^d$ | $\lambda_{1CT \rightarrow 3LE(D)}{}^e$ | $\Delta E_{1CT\text{-}3LE(D)}{}^f$ | $k_{1CT \rightarrow 3LE(D)}{}^h$ |
| | | $[nm]^g$ | $[eV]^b$ | $[nm]^c$ | $[eV]^b$ | $[cm^{-1}]$ | $[eV]$ | $[eV]$ | $10^7\ [s^{-1}]$ |
| | | high energy $^1CT$ species | | | | | | | |
| **H** | PMMA | 419 | 2.96 | 392 | 3.16 | 0.70 | 0.23 | 0.20 | 0.005 |
| **diCl** | | 415 | 2.99 | 410 | 3.02 | 1.20 | 0.24 | 0.03 | 1.542 |
| **diBr** | | 416 | 2.99 | 412 | 3.01 | 3.30 | 0.28 | 0.02 | 15.33 |
| | | low energy $^1CT$ species | | | | | | | |
| **H** | PMMA | 442 | 2.80 | 392 | 3.16 | 0.70 | 0.23 | 0.36 | 0.0001 |
| **diCl** | | 439 | 2.83 | 410 | 3.02 | 1.20 | 0.24 | 0.20 | 0.016 |
| **diBr** | | 440 | 2.82 | 412 | 3.01 | 3.30 | 0.28 | 0.19 | 0.173 |

[a] - experimentally determined from steady-state PL spectra. **Figure S6**;

[b] - energies calculated from relation: $E = 1240/\lambda_{onset}$;

[c] - experimentally determined from phosphorescence spectra of donor fragments (**Figures S6H**);

[d] - SOC values for the $^1CT \rightarrow {}^3LE(D)$ transition calculated for the optimized $^1CT$-state geometry;

[e] - inner reorganization energy for $^1CT \rightarrow {}^3LE(D)$ transition, $\lambda_{out} = 0.05$ eV;

[f] - energy gap determined from the difference of respective onsets of PL spectra: $\Delta E_{1\text{-}2} = (1240/\lambda_{onset1} - 1240/\lambda_{onset2})$;

[g] - determined from time-dependend PL spectra (see **Figure S11** and **Table S2**);

[h] - predicted constant rates calculated from equation (S12).

**Table S9**. Summary of predicted ISC constant rates.

| cmpd | | $k_{1CT \rightarrow 3LE(A)}$ | $\mu_{1CT \rightarrow 3LE(A)}$[a] | $k_{1CT \rightarrow 3LE(D)}$ | $\mu_{1CT \rightarrow 3LE(D)}$[a] | $k_{1CT \rightarrow 3LE(A)} + k_{1CT \rightarrow 3LE(D)}$ | $k_{ISC}$ |
|------|------|------|------|------|------|------|------|
| | | Theoretical | | | | | Experimental |
| | | $10^7$ [s$^{-1}$] | [%] | $10^7$ [s$^{-1}$] | [%] | $10^7$ [s$^{-1}$] | $10^7$ [s$^{-1}$] |
| **H** | ZNX | 6.69 | 100 | 0.016 | 0 | 6.7 | 5.1 |
| **diCl** | | 6.45 | 88 | 0.880 | 12 | 7.3 | 6.1 |
| **diBr** | | 4.27 | 41 | 6.122 | 59 | 10.4 | 38.5 |
| **H** | PMMA | 3.41 | 100 | 0.0003 | 0 | 3.4 | 3.8 |
| **diCl** | | 3.12 | 95 | 0.177 | 5 | 3.3 | 4.1 |
| **diBr** | | 1.98 | 52 | 1.810 | 48 | 3.5 | 30.8 |
| | | high energy $^1$CT species | | | | | |
| **H** | PMMA | 9.19 | 100 | 0.005 | 0 | 9.2 | 3.8 |
| **diCl** | | 7.61 | 83 | 1.542 | 17 | 9.1 | 4.1 |
| **diBr** | | 6.44 | 30 | 15.33 | 70 | 21.8 | 30.8 |
| | | low energy $^1$CT species | | | | | |
| **H** | PMMA | 0.80 | 100 | 0.0001 | 0 | 0.8 | 3.8 |
| **diCl** | | 0.84 | 99 | 0.016 | 1 | 0.8 | 4.1 |
| **diBr** | | 0.52 | 75 | 0.173 | 25 | 0.7 | 30.8 |

[a] - Relative contributions for respective transitions calculated as follows: $\mu_{1CT \rightarrow 3LE(A)} = 100\% \cdot k_{1CT \rightarrow 3LE(A)} /$

$(k_{1CT \rightarrow 3LE(A)} + k_{1CT \rightarrow 3LE(D)})$ and $\mu_{1CT \rightarrow 3LE(D)} = 100\% \cdot k_{1CT \rightarrow 3LE(D)} /(k_{1CT \rightarrow 3LE(A)} + k_{1CT \rightarrow 3LE(D)})$

**Calculations for rISC rate constants.** rISC constant rates were calculated using Marcus-Hush formula (S12), computationally predicted λ values and experimentally determined $\Delta E_{ST}$ values. Due to the coexistence of excited molecules in various triplet states, their contribution to the rISC transition was considered as proportional to the population of respective triplet states (**Table S10**).

*Determination of population of lowest triplet excited states*
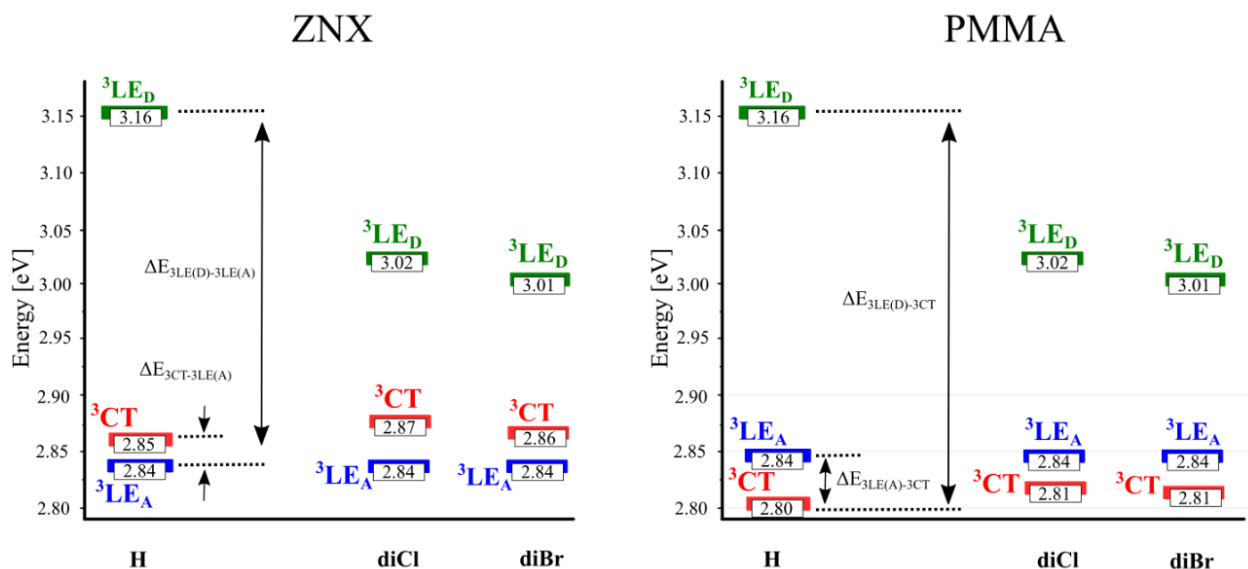


**Figure S16**. Alignment of the excited triplet states of investigated emitters.

Relative population $\chi_i$ of lowest triplet excited states was determinated using Boltzmann distribution law:

$$\chi_i = \frac{\exp\left(-\frac{\Delta E_i}{k_B T}\right)}{\sum_{i=1}^{N} \exp\left(-\frac{\Delta E_i}{k_B T}\right)}, \tag{S22}$$

where $\Delta E_i$ denotes the energy difference between lowest triplet state ($T_1$) and respective triplet state ($T_i$):

$$\Delta E_i = (T_i - T_1), \tag{S23}$$

$$a_i = \exp\left(-\frac{(T_i - T_1)}{k_B T}\right). \tag{S24}$$

**Table S10.** Population of lowest triplet excited states of emitters in ZNX and PMMA.

| | | | | | | | | **$^3$LE(A)** | **$^3$CT** | **$^3$LE(D)** |
|---|---|---|---|---|---|---|---|---|---|---|
| **ZNX** | | | | | | | | | | |
| Alignment of triplet excited states: | $T_3 = {}^3$LE(D) $T_2 = {}^3$CT $T_1 = {}^3$LE(A) | | | | | | | | | |
| | $T_1$ [eV] | $T_2$ [eV] | $T_3$ [eV] | $\Delta E_{T2\text{-}T1}$ [eV] | $\Delta E_{T3\text{-}T1}$ [eV] | $a_1$ | $a_2$ | $a_3$ | $\chi_{3LE(A)}$ [%] | $\chi_{3CT}$ [%] | $\chi_{3LE(D)}$ [%] |
| **H** | 2.84 | 2.85 | 3.16 | 0.01 | 0.32 | 1 | 0.55 | <0.0001 | 64.6 | 35.4 | <0.001 |
| **diCl** | 2.84 | 2.87 | 3.02 | 0.03 | 0.18 | 1 | 0.35 | 0.00061 | 74.0 | 25.9 | 0.045 |
| **diBr** | 2.84 | 2.86 | 3.01 | 0.02 | 0.17 | 1 | 0.43 | 0.00092 | 69.6 | 30.3 | 0.064 |

| | | | | | | | | **$^3$CT** | **$^3$LE(A)** | **$^3$LE(D)** |
|---|---|---|---|---|---|---|---|---|---|---|
| **PMMA** | | | | | | | | | | |
| Alignment of triplet excited states: | $T_3 = {}^3$LE(D) $T_2 = {}^3$LE(A) $T_1 = {}^3$CT | | | | | | | | | |
| | $T_1$ [eV] | $T_2$ [eV] | $T_3$ [eV] | $\Delta E_{T2\text{-}T1}$ [eV] | $\Delta E_{T3\text{-}T1}$ [eV] | $a_1$ | $a_2$ | $a_3$ | $\chi_{3CT}$ [%] | $\chi_{3LE(A)}$ [%] | $\chi_{3LE(D)}$ [%] |
| **H** | 2.80 | 2.84 | 3.16 | 0.04 | 0.36 | 1 | 0.23 | <0.001 | 81.7 | 18.3 | <0.001 |
| **diCl** | 2.81 | 2.84 | 3.02 | 0.03 | 0.21 | 1 | 0.36 | 0.0002 | 73.1 | 26.9 | 0.017 |
| **diBr** | 2.81 | 2.84 | 3.01 | 0.03 | 0.20 | 1 | 0.36 | 0.0003 | 73.1 | 26.9 | 0.029 |

**Table S11**. Computational data for rISC constant rate prediction within $^3$LE(A)→$^1$CT and $^3$LE(D)→$^1$CT transitions.

### $^3$LE(A) → $^1$CT

| | | $V_{3LE(A)\to1CT}{}^a$ [cm$^{-1}$] | $\lambda_{3LE(A)\to1CT}{}^b$ [eV] | $\Delta E_{3LE(A)\text{-}1CT}{}^c$ [eV] | $\chi_{3LE(A)}{}^d$ [%] | $k_{3LE(A)\to1CT}{}^e$ [s$^{-1}$] | $\chi_{3LE(A)}k_{3LE(A)\to1CT}{}^f$ [s$^{-1}$] |
|---|---|---|---|---|---|---|---|
| **H** | ZNX | 0.24 | 0.17 | 0.09 | 64 | 3.2 x 10$^5$ | 2.0 x 10$^5$ |
| **diCl** | | 0.51 | 0.16 | 0.13 | 74 | 5.2 x 10$^5$ | 3.9 x 10$^5$ |
| **diBr** | | 0.24 | 0.22 | 0.11 | 69 | 1.3 x 10$^5$ | 8.3 x 10$^4$ |
| **H** | PMMA | 0.24 | 0.17 | 0.05 | 18 | 1.1 x 10$^6$ | 1.9 x 10$^5$ |
| **diCl** | | 0.51 | 0.16 | 0.07 | 27 | 3.8 x 10$^6$ | 1.0 x 10$^6$ |
| **diBr** | | 0.24 | 0.22 | 0.06 | 27 | 4.8 x 10$^5$ | 1.3 x 10$^5$ |

### $^3$LE(D) → $^1$CT

| | | $V_{3LE(D)\to1CT}{}^a$ [cm$^{-1}$] | $\lambda_{3LE(D)\to1CT}{}^b$ [eV] | $\Delta E_{3LE(D)\text{-}1CT}{}^c$ [eV] | $\chi_{3LE(D)}{}^d$ [%] | $k_{3LE(D)\to1CT}{}^e$ [s$^{-1}$] | $\chi_{3LE(D)}k_{3LE(D)\to1CT}{}^f$ [s$^{-1}$] |
|---|---|---|---|---|---|---|---|
| **H** | ZNX | 0.70 | 0.23 | 0.23 | 0.01 | 1.6 x 10$^4$ | 1.6 x 10$^0$ |
| **diCl** | | 1.21 | 0.24 | 0.05 | 0.05 | 8.9 x 10$^6$ | 4.5 x 10$^3$ |
| **diBr** | | 3.10 | 0.28 | 0.06 | 0.10 | 5.4 x 10$^7$ | 5.4 x 10$^4$ |
| **H** | PMMA | 0.70 | 0.23 | 0.28 | 0.01 | 3.2 x 10$^3$ | 3.2 x 10$^{-1}$ |
| **diCl** | | 1.21 | 0.24 | 0.12 | 0.02 | 1.8 x 10$^6$ | 3.6 x 10$^2$ |
| **diBr** | | 3.10 | 0.28 | 0.11 | 0.03 | 1.6 x 10$^7$ | 4.8 x 10$^3$ |

$^a$ - SOC values for the $^3$LE(A) → $^1$CT transition calculated in optimized $^3$LE(A) – state geometry and for $^3$LE(D) → $^1$CT transition calculated in optimized $^3$LE(D) – state geometry, respectively;
$^b$ - reorganization energies for the $^3$LE(A) → $^1$CT and $^3$LE(D) → $^1$CT transitions, respectively;
$^c$ - energy gap between $^3$LE(A), $^3$LE(D) and $^1$CT states (see **Table S1**);
$^d$ - estimated population of $^3$LE(A) and $^3$LE(D) triplet states (see **Table S10**);
$^e$ - calculated rISC rate constant using equation (S12);
$^f$ - calculated rISC constant rates corrected on population of respective excited triplet states.

## Section S6: Computational details for the prediction of rISC rate constant within rotational model via direct ³CT-¹CT transition

Within the rotational model, the total $k_{3CT \to 1CT}$ consists of fractional rate constant $k_{3CT \to 1CT}[\theta_i]$, originating from various $\theta$-rotamers (as depicted in **Figures 1B** and **1F**):

$$k_{3CT \to 1CT} = \sum_{i=1}^{n} p[\theta_i] \cdot k_{3CT \to 1CT}[\theta_i] \tag{S25}$$

where:

- $p[\theta_i]$ - molar fraction of $i$-th rotamer with $\theta$ dihedral angle between donor and acceptor (**Figure 1B**) within Boltzmann distribution function,

- $n$ is the number of considered rotamers;

- $k_{3CT \to 1CT}[\theta_i]$ - fractional rate constant, calculated using Marcus-Hush equation as follows:

$$k_{3CT \to 1CT}[\theta_i] = \frac{(V_{3CT \to 1CT}[\theta_i])^2}{\hbar} \sqrt{\frac{\pi}{k_B T\, \lambda_{3CT \to 1CT}[\theta_i]}} \exp\left[-\frac{(\Delta E_{3CT-1CT}[\theta_i] + \lambda_{3CT \to 1CT}[\theta_i])^2}{4 k_B T \lambda_{3CT \to 1CT}[\theta_i]}\right], \tag{S26}$$

where:

- $V_{3CT \to 1CT}[\theta_i]$ - SOC constant calculated for $i$-th rotamer with $\theta$ dihedral angle at the ³CT-state geometry,

- $\lambda_{3CT \to 1CT}[\theta_i]$ - reorganization energy,

- $\Delta E_{3CT-1CT}[\theta_i]$ - energy gap between ¹CT and ³CT states of $i$-th rotamer with $\theta$ dihedral angle,

- $k_B$ is Boltzmann constant ($k_B = 8.617 \times 10^{-5}$ eV/K),

- T - temperature (for all of calculations T = 298 K).

Reorganization energy $\lambda_{3CT \to 1CT}[\theta_i]$ consists of two terms (inner $\lambda_{3CT \to 1CT}^{in}[\theta_i]$ and outer $\lambda_{3CT \to 1CT}^{out}$):

$$\lambda_{3CT \to 1CT}[\theta_i] = \lambda_{3CT \to 1CT}^{in}[\theta_i] + \lambda_{3CT \to 1CT}^{out}. \tag{S27}$$

The first term $\lambda_{3CT \to 1CT}^{in}[\theta_i]$ refers to the energy that is dissipated by molecule during relaxation to the equilibrium geometry in a given state.

It can be calculated using the formula:

$$\lambda^{\text{in}}_{3\text{CT}\rightarrow1\text{CT}}[\theta_i] = E^{1\text{CT}}_{3\text{CT}}[\theta_i] - E^{1\text{CT}}_{1\text{CT}},$$ (S28)

where:

- $E^{1\text{CT}}_{3\text{CT}}[\theta_i]$ - TD-DFT energy of $^1$CT state at $^3$CT-state geometry calculated for $i$-th rotamer with $\theta$ dihedral angle,

- $E^{1\text{CT}}_{1\text{CT}}$ − TD-DFT energy of $^1$CT state at optimized $^1$CT-state geometry.

The second term $\lambda^{\text{out}}_{3\text{CT}\rightarrow1\text{CT}}$ is a measure of solvatation effects, and in case of interaction between excited states with the same nature (CT) it can be approximated as follows:

$$\lambda^{\text{out}}_{3\text{CT}\rightarrow1\text{CT}} \approx \Delta E_{3\text{CT}-1\text{CT}}[\theta_i].$$ (S29)

Boltzmann distribution law was used to estimate relative population of rotamers $p[\theta_i]$:

$$p[\theta_i] = Z^{-1} \cdot \exp\left(-\frac{\Delta\text{E}[\theta_i]}{k_B T}\right),$$ (S30)

$$\Delta\text{E}[\theta_i] = E[\theta_i] - E^{1\text{CT}}_{1\text{CT}},$$ (S31)

$$Z = \sum_{i=1}^{n} \exp\left(-\frac{\Delta\text{E}[\theta_i]}{k_B T}\right),$$ (S32)

where:

- $E[\theta_i]$ – energy calculated for $i$-th rotamer with $\theta$ dihedral angle,

- $E^{1\text{CT}}_{1\text{CT}}$ - energy at optimized $^1$CT- state geometry.

Below, complete set of computed parameters for prediction of $k_{3\text{CT}\rightarrow1\text{CT}}$ in **H**, **diCl** and **diBr** within developed rotational model is presented (**Tables S12** – **S14** and **Figures S17** – **S19**).

**Table S12.** Computational parameters for $k_{3CT \to 1CT}$ prediction in **H** using rotational model.

| $\theta_i$ | $\Delta E[\theta_i]$ | $p[\theta_i]$ | $\Delta E_{3CT-1CT}[\theta_i]$ | $V_{3CT \to 1CT}[\theta_i]$ | $\lambda_{3CT \to 1CT}[\theta_i]$ | $k_{3CT \to 1CT}[\theta_i]$ | $p[\theta_i] \cdot k_{3CT \to 1CT}[\theta_i]$ |
|---|---|---|---|---|---|---|---|
| [O] | [meV] | [%] | [meV] | [cm⁻¹] | [meV] | 10⁴ [s⁻¹] | 10⁴ [s⁻¹] |
| 90 | 0.0 | 4.1 | 4.7 | 0 | 0.0 | 0.0 | 0.000 |
| 89 | 0.2 | 4.1 | 4.8 | 0.01 | 0.3 | 0.1 | 0.004 |
| 88 | 0.5 | 4.0 | 5.5 | 0.02 | 1.3 | 0.3 | 0.025 |
| 87 | 1.0 | 3.9 | 6.6 | 0.03 | 3.0 | 1.5 | 0.057 |
| 86 | 1.7 | 3.8 | 8.3 | 0.04 | 5.3 | 2.5 | 0.095 |
| 85 | 2.6 | 3.7 | 10.4 | 0.05 | 8.4 | 2.9 | 0.134 |
| 84 | 3.9 | 3.5 | 13.1 | 0.05 | 12.3 | 4.7 | 0.125 |
| 83 | 5.5 | 3.3 | 16.2 | 0.06 | 16.9 | 4.9 | 0.159 |
| 82 | 7.4 | 3.1 | 19.6 | 0.06 | 22.3 | 5.0 | 0.112 |
| 81 | 9.6 | 2.8 | 23.7 | 0.07 | 28.5 | 5.5 | 0.119 |
| 80 | 12.1 | 2.6 | 28.1 | 0.08 | 35.4 | 5.8 | 0.118 |
| 79 | 14.9 | 2.3 | 33.1 | 0.09 | 43.1 | 5.9 | 0.110 |
| 78 | 18.1 | 2.0 | 38.3 | 0.10 | 51.6 | 5.8 | 0.096 |
| 77 | 21.7 | 1.8 | 44.0 | 0.11 | 60.8 | 5.4 | 0.080 |
| 76 | 25.7 | 1.5 | 50.2 | 0.12 | 70.9 | 4.2 | 0.063 |
| 75 | 30.2 | 1.3 | 56.5 | 0.13 | 81.7 | 3.8 | 0.048 |
| 74 | 35.1 | 1.0 | 63.3 | 0.14 | 93.4 | 3.3 | 0.034 |
| 73 | 40.5 | 0.8 | 70.5 | 0.15 | 105.9 | 2.8 | 0.024 |
| 72 | 46.5 | 0.7 | 77.9 | 0.16 | 119.2 | 2.1 | 0.016 |
| 71 | 52.9 | 0.5 | 85.6 | 0.16 | 133.4 | 1.7 | 0.009 |
| 70 | 60.0 | 0.4 | 93.6 | 0.16 | 148.4 | 1.2 | 0.005 |
| 69 | 67.8 | 0.3 | 101.7 | 0.16 | 164.2 | 0.8 | 0.002 |
| 68 | 76.3 | 0.2 | 110.2 | 0.16 | 181.2 | 0.6 | 0.001 |
| 67 | 85.7 | 0.1 | 118.3 | 0.17 | 199.2 | 0.4 | 0.001 |
| 66 | 95.9 | 0.1 | 127.8 | 0.17 | 218.2 | 0.3 | 0.000 |
| 65 | 107.0 | 0.1 | 136.8 | 0.17 | 238.3 | 0.3 | 0.000 |
| 64 | 119.1 | 0.0 | 145.9 | 0.18 | 259.4 | 0.2 | 0.000 |
| 63 | 132.2 | 0.0 | 155.3 | 0.18 | 281.2 | 0.1 | 0.000 |
| 62 | 146.5 | 0.0 | 164.7 | 0.18 | 305.4 | 0.1 | 0.000 |
| 61 | 163.4 | 0.0 | 172.6 | 0.19 | 330.2 | 0.0 | 0.000 |
| 60 | 182.4 | 0.0 | 180.1 | 0.19 | 356.5 | 0.0 | 0.000 |

Rate constant calculated for **H** within rotational model $\quad k_{3CT \to 1CT} \quad = \quad$ **2.81** [10⁴ s⁻¹]
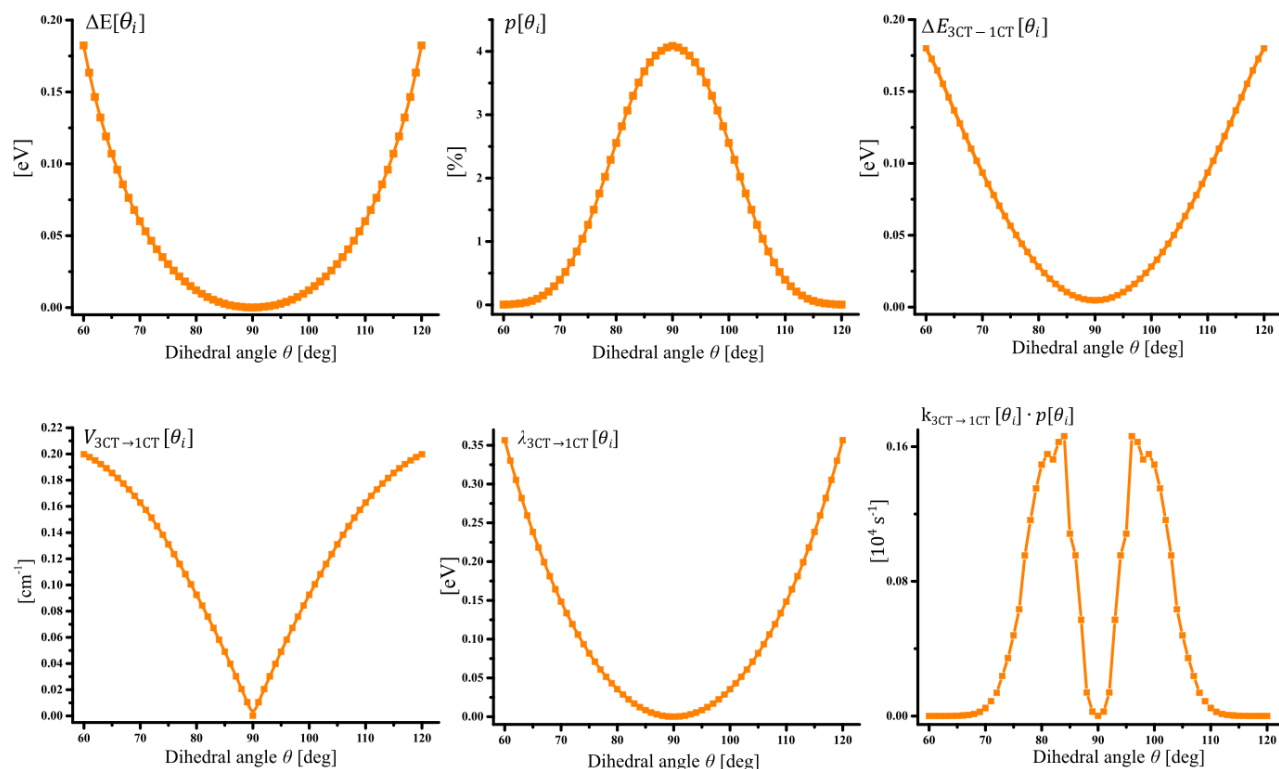


**Figure S17.** Computational parameters for the prediction of $k_{3CT \to 1CT}$ in **H** calculated within rotational model.

| | | | | Computational parameters for prediction $k_{3CT \rightarrow 1CT}$ in **diCl** | | | |
|---|---|---|---|---|---|---|---|
| $\theta_i$ | $\Delta E[\theta_i]$ | $p[\theta_i]$ | $\Delta E_{3CT-1CT}[\theta_i]$ | $V_{3CT \rightarrow 1CT}[\theta_i]$ | $\lambda_{3CT \rightarrow 1CT}[\theta_i]$ | $k_{3CT \rightarrow 1CT}[\theta_i]$ | $p[\theta_i] \cdot k_{3CT \rightarrow 1CT}[\theta_i]$ |
| [$^O$] | [meV] | [%] | [meV] | [cm$^{-1}$] | [meV] | $10^4$ [s$^{-1}$] | $10^4$ [s$^{-1}$] |
| 90 | 0.0 | 3.5 | 5.2 | 0.00 | 0.0 | 0.0 | 0.000 |
| 89 | 0.4 | 3.4 | 5.4 | 0.01 | 0.1 | 0.1 | 0.000 |
| 88 | 0.7 | 3.4 | 5.8 | 0.01 | 1.0 | 0.5 | 0.005 |
| 87 | 0.9 | 3.3 | 7.1 | 0.02 | 2.3 | 0.6 | 0.021 |
| 86 | 1.2 | 3.3 | 8.6 | 0.03 | 4.3 | 1.3 | 0.045 |
| 85 | 1.8 | 3.2 | 11.2 | 0.04 | 7.9 | 2.3 | 0.058 |
| 84 | 2.6 | 3.1 | 13.5 | 0.05 | 10.9 | 3.2 | 0.089 |
| 83 | 3.4 | 3.0 | 16.6 | 0.05 | 14.9 | 2.9 | 0.087 |
| 82 | 4.5 | 2.9 | 20.1 | 0.06 | 19.4 | 3.6 | 0.091 |
| 81 | 5.8 | 2.8 | 24.2 | 0.06 | 24.7 | 4.2 | 0.082 |
| 80 | 7.4 | 2.6 | 28.6 | 0.07 | 30.8 | 3.5 | 0.084 |
| 79 | 9.3 | 2.4 | 34.3 | 0.07 | 38.4 | 3.7 | 0.068 |
| 78 | 11.5 | 2.2 | 39.7 | 0.08 | 45.9 | 3.0 | 0.066 |
| 77 | 13.9 | 2.0 | 45.4 | 0.08 | 54.1 | 3.0 | 0.047 |
| 76 | 16.7 | 1.8 | 51.6 | 0.09 | 63.0 | 2.3 | 0.042 |
| 75 | 19.9 | 1.6 | 58.1 | 0.09 | 72.6 | 2.2 | 0.029 |
| 74 | 23.4 | 1.4 | 64.9 | 0.09 | 83.0 | 1.7 | 0.019 |
| 73 | 27.4 | 1.2 | 72.1 | 0.09 | 94.0 | 1.3 | 0.012 |
| 72 | 31.8 | 1.0 | 79.7 | 0.10 | 105.9 | 1.1 | 0.009 |
| 71 | 36.7 | 0.8 | 87.5 | 0.11 | 118.7 | 0.8 | 0.007 |
| 70 | 42.2 | 0.7 | 95.6 | 0.11 | 132.2 | 0.6 | 0.004 |
| 69 | 48.4 | 0.5 | 104.0 | 0.12 | 146.7 | 0.4 | 0.003 |
| 68 | 55.2 | 0.4 | 112.6 | 0.13 | 162.1 | 0.3 | 0.002 |
| 67 | 62.8 | 0.3 | 121.4 | 0.14 | 178.5 | 0.2 | 0.001 |
| 66 | 71.2 | 0.2 | 130.4 | 0.13 | 195.8 | 0.1 | 0.000 |
| 65 | 80.6 | 0.2 | 139.5 | 0.14 | 214.2 | 0.1 | 0.000 |
| 64 | 90.8 | 0.1 | 148.8 | 0.14 | 233.7 | 0.1 | 0.000 |
| 63 | 102.2 | 0.1 | 158.4 | 0.14 | 254.5 | 0.0 | 0.000 |
| 62 | 114.7 | 0.0 | 167.8 | 0.15 | 276.4 | 0.0 | 0.000 |
| 61 | 128.5 | 0.0 | 177.7 | 0.15 | 299.8 | 0.0 | 0.000 |
| 60 | 143.8 | 0.0 | 187.4 | 0.16 | 324.8 | 0.0 | 0.000 |

Rate constant calculated for **diCl** within rotational model    $k_{3CT \rightarrow 1CT}$    =    **1.75** [$10^4$ s$^{-1}$]
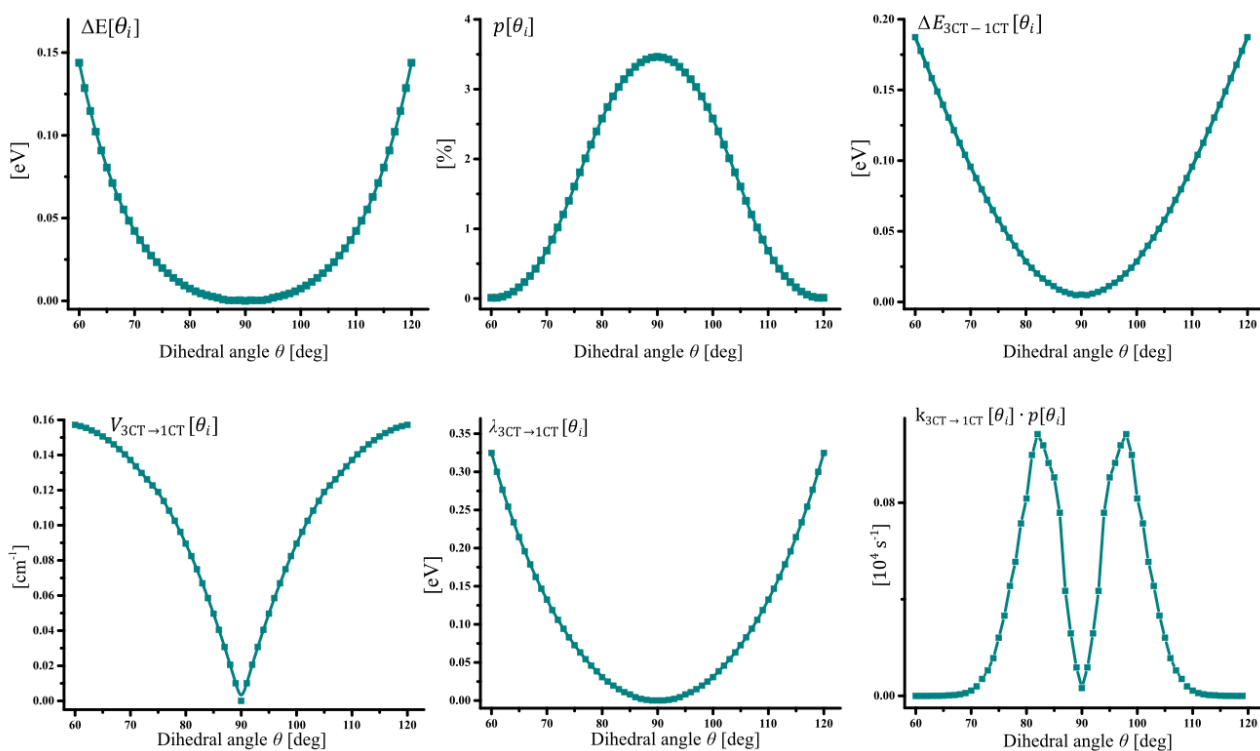


**Figure S18.** Computational parameters for prediction $k_{3CT \rightarrow 1CT}$ in **diCl** calculated within rotational model.

**Table S14** Computational parameters for $k_{3CT \to 1CT}$ prediction in **diBr** using rotational model.

| $\theta_i$ | $\Delta E[\theta_i]$ | $p[\theta_i]$ | $\Delta E_{3CT-1CT}[\theta_i]$ | $V_{3CT \to 1CT}[\theta_i]$ | $\lambda_{3CT \to 1CT}[\theta_i]$ | $k_{3CT \to 1CT}[\theta_i]$ | $p[\theta_i] \cdot k_{3CT \to 1CT}[\theta_i]$ |
|---|---|---|---|---|---|---|---|
| [$^O$] | [meV] | [%] | [meV] | [cm$^{-1}$] | [meV] | 10$^4$ [s$^{-1}$] | 10$^4$ [s$^{-1}$] |
| 90 | 0.0 | 3.4 | 4.8 | 0.00 | 0.00 | 0.00 | 0.000 |
| 89 | 0.0 | 3.4 | 5.1 | 0.01 | 0.00 | 0.01 | 0.009 |
| 88 | 0.1 | 3.4 | 5.8 | 0.01 | 0.00 | 0.27 | 0.030 |
| 87 | 0.2 | 3.3 | 6.9 | 0.02 | 0.00 | 0.87 | 0.043 |
| 86 | 0.4 | 3.3 | 8.5 | 0.02 | 0.00 | 1.26 | 0.039 |
| 85 | 0.9 | 3.3 | 10.8 | 0.03 | 0.01 | 1.18 | 0.049 |
| 84 | 1.6 | 3.2 | 13.1 | 0.03 | 0.01 | 1.50 | 0.058 |
| 83 | 2.7 | 3.1 | 16.1 | 0.04 | 0.01 | 1.86 | 0.056 |
| 82 | 4.0 | 2.9 | 19.5 | 0.04 | 0.02 | 1.89 | 0.047 |
| 81 | 5.5 | 2.8 | 23.4 | 0.05 | 0.02 | 1.70 | 0.041 |
| 80 | 7.3 | 2.6 | 27.7 | 0.05 | 0.03 | 1.57 | 0.037 |
| 79 | 9.3 | 2.4 | 32.4 | 0.06 | 0.04 | 1.54 | 0.028 |
| 78 | 11.6 | 2.2 | 37.5 | 0.06 | 0.04 | 1.26 | 0.029 |
| 77 | 14.1 | 2.0 | 43.0 | 0.07 | 0.05 | 1.45 | 0.020 |
| 76 | 16.9 | 1.8 | 48.9 | 0.07 | 0.06 | 1.15 | 0.014 |
| 75 | 20.1 | 1.6 | 55.1 | 0.08 | 0.07 | 0.89 | 0.013 |
| 74 | 23.5 | 1.4 | 61.7 | 0.08 | 0.08 | 0.93 | 0.008 |
| 73 | 27.5 | 1.2 | 68.6 | 0.08 | 0.09 | 0.70 | 0.007 |
| 72 | 32.1 | 1.0 | 75.7 | 0.09 | 0.10 | 0.68 | 0.004 |
| 71 | 37.3 | 0.8 | 83.2 | 0.09 | 0.12 | 0.50 | 0.002 |
| 70 | 43.1 | 0.6 | 91.0 | 0.09 | 0.13 | 0.36 | 0.002 |
| 69 | 49.6 | 0.5 | 98.5 | 0.10 | 0.14 | 0.33 | 0.001 |
| 68 | 56.7 | 0.4 | 106.7 | 0.10 | 0.16 | 0.24 | 0.001 |
| 67 | 64.5 | 0.3 | 115.2 | 0.10 | 0.17 | 0.20 | 0.000 |
| 66 | 73.1 | 0.2 | 123.7 | 0.11 | 0.19 | 0.17 | 0.000 |
| 65 | 82.5 | 0.1 | 132.5 | 0.11 | 0.21 | 0.12 | 0.000 |
| 64 | 92.9 | 0.1 | 141.4 | 0.11 | 0.23 | 0.08 | 0.000 |
| 63 | 104.4 | 0.1 | 150.4 | 0.11 | 0.25 | 0.06 | 0.000 |
| 62 | 117.0 | 0.0 | 159.6 | 0.11 | 0.27 | 0.04 | 0.000 |
| 61 | 130.8 | 0.0 | 168.8 | 0.12 | 0.29 | 0.03 | 0.000 |
| 60 | 143.1 | 0.0 | 181.2 | 0.12 | 0.32 | 0.02 | 0.000 |

Rate constant calculated for **diBr** within rotational model $\quad k_{3CT \to 1CT} \quad = \quad$ **1.08** [10$^4$ s$^{-1}$]
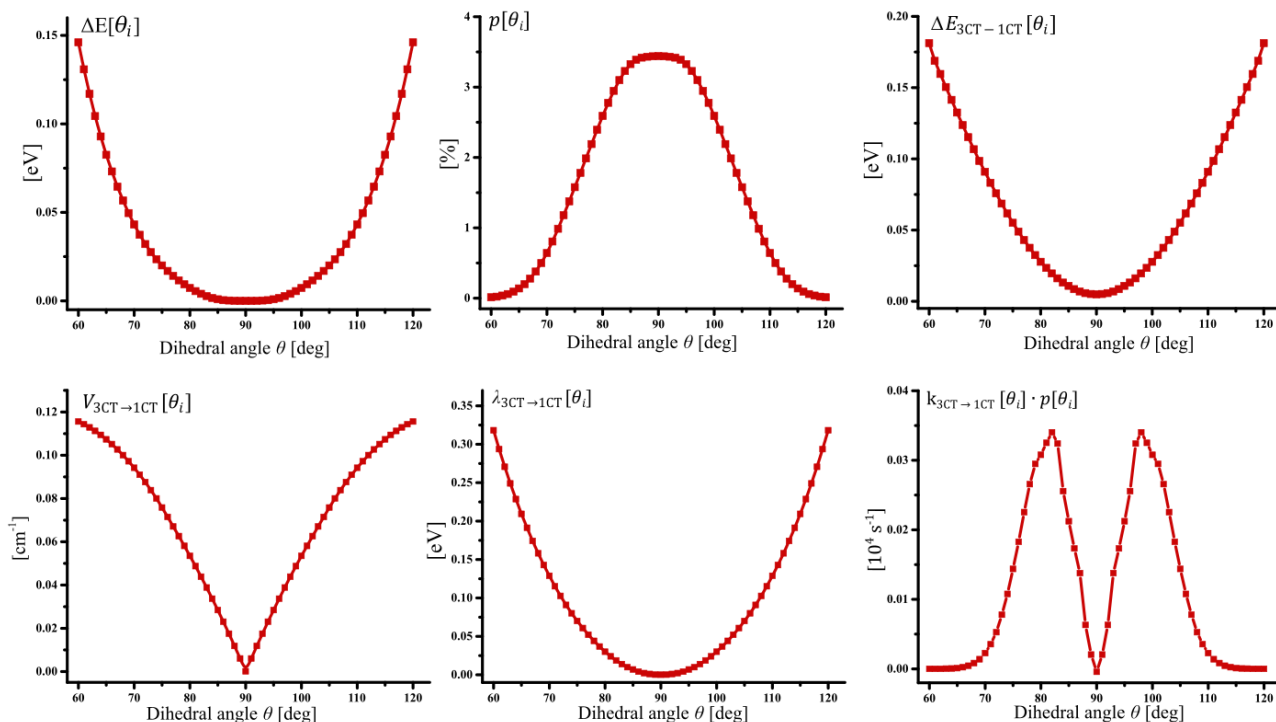


**Figure S19.** Computational parameters for the prediction of $k_{3CT \to 1CT}$ in **diBr** calculated within rotational model.

The statistically weighted oscillator strengths ($f$) values for all rotamers were calculated according to the procedure reported previously.[S3] Thus obtained $f$ value slightly increases with the introduction of halogen from 0.016 (**H**) to 0.020 (**diCl** and **diBr**). One can thus suggest that the value of oscillator strength reversely correlates with the CT strength.

## Section S7: Computational details for the prediction of rISC rate constant within the vibrational model via direct ³CT-¹CT transition

Within the vibrationally-assisted direct SOC model presented below, total $k_{3CT\rightarrow1CT}$ consists of fractional constant rates $k_{3CT\rightarrow1CT}^{\omega_i}$, originating from one $\theta$-rotamer ($\theta=90°$) at various deviations from optimal geometry induced by low-frequency vibrations ($<100$ cm$^{-1}$):

$$k_{3CT\rightarrow1CT} = \sum_{i=1}^{n} k_{3CT\rightarrow1CT}^{\omega_i} \tag{S33}$$

where $\omega_i$ is $i$-th vibrational mode, $n$ is the number of considered modes (here $n = 8$, see **Figure S19**).
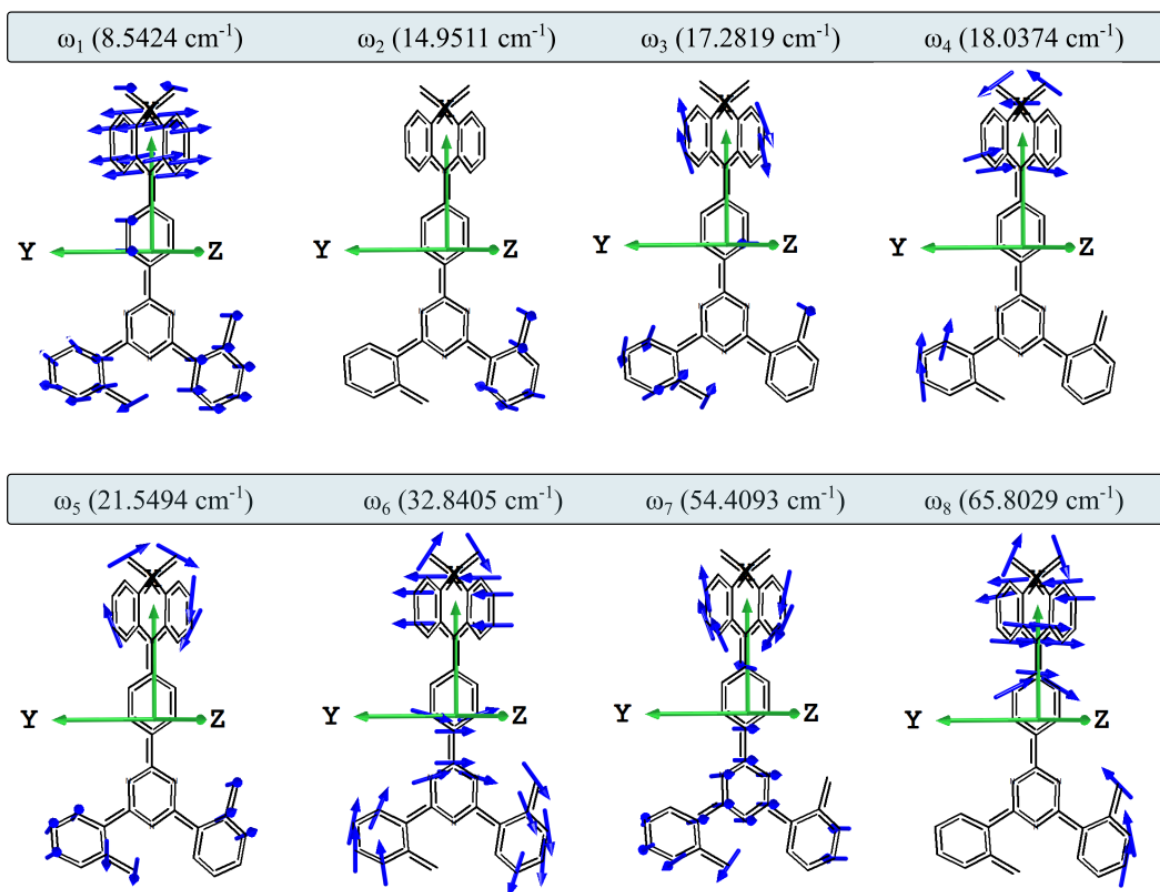


**Figure S20.** Vibrational modes of **H** calculated in $S_0$-state geometry with displacement vectors shown.

Single point TD-DFT calculations of energetic and SOC parameters were performed for various modifications of the $S_0$-state 90-rotamer structure, in which each vibration was "scanned" by changing its amplitude $A$ in a $-2 - +2$ range. Such structures were generated using Chemchraft software, version 1.8. For the $i$ vibrational mode, fractional constant rate $k_{^3CT\to^1CT}^{\omega_i}$ was performed taking into account contribution of each vibrational isomer as follows:

$$k_{^3CT\to^1CT}^{\omega_i} = \sum_{j=1}^{m} k_{\omega_i}[A_j] \cdot p_{\omega_i}[A_j], \tag{S34}$$

where:

- $p_{\omega_i}[A_j]$ - Boltzmann distribution function, molar fraction of $j$-th isomer with $A_j$ amplitude in the $\omega_i$ vibration,

- $m$ - number of calculated isomers, usually $m = 29$ unless mentioned differently.

- $k_{\omega_i}[A_j]$ – the $^3CT$-$^1CT$ transition rate constant calculated for the $j$-th vibrational isomer using Marcus-Hush equation:

$$k_{\omega_i}[A_j] = \frac{(V_{^3CT\to^1CT}[A_j])^2}{\hbar} \sqrt{\frac{\pi}{k_BT\,\lambda_{^3CT\to^1CT}[A_j]}} \exp\left[-\frac{(\Delta E_{^3CT-^1CT}[A_j] + \lambda_{^3CT\to^1CT}[A_j])^2}{4k_BT\,\lambda_{^3CT\to^1CT}[A_j]}\right], \tag{S35}$$

where:

- $V_{^3CT\to^1CT}[A_j]$ – SOC constant of the $j$-th isomer at the $^3CT$-state geometry,

- $\lambda_{^3CT\to^1CT}[A_j]$ – reorganization energy of the $j$-th isomer at the $^3CT$-state geometry,

- $\Delta E_{^3CT-^1CT}[A_j]$ – energy gap between $^1CT$ and $^3CT$ states in $j$-th isomer,

- $k_B$ is Boltzmann constant ($k_B = 8.617 \times 10^{-5}$ eV/K),

- $T$ – temperature, for all calculations $T = 298$ K.

Reorganization energy consists of two terms (inner and outer):

$$\lambda_{^3CT\to^1CT}[A_j] = \lambda_{^3CT\to^1CT}^{in}[A_j] + \lambda_{^3CT\to^1CT}^{out} \tag{S36}$$

The first term $\lambda_{^3CT\to^1CT}^{in}[A_j]$ refers to the energy that is dissipated by the molecule relaxing to the equilibrium geometry at given state. It can be calculated using the formula:

S37

$$\lambda^{\text{in}}_{3\text{CT}\rightarrow1\text{CT}}[A_j] = E^{1\text{CT}}_{3\text{CT},\omega_i}[A_j] - E^{1\text{CT}}_{1\text{CT},\omega_i}[A_0],$$

(S37)

where:

- $E^{1\text{CT}}_{3\text{CT},\omega_i}[A_j]$ − TD-DFT energy of $^1$CT state at $^3$CT-state geometry calculated for $j$-th isomer within $\omega_i$ vibration,

- $E^{1\text{CT}}_{1\text{CT},\omega_i}[A_0]$ − TD-DFT energy of $^1$CT state at optimized ($A_0$ refers to amplitude = 0) $^1$CT-state geometry calculated within $\omega_i$ vibration.

The second term $\lambda^{\text{out}}_{3\text{CT}\rightarrow1\text{CT}}$ is a measure of solvatation effects, and in case of interaction between excited states with the same nature (CT) can be approximated as follows:

$$\lambda^{\text{out}}_{3\text{CT}\rightarrow1\text{CT}} \approx \Delta E_{3\text{CT}-1\text{CT}}[A_j].$$

(S38)

Boltzmann distribution law was used to estimate relative population of isomers ($p_{\omega_i}[A_j]$), which was calculated for the ground $S_0$-state:

$$p_{\omega_i}[A_j] = Z^{-1} \cdot \exp\left(-\frac{\Delta\text{E}_{\omega_i}[A_j]}{k_B T}\right)$$

(S39)

$$\Delta\text{E}_{\omega_i}[A_j] = E_{\omega_i}[A_j] - E[A_0]$$

(S40)

$$Z = \sum_{j=1}^{m} \exp\left(-\frac{\Delta\text{E}_{\omega_i}[A_j]}{k_B T}\right)$$

(S41)

$E_{\omega_i}[A_j]$ – energy calculated for $j$-th isomer within the $\omega_i$ vibration at $S_0$ state,

$E[A_0]$ - energy at the $S_0$-state optimized geometry.

At the end, contribution of the $^3$CT-$^1$CT transition rate constant from each vibrational mode $\mu^{\omega_i}_{3\text{CT}\rightarrow1\text{CT}}$ to the total $k_{3\text{CT}\rightarrow1\text{CT}}$ was calculated (see **Table S18**) using:

$$\mu^{\omega_i}_{3\text{CT}\rightarrow1\text{CT}} = \frac{k^{\omega_i}_{3\text{CT}\rightarrow1\text{CT}}}{\sum_{i=1}^{n=8} k^{\omega_i}_{3\text{CT}\rightarrow1\text{CT}}}.$$

(S42)

As an example, below we present a complete set of computed parameters for the prediction of the

$^3$CT-$^1$CT transition rate constant within the first vibrational mode ($k^{\omega_1}_{3CT\to1CT}$) in **H, diCl** and **diBr** (**Tables S15 – S17** and **Figures S20 – S24**).

**Table S15**. Computational parameters for the prediction of $k_{3CT \to 1CT}^{\omega_1}$ in **H**.

| | | | Computational parameters for prediction $k_{3CT \to 1CT}^{\omega_1}$ in **H** | | | | |
|---|---|---|---|---|---|---|---|
| $A_j$ | $\Delta E_{\omega_1}[A_j]$ | $p_{\omega_1}[A_j]$ | $\Delta E_{3CT-1CT}[A_j]$ | $V_{3CT \to 1CT}[A_j]$ | $\lambda_{3CT \to 1CT}[A_j]$ | $k_{\omega_1}[A_j]$ | $k_{\omega_1}[A_j] \cdot p_{\omega_1}[A_j]$ |
| | [eV] | [%] | [meV] | [cm$^{-1}$] | [meV] | $10^4$ [s$^{-1}$] | $10^4$ [s$^{-1}$] |
| -2.00 | 0.0814 | 0.23 | 11.46 | 0.044 | 136.23 | 0.844 | 0.0019 |
| -1.80 | 0.0624 | 0.48 | 10.18 | 0.040 | 107.72 | 1.041 | 0.0049 |
| -1.50 | 0.0401 | 1.14 | 8.46 | 0.033 | 72.86 | 1.276 | 0.0146 |
| -1.40 | 0.0339 | 1.45 | 7.95 | 0.031 | 63.15 | 1.325 | 0.0192 |
| -1.20 | 0.0236 | 2.16 | 7.05 | 0.026 | 46.37 | 1.360 | 0.0294 |
| -1.00 | 0.0155 | 2.96 | 6.23 | 0.022 | 32.71 | 1.301 | 0.0386 |
| -0.80 | 0.0094 | 3.77 | 5.61 | 0.018 | 22.05 | 1.126 | 0.0429 |
| -0.50 | 0.0032 | 4.78 | 4.90 | 0.011 | 10.99 | 0.707 | 0.0337 |
| -0.40 | 0.0019 | 5.03 | 4.73 | 0.009 | 8.53 | 0.524 | 0.0269 |
| -0.30 | 0.0010 | 5.22 | 4.57 | 0.007 | 6.62 | 0.340 | 0.0178 |
| -0.25 | 0.0006 | 5.30 | 4.54 | 0006 | 5.93 | 0.251 | 0.0133 |
| -0.20 | 0.0003 | 5.35 | 4.46 | 0.004 | 5.30 | 0.171 | 0.0091 |
| -0.15 | 0.0001 | 5.39 | 4.44 | 0.003 | 4.87 | 0.102 | 0.0054 |
| -0.10 | 0.0000 | 5.42 | 4.44 | 0.002 | 4.61 | 0.045 | 0.0025 |
| 0 | 0.0000 | 5.42 | 4.38 | 0.000 | 4.38 | 0.000 | 0.0000 |
| 0.10 | 0.0003 | 5.35 | 4.41 | 0.002 | 4.77 | 0.045 | 0.0025 |
| 0.15 | 0.0006 | 5.29 | 4.41 | 0.003 | 5.13 | 0.101 | 0.0053 |
| 0.20 | 0.0010 | 5.22 | 4.44 | 0.004 | 5.66 | 0.162 | 0.0088 |
| 0.25 | 0.0014 | 5.13 | 4.49 | 0.006 | 6.34 | 0.242 | 0.0124 |
| 0.30 | 0.0019 | 5.03 | 4.49 | 0.007 | 7.07 | 0.332 | 0.0165 |
| 0.40 | 0.0032 | 4.78 | 4.63 | 0.009 | 9.10 | 0.521 | 0.0243 |
| 0.50 | 0.0048 | 4.49 | 4.76 | 0.011 | 11.65 | 0.679 | 0.0308 |
| 0.80 | 0.0119 | 3.41 | 5.41 | 0.018 | 22.78 | 1.121 | 0.0381 |
| 1.00 | 0.0187 | 2.62 | 6.04 | 0.022 | 33.34 | 1.292 | 0.0337 |
| 1.20 | 0.0274 | 1.86 | 6.78 | 0.026 | 46.48 | 1.367 | 0.0254 |
| 1.40 | 0.0383 | 1.22 | 7.65 | 0.031 | 62.56 | 1.345 | 0.0164 |
| 1.50 | 0.0447 | 0.95 | 8.14 | 0.033 | 71.79 | 1.310 | 0.0123 |
| 1.80 | 0.0683 | 0.38 | 9.82 | 0.040 | 104.75 | 1.093 | 0.0041 |
| 2.00 | 0.0881 | 0.18 | 11.13 | 0.044 | 131.62 | 0.898 | 0.0016 |

Fractional rate constant calculated for **H** within $\omega_1$ vibration: $\quad k_{3CT \to 1CT}^{\omega_1} \quad = \quad$ **0.4923**



**Figure S21.** Computational parameters for the prediction of $k_{3CT \to 1CT}^{\omega_1}$ in **H**.

**Table S16**. Computational parameters for the prediction of $k^{\omega_1}_{3CT\rightarrow1CT}$ in **diCl**.

| | Computational parameters for the prediction of $k^{\omega_1}_{3CT\rightarrow1CT}$ in **diCl** | | | | | | |
|---|---|---|---|---|---|---|---|
| $A_j$ | $\Delta E_{\omega_1}[A_j]$ | $p_{\omega_1}[A_j]$ | $\Delta E_{3CT-1CT}[A_j]$ | $V_{3CT\rightarrow1CT}[A_j]$ | $\lambda_{3CT\rightarrow1CT}[A_j]$ | $k_{\omega_1}[A_j]$ | $k_{\omega_1}[A_j]\cdot p_{\omega_1}[A_j]$ |
| | [eV] | [%] | [meV] | [cm$^{-1}$] | [meV] | $10^4$ [s$^{-1}$] | $10^4$ [s$^{-1}$] |
| -2.00 | 0.0778 | 0.26 | 16.03 | 0.034 | 118.61 | 0.580 | 0.0015 |
| -1.80 | 0.0612 | 0.51 | 14.01 | 0.031 | 96.03 | 0.677 | 0.0033 |
| -1.50 | 0.0408 | 1.10 | 11.43 | 0.026 | 67.65 | 0.778 | 0.0085 |
| -1.40 | 0.0351 | 1.37 | 10.64 | 0.024 | 59.48 | 0.795 | 0.0109 |
| -1.20 | 0.0252 | 2.02 | 9.22 | 0.020 | 44.52 | 0.802 | 0.0162 |
| -1.00 | 0.0172 | 2.76 | 8.05 | 0.017 | 32.54 | 0.748 | 0.0206 |
| -0.80 | 0.0108 | 3.53 | 7.02 | 0.014 | 22.75 | 0.642 | 0.0227 |
| -0.50 | 0.0042 | 4.57 | 5.82 | 0.009 | 12.12 | 0.389 | 0.0177 |
| -0.40 | 0.0026 | 4.85 | 5.52 | 0.007 | 9.63 | 0.286 | 0.0138 |
| -0.30 | 0.0015 | 5.07 | 5.25 | 0.005 | 7.63 | 0.184 | 0.0093 |
| -0.25 | 0.0010 | 5.17 | 5.17 | 0.004 | 6.87 | 0.134 | 0.0070 |
| -0.20 | 0.0006 | 5.24 | 5.06 | 0.003 | 6.18 | 0.092 | 0.0048 |
| -0.15 | 0.0004 | 5.30 | 4.98 | 0.003 | 5.66 | 0.054 | 0.0028 |
| -0.10 | 0.0002 | 5.34 | 4.90 | 0.002 | 5.22 | 0.025 | 0.0013 |
| 0 | 0.0000 | 5.38 | 4.79 | 0.000 | 4.79 | 0.000 | 0.0000 |
| 0.10 | 0.0002 | 5.35 | 4.71 | 0.002 | 4.86 | 0.026 | 0.0014 |
| 0.15 | 0.0004 | 5.31 | 4.70 | 0.003 | 5.11 | 0.058 | 0.0031 |
| 0.20 | 0.0006 | 5.25 | 4.70 | 0.003 | 5.44 | 0.098 | 0.0052 |
| 0.25 | 0.0009 | 5.18 | 4.76 | 0.004 | 5.97 | 0.148 | 0.0077 |
| 0.30 | 0.0014 | 5.09 | 4.76 | 0.005 | 6.59 | 0.201 | 0.0103 |
| 0.40 | 0.0025 | 4.87 | 4.78 | 0.007 | 8.22 | 0.319 | 0.0155 |
| 0.50 | 0.0043 | 4.61 | 4.91 | 0.009 | 10.37 | 0.436 | 0.0200 |
| 0.80 | 0.0105 | 3.58 | 5.52 | 0.014 | 20.22 | 0.724 | 0.0258 |
| 1.00 | 0.0167 | 2.81 | 6.18 | 0.017 | 29.70 | 0.841 | 0.0236 |
| 1.20 | 0.0245 | 2.08 | 7.02 | 0.020 | 41.67 | 0.896 | 0.0186 |
| 1.40 | 0.0340 | 1.43 | 8.05 | 0.024 | 56.28 | 0.893 | 0.0127 |
| 1.50 | 0.0395 | 1.15 | 8.63 | 0.026 | 64.59 | 0.876 | 0.0100 |
| 1.80 | 0.0592 | 0.54 | 10.67 | 0.031 | 94.11 | 0.754 | 0.0040 |
| 2.00 | 0.0753 | 0.29 | 12.23 | 0.034 | 117.74 | 0.638 | 0.0018 |

Fractional rate constant calculated for **diCl** within $\omega_1$ vibration: $\quad k^{\omega_1}_{3CT\rightarrow1CT} \quad = \quad$ **0.3012**
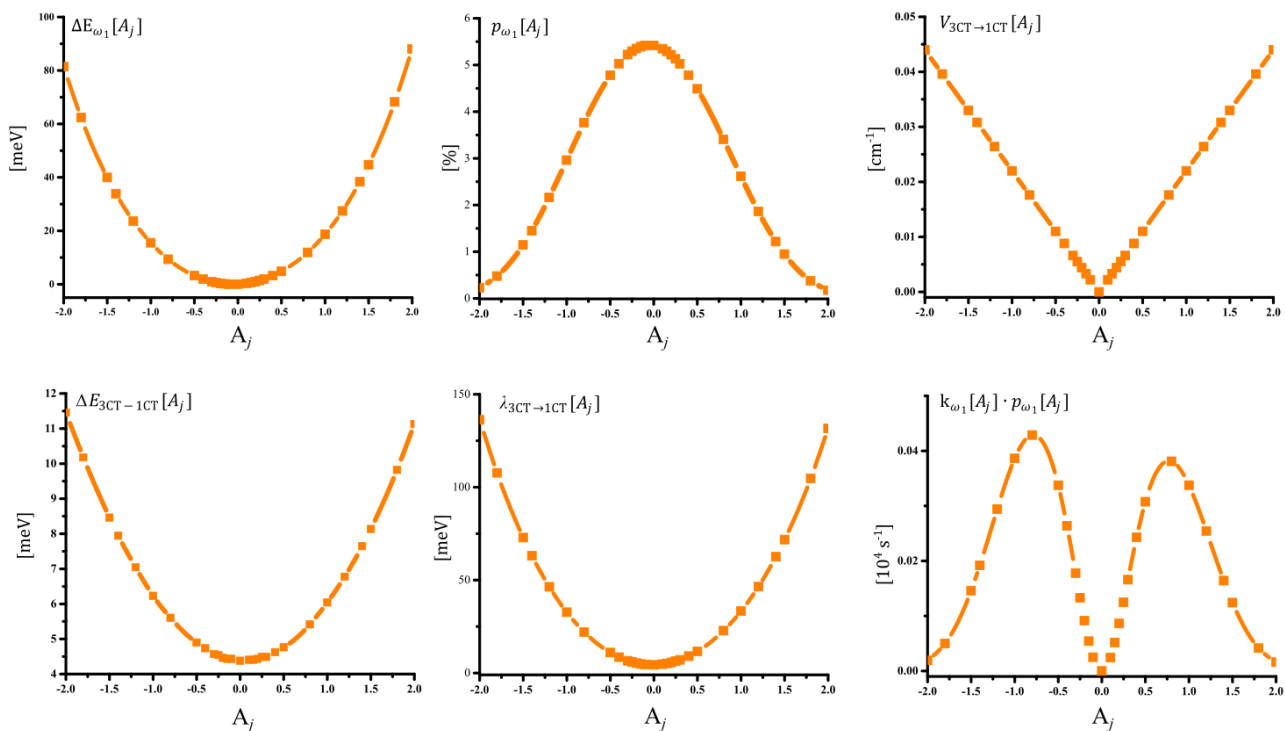


**Figure S22.** Computational parameters for the prediction of $k^{\omega_1}_{3CT\rightarrow1CT}$ in **diCl**.

**Table S17**. Computational parameters for the prediction of $k^{\omega_1}_{3CT \to 1CT}$ in **diBr**.

| | | | | Computational parameters for the prediction of $k^{\omega_1}_{3CT \to 1CT}$ in **diBr** | | | |
|---|---|---|---|---|---|---|---|
| $A_j$ | $\Delta E_{\omega_1}[A_j]$ | $p_{\omega_1}[A_j]$ | $\Delta E_{3CT-1CT}[A_j]$ | $V_{3CT \to 1CT}[A_j]$ | $\lambda_{3CT \to 1CT}[A_j]$ | $k_{\omega_1}[A_j]$ | $k_{\omega_1}[A_j] \cdot p_{\omega_1}[A_j]$ |
| | [eV] | [%] | [meV] | [cm$^{-1}$] | [meV] | $10^4$ [s$^{-1}$] | $10^4$ [s$^{-1}$] |
| -2.00 | 0.0842 | 0.21 | 12.54 | 0.028 | 91.31 | 0.628 | 0.0013 |
| -1.80 | 0.0659 | 0.43 | 11.16 | 0.025 | 73.74 | 0.691 | 0.0030 |
| -1.50 | 0.0435 | 1.02 | 9.33 | 0.021 | 51.98 | 0.732 | 0.0075 |
| -1.40 | 0.0373 | 1.30 | 8.79 | 0.020 | 45.84 | 0.728 | 0.0095 |
| -1.20 | 0.0265 | 1.97 | 7.81 | 0.017 | 35.07 | 0.692 | 0.0137 |
| -1.00 | 0.0178 | 2.77 | 6.97 | 0.014 | 26.19 | 0.616 | 0.0171 |
| -0.80 | 0.0110 | 3.61 | 6.23 | 0.011 | 17.88 | 0.523 | 0.0189 |
| -0.50 | 0.0040 | 4.75 | 5.41 | 0.007 | 10.17 | 0.295 | 0.0140 |
| -0.40 | 0.0024 | 5.04 | 5.17 | 0.006 | 8.31 | 0.213 | 0.0107 |
| -0.30 | 0.0013 | 5.28 | 5.01 | 0.004 | 6.88 | 0.133 | 0.0070 |
| -0.25 | 0.0008 | 5.37 | 4.90 | 0.004 | 6.25 | 0.098 | 0.0052 |
| -0.20 | 0.0005 | 5.44 | 4.84 | 0.003 | 5.76 | 0.065 | 0.0036 |
| -0.15 | 0.0002 | 5.49 | 4.79 | 0.002 | 5.37 | 0.038 | 0.0021 |
| -0.10 | 0.0001 | 5.53 | 4.73 | 0.001 | 5.04 | 0.018 | 0.0010 |
| 0 | 0.0000 | 5.54 | 4.63 | 0.000 | 4.63 | 0.000 | 0.0000 |
| 0.10 | 0.0002 | 5.49 | 4.53 | 0.001 | 4.61 | 0.018 | 0.0010 |
| 0.15 | 0.0005 | 5.41 | 4.53 | 0.002 | 4.70 | 0.041 | 0.0022 |
| 0.20 | 0.0010 | 5.33 | 4.54 | 0.003 | 4.93 | 0.072 | 0.0038 |
| 0.25 | 0.0015 | 5.23 | 4.55 | 0.004 | 5.24 | 0.108 | 0.0057 |
| 0.30 | 0.0020 | 5.12 | 4.57 | 0.004 | 5.62 | 0.151 | 0.0077 |
| 0.40 | 0.0034 | 4.85 | 4.65 | 0.006 | 6.66 | 0.245 | 0.0119 |
| 0.50 | 0.0052 | 4.52 | 5.03 | 0.007 | 8.11 | 0.342 | 0.0155 |
| 0.80 | 0.0129 | 3.35 | 5.44 | 0.011 | 14.72 | 0.611 | 0.0205 |
| 1.00 | 0.0201 | 2.53 | 5.99 | 0.014 | 21.20 | 0.744 | 0.0188 |
| 1.20 | 0.0291 | 1.78 | 6.33 | 0.017 | 29.49 | 0.830 | 0.0148 |
| 1.40 | 0.0401 | 1.16 | 6.67 | 0.020 | 39.74 | 0.870 | 0.0101 |
| 1.50 | 0.0464 | 0.91 | 7.05 | 0.021 | 45.65 | 0.874 | 0.0079 |
| 1.80 | 0.0689 | 0.38 | 8.44 | 0.025 | 67.93 | 0.808 | 0.0031 |
| 2.00 | 0.0871 | 0.19 | 9.47 | 0.028 | 85.18 | 0.738 | 0.0014 |

Fractional rate constant calculated for **diBr** within $\omega_1$ vibration:  $k^{\omega_1}_{3CT \to 1CT}$  =  **0.2381**
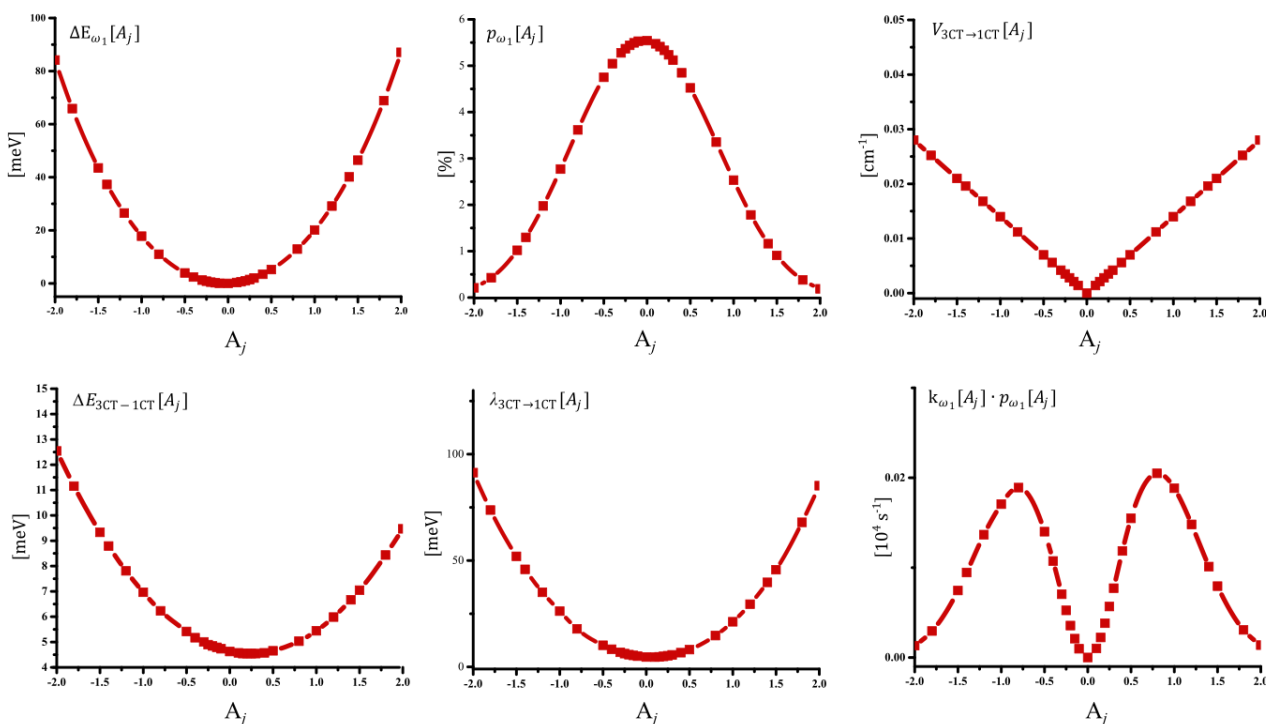


**Figure S23.** Computational parameters for the prediction of $k^{\omega_1}_{3CT \to 1CT}$ in **diBr**.

**Table S18**. Computed fractional rate constant within vibrational model via direct $^3$CT-$^1$CT transition.

| | Fractional constant rates | | | Contribution of each mode to total $k_{3CT \to 1CT}$ | | |
|---|---|---|---|---|---|---|
| | $k_{3CT \to 1CT}^{\omega_i}$ [$10^4$ s$^{-1}$]$^a$ | | | $\mu_{3CT \to 1CT}^{\omega_i}$ [%]$^b$ | | |
| $i$ | **H** | **diCl** | **diBr** | **H** | **diCl** | **diBr** |
| 1 | 0.4923 | 0.3012 | 0.2381 | 87.3 | 57.7 | 21.6 |
| 2 | 0.0004 | 0.0042 | 0.0105 | 0.1 | 0.8 | 1.0 |
| 3 | 0.0032 | 0.0771 | 0.0038 | 0.6 | 14.7 | 0.3 |
| 4 | 0.0104 | 0.0259 | 0.2078 | 1.8 | 4.9 | 18.8 |
| 5 | 0.0004 | 0.0507 | 0.0528 | 0.1 | 9.7 | 4.8 |
| 6 | 0.0007 | 0.0041 | 0.0287 | 0.1 | 0.8 | 2.6 |
| 7 | 0.0025 | 0.0058 | 0.0216 | 0.4 | 1.1 | 2.0 |
| 8 | 0.0542 | 0.0535 | 0.5403 | 9.6 | 10.2 | 49.0 |
| $k_{3CT \to 1CT}$ [$10^4$ s$^{-1}$]$^c$ | **0.5641** | **0.5236** | **1.1036** | | | |

$^a$ – calculated using equation (S34);
$^b$ – calculated using equation (S42);
$^c$ – calculated using equation (S33).
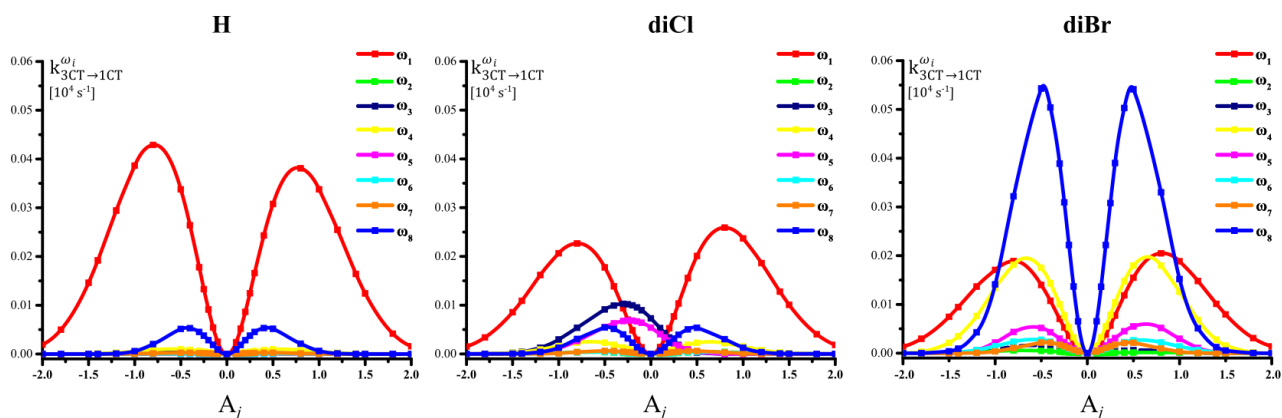


**Figure S24.** Computed fractional rates $k_{3CT \to 1CT}^{\omega_i}$ for various vibrational modes.
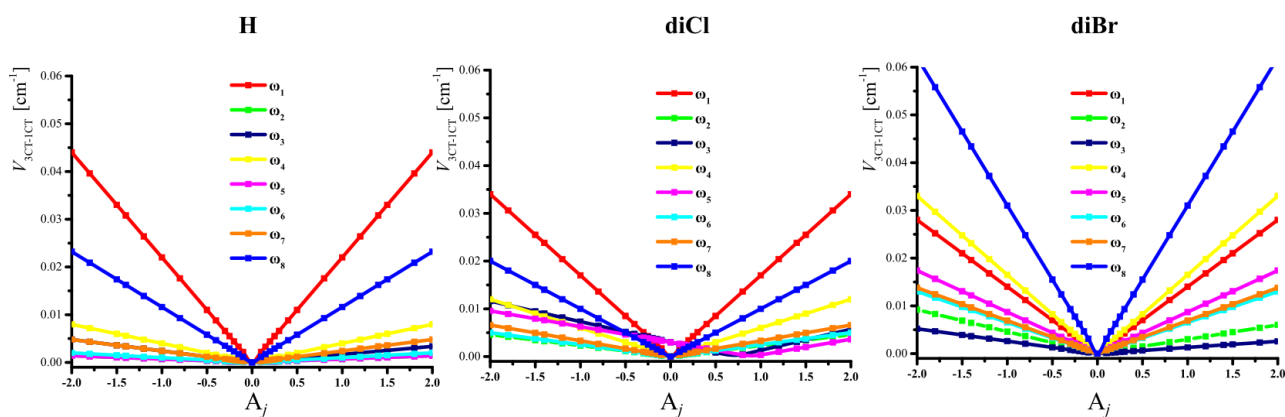


**Figure S25** Computed SOC dependences on amplitudes $A_j$ of various vibrational modes.

## Section S8: The assumptions towards rotational-vibronic model of direct $^3$CT-$^1$CT transition

Analysis of the results obtained by rotational and vibronic models can lead to the following conclusions. The rotational model describes SOC enhancement of the $^3$CT-$^1$CT transition thanks to the specific molecular rotations – deviations of the $\theta$ dihedral angle. Such a model thus reflects the structural diversity of emitter in macroscopic condenced medium and takes into account only most important conformations – $\theta$-rotamers. The rotational model seems to be optimal solution for the description of photophysics of light-atom emitters with orthogonal structure.

The presented vibronic model describes further SOC enhancement of the $^3$CT-$^1$CT transition in selected emitter molecule ($\theta$-rotamer) thanks to the low-energy molecular vibrations. Analysis of the effect of relatively low-amplitude atomic movements on the electronic structure provides fine prediction of SOC, energy gaps and finally spin-flip rate constants.

Obviously, complete TADF model should combine such rotational and vibronic models. For all $\theta$-rotamers existing at room temperature, the effect of molecular vibrations on the electronic structure should be analyzed quantitatively. This task is, however, extremely time-consuming and computationally expensive.

To approximate such a rotational-vibronic model, we assumed that vibrational SOC enhancement in the 90°-rotamer is similar to that in other $\theta$-rotamers. To estimate the value of such enhancement, relative contribution of transition via the $\omega_1$ rotational channel versus all vibrational channels was used: $\mu_{3CT \to 1CT}^{\omega_1} = \frac{k_{3CT \to 1CT}^{\omega_1}}{\sum_{i=1}^{n} k_{3CT \to 1CT}^{\omega_i}}$, calculated for the 90°-rotamers of **H**, **diCl**, and **diBr** (**Table S18**). The statistical sum of $k_{3CT \to 1CT}$ obtained from rotational model (**Tables S15-S17**) was divided by the $\mu_{3CT \to 1CT}^{\omega_1}$ giving rotational-vibronic values of $k_{3CT \to 1CT}$ presented in **Table S19**. Such values showed the best correlation with the experimental rISC rate constants confirming the correctness of the above mentioned assumptions.

**Table S19.** Summary of developed theoretical models and comparasion with experimental results.

| | Experimental[a] $k_{rISC}$ [$10^4$ s$^{-1}$] | | Theoretical models $k_{3CT \rightarrow 1CT}$ [$10^4$ s$^{-1}$] | | |
|---|---|---|---|---|---|
| | ZNX | PMMA | "Rotational"[b] | "Vibrational"[c] | "Rotational-vibronic" |
| **H** | 1.03 | 2.92 | 2.81 | 0.56 | 3.22 |
| **diCl** | 0.87 | 1.85 | 1.75 | 0.52 | 3.07 |
| **diBr** | 1.74 | 8.23 | 1.09 | 1.10 | 5.05 |

[a] - experimental determination of rate constant described in **Section S3: Determination of photophysical parameters**;

[b] - prediction of rate constant within "rotational" model described in **Section S6: Computational details for prediction rISC** rate constant **within rotational model via direct $^3$CT-$^1$CT transition**;

[c] - prediction of rate constant within "vibrational" model described in **Section S7: Computational details for the prediction of rISC** rate constant **within rotational model via direct $^3$CT-$^1$CT transition**.

## Section S9: Molecular electronic orbitals

Molecular orbitals involved in the formation of key excited electronic states are presented below.
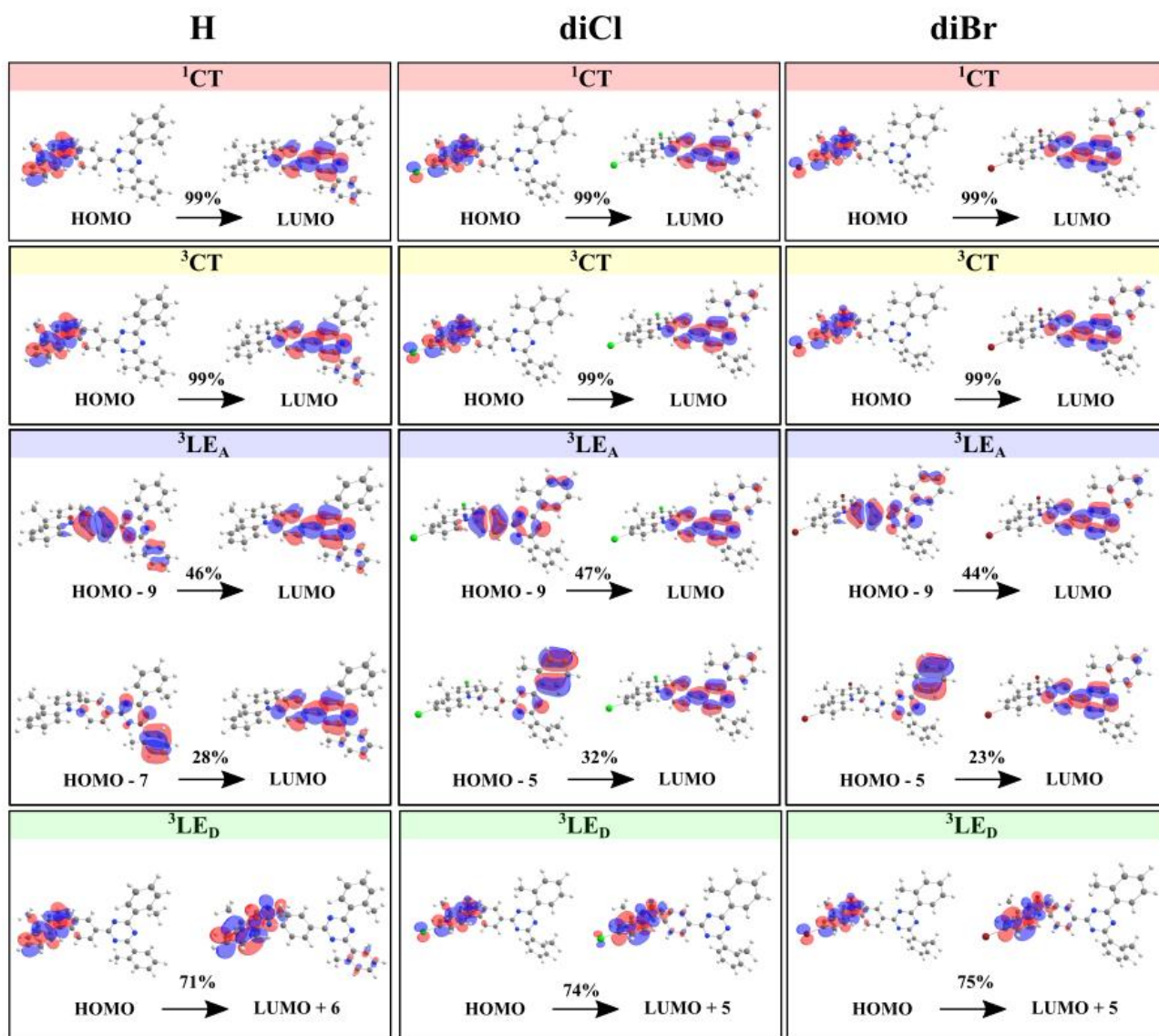


**Figure S26.** Computed MOs

As can be seen from the respective MO, the 1CT and 3CT states are formed via electron density transfer from DMAC donor to aryl-s-triazine acceptor. The $^3LE_A$ state is formed due to redistribution of electronic density within the acceptor fragment. The $^3LED$ state is formed due to redistribution of electronic density within the donor fragment. These data support the conclusions made on the basis of spectral analysis in main text and page S4-S5.

# REFERENCES

[S1] Dias, F. B.; Penfold, T. J.; Monkman, A. P. Photophysics of thermally activated delayed fluorescence molecules. *Methods Appl. Fluoresc*. **2017**, *5*, 012001.

[S2] Stavrou, K.; Franca L. G.; Monkman, A. P. Photophysics of TADF Guest-Host Systems: Introducing the Idea of Hosting Potential. *ASC Appl. Electron. Mater.* **2020**, *2*, 2868 – 2881.

[S3] Serdiuk, I. E.; Mońka, M.; Kozakiewicz, K.; Liberek, B.; Bojarski, P.; Park, S. Y. Vibrationally Assisted Direct Intersystem Crossing between the Same Charge-Transfer States for Thermally Activated Delayed Fluorescence: Analysis by Marcus-Hush Theory Including Reorganization Energy. *J. Phys Chem. B* **2021**, *125*, 2696 – 2706.

[S4] Tao, Y.; Yuan, K.; Chen, T.; Xu, P.; Li, H.; Chen, R.; Zheng, C.; Zhang, L.; Huang, W. Thermally Activated Delayed Fluorescence Materials Towards the Breakthrough of Organoelectronics. *Adv. Mater.* **2015**, *26*, 7931 – 7958.

[S5] IUPAC. Compendium of Chemical Terminology, 2nd ed. (the "Gold Book"). Compiled by A. D. McNaught and A. Wilkinson. Blackwell Scientific Publications, Oxford (1997). Online version (2019-) created by S. J. Chalk. ISBN 0-9678550-9-8. https://doi.org/10.1351/goldbook.

## PAPER

# Decisive role of heavy-atom orientation for efficient enhancement of spin–orbit coupling in organic thermally activated delayed fluorescence emitters†

Michał Mońka,[a] Daria Grzywacz,[b] Estera Hoffman,[a] Vladyslav Ievtukhov,[b] Karol Kozakiewicz,[b] Radoslaw Rogowski,[a] Aleksander Kubicki,[a] Beata Liberek, [ID][b] Piotr Bojarski[a] and Illia E. Serdiuk [ID] *[a]

In view of the rapidly growing interest in the hybrid materials for heavy-metal-free optoelectronics, the research described here aimed to confirm the potential ability of abundant heavy atoms (HAs) in improving key parameters of organic emitters with thermally activated delayed fluorescence. Namely, the enhancement of reverse intersystem crossing (rISC) while keeping a reasonable value of fluorescence rate was investigated in red emitters with bromine atom(s) introduced into the ortho positions of the *N,N*-ditolylaniline donor fragment. The results of photophysical investigations and quantum chemical calculations indicate that selective acceleration of rISC by HAs without a substantial decrease of the fluorescence rate is possible. Molecular design principles of such hybrid materials, however, do not seem simple. In the investigated emitters, the oscillator strength of the $S_1$–$S_0$ transition which defines the fluorescence rate is not directly influenced by the bromine atoms, and remains similar or decreases weakly for the brominated emitters. The maximal enhancement of spin–orbit coupling (SOC) does not depend directly on the number of HAs either, but on their relative position and orientation in the emitter. The analysis of numerous rotational isomers of emitters revealed that SOC enhancement cannot be explained by either the internal or the external HA effect. Taking into account the lack of significant contribution of bromines in orbital and spin momentum of the $T_1$–$S_1$ transition, but yet significant SOC enhancement, we explain the observed phenomenon as a heavy-atom field effect (HAFE) which increases the total angular momentum. The most impressive SOC enhancement by the HAFE up to 60 times is observed when HAs align asymmetrically and are oriented towards the chromophore fragment with the largest orbital momentum change. Another important observation reveals that, in the case of symmetrical structures, the field of a heavy atom can be compensated by another one leading to almost zero SOC and 650-fold rISC inhibition. Such species should be avoided at the stage of molecular design planning.

*[a] Faculty of Mathematics, Physics and Informatics, University of Gdańsk, Wita Stwosza 57, 80-308 Gdańsk, Poland. E-mail: illia.serdiuk@ug.edu.pl; Tel: +48 58 523 22 44*

*[b] Faculty of Chemistry, University of Gdańsk, Wita Stwosza 63, 80-308 Gdańsk, Poland*

† Electronic supplementary information (ESI) available: additional results of photophysical investigations, computationally predicted electronic parameters and calculated rISC rate constants for various rotamers, NMR spectra. See DOI: https://doi.org/10.1039/d2tc01729f

## Introduction

Hybrid organic emitters bearing cheap and abundant non-metallic heavy atoms (HAs) attract more and more attention lately.[1–4] Such materials can be the Golden mean between all-organic materials and heavy-metal complexes or inorganic analogues. Potentially, the rational design of such hybrid materials can preserve the advantages of organic and heavy-metal materials to enable fast conversion of electric energy into light in a submicrosecond regime but avoid low efficiency of organics and high cost and environmental issues connected with the use of heavy metals.

Nowadays, the application of various emitters in organic light emitting diodes (OLEDs) is realized *via* two main strategies which represent separate solutions for the problem of triplet harvesting under electric excitation. Widely commercialized generation of phosphorescent heavy-metal complexes converts all the electrically generated excitons to the triplet ones.[5] Due to very high values of spin–orbit coupling (SOC) of the $T_1$–$S_0$ transition caused by the presence of a heavy-metal, such excitons are deactivated radiatively within 1–10 µs.

This journal is © The Royal Society of Chemistry 2022

*J. Mater. Chem. C*, 2022, **10**, 11719–11729 | 11719

Recently, various attempts were made to substitute such heavy-metal materials with organic analogues for application in such phosphorescence OLEDs.[6–8] However, the best pure organic candidates phosphoresce in the second or millisecond time domain and/or with low quantum yields.[9–11] Very recent approaches of incorporation of abundant non-metallic heavy atoms like selenium in organic materials provide submillisecond phosphorescence (385 µs) with a 20% quantum yield.[6] These data indicate that we are still far away from efficient organic phosphors.

The second strategy for OLED emitters expected to be closer to commercialization utilizes the thermally activated delayed fluorescence (TADF) phenomenon.[12] In TADF materials, the radiative deactivation of all excitons occurs from the singlet $S_1$ state. Conversion of triplet excitons to singlet ones occurs via endothermic spin–flip transition named reverse intersystem crossing (rISC). It is enabled by the energetic proximity of the lowest excited singlet and triplet states in TADF emitters. Being "spin–forbidden", rISC still depends on SOC. However, in contrast to the all-organic phosphorescent materials, some of their TADF analogues are capable of 100% quantum yields of luminescence within micro- and submicrosecond regimes.[13] Taking into account the most recent achievements,[14–17] development of organic and hybrid TADF materials seems to be the most promising direction for environment friendly multifunctional optoelectronics.

One of the most critical problems of organic TADF materials remains the slow rate of triplet harvesting.[18,19] Acceleration of rISC while maintaining the fast fluorescence rate is supposed to be a solution for the minimization of the external quantum efficiency (EQE) roll-off under increasing current density and low stability of OLED devices in general. In light-atom organic materials due to weak SOC, efficient rISC can be achieved mainly via minimization of the energy gap between the $S_1$ and $T_1$ states ($\Delta E_{ST}$): the lower the $\Delta E_{ST}$ value, the higher the rate constant of rISC ($k_{rISC}$). In general, small $\Delta E_{ST}$ requires strong spatial separation of the highest occupied (HOMO) and lowest unoccupied molecular orbital (LUMO). For this reason an overwhelming number of TADF emitters are strong electron donor–

acceptor (D–A) molecular systems whose $S_1$ and $T_1$ states have charge-transfer (CT) nature with a high transition dipole moment.

Another important parameter of a TADF emitter is its emissive rate. In donor–acceptor emitters, the latter is proportional to the oscillator strength of the $^1CT$-$S_0$ transition ($f_{1CT-S0}$). The above mentioned separation of HOMO and LUMO unavoidably leads to the decrease of $f_{1CT-S0}$, or in terms of selection rules, the $^1CT$-$S_0$ transition becomes forbidden. Low oscillator strength is clearly a negative factor for an OLED emitter, which elongates the conversion of excitation energy to light. Taking this into account, the relation of key parameters of D–A type TADF emitters can be expressed as:

$$f_{1CT-S0} \sim 1/k_{rISC}. \qquad (1)$$

Within the light-atom organic D–A materials, a solution to this dilemma is extremely challenging, because most of the structural changes sacrifice either the rISC rate and thus triplet harvesting efficiency or the $^1CT$-state radiative deactivation rate constant ($k_r$) and thus fluorescence efficiency (Fig. 1). Fastly evolving hybrid materials based on organic emitters modified with HAs can potentially solve this dilemma. As correlation (1) is caused by different indirect electronic reasons, the presence of HAs can increase SOC, but hypothetically should not affect the fluorescence rate. However, in spite of the rapidly growing interest in such materials,[14–17] very scarce knowledge on the mechanism of HA action on organic TADF emitters prevents their targeted rational molecular design. Taking into account the complex nature of TADF, the effect of a particular heavy atom on the nature of electronic states and other parameters connected with $f_{1CT-S0}(k_r)$ and $k_{rISC}$(SOC) is highly unintuitive and should be extensively investigated.

In this research, we aimed to find a molecular strategy for the HA-modification of an organic TADF emitter so that it could preserve its fluorescence rate but enhance the rISC rate. The most suitable molecular design strategy for such modifications seems to be the one compromising the $\Delta E_{ST}$ and $f_{1CT-S0}$ values as reported recently.[20] This strategy relies on a smaller separation of HOMO and LUMO in red and NIR emitters with a highly
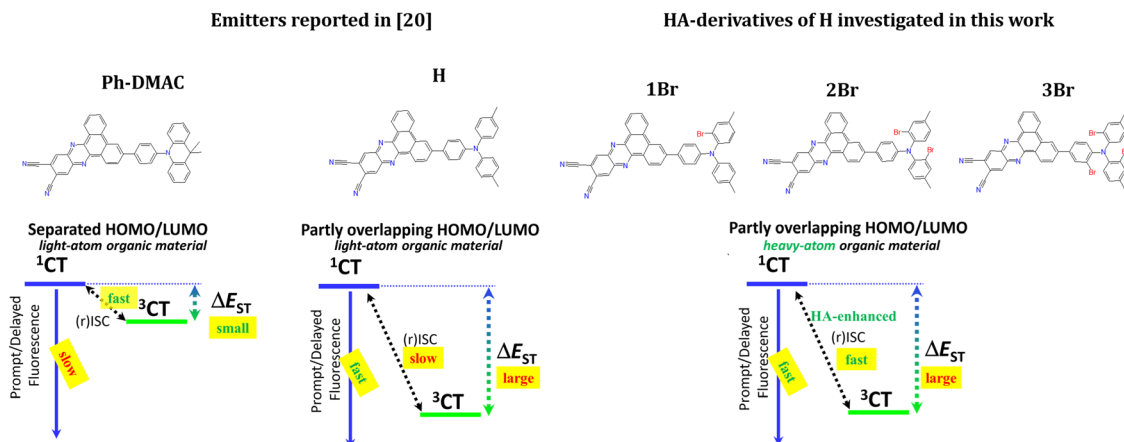


Fig. 1 Canonic structures of the investigated emitters with a schematic representation of excited states and key processes leading to light emission.

**11720** | *J. Mater. Chem. C*, 2022, **10**, 11719–11729

This journal is © The Royal Society of Chemistry 2022

stabilized CT state. It utilizes a partly conjugated donor with a strong acceptor fragment[20,21] and sacrifices the reduction of $\Delta E_{ST}$ for a higher $f_{1CT-S0}$ value. The thus developed 11,12-dicyanodibenzo[a,c]phenazine emitter bearing a more planar N,N-ditolylaniline (DTA) donor (emitter **H**, Fig. 1) in comparison with a highly twisted 10-phenyl-9,9-dimethylacridan (**Ph-DMAC**) donor was reported to have a 12 times higher $k_r$ value. Simultaneously, the $\Delta E_{ST}$ increased almost 3.7 times causing a 30-fold drop in $k_{rISC}$. The authors also performed OLED tests, which confirmed that in spite of $k_r$ increase, rISC inhibition led to worse device work due to a much higher EQE roll-off. One should also note that the described emitters are one of the best representatives of red/NIR TADF emitters,[22] and thus their further improvement seems to be very topical for OLED technology.

Taking into account the good fluorescent properties but unsatisfactory slow rISC, in this work, **H** was modified with heavy atoms. Bromine was selected as HAs thanks to its abundance, low cost and easiness of introduction into organic molecules. Next, possible positions of HAs in the emitter's structure were analyzed. According to our previous findings,[23] one should avoid direct electronic interaction of HAs with the fragment responsible for the lowest excited triplet state of local character ($^3$LE) to avoid intersystem crossing (ISC) enhancement via the $^1$CT→$^3$LE(HA) channel, which is a negative factor regarding triplet harvesting efficiency. The reported phosphorescence investigations indicate that a triplet state localized on a triarylamino donor fragment has energy near 3.05 eV.[24] Triplet energy of dibenzo[a,c]phenazine acceptor derivatives is below 2.50 eV,[25] which makes it the lowest $^3$LE state in such kinds of emitters. For these reasons, one, two, and three bromine atoms were introduced into the donor, namely, at the ortho position of each of the benzene rings of the DTA fragment, providing emitters **1Br**, **2Br**, and **3Br**, respectively (Fig. 1). Thorough analysis of the photophysical properties with the help of DFT calculations allowed us to reveal and explain rISC enhancement whilst maintaining a reasonable $k_r$ value. In the example of red TADF emitters, it was found that HAs in ortho positions of triarylamine donors enrich rotational isomerism of emitting species. The analysis of electronic features of such rotamers

afforded valuable conclusions on the effect of relative positions of HAs on spin–orbit coupling and rISC.

## Synthesis

3-(4-(Di-p-tolylamino)phenyl)dibenzo[a,c]phenazine-11,12-dicarbonitrile (**H**) was synthesized by the reaction of 3-(4-(di-p-tolyl-amino)phenyl)phenanthrene-9,10-dione (**1**) with 4,5-diaminophthalonitrile (Scheme 1), conducted according to the procedure described in the literature.[20] Bromination of **H** with 1.1 eq. of NBS gave **1Br**. Analogous bromination of **H** with 2.1 and 3.1 eq. of NBS was less selective. Therefore, we decided to brominate first substrate **1** with 2.1 and 3.1 eq. of NBS, which gave us **2** and **3**, respectively. Finally, **2Br** and **3Br** were obtained by cyclization of **2** and **3** with 4,5-diaminophthalonitrile.

# Experimental section

## Generals

Zeonex® (ZNX, Zeonex480R, density = 1.01 g cm$^{-3}$), 4,4′-bis(N-carbazolyl)-1,1′-biphenyl (CBP, sublimated), reagents for synthesis, and solvents of respective grades for spectroscopy and synthesis were purchased and used without further purification.

## Synthesis and analysis

The $^1$H NMR spectra were recorded on a Bruker AVANCE III 500 (500.13/125.76 MHz) instrument, under standard experimental conditions in CDCl$_3$ with internal Me$_4$Si. The $^{13}$C NMR spectra were unavailable due to the low solubility of the investigated compounds. Positive-ion mode MALDITOF mass spectra were obtained using a Bruker Biflex III spectrometer with 2,5-dihydroxybenzoic acid matrixes. Purification by column chromatography was performed on silica gel (70–230 mesh).

3-(4-(Di-p-tolylamino)phenyl)phenanthrene-9,10-dione (**1**) and 3-(4-(di-p-tolylamino)phenyl)dibenzo[a,c]phenazine-11,12-dicarbonitrile (**H**) were obtained according to the procedures described in the literature.[20]
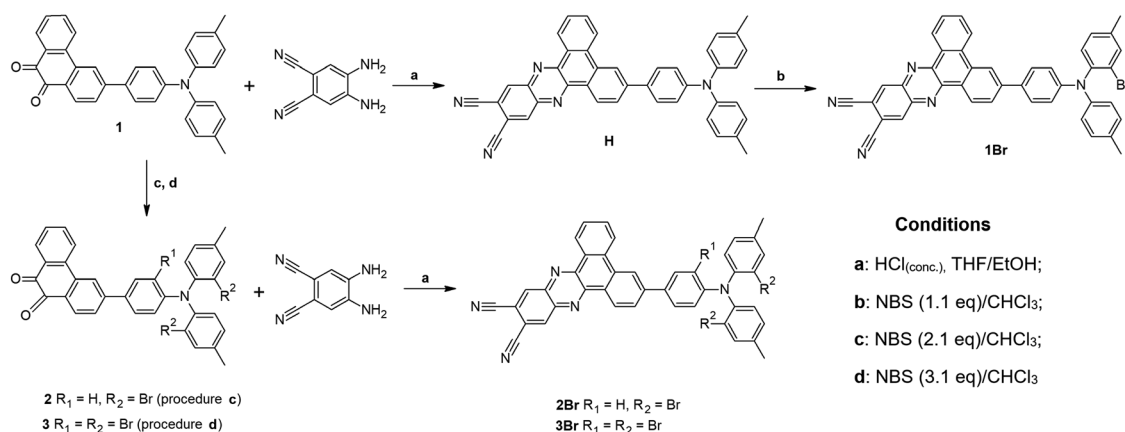


**Scheme 1** Synthetic scheme for the investigated emitters.

This journal is © The Royal Society of Chemistry 2022

J. Mater. Chem. C, 2022, **10**, 11719–11729 | 11721

### General procedure for bromination of 1 and H

NBS (1.1 eq., 2.1 eq., or 3.1 eq., respectively) was added to **1** or **H** and dissolved in $CHCl_3$ (8 mL). After stirring overnight at rt in the absence of light, the solution was concentrated and MeOH (5 mL) was added to the residue. The precipitated solid was filtered, washed and purified by silica gel column chromatography (eluent: $CHCl_3$/n-hexane 1/5).

### 3-(4-(Bis(2-bromo-4-methylphenyl)amino)phenyl)phenanthrene-9,10-dione (2)

Bromination of **1** (60 mg, 0.13 mmol) with 2.1 eq. of NBS (49 mg, 0.27 mmol) gave **2** (red solid, 70 mg, 84%). ^{1}H NMR (500 MHz, $CDCl_3$-d): $\delta$ ppm 2.36 (s, 6 H), 6.71 (d, $J$ = 8.85 Hz, 2 H), 7.12 (dd, $J$ = 7.93, 0.61 Hz, 2 H), 7.19 (d, $J$ = 7.93 Hz, 2 H), 7.48 (td, $J$ = 7.62, 0.61 Hz, 1 H), 7.50 (d, $J$ = 1.53 Hz, 2 H), 7.56 (dt, $J$ = 8.85, 2.14 Hz, 2 H), 7.65 (dd, $J$ = 8.24, 1.53 Hz, 1 H), 7.72 (td, $J$ = 7.33, 1.53 Hz, 1 H), 8.10 (d, $J$ = 7.93 Hz, 1 H), 8.18 (d, $J$ = 1.53 Hz, 1 H), 8.21 (dd, $J$ = 7.93, 1.53 Hz, 1 H), 8.22 (d, $J$ = 8.24 Hz, 1 H); MALDITOF-MS: $m/z$: calcd for $C_{34}H_{23}Br_2NO_2$ 637.2, found 638.0 $[M + 1]^+$.

### 3-(4-(Bis(2-bromo-4-methylphenyl)amino)-3-bromophenyl)-phenanthrene-9,10-dione (3)

Bromination of **1** (60 mg, 0.13 mmol) with 3.1 eq. of NBS (70 mg, 0.40 mmol) gave **3** (orange solid, 79 mg, 85%). ^{1}H NMR (500 MHz, $CDCl_3$-d): $\delta$ ppm 2.34 (s, 6 H), 6.77 (d, $J$ = 8.54 Hz, 1 H), 6.80 (d, $J$ = 8.24 Hz, 1 H), 6.93 (d, $J$ = 8.24 Hz, 1 H), 7.05 (2 × d, $J$ = 7.93 Hz, 2 H), 7.45 (2 × s, 2 H), 7.51 (t, $J$ = 7.63/7.33 Hz, 1 H), 7.52 (dd, $J$ = 8.24 Hz, $J$ = 2.14 Hz, 1 H), 7.64 (d, $J$ = 8.24 Hz, 1 H), 7.75 (t, $J$ = 7.63/7.47 Hz, 1 H), 7.93 (d, $J$ = 2.14 Hz, 1 H), 8.12 (d, $J$ = 8.24 Hz, 1 H), 8.17 (s, 1 H), 8.22 (d, $J$ = 7.63 Hz, 1 H), 8.25 (d, $J$ = 7.94 Hz, 1 H); MALDITOF-MS: $m/z$: calcd for $C_{34}H_{22}Br_3NO_2$ 715.2, found 716.1 $[M + 1]^+$.

### 3-(4-((2-Bromo-4-methylphenyl)(p-tolyl)amino)phenyl)dibenzo[a,c]phenazine-11,12-dicarbonitrile (1Br)

Bromination of **H** (42 mg, 0.07 mmol) with 1.1 eq. of NBS (14 mg, 0.08 mmol) led to **1Br** (red solid, 40 mg, 84%). ^{1}H NMR (500 MHz, $CDCl_3$-d): $\delta$ ppm 2.35–2.40 (4 × s, 6 H), 7.03 (d, $J$ = 8.85 Hz, 1 H), 7.05–7.15 (m, 5 H), 7.17–7.23 (m, 2 H), 7.52 (dd, $J$ = 10.38, 1.83 Hz, 1 H), 7.67 (d, $J$ = 8.54 Hz, 1 H); 7.68 (d, $J$ = 8.85 Hz, 1 H), 7.80 (tdd, $J$ = 7.94, 2.75, 1.53 Hz, 1 H), 7.91 (tdd, $J$ = 7.63, 2.75, 1.53 Hz, 1 H), 7.98 (dt, $J$ = 8.54, 1.53 Hz, 1 H), 8.64 (dd, $J$ = 8.09, 3.36 Hz, 1 H), 8.71 (bs, 1 H), 8.76 (dd, $J$ = 1.83, 0.61 Hz, 1 H); 8.77 (t, $J$ = 0.61 Hz, 1 H); 9.32 (dd, $J$ = 8.24, 3.66 Hz, 1 H), 9.34 (dt, $J$ = 8.24, 1.52 Hz, 1 H); MALDITOF-MS: $m/z$: calcd for $C_{42}H_{26}Br_1N_5$ 679.2, found 680.2 $[M + 1]^+$.

### General procedure for the synthesis of 2Br and 3Br

4,5-Diaminophthalonitrile (1.2 eq.) was added to **2** or **3** and dissolved in THF/EtOH (1 : 1; 5 mL) with $HCl_{(conc)}$ (10 µL). After stirring overnight at rt the solution was concentrated and purified by silica gel column chromatography (eluent: $CHCl_3$/n-hexane 1/3).

### 3-(4-(Bis(2-bromo-4-methylphenyl)amino)phenyl)dibenzo[a,c] phenazine-11,12-dicarbonitrile (2Br)

Reaction of 4,5-diaminophthalonitrile (12 mg, 0.076 mmol) with **2** (40 mg, 0.063 mmol) gave **2Br** (red solid, 40 mg, 83%). ^{1}H NMR (500 MHz, $CDCl_3$-d); 2.37 (s, 6 H), 6.79 (dt, $J$ = 8.85, 2.14 Hz, 2 H), 7.13 (ddd, $J$ = 8.24, 2.14, 0.61 Hz, 2 H), 7.19 (d, $J$ = 8.24 Hz, 2 H), 7.51 (dd, $J$ = 1.83, 0.61 Hz, 2 H), 7.69 (dt, $J$ = 8.85, 2.14 Hz, 2 H), 7.80 (td, $J$ = 7.02, 2.14 Hz, 1 H), 7.91 (td, $J$ = 7.32, 1.53 Hz, 1 H), 7.99 (dd, $J$ = 8.54, 1.53 Hz, 1 H), 8.65 (d, $J$ = 7.94 Hz, 1 H), 8.73 (d, $J$ = 1.53 Hz, 1 H), 8.79 (dd, $J$ = 3.66, 0.61 Hz, 2 H), 9.33 (d, $J$ = 8.24 Hz, 1 H), 9.36 (dd, $J$ = 7.93, 1.53 Hz, 1 H); MALDITOF-MS: $m/z$ calcd for $C_{42}H_{25}Br_2N_5$ 759.2, found 759.2 $[M]^+$.

### Synthesis of 3-(4-(bis(2-bromo-4-methylphenyl)amino)phenyl) dibenzo[a,c]phenazine-11,12-dicarbo-nitrile (3Br)

Reaction of 4,5-diaminophthalonitrile (10 mg, 0.067 mmol) with **3** (40 mg, 0.056 mmol) gave **3Br** (yellow solid, 38 mg, 81%). ^{1}H NMR (500 MHz, $CDCl_3$-d); 2.37 (s, 6 H), 6.83 (d, $J$ = 8.24 Hz, 1 H), 6.87 (d, $J$ = 7.96 Hz, 1 H), 7.01 (d, $J$ = 8.24 Hz, 1 H), 7.09 (dd, $J$ = 7.96 Hz, $J$ = 1.37 Hz, 2 H), 7.49 (bs, 2 H), 7.68 (dd, $J$ = 8.51, 2.20 Hz, 1 H), 7.85 (t, $J$ = 7.69 Hz, 1 H), 7.96 (ddd, $J$ = 8.51 Hz, $J$ = 7.14, $J$ = 1.37 Hz, 1 H), 8.00 (dd, $J$ = 8.51, 1.65 Hz, 1 H), 8.09 (d, $J$ = 1.92 Hz, 1 H), 8.69 (d, $J$ = 8.24 Hz, 1 H), 8.74 (d, $J$ = 1.37 Hz, 1 H), 8.82 (d, $J$ = 1.1 Hz, 1 H), 8.82 (m, 1 H), 9.38 (dd, $J$ = 7.96, $J$ = 1.1 Hz, 1 H), 9.39 (d, $J$ = 8.51 Hz, 1 H); MALDITOF-MS: $m/z$: calcd for $C_{42}H_{24}Br_3N_5$ 837.2, found 838.1 $[M + 1]^+$.

The NMR spectra of the obtained compounds can be found in the ESI.†

### Sample preparation for photophysical measurements

Films in ZNX and CBP were prepared by the spin-coating method; the final mass fractions of dispersed emitters were *ca.* 0.1% and 6%, 10%.

### Photoluminescence measurements

UV-Vis absorption spectra were recorded using a Shimadzu UV-1900 spectrophotometer. Steady-state photoluminescence spectra were recorded using an FS5 spectrofluorometer (Edinburgh Instruments) using front-face excitation geometry. Absolute PL quantum yields (PLQYs) were measured using an integrating sphere (Quantaurus C11347-11, Hamamatsu). Time-resolved measurements were performed at different temperatures using a customized system[26] consisting of a pulsed YAG:Nd laser (PL2251A, EKSPLA) coupled with an optical parametric generator (PG 401/SH) as the excitation light source and 2501S grating spectrometer (Bruker Optics) combined with a streak camera system (C4334-01 Hamamatsu) as the detection unit. The system was equipped with a double-stage high vacuum pump (T-Station 85 Edwards) coupled with a closed-cycle helium cryostat (APD DE-202) and a temperature controller (LakeShore 336). To reduce scattering, reflections and secondary order artifacts, a set of various high performance optical bandpass (BP) and longpass (LP) filters were used, in the excitation path 325/50BP or 375/50BP (CWL/FWHM), depending on the selected excitation wavelength, together with

LP filters: 375LP or 350LP (Edmund Optics). In order to build PL intensity decay profiles, streak camera images were integrated over a constant specified wavelength interval. Radiative rate constants $k_r$ and (reverse) intersystem crossing rates $k_{(r)ISC}$ were calculated using procedures described in detail previously and in Section S4 (ESI†).[23]

### Quantum chemical calculations

Quantum chemical calculations were conducted at the DFT/TD-DFT level of theory using the Gaussian 16 program package.[27] The B3LYP functional was used with the LAN2LDZ basis set.[28] Unspecific solvent effect (toluene) was included at the level of the Polarized Continuum Model (PCM).

First, for each compound, unconstrained geometry optimizations were performed for the ground ($S_0$), excited singlet ($S_1$) and excited triplet electronic ($T_1$, $T_2$) states. Convergence of all geometry optimizations was verified by the vibrational analysis, and no negative frequencies were observed; therefore, the calculated minima correspond to "true" stationary points. The nature of electronically excited states was determined by the analysis of molecular orbitals. Spin–orbit coupling constants were computed using the ORCA 4.2 software package[29] with B3LYP functional and DEF2-TZVP basis set with included relativistic zero-order regular approximation (ZORA).

## Results and discussion

### Absorption spectra

The effect of bromine substitution on the ground state ($S_0$) of emitters can be analyzed from the absorption spectra (Fig. 2A).

In solutions, the long wavelength absorption maximum responsible for the $S_0$–$^1$CT transition shifts gradually to higher energies with the number of introduced bromines. There are two main factors which can cause such an effect: (*i*) the electron-withdrawing feature of bromine as a halogen, which reduces the donor strength and thus increases the energy of the CT state and (*ii*) the increase of the dihedral angle between the donor and acceptor fragment due to the large size of bromine atoms in the *ortho* position, leading to further HOMO–LUMO separation and reduction of conjugation between molecular fragments. The important consequence of the *ii* factor is the decrease of oscillator strength $f_{S0-1CT}$. This is not the case for **1Br** and **2Br**, as determined oscillator strength is almost equal or increases as compared to **H** (Table 1).

This indicates that the electron-withdrawing feature of bromine has a key influence on the CT absorption band. Compound **3Br** exhibits the highest blue shift together with an imaginary increase of the *f* value. The latter is explained by a

**Table 1** Absorption parameters for dichloromethane solutions of emitters

| Cmpd | $\lambda_{abs}$ [nm] | $f_{S0-1CT}$ Experimental | $f_{S0-1CT}$ Calculated[a] |
|---|---|---|---|
| **H** | 502 | 0.214 | 0.107 |
| **1Br** | 483 | 0.206 | 0.131 |
| **2Br** | 474 | 0.289 | 0.216 |
| **3Br** | 435 | 0.450 | 0.118 |

[a] Calculated $f_{S0-1CT}$ is a statistical mean value for various rotamers discussed further; calculated by taking into account the probability of each rotamer predicted by Boltzmann distribution at 298 K.
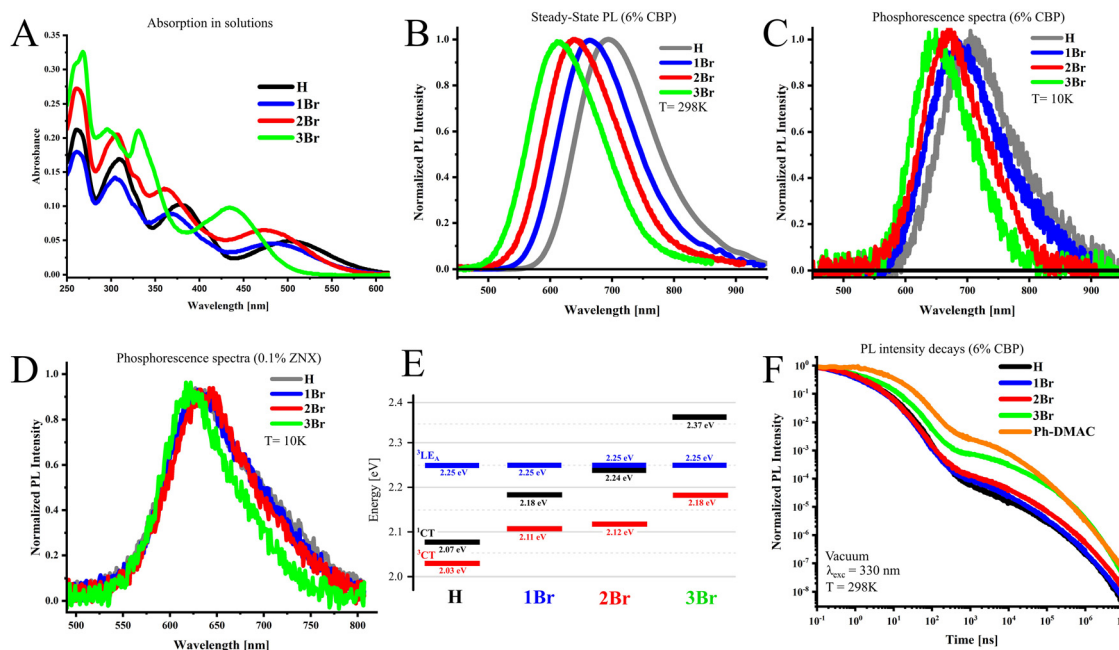


**Fig. 2** Absorption spectra in dichloromethane solutions (A); steady-state PL spectra of the investigated compounds in 6% CBP measured under excitation wavelength $\lambda_{exc}$ = 330 nm (B); phosphorescence spectra in 6% CBP (*T* = 10 K, 20 ms delay after excitation pulse) (C); phosphorescence spectra in 0.1% ZNX (*T* = 10 K, 20 ms delay) (D); alignment of excited states in respective compounds determined from steady-state PL and phosphorescence onsets (E); and PL intensity decays of the investigated compounds in 6% CBP (F).

This journal is © The Royal Society of Chemistry 2022

*J. Mater. Chem. C*, 2022, **10**, 11719–11729 | **11723**

strong overlap of the CT absorption with the next band near 400 nm, which disables experimental determination of $f_{S0–1CT}$. As discussed further, DFT calculations confirm close $f_{S0–1CT}$ values for all compounds.

### Photoluminescence spectra and alignment of excited states

The photoluminescence (PL) features of emitters were investigated in the amorphous film media, namely, 4,4′-bis(N-carbazolyl)-1,1′-biphenyl (CBP), widely used as a host material for OLEDs. In CBP films, the PL maximum of the investigated emitters shifts from red-NIR to orange-red with the increasing number of bromine atoms in the donor fragment (Fig. 2B, Table 2). In 6% w/w films, according to the PL onset values (Fig. S1A, ESI†), the $^1$CT state energy increases from 2.07 eV in **H** by 0.11 eV (**1Br**, 2.18 eV) and by 0.17 eV (**2Br**, 2.24 eV), when the first and second bromine atoms are introduced into the side phenyl rings (Table S1, ESI†). Similarly to absorption, the appearance of third bromine in the linker phenyl ring (**3Br**) causes the strongest $^1$CT-energy increase by 0.30 eV, reaching 2.37 eV. PL quantum yields vary from moderate high 61% in **3Br** to almost absolute in **2Br**. The phosphorescence spectra measured at 10 K with a 20 ms delay after the excitation pulse exhibit similar dependence, but the absolute shifts are smaller (Fig. 2C, Table 2). The energy of the $^3$CT-state derived from phosphorescence onsets (Fig. S1B, ESI†) increases thus by 0.06 eV (**1Br**), 0.08 eV (**2Br**), and 0.13 eV (**3Br**) compared to **H**. The described spectral measurements indicate that $\Delta E_{ST}$ increases from 0.04 eV in **H** to 0.08 eV (**1Br**) and 0.13 eV (**2Br**) and reaches maximal 0.20 eV for **3Br**. At a higher doping concentration (10%), spectral behavior is generally similar (Fig. S1C and D, ESI†); however, PL spectra shift 5–10 nm to the red which results in a slight decrease of $\Delta E_{ST}$ by 10–30 meV (Table S1, ESI†).

To estimate the energy of the higher triplet state, phosphorescence measurements were performed in nonpolar Zeonex® (ZNX) polymer, where the CT states are destabilized. In ZNX films, the phosphorescence onset is almost identical for all emitters and provides the energy of a triplet state near 2.25 eV (Fig. 2D and Fig. S2, ESI†). Under such conditions, phosphorescence most likely occurs from the triplet state with a dominating locally-excited character ($^3$LE). As substitution in the donor does not affect its energy, such a $^3$LE-state is localized on the acceptor fragment identical to all emitters, which is supported by the phosphorescence spectra of the acceptor molecule (Fig. S2, ESI†). Thus estimated alignment of the lowest

excited states is summarized in Fig. 2E, and will be further used for the discussion of photophysical properties.

### PL decays and rates of photophysical processes

The analysis of time-resolved emission spectra and PL decay curves evidences that all emitters dispersed in the CBP host exhibit TADF (Fig. 2F and Fig. S3A–D, ESI†). In the region of prompt fluorescence (PF), **H** and emitters with bromines in the side rings of the DTA donor (**1Br** and **2Br**) fluoresce with a similar lifetime $\tau_{PF}$ close to 15 ns (Table 2). The $k_r$ values seem to depend on the doping ratio more than on the bromine contamination. At 6% and 10% doping with **1Br**, $k_r$ slightly decrease and increase, respectively, by around 15%. In the case of **2Br** in 6% films, $k_r$ decreases twice, but at a higher doping ratio, $k_r$ is only 20% lower as compared to **H**. In **3Br**, PF lifetime increases to 27 ns, which is mainly caused by an almost fivefold $k_r$ decrease. **2Br** and **3Br** exhibit a *ca.* twice faster ISC rate than the rest of the emitters. This is the result of the energetic closeness of the $^1$CT and $^3$LE states (Fig. 2E), as the latter state plays an important role in ISC as was revealed previously.[23,30]

As compared to **H**, the delayed fluorescence lifetime ($\tau_{DF}$) of **1Br** and **3Br** shortens *ca.* 1.5-fold. This indicates that the presence of one and/or three heavy atoms in the TDA donor helps to convert triplet excitons to light more than 1.5 times faster. This becomes possible because of 2 and 8 times faster rISC, respectively, as for 6% CBP films. Importantly, in **3Br**, rISC enhancement outranges the decrease of the $k_r$ value.

Surprisingly, the $\tau_{DF}$ value of **2Br** is higher than that of **H**, because of the more efficient enhancement of ISC than rISC. As compared to **1Br**, the introduction of a second Br atom has either negligible (6% doping) or even negative (10% doping) effects on the rISC rate (Fig. S4 (ESI†), Table 2). Apparently, in the investigated emitters, the HA-effect is not additive by the number of bromines, hence their relative position should play an important role. Such a peculiar rISC behavior is further explained with the help of quantum chemical calculations.

From the point of view of the geometry–property relationship, it is interesting to compare **3Br** with **Ph-DMAC** (Fig. 1, Fig. S1E and F, ESI†). Due to the large size of three bromine atoms, the donor fragment of **3Br** can have a more twisted structure than **1Br** and **2Br**, but a less rigid one than 9,9-dimethylacridan in **Ph-DMAC**. Under the same conditions, as compared to **Ph-DMAC**, **3Br** exhibits an almost 1.5-fold higher $k_r$ value and a

**Table 2** Spectral and photophysical parameters in CBP films

| | $w_{X/CBP}$ (%) | PLQY [%] | $\lambda_{PL}$ [nm] | $\lambda_{Ph}$ [nm] | $\Delta E_{ST}$ [eV] | $\tau_{PF}$ [ns] | $\tau_{DF}$ [μs] | $k_r$ [$10^7$ s$^{-1}$] | $k_{ISC}$ [$10^7$ s$^{-1}$] | $k_{rISC}$ [$10^4$ s$^{-1}$] |
|---|---|---|---|---|---|---|---|---|---|---|
| **H** | 6 | 83 | 692 | 706 | 0.04 | 16.7 | 646 | 3.2 | 2.1 | 0.25 |
| | 10 | 51 | 704 | 709 | 0.03 | 18.8 | 356 | 2.7 | 2.0 | 0.50 |
| **1Br** | 6 | 76 | 665 | 684 | 0.08 | 15.5 | 422 | 2.6 | 3.0 | 0.48 |
| | 10 | 77 | 671 | 690 | 0.06 | 15.2 | 296 | 2.9 | 2.9 | 0.60 |
| **2Br** | 6 | 98 | 641 | 669 | 0.13 | 14.8 | 781 | 1.6 | 5.5 | 0.50 |
| | 10 | 97 | 647 | 672 | 0.10 | 15.0 | 442 | 2.1 | 3.9 | 0.50 |
| **3Br** | 6 | 61 | 602 | 648 | 0.20 | 27.2 | 403 | 0.51 | 5.0 | 1.9 |
| | 10 | 71 | 606 | 633 | 0.19 | 23.3 | 267 | 0.58 | 3.5 | 2.0 |
| **Ph-DMAC** | 6 | 71 | 600 | 601 | 0.09 | 39.4 | 272 | 0.39 | 2.0 | 1.7 |

**11724** | *J. Mater. Chem. C*, 2022, **10**, 11719–11729

This journal is © The Royal Society of Chemistry 2022

slightly faster rISC rate, whilst $\Delta E_{ST}$ is more than twice higher. Taking into account the exponential dependence of $k_{rISC}$ on $-\Delta E_{ST}$ from the Marcus–Hush formula (eqn (S1), ESI†) this indicates *ca.* a hundred times higher SOC in **3Br**. This is an important conclusion for further design of **3Br** analogues with lower $\Delta E_{ST}$ towards fast rISC emitters.

### Rotational isomerism and calculations of the rISC rates

Due to the large size of bromine at the *ortho* positions of benzene rings in the DTA donor, rotations of these rings have increased the energy barrier. This leads to various rotational isomers which can coexist at room temperature in a medium of low viscosity. In amorphous films, which are the media of interest for OLED emitters, high viscosity disables the rotations of large molecular fragments and thus such rotational isomers become individual photophysical species with restricted donor fragment geometries. In the investigated emitters there are three types of dihedral angles which provide rotational isomerism (Fig. 3). First is the dihedral angle $\theta_L$ between the plane of the dibenzo[a,c]phenazine acceptor and linker phenyl ring. In all the investigated rotamers, the optimal value $\theta_L$ is near $+35°$ or $-35°$ (Table 3), where the sign defines whether the donor fragment is above or beyond the acceptor plane (relatively to the molecular orientation depicted in Fig. 3). Two next dihedral angles between the linker phenyl ring and side rings A and B are depicted as $\theta_A$ and $\theta_B$, respectively.

Due to a large number of structural and electronic parameters, and very poor knowledge of the mechanism of their influence on spin–flip transitions, geometry optimizations and calculations of excited state properties were performed for all possible rotamers. The analysis of electronic properties included radiative deactivation $^1CT$–$S_0$ and the parameters of $^3CT \rightarrow {}^1CT$ transition: SOC constants, $\Delta E_{ST}$, activation energy ($E_a$), which takes into account the internal reorganization energy, and finally calculation of the $^3CT \rightarrow {}^1CT$ rate constants ($k_{3CT-1CT}$) using the Marcus–Hush equation ((S1), ESI†). To obtain statistically weighted values of $f_{1CT\text{-}S0}$ and $k_{3CT\text{-}1CT}$, the respective values of all rotamers were added taking into account the contribution of each rotamer provided by relative energies of rotamers and Boltzmann distribution law (S2) (ESI†). As was reported previously, in donor–acceptor type TADF emitters including their HA-derivatives, the rotational[30]
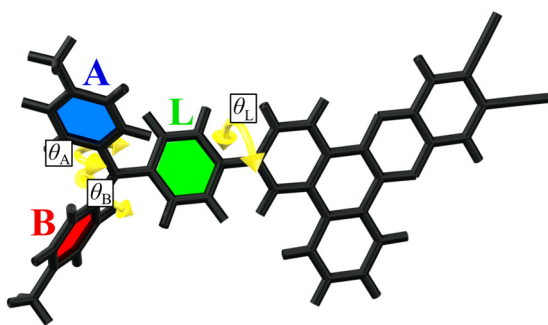


**Fig. 3** Structure of the investigated emitters with three types of dihedral angles ($\theta_A$, $\theta_B$ and $\theta_L$) highlighted which provide rotational isomerism.

**Table 3** Calculated geometry and electronic parameters of the key rotamers

| | Unit | H-1 | H-2 | 1Br-exo | 1Br-endo | 2Br-syn | 2Br-anti | 3Br-c3V | 3Br-A | 3Br-B | 3Br-C |
|---|---|---|---|---|---|---|---|---|---|---|---|
| $\theta_L$ | [°] | 27.9 | -28.8 | -23.1 | -22.5 | 17.8 | 17.6 | 19.0 | 19.5 | 17.8 | 18.1 |
| $\theta_A$ | [°] | -64.6 | -65.1 | -69.1 | -74.9 | -63.5 | -68.5 | 76.6 | 76.5 | -77.5 | -71.0 |
| $\theta_B$ | [°] | -64.8 | -65.2 | 55.3 | -74.9 | 77.3 | -68.4 | -78.0 | 61.7 | -73.6 | 61.4 |
| $\Delta G(S_1)$ | [a.u.] | -1889.647927 | -1889.647680 | -1902.208629 | -1902.206972 | -1914.764972 | -1914.765059 | -1927.32269 | -1927.324124 | -1927.322466 | -1927.321232 |
| $\Delta G(T_1)$ | [a.u.] | -1889.650547 | -1889.649878 | -1902.211800 | -1902.211480 | -1914.773697 | -1914.774187 | -1927.33009 | -1927.328483 | -1927.330665 | -1927.331147 |
| $S_1$-$S_0$ | [eV] | 1.38 | 1.37 | 1.58 | 1.59 | 1.74 | 1.77 | 1.84 | 1.77 | 1.85 | 1.80 |
| $S_1$-$S_0$ | [nm] | 899 | 907 | 787 | 779 | 713 | 702 | 674 | 702 | 670 | 687 |
| $f_{CT\text{-}S0}$ | | 0.228 | 0.209 | 0.331 | 0.335 | 0.438 | 0.461 | 0.407 | 0.340 | 0.450 | 0.39 |
| $T_1$-$S_0$ | [eV] | 1.26 | 1.26 | 1.38 | 1.38 | 1.45 | 1.43 | 1.55 | 1.55 | 1.53 | 1.54 |
| $T_1$-$S_0$ | [nm] | 980 | 984 | 896 | 892 | 854 | 864 | 797 | 800 | 810 | 805 |
| $T_2$-$S_0$ | [eV] | 1.92 | 1.91 | 1.96 | 1.96 | 2.01 | 2.03 | 2.00 | 1.96 | 2.02 | 1.99 |
| $T_2$-$S_0$ | [nm] | 645 | 646 | 632 | 631 | 616 | 610 | 619 | 630 | 613 | 622 |
| $SOC_{T1\text{-}S1}$ | [cm$^{-1}$] | 0.06 | 0.08 | 0.32 | 0.44 | 0.58 | 0.04 | 0.58 | 0.88 | 2.3 | 3.45 |
| $SOC_{T2\text{-}S1}$ | [cm$^{-1}$] | 0.23 | 0.17 | 0.58 | 0.74 | 0.40 | 0.13 | 0.39 | 0.65 | 0.87 | 3.08 |
| $\Delta E_{3CT\text{-}1CT}$ | [eV] | 0.03 | 0.03 | 0.11 | 0.12 | 0.10 | 0.15 | 0.20 | 0.14 | 0.24 | 0.18 |
| $\lambda_{3CT\text{-}1CT}$ | [eV] | 0.34 | 0.33 | 0.38 | 0.38 | 0.39 | 0.39 | 0.41 | 0.41 | 0.41 | 0.41 |
| $E_a$ | [eV] | 0.18 | 0.17 | 0.23 | 0.23 | 0.23 | 0.25 | 0.29 | 0.25 | 0.32 | 0.28 |
| $k_{3CT\text{-}1CT} \cdot \chi_{3CT}$ | [$10^4$ s$^{-1}$] | 0.16 | 0.30 | 0.56 | 0.80 | 1.8 | $2.8 \times 10^{-3}$ | 0.14 | 1.54 | 0.93 | 8.0 |
| $k_{3LE\text{-}1CT} \cdot \chi_{3LE}$ | [$10^4$ s$^{-1}$] | 0.032 | $9 \times 10^{-3}$ | $1 \times 10^{-3}$ | $1 \times 10^{-3}$ | $1 \times 10^{-3}$ | $1 \times 10^{-3}$ | $<1 \times 10^{-3}$ | $<1 \times 10^{-3}$ | $<1 \times 10^{-3}$ | $3 \times 10^{-3}$ |

$\theta_L$, $\theta_A$, $\theta_B$ – dihedral angles between phenyl rings of the donor fragment (Fig. 3). $\Delta G(S_1)$, $\Delta G(T_1)$ – Gibbs free energies of $S_1$ and $T_1$ electronic states, respectively. $S_1$–$S_0$, $T_1$–$S_0$, $T_2$–$S_0$ – predicted energies of respective vertical transitions. $f_{1CT\text{-}S0}$ – oscillator strength of the $S_1$–$S_0$ transition. $SOC_{T1\text{-}S1}$, $SOC_{T2\text{-}S1}$ – SOC constants for $T_1$–$S_1$ and $T_2$–$S_1$ transitions, respectively. $\Delta E_{3CT\text{-}1CT}$ – energy gap between $^3CT$ and $^1CT$ states. $\lambda_{3CT\text{-}1CT}$ – reorganization energy. $E_a$ – activation energy; $\chi_{3CT}$/$\chi_{3LE}$ – relative population of $^3CT$ and $^3LE$ states at room temperature predicted by Boltzmann distribution (Section S2, ESI). $^1CT$ states.

This journal is © The Royal Society of Chemistry 2022

*J. Mater. Chem. C*, 2022, **10**, 11719–11729 | **11725**

and vibrational[23] isomerism has key importance for efficient rISC *via* the $^3CT \rightarrow {}^1CT$ pathway.

According to the experimental data, the $k_r$ values show complex behavior depending on the number of bromine atoms and the emitter/CBP doping ratio indicating the specific role of intermolecular interactions in amorphous films (Table 2). Regarding the aim of this study, the important observation is that **H**, **1Br**, and **2Br** show rather similar $k_r$ values in the $2–3 \times 10^7$ s$^{-1}$ range. Neither statistically weighted calculated $f_{1CT-S0}$ values (Table 1) nor $f_{1CT-S0}$ of individual rotamers (Fig. S5, S6, Table S2, ESI†) show a substantial decrease with the growing number of bromines in the emitter.

The statistically weighted $k_{3CT-1CT}$ correlate very well with the experimental $k_{rISC}$ values (Fig. 4), which confirms that various rotamers are responsible for the photophysical behavior of emitters in films. This also enables the analysis of $^3CT \rightarrow {}^1CT$ transition parameters in key rotamers as discussed below. We should note that the contribution of the second triplet state in rISC was found to be negligible even in **3Br**, where the $^3LE$-state is relatively close to the $^3CT$ one (Fig. 2E). The statistically weighted $k_{3LE-1CT}$ values do not exceed $1 \times 10^3$ s$^{-1}$, which is only 5% of the $k_{3CT-1CT}$ one (Fig. 4 and Section S2, ESI†). In other compounds, the $^3LE \rightarrow {}^1CT$ transition is slower. One can conclude that such a slow rISC pathway can only compete in rotamers with the slowest $^3CT \rightarrow {}^1CT$ transition such as **2Br**-*anti* ones (Table 3), but even in the latter case, $k_{3LE-1CT}$ is three times lower than $k_{3CT-1CT}$.

In **H**, two rotamers with different $\theta_L$ (**H-1** and **H-2** in Table 3, Table S2, Fig. S5 and S7, ESI†) have different SOC constants: 0.06 and 0.08 cm$^{-1}$, in spite of the absence of HAs and minor differences in the electronic parameters including $\Delta E_{ST}$ and $E_a$ (Fig. S5, ESI†). Different positions of linker phenyl provide different orientations of donor *versus* acceptor; in the rotamer **H-2** with $\theta_L = -29°$, the donor fragment is more twisted *versus* the acceptor, providing larger change in the orbital moment $\Delta L$ during the $^3CT \rightarrow {}^1CT$ transition (Fig. S7, ESI†). One should note that the change of orbital moment is typically small as for transition between states of very close nature. In spite of minor changes in $\Delta L$ and SOC, the calculated $k_{3CT-1CT}$ values of **H** rotamers differ by 2 times.

In **1Br**, the highly asymmetric donor fragment enables 16 rotamers. The calculated $f_{1CT-S0}$ values are very similar for all rotamers (Fig. S5, ESI†). As compared to **H**, the calculated $\Delta E_{ST}$ values are increased more than 3 times, and for all rotamers of **1Br** they exceed 100 meV. The presence of a heavy atom causes more than a fivefold SOC constant rise up to 0.31–0.45 cm$^{-1}$, depending on the rotamer structure. The highest SOC is observed when the bromine atom in the donor fragment is oriented towards the acceptor (8 rotamers are attributed to **1Br**-*endo* group in Fig. 5 and Fig. S5, ESI†), whilst the opposite direction provides the lowest value (8 rotamers, **1Br**-*exo*). SOC rise is, however, partially compensated by the $\Delta E_{ST}$ increase, which provides more than 3 times rISC acceleration as compared to **H**. As neither experimental $k_r$ nor calculated $f_{1CT-S0}$ values of **1Br** are substantially lower than those of **H**, one can conclude that the introduction of one

bromine atom has a positive effect on triplet harvesting in such emitters.

Regarding the relative position of two bromine atoms, 16 rotamers of **2Br** can be divided into two main groups: *syn* and *anti*. The expected strong heavy-atom effect is realized only in the *syn* rotamers with both bromines on the same side of the acceptor plane (Fig. 5 and Fig. S5 (ESI†), Table 3). In such HA configurations, the increased SOC constants reach 0.60 cm$^{-1}$. In the *anti* rotamers, bromines on the different sides of the acceptor plane cause surprisingly low SOC constants, dropping below 0.05 cm$^{-1}$, resembling those for an HA-free emitter **H**. In the result, the $k_{3CT-1CT}$ of the most efficient *syn* rotamer is 650 higher than that of the least efficient *anti* one. These observations indicate that the HA effect can be zeroed when heavy atoms are situated in a symmetric way or at the opposite sides of the donor fragment.

**3Br** exhibits the most complex isomerism. Regarding the relative position of three bromine atoms, its 32 rotamers can be divided into four groups. The rotamers in which bromines and the nitrogen atom form a symmetric pyramid-like structure of $C_{3V}$ symmetry (**3Br-c_{3V}** in Fig. 5) exhibit the lowest SOC values below 0.70 cm$^{-1}$ (Fig. S6 (ESI†), Table 3 and Table S2, ESI†). When such a symmetry is broken by the rotation of A or B rings so that side bromines occur in the *anti* configuration (**3Br-A** on Fig. 5 and Fig. S6, ESI†), the SOC increases slightly up to 0.9 cm$^{-1}$. As an exception, another group of *anti* rotamers with bromine atoms of the side rings oriented towards the acceptor fragment exhibit a high SOC reaching 2.40 cm$^{-1}$ (**3Br-B**). In such rotamers, in contrast to *anti* rotamers of **2Br**, the symmetry of the *anti* configuration is broken by the bromine in the linker phenyl of **3Br**. The most impressive SOC values reaching 3.50 cm$^{-1}$ are observed in the case when the $C_{3V}$ symmetry is broken *via* rotation of the linker phenyl ring, so that bromines in the side phenyl rings remain in the *syn* configuration (**3Br-C**). Such a dependence on the relative positions of bromine atoms supports the conclusion that the asymmetric configuration of HAs favors the maximal increase of SOC. From the point of view of rISC efficiency, a negative factor of all **3Br** rotamers is high $\Delta E_{ST}$ which ranges from 140 to 240 meV. Remarkably, in spite of such a high $\Delta E_{ST}$ value of 180 meV, high SOC in the most efficient rotamers **3Br-C** enables $k_{3CT-1CT}$ above $8 \times 10^4$ s$^{-1}$ outranging more than 25 times that in **H**.

The increase of SOC within an isolated atom or molecular system is usually explained by the increase of the orbital and/or spin transition moment, because these two quantum values define the change of the total angular momentum and thus the spin–orbit coupling.[6] Thorough analysis of electronic parameters led us to the conclusion that, regarding total angular momentum, the $^3CT \rightarrow {}^1CT$ transition in various rotamers bearing heavy atom(s) remains very similar. None of the calculated electronic parameters by itself can explain the drastic change of SOC and rISC rates. Neither calculated changes in the NTO orbitals of $^3CT \rightarrow {}^1CT$ transitions nor partial contributions of electronic densities on the bromine atom below (Fig. S8 and S9, ESI†) reveal a substantial change in the orbital transition moment. Triplet spin density distribution (TSDD, Fig. S10, ESI†)
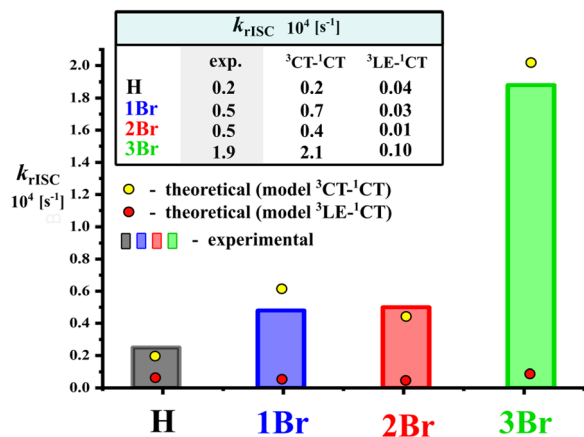
**11726** | *J. Mater. Chem. C*, 2022, **10**, 11719–11729

This journal is © The Royal Society of Chemistry 2022

**Fig. 4** Comparison of experimental $k_{rISC}$ with calculated statistically weighted $k_{3CT-1CT}$ and $k_{3LE-1CT}$.

maps remain similar and the contribution of bromine atom(s) is negligible too, which indicates that the change of spin transition moment is very similar for all isomers. Therefore, the observed heavy-atom effect cannot be regarded as the internal one. On the other hand, the notion "external heavy-atom effect" cannot be applied either, as heavy atoms are covalently bonded to the chromophore fragment.

In spite of the absence of direct influence of heavy atom(s) on the electronic spin–flip transition, their presence and orientation change immensely the SOC matrix elements and thus the direction and value of total angular momentum. The observed phenomenon can be regarded as the heavy-atom field effect (HAFE). Such a field interacts with the electron density during the electronic transition enhancing the change of spin. The peculiarity of the observed HAFE phenomenon, namely the inactivity of HAs in either $^1CT$-$S_0$ or $^3CT \rightarrow {}^1CT$ transitions as one can conclude on the basis of NTO analysis (Fig. S8, ESI†) can be explained by the electron-withdrawing effect of bromine which disables its participation in the charge-transfer transition in the role of the donor.

Most likely, the HAFE has a direction defined by the orientation of heavy atoms. In fact, the analysis of the SOC matrix elements within the geometry coordinates of each rotamer (Fig. 5) indicates that maximal strengths of the HAFE and thus the highest SOC are achieved in two cases. The first one with the most substantial growth of SOC matrix elements is observed when HAs' relative alignment is asymmetrical (compare **3Br-c_{3v}** and other rotamers of **3Br**, Fig. 5) and the field of one heavy atom cannot be compensated by another one (compare *syn* and *anti* **2Br** rotamers). The second case is when heavy atoms are orientated towards the change of electronic density during the $^3CT \rightarrow {}^1CT$ transition (compare *endo* with *exo* **1Br** rotamers, and **2Br**-*syn* with **2Br**-*anti*, Fig. 5). In fact, the symmetric orientation of bromines in **3Br-C_{3V}** and especially **2Br**-*anti* rotamers results in self-compensation or even zeroing of the HA effect.



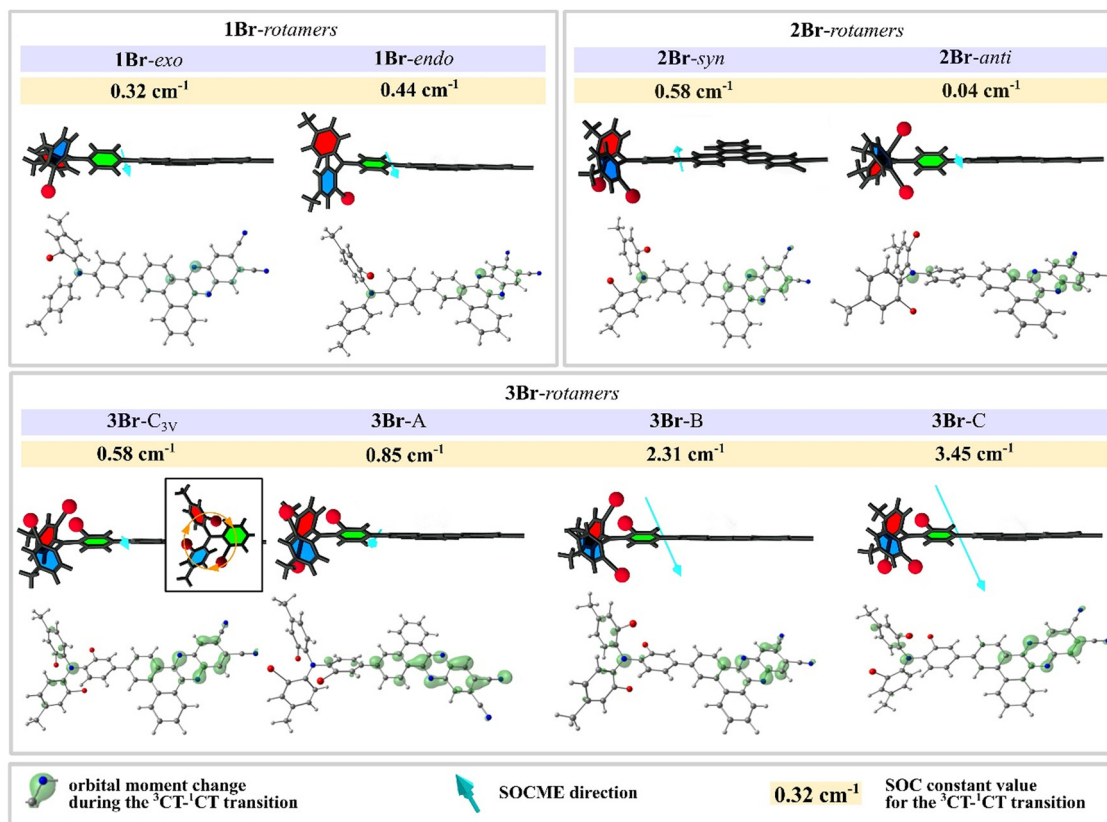**Fig. 5** Optimized structures of key rotamers (see Fig. S5 and S6, ESI†) of **1Br**, **2Br**, and **3Br** with SOCME value, SOCME direction (turquoise arrows), and $\Delta L$ (green clouds, contour value 0.02); illustrations show the simplified orientation of heavy atoms relative to the acceptor plane.

This journal is © The Royal Society of Chemistry 2022

*J. Mater. Chem. C*, 2022, **10**, 11719–11729 | **11727**

To the best of our knowledge, neither observation of the HAFE nor the possibility of self-compensation of the HA effect was reported before. The latter peculiarity is not intuitive for materials with more than one HA, and can lead to an imaginary lack of the HA effect or even the opposite result of SOC decrease. The possibility of formation of rotamers with zero HAFE during synthesis or sample preparation evidences another challenge for hybrid material engineers to analyze and eliminate such species at the stage of molecular design planning to achieve efficient rISC.

## Conclusions

The results of the above discussed experimental and computational investigations evidence that hybrid organic materials bearing abundant heavy atoms in fact can solve the dilemma of all-organic TADF materials given by eqn 1. In the investigated example, selective acceleration of the $^3CT \rightarrow {}^1CT$ rISC pathway without a drastic decrease of the $S_1$–$S_0$ oscillator strength is possible in a partially conjugated D–A type emitter, when heavy atoms do not self-compensate the created field and are oriented towards the fragment transition orbital moment. The most representative examples are various rotamers of **2Br** and **3Br** with similar oscillator strength values but very different SOC and rISC rates (Fig. S5 and S6, ESI†). This is a clear evidence that in contrast to pure organic emitters such hybrid molecular systems disobey the inverse relationship of $f_{1CT\text{-}S0}$ and $k_{rISC}$. This is supported by the following:

(1) the $f_{1CT\text{-}S0}$ values measured for absorption as well as calculated ones, which indicate that bromine in the role of a heavy atom does not decrease the rate of radiative deactivation *via* $S_1$–$S_0$ transition;

(2) photophysical features of **1Br** in 10% ww. film, which in comparison to **H** has twice higher $k_{rISC}$ and only 1.2 times smaller $k_r$;

(3) different rotamers of **2Br** and **3Br**, which have extremely different $k_{rISC}$ rates, but close $f_{1CT\text{-}S0}$ ones.

On the one hand, the applied bromine is a good choice for the role of a heavy atom as it can be easily introduced by common and powerful synthetic methods. However, its pronounced electron-withdrawing influence on the donor fragment reduces the charge-transfer strength leading to the blue-shift of TADF and increase of $\Delta E_{ST}$. Both these factors are undesired for red emitters, whilst the latter one is negative for all TADF materials in general. Nevertheless, thanks to high SOC, in **3Br** with a 200 meV energy gap almost disabling TADF, the rISC rate is the highest one. Another negative factor of the increase of $^1CT$ energy especially in **2Br** and **3Br** is the decrease of the $^1CT \rightarrow {}^3LE$ energy gap. This leads to the acceleration of ISC, and thus faster conversion of singlet states to triplet ones.

The analysis of various rotational isomers of the investigated emitters evidences that further improvement of hybrid organic emitters with the HAFE can be probably achieved *via* the stereoselective control of the position of HAs in the molecular structure. In the example of **3Br**, selective synthesis or isolation of **3Br-C** rotamers could provide a further fourfold rISC enhancement without the decrease of the fluorescence rate, making such an emitter more attractive commercially.

## Conflicts of interest

There are no conflicts to declare.

## Acknowledgements

## References

1 S. H. Mir, L. A. Nagahara, T. Thundat, P. Mokarian-Tabari, H. Furukawa and A. Khosla, *J. Electrochem. Soc.*, 2018, **165**, 3137–3156.

2 V. Trifiletti, C. Asker, G. Tseberlidis, S. Riva, K. Zhao, W. Tang, S. Binetti and O. Fenwic, *Front. Electron.*, 2021, **2**, 758603.

3 T. Hua, L. Zhan, N. Li, Z. Huang, X. Cao, Z. Xiao, S. Gong, C. Zhou, C. Zhong and C. Yang, *Chem. Eng. J.*, 2021, **426**, 131169.

4 Y. Xiang, Y. Zhao, N. Xu, S. Gong, F. Ni, K. Wu, J. Luo, G. Xie, Z.-H. Lu and C. Yang, *J. Mater. Chem. C*, 2017, **5**, 12204–12210.

5 E. Longhi and L. De Cola, *Iridium(III) Complexes for OLED Application, Iridium(III) in Optoelectronic and Photonics Applications*, John Wiley & Sons, Ltd, Chichester, UK, 2017, p. 205.

6 W. Shao, H. Jiang, R. Ansari, P. M. Zimmerman and J. Kim, *Chem. Sci.*, 2022, **13**, 789–797.

7 M. Godumala, A. V. Kumar and R. Chandrasekar, *J. Mater. Chem. C*, 2021, **9**, 14115–14132.

8 H. F. Higginbotham, M. Okazaki, P. de Silva, S. Minakata, Y. Takeda and P. Data, *ACS Appl. Mater. Interfaces*, 2021, **13**, 2899–2907.

9 D. Lee, O. Bolton, B. C. Kim, J. H. Youk, S. Takayama and J. Kim, *J. Am. Chem. Soc.*, 2013, **135**, 6325–6329.

10 A. Lv, W. Ye, X. Jiang, N. Gan, H. Shi, W. Yao, H. Ma, Z. An and W. Huang, *J. Phys. Chem. Lett.*, 2019, **10**, 1037–1042.

11 Z.-Y. Zhang, Y. Chen and Y. Liu, *Angew. Chem., Int. Ed.*, 2019, **58**, 6028–6032.

12 H. Uoyama, K. Goushi, K. Shizu, H. Nomura and C. Adachi, *Nature*, 2012, **492**, 234–238.

13 X. Yin, Y. He, X. Wang, Z. Wu, E. Pang, J. Xu and J. Wang, *Front. Chem.*, 2020, **8**, 725.

14 T. Huang, X. Song, M. Cai, D. Zhang and L. Duan, *Mater. Today Energy*, 2021, **21**, 100705.

**11728** | *J. Mater. Chem. C*, 2022, **10**, 11719–11729

This journal is © The Royal Society of Chemistry 2022

15 Y. Ren, Y. Wada, K. Suzuki, Y. Kusakabe, J. Geldsetzer and H. Kaji, *Appl. Phys. Express*, 2021, **14**, 071003.

16 D. Song, Y. Yu, L. Yue, D. Zhong, Y. Zhang, X. Yang, Y. Sun, G. Zhou and Z. Wu, *J. Mater. Chem. C*, 2019, **7**, 11953.

17 T. Hua, L. Zhan, N. Li, Z. Huang, X. Cao, Z. Xiao, S. Gong, C. Zhou, C. Zhong and C. Yang, *Chem. Eng. Sci.*, 2021, **426**, 131169.

18 K. Masui, H. Nakanotani and C. Adachi, *Org. Electron.*, 2013, **14**, 2721–2726.

19 Y. Zhang and S. R. Forrest, *Phys. Rev. Lett.*, 2012, **108**, 267404.

20 R. Furue, K. Matsuo, Y. Ashikari, H. Ooka, N. Amanokura and T. Yasuda, *Adv. Opt. Mater.*, 2018, **6**, 1701147.

21 Y.-L. Zhang, Q. Ran, Q. Wang, Y. Liu, C. Hanisch, S. Reineke, J. Fan and L.-S. Liao, *Adv. Mater.*, 2019, **31**, 1902368.

22 J. H. Kim, J. H. Yun and J. Y. Lee, *Adv. Opt. Mater.*, 2018, **6**, 1800255.

23 M. Mońka, I. E. Serdiuk, K. Kozakiewicz, E. Hoffman, J. Szumilas, A. Kubicki, S. Y. Park and P. Bojarski, *J. Mater. Chem. C*, 2022, **10**, 7925–7934.

24 R. D. Burkhart and N. I. John, *J. Phys. Chem.*, 1991, **95**, 7189–7196.

25 U. Balijapalli, Y.-T. Lee, B. S. B. Karunathilaka, G. Tumen-Ulzii, M. Auffray, Y. Tsuchiya, H. Nakanotani and C. Adachi, *Angew. Chem., Int. Ed.*, 2021, **60**, 19364–19373.

26 A. A. Kubicki, P. Bojarski, M. Grinberg, M. Sadownik and B. Kukliński, *Opt. Commun.*, 2006, **269**, 275–280.

27 M. J. Frisch, G. W. Trucks, H. B. Schlegel, G. E. Scuseria, M. A. Robb, J. R. Cheeseman, G. Scalmani, V. Barone, G. A. Petersson and H. Nakatsuji, *et al.*, *Gaussian 16, Revision C.01*, Gaussian, Inc., Wallingford, CT, 2016.

28 A. D. Becke, *J. Chem. Phys.*, 1993, **98**, 1372–1377.

29 F. Neese, *Wiley Interdiscip. Rev.: Comput. Mol. Sci.*, 2012, **2**, 73–78.

30 I. E. Serdiuk, M. Mońka, K. Kozakiewicz, B. Liberek, P. Bojarski and S. Y. Park, *J. Phys. Chem. B*, 2021, **125**, 2696–2706.

This journal is © The Royal Society of Chemistry 2022

*J. Mater. Chem. C*, 2022, **10**, 11719–11729 | **11729**

Supporting information

**Decisive Role of Heavy-Atom Orientation for Efficient Enhancement of Spin-Orbit Coupling in Organic Thermally Activated Delayed Fluorescence Emitters**

Michał Mońka,[1] Daria Grzywacz,[2] Estera Hoffman,[1] Vladyslav Ievtukhov,[2] Karol Kozakiewicz,[2] Radoslaw Rogowski,[1] Aleksander Kubicki,[1] Beata Liberek,[2] Piotr Bojarski,[1] Illia E. Serdiuk[1]*

[1] Faculty of Mathematics, Physics and Informatics, University of Gdańsk, Wita Stwosza 57, 80-308 Gdańsk, Poland

[2] Faculty of Chemistry, University of Gdańsk, Wita Stwosza 63, 80-308 Gdańsk, Poland

*Corresponding author. E-mail: illia.serdiuk@ug.edu.pl, phone + 48 58 523 22 44

**Table of contents**

# Section S1: Photophysical measurements



Steady-State PL (6% CBP)

A

$\lambda_{onset} = 521nm$
$\lambda_{onset} = 552nm$
$\lambda_{onset} = 569nm$
$\lambda_{onset} = 597nm$

H
1Br
2Br
3Br

T= 298K



Phosphorescence (6% CBP)

B

$\lambda_{onset} = 571nm$
$\lambda_{onset} = 585nm$
$\lambda_{onset} = 589nm$
$\lambda_{onset} = 608nm$

H
1Br
2Br
3Br

T= 10K



Steady-State PL (10% CBP)

C

$\lambda_{onset} = 527nm$
$\lambda_{onset} = 560nm$
$\lambda_{onset} = 579nm$
$\lambda_{onset} = 600nm$

H
1Br
2Br
3Br

T= 298K



Phosphorescence (10% CBP)

D

$\lambda_{onset} = 575nm$
$\lambda_{onset} = 585nm$
$\lambda_{onset} = 595nm$
$\lambda_{onset} = 609nm$

H
1Br
2Br
3Br

T= 10K



Steady-State PL (6% CBP)

E

Ph-DMAC

T= 298K

$\lambda_{onset} = 525nm$



Phosphorescence (6% CBP)

F

Ph-DMAC
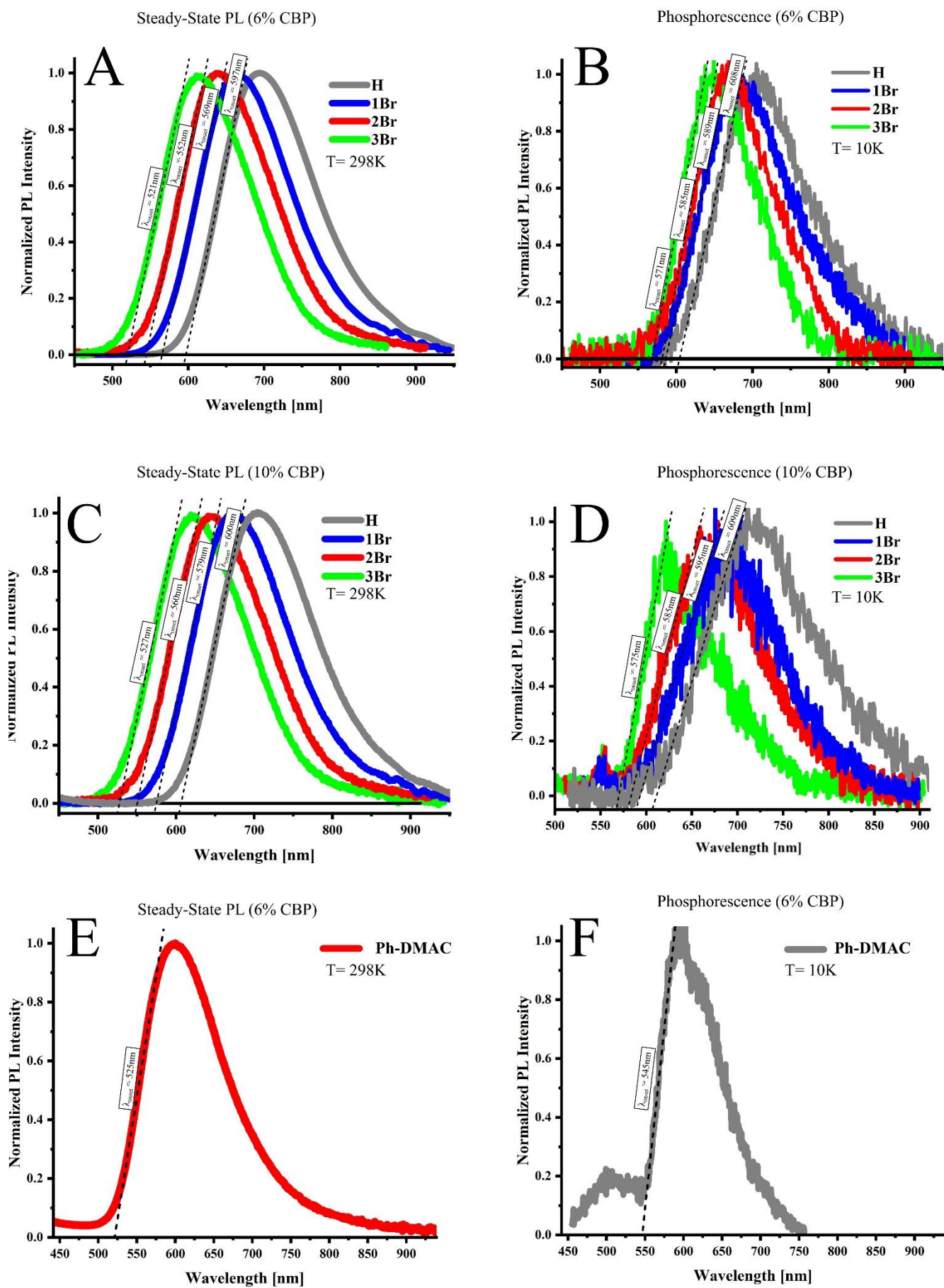
T= 10K

$\lambda_{onset} = 545nm$

**Figure S1.** Steady-State PL spectra of investigated compounds: 6% (A, E) and 10% (C) CBP with onsets and phosphorescence spectra measured in 10K, 6% (B, F) and 10% (D) CBP.

**Table S1.** Experimental determination of $^{1}CT$, $^{3}CT$ and $^{3}LE$ - onset values.

| | $w_{X/CBP}$ | Fluorescence $\lambda_{onset}$ | $^{1}CT$ energy | Phosphorescence $\lambda_{onset}$ | $^{3}CT$ energy | $\Delta E_{1CT-3CT}$ | | | Phosphorescence $\lambda_{onset}$ | $^{3}LE$ energy | $\Delta E_{1CT-3LE}$ |
|---|---|---|---|---|---|---|---|---|---|---|---|
| | | [nm] | [eV] | [nm] | [eV] | [eV] | | | [nm] | [eV] | [eV] |
| **H** | 6% | 597 | 2.07 | 608 | 2.04 | 0.04 | | | 552 | 2.25 | -0.18 |
| | 10% | 600 | 2.07 | 609 | 2.04 | 0.03 | | | | | |
| **1Br** | 6% | 569 | 2.18 | 589 | 2.10 | 0.08 | **ZNX** | | 552 | 2.25 | -0.07 |
| | 10% | 579 | 2.14 | 595 | 2.08 | 0.06 | 0.1% | | | | |
| **2Br** | 6% | 552 | 2.25 | 585 | 2.12 | 0.13 | | | 552 | 2.25 | 0.00 |
| | 10% | 560 | 2.21 | 585 | 2.11 | 0.10 | | | | | |
| **3Br** | 6% | 521 | 2.37 | 571 | 2.17 | 0.20 | | | 552 | 2.25 | 0.13 |
| | 10% | 527 | 2.35 | 575 | 2.16 | 0.19 | | | | | |



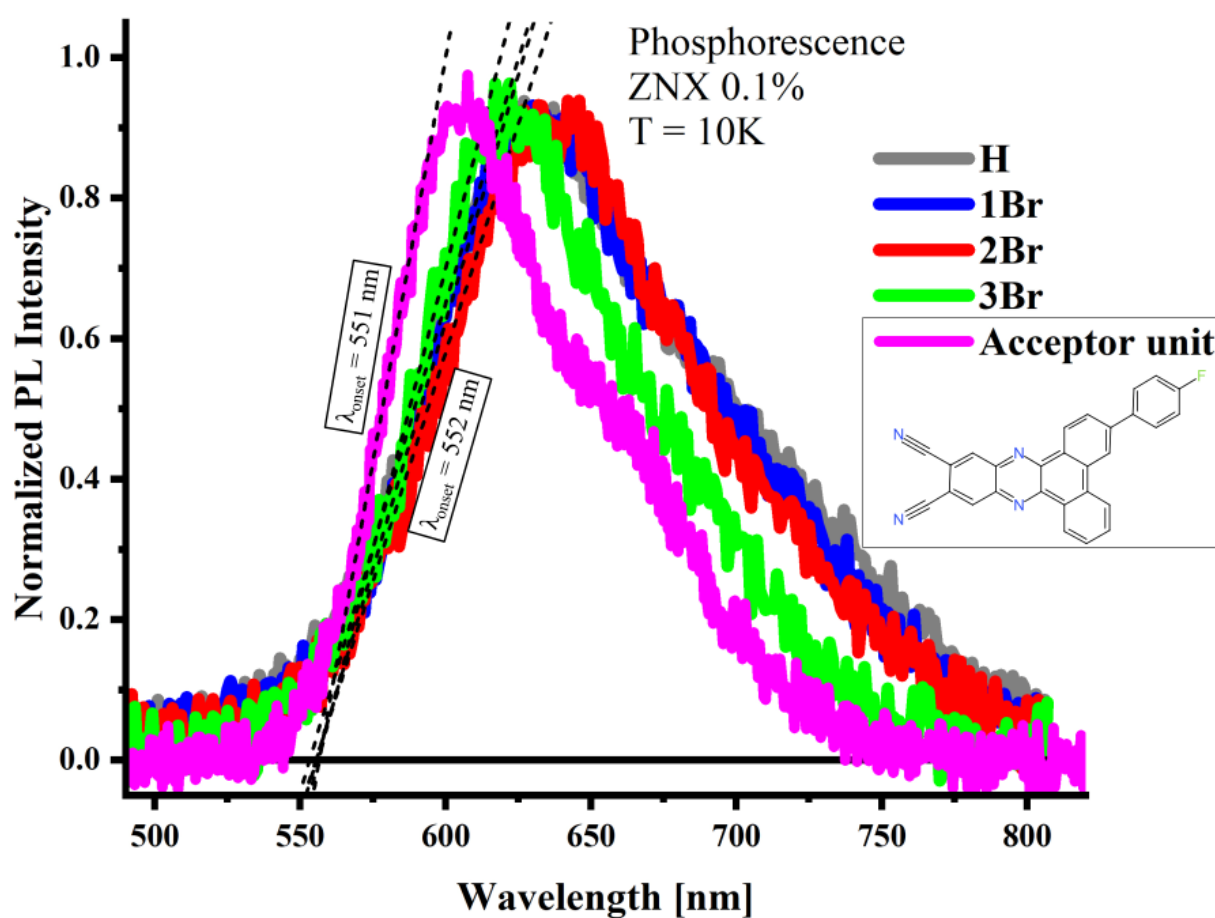**Figure S2.** Phosphorescence spectra of investigated compounds dispersed in ZNX, measured in 10K under excitation wavelength $\lambda_{exc} = 370$ nm with a 20ms delay after excitation pulse.
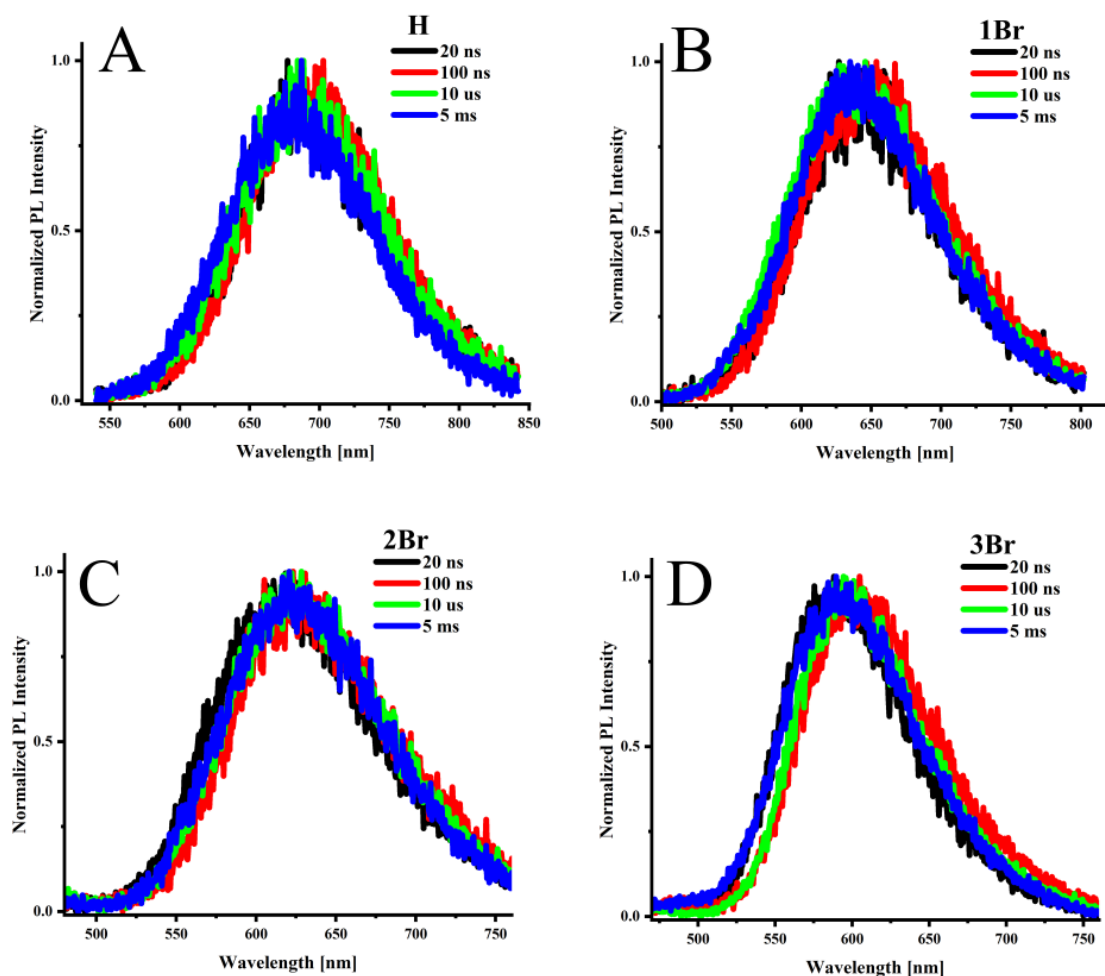
**Figure S3.** PL spectra of **H** (A), **1Br** (B), **2Br** (C), and **3Br** (D) in 6% CBP, taken at different time delays.
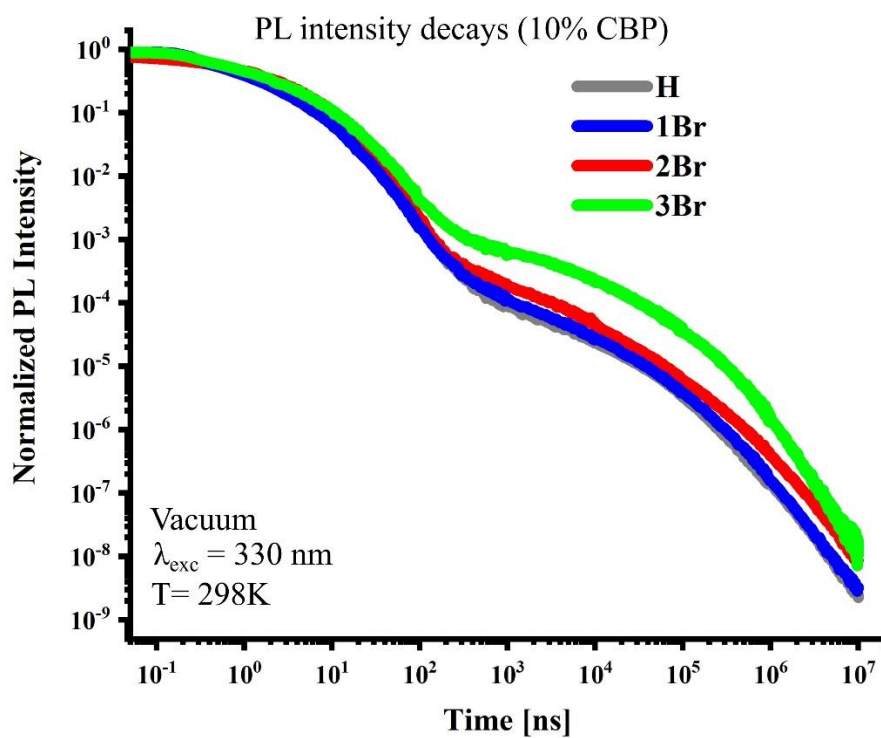


**Figure S4.** PL intensity decays of investigated compounds (10% CBP) measured in vacuum under excitation wavelength $\lambda_{exc}$ = 330 nm.

## Section S2: Quantum chemical calculations

Theoretical rate constants of rISC were calculated using Marcus-Hush equation:

$$k_{(r)ISC} = \frac{V^2}{\hbar} \sqrt{\frac{\pi}{k_B T \lambda}} \exp\left[-\frac{(\Delta E_{ST} + \lambda)^2}{4 k_B T \lambda}\right], \tag{S1}$$

where $V$ is SOC constant, $\hbar$ is reduced Planck constant, $\lambda$ is sum of internal $\lambda_{int}$ and external ($\lambda_{solv}$) reorganization energies for respective transition (in our calculations we assumed $\lambda_{solv}$, = 0.3 eV) $\Delta E_{ST}$ is the energy gap between singlet and respective triplet state, $k_B$ stands for Boltzmann constant, T is temperature.

Relative contribution of $i$-th rotamers in **H**, **1Br**, **2Br** and **3Br**-rotamers was calculated using Boltzmann distribution law:

$$\mu_i[\%] = \frac{\exp\left(-\frac{\Delta E_i}{k_B T}\right)}{\sum_{i=1}^{N} \exp\left(-\frac{\Delta E_i}{k_B T}\right)}, \tag{S2}$$

where $N$ is the number of existing isomers (for **H**, **1Br 2Br** and **3Br**-rotamers $N$ = 2, 16, 16 and 32, respectively), $\Delta E_i$ denotes the energy difference between $i$-th rotamer and most stable rotamer (with lowest energy). Procedure for theoretical prediction rate constants described in details in [1].

**Figure S5.** Calculated electronic parameters of all **H**, **1Br** and **2Br** – rotamers. In main text, key rotamers (depicted in **Figure 5**, **Table 3**) from each group: **H**-*rotamers*: **1** (as **H-1**) and **2** (as **H-2**); **1Br**-*rotamers:* **3** (as **1Br**-*endo*) and **12** (as **1Br**-*exo*); **2Br**-*rotamers*: **5** (as **2Br**-*syn*) and **9** (as **2Br**-*anti*).

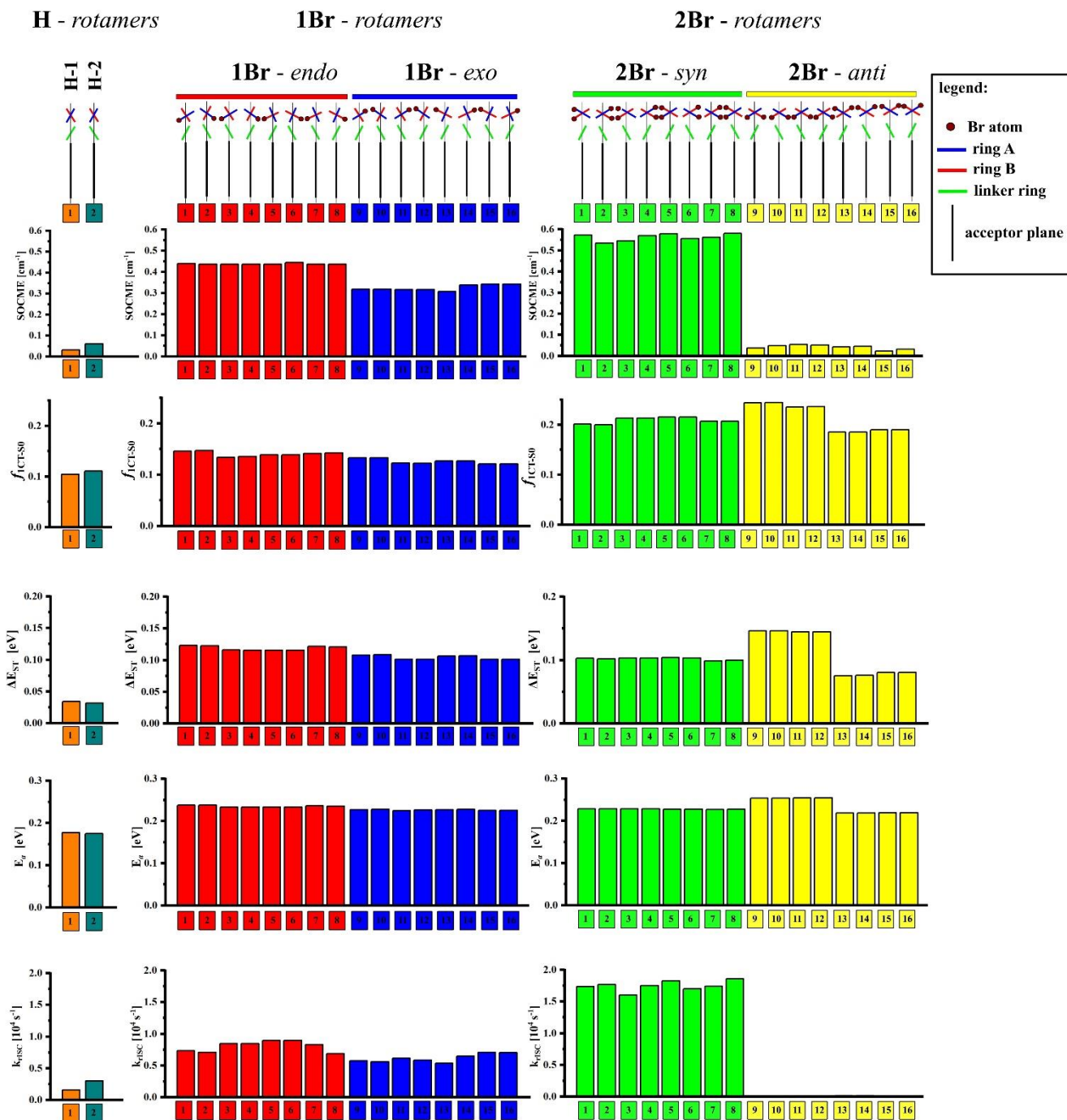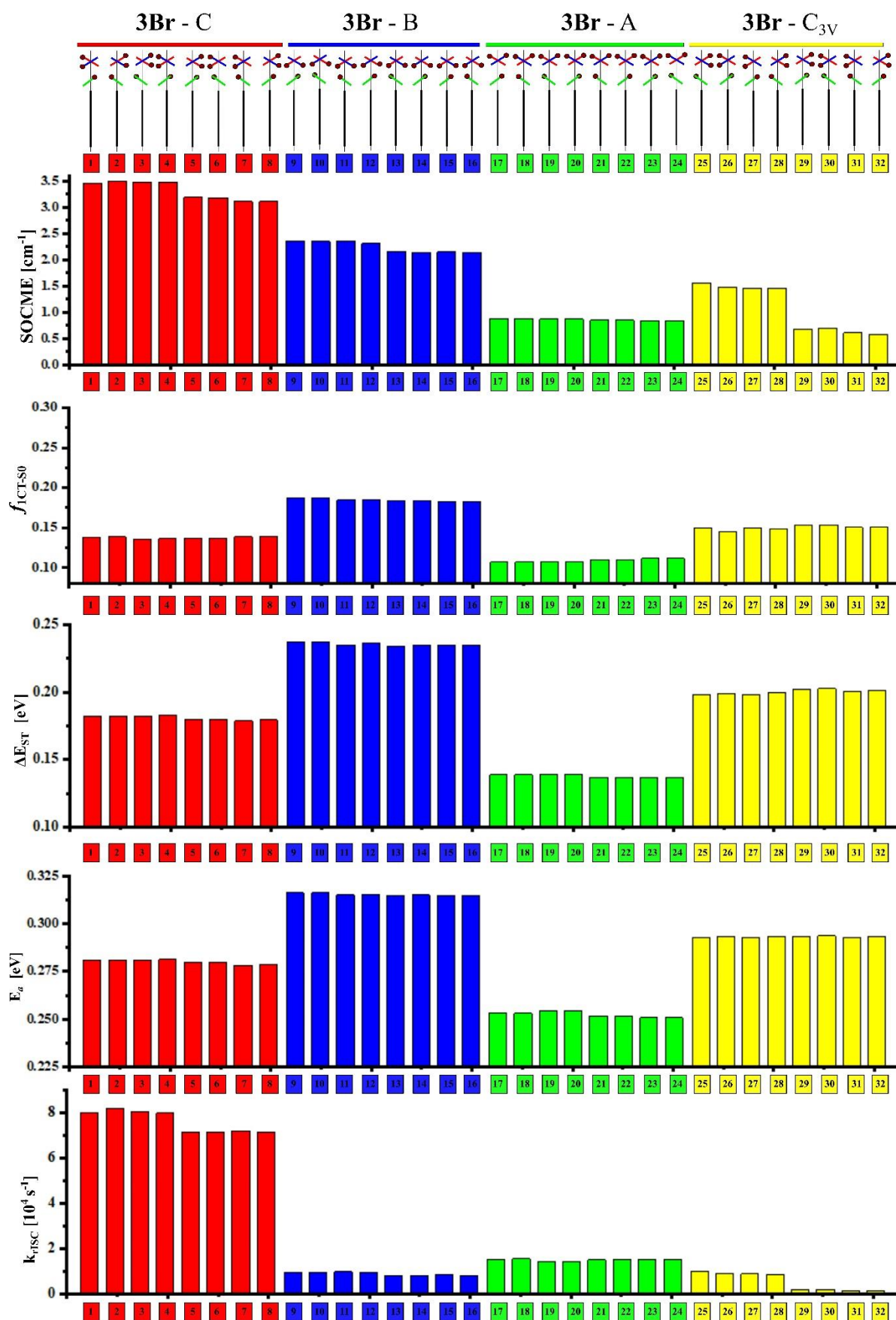**Figure S6.** Calculated electronic parameters of all **3Br** rotamers. In main text, key rotamers (depicted in **Figure 5**, **Table 3**) from 3Br-rotamers group: **32** (as **3Br**-C$_{3V}$), **17** (as **3Br**-A), **21** (as **3Br**-A), **12** (as **3Br**-B), **1** (as **3Br**-C).

**Table S2.** Calculated values of different geometry (dihedrals $\theta_L$, $\theta_A$, and $\theta_B$) and electronic parameters (plotted in **Figures S5** and **S6**) of all rotamers.

**H - rotamers**

| | 1 | 2 | $X^a$ |
|---|---|---|---|
| $SOC_{T1-S1}$ [cm$^{-1}$] | 0.06 | 0.08 | -- |
| $\Delta E_{3CT-1CT}$ [eV] | 0.03 | 0.03 | **0.03** |
| $f_{S1-S0}$ | 0.10 | 0.11 | **0.107** |
| $E_a$ [eV] | 0.18 | 0.17 | -- |
| $\mu$ [%] | 67.2 | 32.8 | -- |
| $k_{rISC}$ [10$^4$ s$^{-1}$] | 0.16 | 0.30 | **0.20** |
| | | | |
| $\theta_L$ | 27.9 | -28.8 | |
| $\theta_A$ | -64.6 | -65.1 | |
| $\theta_B$ | -64.8 | -65.2 | |

**1Br - rotamers**

| | 1 | 2 | 3 | 4 | 5 | 6 | 7 | 8 | 9 | 10 | 11 | 12 | 13 | 14 | 15 | 16 | $X^a$ |
|---|---|---|---|---|---|---|---|---|---|---|---|---|---|---|---|---|---|
| $SOC_{T1-S1}$ [cm$^{-1}$] | 0.44 | 0.43 | 0.44 | 0.44 | 0.44 | 0.44 | 0.45 | 0.41 | 0.32 | 0.32 | 0.32 | 0.32 | 0.31 | 0.34 | 0.34 | 0.34 | -- |
| $\Delta E_{3CT-1CT}$ [eV] | 0.12 | 0.12 | 0.12 | 0.12 | 0.12 | 0.12 | 0.12 | 0.12 | 0.11 | 0.11 | 0.10 | 0.10 | 0.11 | 0.11 | 0.10 | 0.10 | **0.11** |
| $f_{S1-S0}$ | 0.15 | 0.15 | 0.13 | 0.14 | 0.14 | 0.14 | 0.14 | 0.14 | 0.13 | 0.13 | 0.12 | 0.12 | 0.13 | 0.13 | 0.12 | 0.12 | **0.131** |
| $E_a$ [eV] | 0.24 | 0.24 | 0.23 | 0.23 | 0.23 | 0.23 | 0.24 | 0.24 | 0.23 | 0.23 | 0.22 | 0.23 | 0.23 | 0.23 | 0.23 | 0.23 | -- |
| $\mu$ [%] | 7.0 | 4.3 | 1.5 | 2.0 | 7.3 | 10.6 | 3.9 | 21.8 | 7.6 | 2.1 | 9.0 | 3.3 | 6.6 | 5.0 | 3.0 | 5.1 | -- |
| $k_{rISC}$ [10$^4$ s$^{-1}$] | 0.7 | 0.7 | 0.8 | 0.8 | 0.9 | 0.9 | 0.8 | 0.7 | 0.6 | 0.6 | 0.6 | 0.6 | 0.5 | 0.6 | 0.7 | 0.7 | **0.71** |
| | | | | | | | | | | | | | | | | | |
| $\theta_L$ | 21.3 | -21.1 | -22.6 | 22.5 | 22.3 | -22.3 | -22.6 | 22.7 | 23.2 | -23.1 | -23.0 | 22.4 | 23.6 | -23.6 | -21.9 | 21.9 | |
| $\theta_A$ | -74.6 | 74.7 | -74.9 | 74.9 | 56.0 | -56.0 | 55.9 | -55.9 | 69.2 | -69.1 | 68.4 | -68.8 | -55.3 | 55.2 | -55.3 | 55.2 | |
| $\theta_B$ | -56.1 | 56.5 | -56.1 | 56.2 | 75.1 | -75.1 | 74.9 | -74.9 | -55.4 | 55.3 | -55.3 | 55.1 | 69.5 | -69.2 | 69.0 | -68.8 | |

**2Br - rotamers**

| | 1 | 2 | 3 | 4 | 5 | 6 | 7 | 8 | 9 | 10 | 11 | 12 | 13 | 14 | 15 | 16 | $X^a$ |
|---|---|---|---|---|---|---|---|---|---|---|---|---|---|---|---|---|---|
| $SOC_{T1-S1}$ [cm$^{-1}$] | 0.57 | 0.53 | 0.54 | 0.57 | 0.58 | 0.56 | 0.56 | 0.58 | 0.04 | 0.05 | 0.05 | 0.05 | 0.04 | 0.05 | 0.02 | 0.03 | -- |
| $\Delta E_{3CT-1CT}$ [eV] | 0.10 | 0.10 | 0.10 | 0.10 | 0.10 | 0.10 | 0.10 | 0.10 | 0.15 | 0.15 | 0.14 | 0.14 | 0.08 | 0.08 | 0.08 | 0.08 | **0.13** |
| $f_{S1-S0}$ | 0.20 | 0.20 | 0.21 | 0.21 | 0.22 | 0.22 | 0.21 | 0.21 | 0.24 | 0.24 | 0.24 | 0.24 | 0.19 | 0.19 | 0.19 | 0.19 | **0.216** |
| $E_a$ [eV] | 0.23 | 0.23 | 0.23 | 0.23 | 0.23 | 0.23 | 0.23 | 0.23 | 0.25 | 0.25 | 0.25 | 0.25 | 0.22 | 0.22 | 0.22 | 0.22 | -- |
| $\mu$ [%] | 0.8 | 3.3 | 1.1 | 1.1 | 7.2 | 1.5 | 1.6 | 5.0 | 12.1 | 8.3 | 27.5 | 27.8 | 1.0 | 0.8 | 0.4 | 0.4 | -- |
| $k_{rISC}$ [10$^4$ s$^{-1}$] | 1.7 | 1.8 | 1.6 | 1.8 | 1.8 | 1.7 | 1.7 | 1.9 | 0.0 | 0.0 | 0.0 | 0.0 | 0.0 | 0.0 | 0.0 | 0.0 | **0.40** |
| | | | | | | | | | | | | | | | | | |
| $\theta_L$ | 16.2 | -16.1 | -18.0 | 17.8 | 17.8 | -17.9 | -16.3 | 16.8 | 17.6 | -17.7 | -15.1 | 15.1 | 17.2 | -17.1 | -18.2 | 18.2 | |
| $\theta_A$ | -77.5 | 77.5 | -77.3 | 77.2 | -63.5 | 63.5 | -63.3 | 63.4 | -68.5 | 68.5 | -68.3 | 68.3 | -78.4 | 78.2 | -78.9 | -68.7 | |
| $\theta_B$ | 63.3 | -63.2 | 63.1 | -63.2 | 77.3 | -77.4 | 77.1 | -77.1 | -68.4 | 68.3 | -68.3 | 68.3 | -78.1 | 78.2 | -78.4 | 78.4 | |

**3Br - rotamers**

| | 1 | 2 | 3 | 4 | 5 | 6 | 7 | 8 | 9 | 10 | 11 | 12 | 13 | 14 | 15 | 16 | 17 | 18 | 19 | 20 | 21 | 22 | 23 | 24 | 25 | 26 | 27 | 28 | 29 | 30 | 31 | 32 | $X^a$ |
|---|---|---|---|---|---|---|---|---|---|---|---|---|---|---|---|---|---|---|---|---|---|---|---|---|---|---|---|---|---|---|---|---|---|
| $SOC_{T1-S1}$ [cm$^{-1}$] | 3.45 | 3.50 | 3.47 | 3.48 | 3.19 | 3.18 | 3.11 | 3.11 | 2.35 | 2.35 | 2.36 | 2.31 | 2.15 | 2.14 | 2.15 | 2.14 | 0.88 | 0.88 | 0.87 | 0.87 | 0.85 | 0.85 | 0.84 | 0.84 | 1.56 | 1.48 | 1.46 | 1.46 | 0.68 | 0.69 | 0.61 | 0.58 | -- |
| $\Delta E_{3CT-1CT}$ [eV] | 0.18 | 0.18 | 0.18 | 0.18 | 0.18 | 0.18 | 0.18 | 0.18 | 0.24 | 0.24 | 0.24 | 0.24 | 0.23 | 0.23 | 0.23 | 0.23 | 0.14 | 0.14 | 0.14 | 0.14 | 0.14 | 0.14 | 0.14 | 0.14 | 0.20 | 0.20 | 0.20 | 0.20 | 0.20 | 0.20 | 0.20 | 0.20 | **0.20** |
| $f_{S1-S0}$ | 0.14 | 0.14 | 0.14 | 0.14 | 0.14 | 0.14 | 0.14 | 0.14 | 0.19 | 0.19 | 0.18 | 0.19 | 0.18 | 0.18 | 0.18 | 0.18 | 0.11 | 0.11 | 0.11 | 0.11 | 0.11 | 0.11 | 0.11 | 0.11 | 0.15 | 0.15 | 0.15 | 0.15 | 0.15 | 0.15 | 0.15 | 0.15 | **0.118** |
| $E_a$ [eV] | 0.28 | 0.28 | 0.28 | 0.28 | 0.28 | 0.28 | 0.28 | 0.28 | 0.32 | 0.32 | 0.32 | 0.32 | 0.31 | 0.32 | 0.31 | 0.31 | 0.25 | 0.25 | 0.25 | 0.25 | 0.25 | 0.25 | 0.25 | 0.25 | 0.29 | 0.29 | 0.29 | 0.29 | 0.29 | 0.29 | 0.29 | 0.29 | -- |
| $\mu$ [%] | 6.90 | 0.92 | 2.12 | 1.97 | 1.12 | 0.95 | 2.49 | 2.67 | 2.18 | 2.18 | 3.86 | 4.14 | 4.63 | 4.61 | 14.68 | 2.94 | 0.41 | 0.46 | 0.74 | 0.67 | 0.56 | 1.96 | 0.70 | 0.65 | 4.13 | 3.48 | 3.53 | 3.57 | 5.66 | 10.15 | 2.73 | 2.24 | -- |
| $k_{rISC}$ [10$^4$ s$^{-1}$] | 8.0 | 8.2 | 8.0 | 8.0 | 7.1 | 7.1 | 7.2 | 7.1 | 0.9 | 0.9 | 1.0 | 1.0 | 0.8 | 0.8 | 0.8 | 0.8 | 1.5 | 1.6 | 1.4 | 1.5 | 1.5 | 1.5 | 1.5 | 1.5 | 1.0 | 0.9 | 0.9 | 1.0 | 0.2 | 0.2 | 0.2 | 0.1 | **2.09** |
| | | | | | | | | | | | | | | | | | | | | | | | | | | | | | | | | | |
| $\theta_L$ | 18.1 | -18.2 | 17.5 | -17.5 | -16.9 | 16.9 | -17.3 | 17.3 | -16.6 | 16.6 | -17.7 | 17.8 | 15.5 | -15.5 | 15.7 | -15.6 | 19.5 | -19.7 | 17.5 | -17.4 | -18.0 | 18.0 | -18.8 | 18.8 | 16.1 | -15.8 | 14.5 | -14.3 | -17.7 | 17.6 | -19.0 | 18.9 | |
| $\theta_A$ | -71.0 | 71.0 | 61.2 | -61.2 | 60.9 | -60.9 | -71.5 | 71.5 | 77.8 | -77.8 | 77.8 | -77.5 | 77.9 | -77.9 | 78.0 | -77.9 | 76.5 | -76.4 | -83.5 | -61.8 | 75.9 | -75.9 | 61.0 | -61.0 | 75.4 | -75.3 | -75.8 | 75.9 | 75.1 | -75.1 | 74.8 | 76.6 | |
| $\theta_B$ | 61.4 | -61.3 | -70.9 | 70.9 | -71.4 | 71.4 | 60.9 | -60.9 | 73.6 | -73.6 | 73.6 | -73.6 | 74.0 | -74.0 | 74.0 | -74.0 | 61.7 | -61.7 | 76.8 | -76.7 | 60.8 | -60.8 | 75.5 | -75.5 | -75.7 | 75.7 | 75.2 | -75.1 | -76.2 | 76.3 | -76.6 | -74.8 | |

$^a$ – statistical mean values (weighted using Boltzmann distribution law - equation S2);

$SOC_{T1-S1}$ [cm$^{-1}$] – SOC constant value for $^3CT \rightarrow ^1CT$ transition;

$\Delta E_{3CT-1CT}$ [eV] – Energy gap between $^3CT$ and $^1CT$ excited states;

$f_{S1-S0}$ – oscillator strength;

$E_a$ [eV] – Activation energy;

$\mu$ [%] – relative contribution estimated using Boltzmann distribution law - equation S2);

$k_{rISC}$ [10$^4$ s$^{-1}$] – calculated rate constant for $^3CT \rightarrow ^1CT$ transition.

$\theta_L$ $\theta_A$ $\theta_B$ – dihedral angles (**Figure 3**)

**Calculations of the $^3$LE→$^1$CT rate constants.** To verify whether $^3$LE→$^1$CT channel has an impact on rISC, we performed theoretical calculations of its rate constants ($k_{3LE-1CT}$) using Marcus-Hush equation (S1) and experimental $\Delta E_{3LE-1CT}$ values. Since we consider two triplet states from which rISC is potentially possible, at first, we estimated relative population of these levels using Boltzmann distribution law:

$$\chi_i[\%] = \frac{\exp\left(-\frac{\Delta E_i}{k_B T}\right)}{\sum_{i=1}^{N} \exp\left(-\frac{\Delta E_i}{k_B T}\right)}, \tag{S3}$$

where $\Delta E_i$ denotes the energy difference between lowest triplet state ($T_1$) and respective triplet state ($T_i$):

$$\Delta E_i = (T_i - T_1), \tag{S4}$$

$$a_i = \exp\left(-\frac{(T_i - T_1)}{k_B T}\right). \tag{S5}$$

**Table S3.** Theoretical constant rates $k_{3LE-1CT}$ with determined population of lowest triplet excited states of emitters.

| Alignment of triplet excited states: | | | | | | CBP 10%<br>$T_2 = {}^3$**LE(A)**<br>$T_1 = {}^3$**CT** | | | |
| --- | --- | --- | --- | --- | --- | --- | --- | --- | --- |
| | | | | | | $^3$**LE(A)** | $^3$**CT** | | |
| | $T_1$ | $T_2$ | $\Delta E_{T2-T1}$ | $a_1$ | $a_2$ | $\chi_{3LE(A)}$ | $\chi_{3CT}$ | $k_{3LE-1CT}$ | $\chi_{3LE(A)}k_{3LE-1CT}$ |
| | [eV] | [eV] | [eV] | | | [%] | [%] | [$10^4$ s$^{-1}$] | [$10^4$ s$^{-1}$] |
| **H** | 2.03 | 2.25 | 0.22 | 1 | 0.0003 | 0.03 | 99.97 | 186.2 | **0.04** |
| **1Br** | 2.08 | 2.25 | 0.17 | 1 | 0.0018 | 0.18 | 99.82 | 24.4 | **0.03** |
| **2Br** | 2.11 | 2.25 | 0.14 | 1 | 0.0070 | 0.70 | 99.30 | 1.1 | **0.01** |
| **3Br** | 2.16 | 2.25 | 0.09 | 1 | 0.0281 | 2.92 | 97.08 | 3.8 | **0.10** |

From the results included in Table S3, it can be seen, that population of triplet states is strongly dominated by $^3$CT state due to large difference in energies between $^3$CT and $^3$LE levels.

Next, values of $k_{3LE-1CT}$ for each emitter were calculated just as $k_{3CT-1CT}$, taking into account population of $^3$LE state $\chi_{3LE(A)}$. Results are presented in **Table S3** and **Figure 4.**

Since theoretical predictions of rISC constant rates based on exclusively $^3$LE-$^1$CT channel did not showed a good correlation with experimental values, we conclude that $^3$LE-$^1$CT channel has not considerable impact on rISC in most of the cases except for the rotamers with very low rates of $^3$CT-$^1$CT transition as **2Br**-*anti* ones.

**³CT-¹CT orbital moment change**

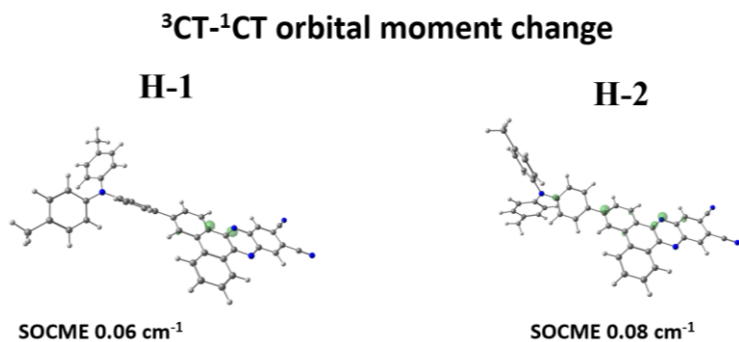H-1

H-2

SOCME 0.06 cm⁻¹

SOCME 0.08 cm⁻¹

**Figure S7**. Differences in the orbital transition moment of **H** rotamers. *note that contour value is 0.01 (high)*
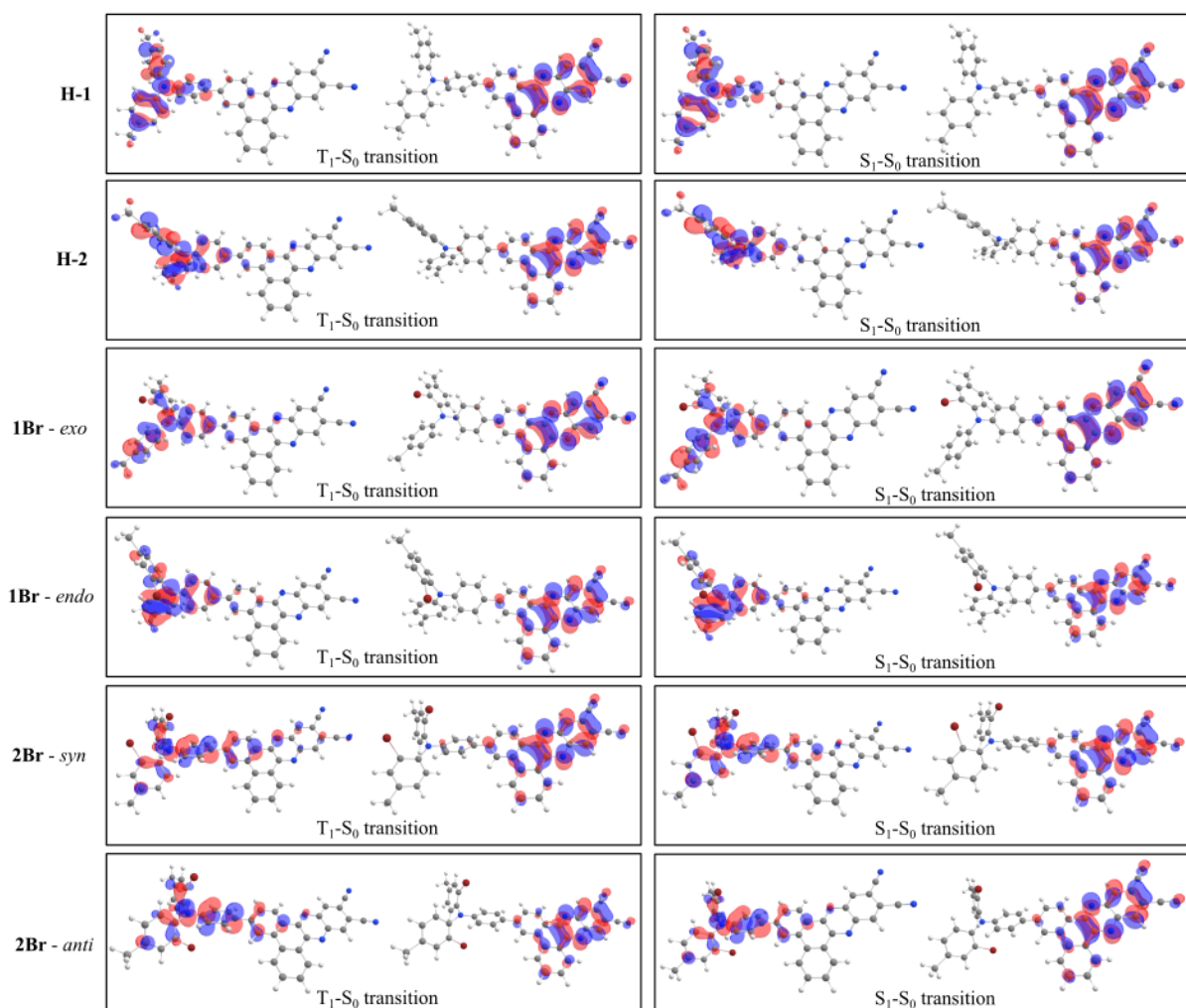


**Figure S8.** Natural transition orbitals for the $S_1$-$S_0$ and $T_1$-$S_0$ transitions for selected **H, 1Br** and **2Br** rotamers. NTO indicate almost negligible role of bromine atoms in the electronic transitions.
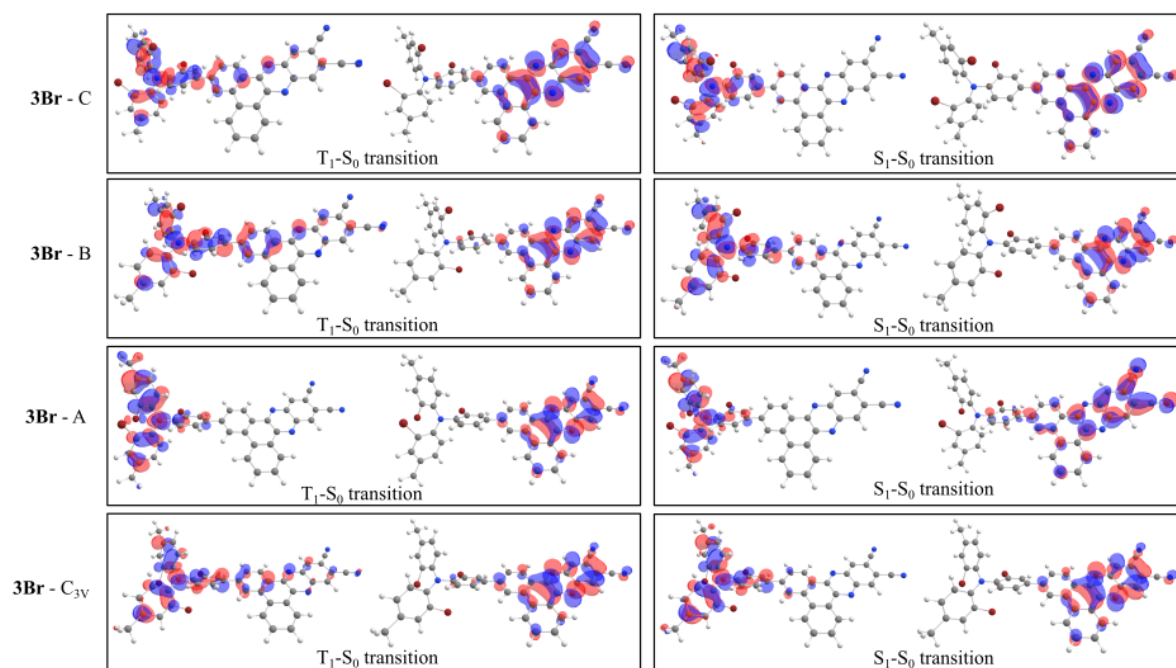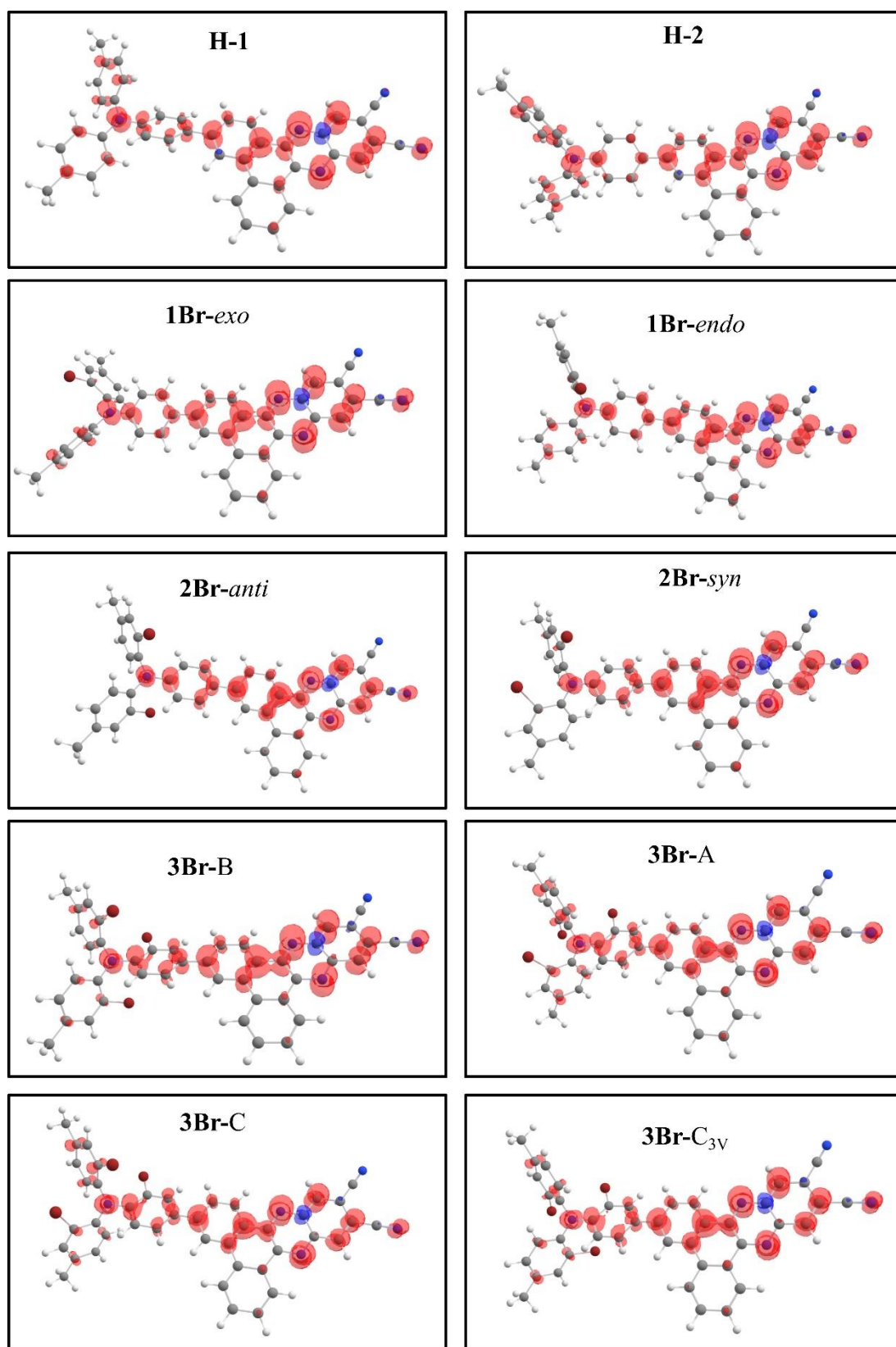
**Figure S9.** Natural transition orbitals for the $S_1$-$S_0$ and $T_1$-$S_0$ transitions for selected **3Br** rotamers. NTO indicate almost negligible role of bromine atoms in the electronic transitions.

**H-1**

**H-2**

**1Br-***exo*

**1Br-***endo*

**2Br-***anti*

**2Br-***syn*

**3Br-**B

**3Br-**A

**3Br-**C

**3Br-**C$_{3V}$

**Figure S10**. Triplet spin density distribution (TSDD) maps

# Section S3: NMR spectra of target emitters

$^1$H NMR spectrum of 3-(4-((2-bromo-4-methylphenyl)(*p*-tolyl)amino)phenyl)-dibenzo[*a,c*] phenazine-11,12-dicarbonitrile (**1Br**) in CDCl$_3$
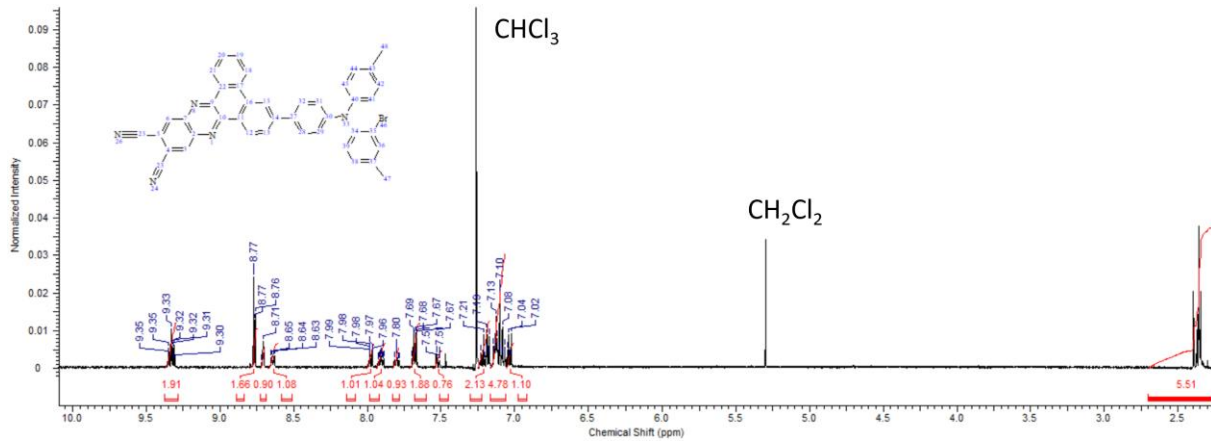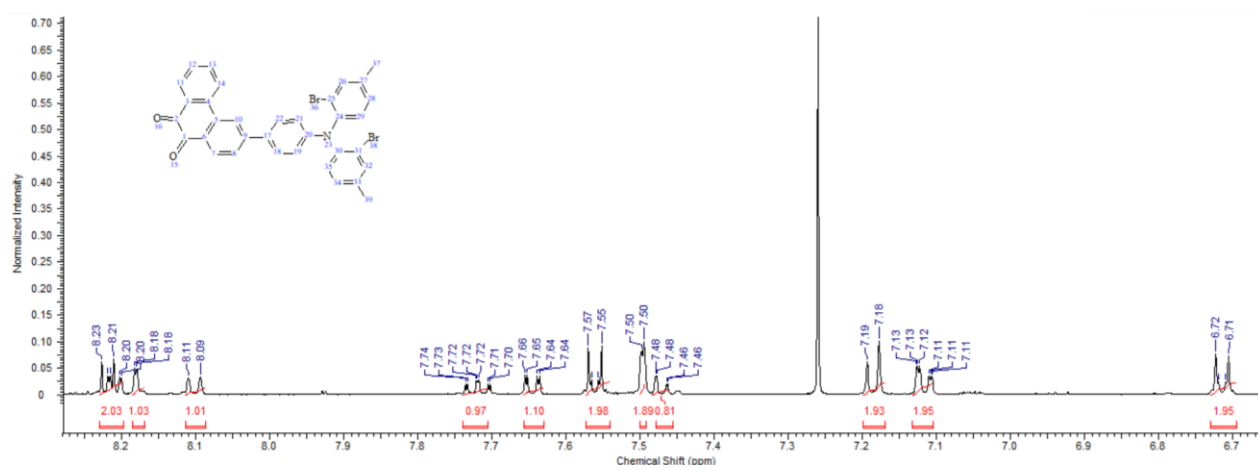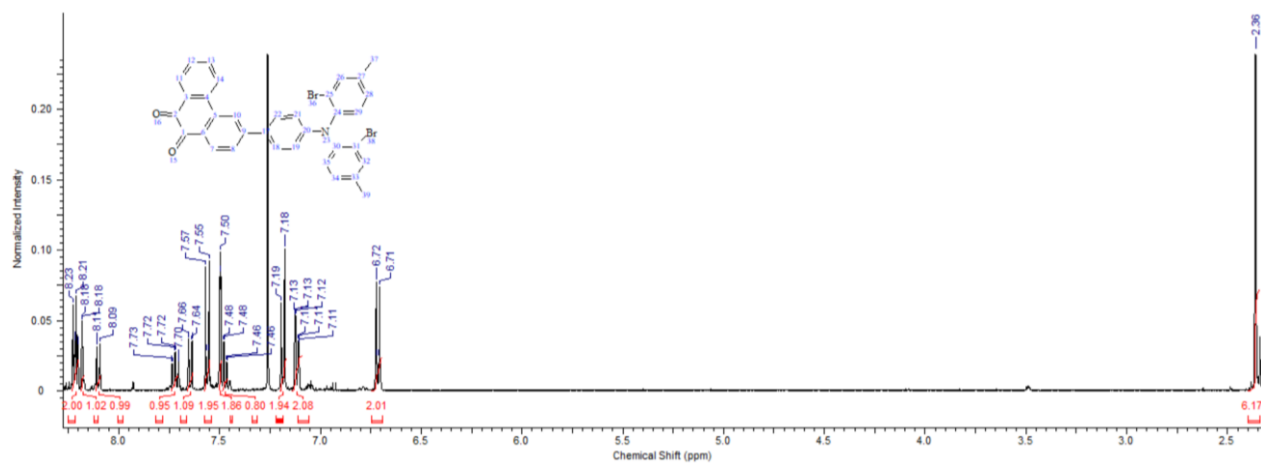
<sup>1</sup>H NMR spectrum of 3-(4-(bis(2-bromo-4-methylphenyl)amino)phenyl)dibenzo[*a,c*] phenazine-11,12-dicarbonitrile (**2Br**) in CDCl<sub>3</sub>.
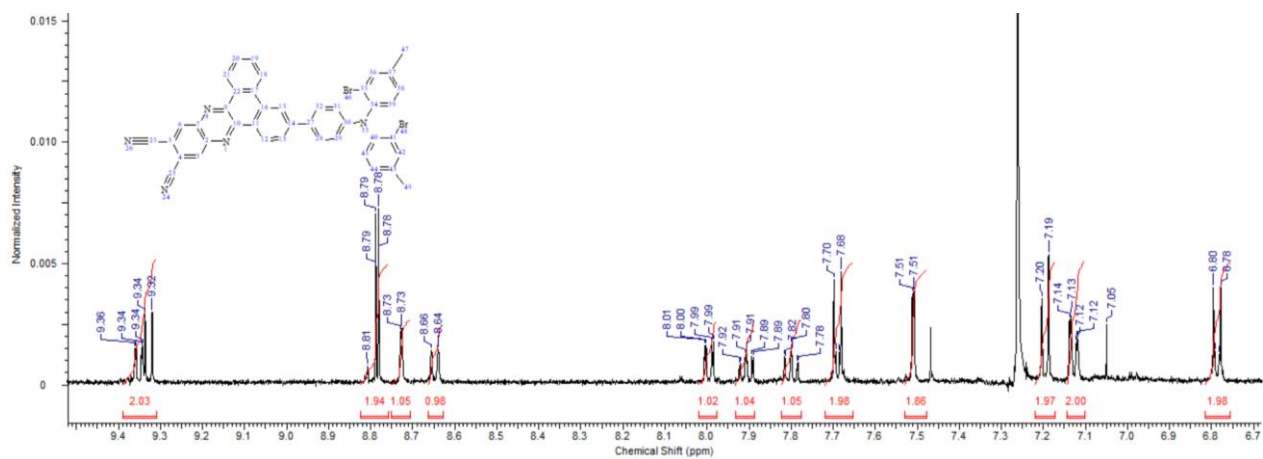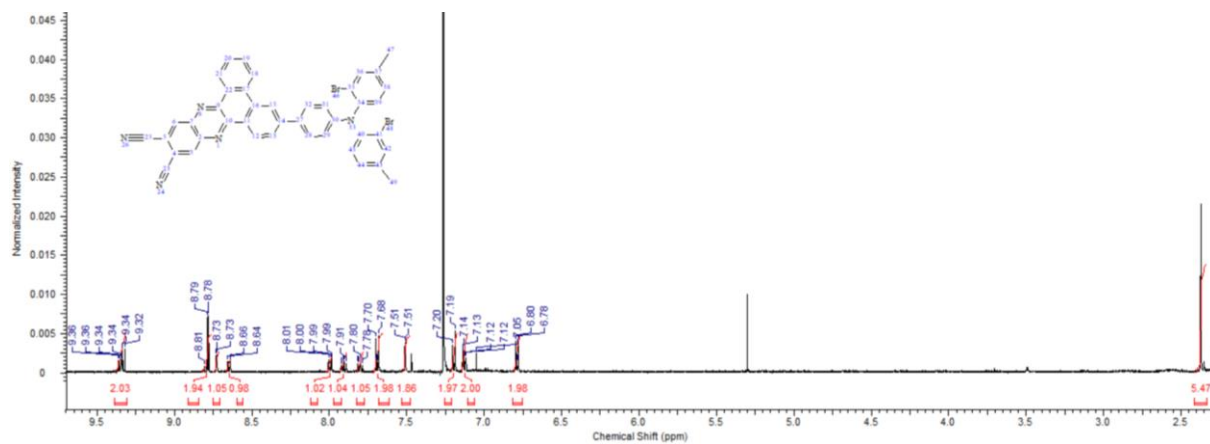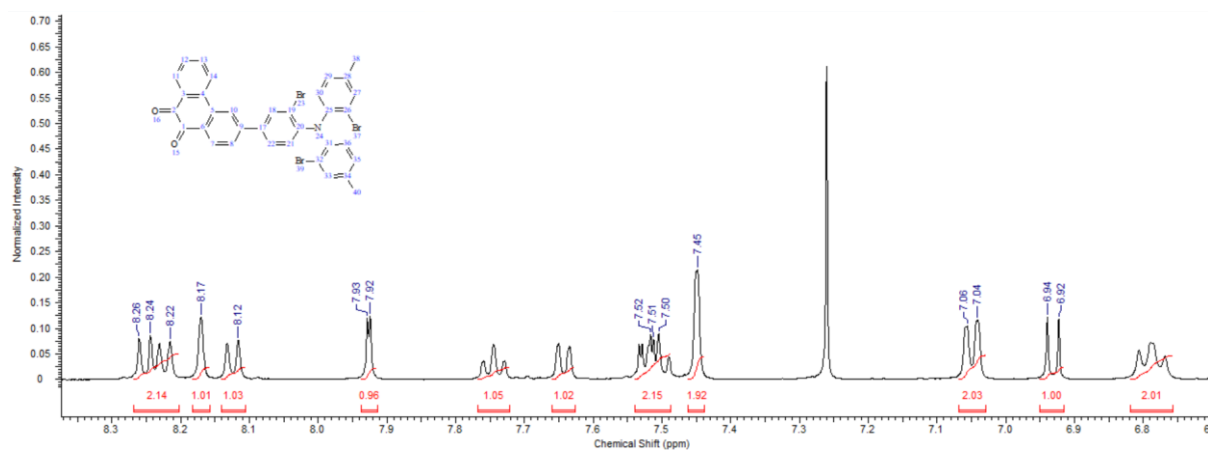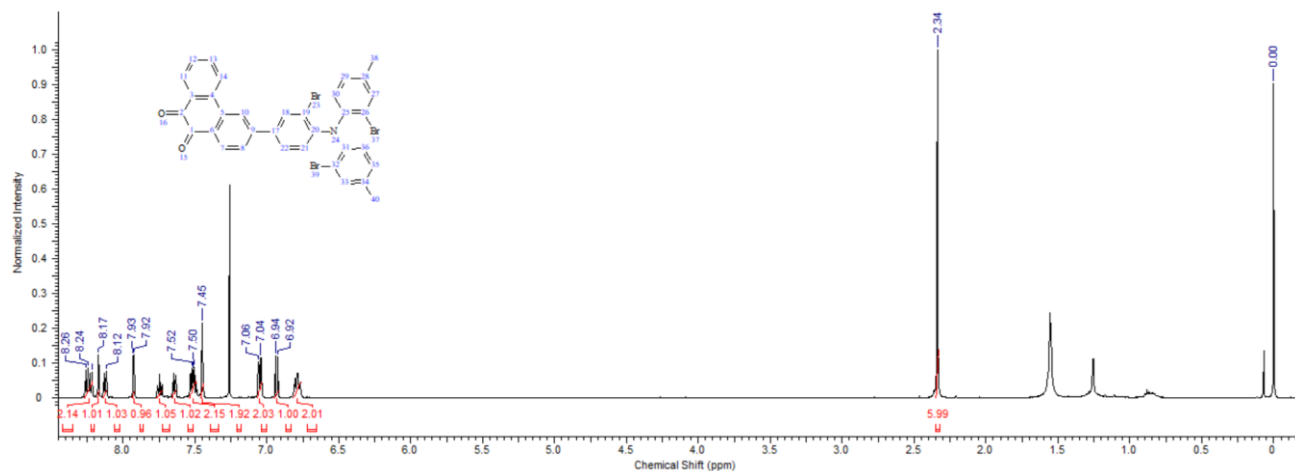
<sup>1</sup>H NMR spectrum of 3-(4-(bis(2-bromo-4-methylphenyl)amino)phenyl)dibenzo[*a,c*]phenazine-11,12-dicarbonitrile (**3Br**) in CDCl₃.
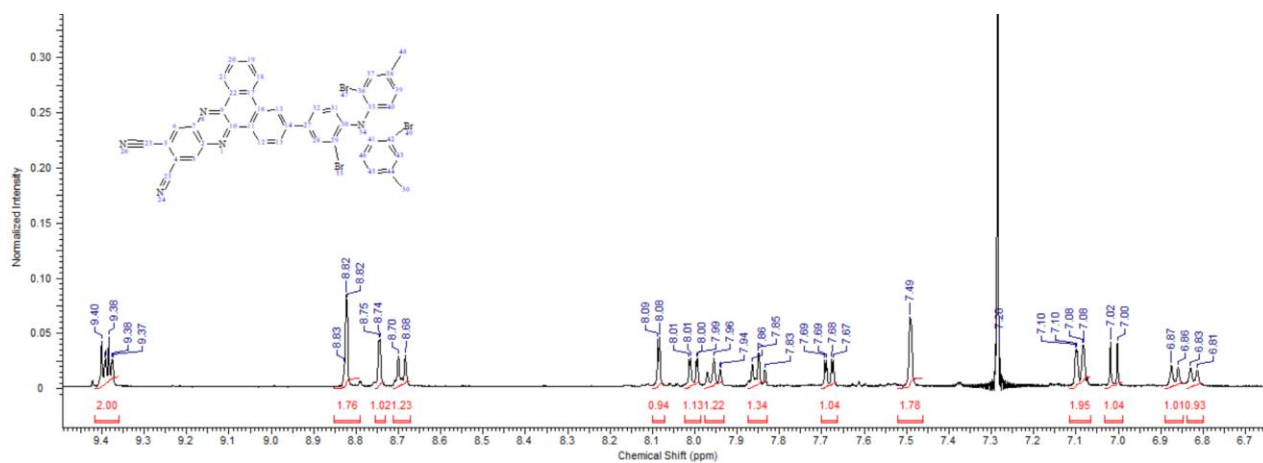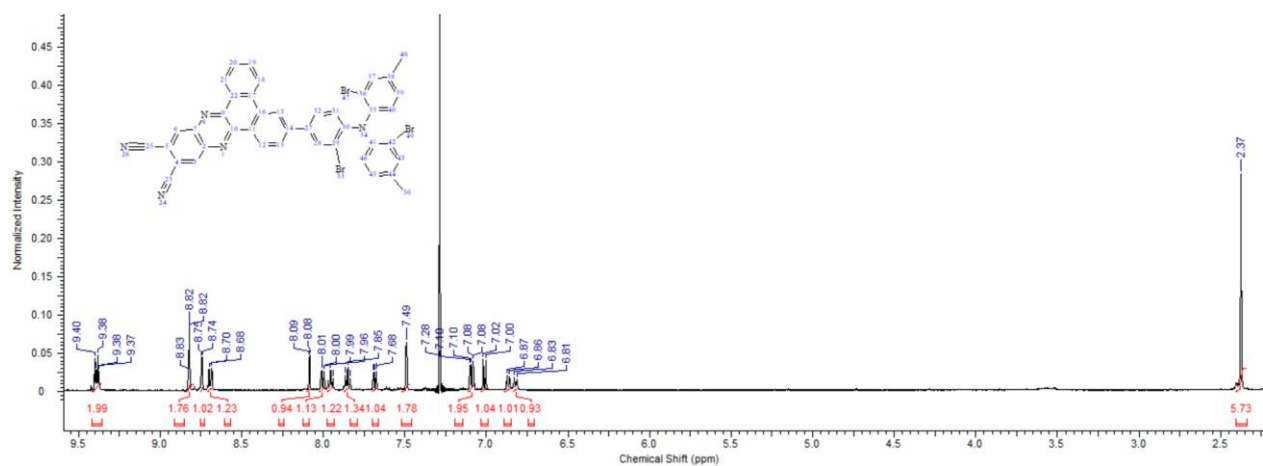
<sup>1</sup>H NMR spectrum of 3-(4-(bis(2-bromo-4-methylphenyl)amino)phenyl)phenanthrene-9,10-dione (**2**) in CDCl<sub>3</sub>.

<sup>1</sup>H NMR spectrum of 3-(4-(bis(2-bromo-4-methylphenyl)amino)-3-bromophenyl)-phenanthrene-9,10-dione (**3**) in CDCl<sub>3</sub>

## Section S4: Determination of photophysical parameters

PL decay curves (presented in **Figures 2F** and **S4**) were fitted with the multiexponential equation:

$$I(t) = A_0 + \sum_{i=1}^{n} A_i \exp\left(-{}^t/_{\tau_i}\right) \tag{S6}$$

where $A_i$ is the pre-exponential factor, $\tau_i$ is the decay time and $I(t)$ is emission intensity. Average lifetimes of prompt ($\tau_{PF}$) and delayed fluorescence ($\tau_{DF}$) were determined using the following formula:

$$\tau_{PF}, \tau_{DF} = \sum_{i=1}^{n} f_i \tau_i, \tag{S7}$$

where $f_i$ is fractional contribution of $i$-th component expressed as:

$$f_i = \frac{A_i \tau_i}{\sum_{i=1}^{n} A_i \tau_i} \tag{S8}$$

The ratio of DF and PF quantum yields $\varphi_{DF}/\varphi_{PF}$ was determined as follows:

$$\frac{\varphi_{DF}}{\varphi_{PF}} = \frac{\sum_{i=1}^{n} \tau_{DF(i)} A_{DF(i)}}{\sum_{j=1}^{n} \tau_{PF(j)} A_{PF(j)}} \tag{S9}$$

where $A_{DF(i)}$ and $A_{PF(j)}$ is the pre-exponential factor of delayed and prompt fluorescence component, respectively; $\tau_{DF(i)}$ and $\tau_{PF(j)}$ is the lifetime of delayed and prompt fluorescence component, respectively. The rate constants of radiative ($k_r$) and nonradiative ($k_{nr}$) decay and intersystem crossing ($k_{ISC}$) are given by equations[S2]:

$$k_r = \frac{\varphi_{PF}}{\tau_{PF}}, \tag{S10}$$

$$k_{ISC} = \frac{\varphi_{DF}}{\varphi \, \tau_{PF}}, \tag{S11}$$

$$k_{nr} = \frac{1}{\tau_{PF}} - (k_r + k_{ISC}). \tag{S12}$$

where $\varphi$ is PLQY ($\varphi_{DF} + \varphi_{PF}$). Further, the quantum yields for ISC and rISC were calculated as

$$\varphi_{ISC} = k_{ISC} \tau_{PF}, \tag{S13}$$

$$\varphi_{rISC} = \frac{1 - \varphi_{PF}/\varphi}{\varphi_{ISC}}. \tag{S14}$$

Finally, the rate constant of rISC ($k_{rISC}$) was calculated as

$$k_{rISC} = \frac{\varphi_{rISC}}{\tau_{DF}} \left( \frac{\varphi}{\varphi_{PF}} \right). \tag{S15}$$

Thus obtained photophysical parameters are presented in **Table 2** (main text).

**References**

[S1] M. Mońka, I. E. Serdiuk, K. Kozakiewicz, E. Hoffman, J. Szumilas, A. Kubicki, S. Y. Park and P. Bojarski, *Mater. Chem. C*. 2022, **10**, 7925-7934.

[S2] Tao, Y.; Yuan, K.; Chen, T.; Xu, P.; Li, H.; Chen, R.; Zheng, C.; Zhang, L.; Huang, W. Thermally Activated Delayed Fluorescence Materials Towards the Breakthrough of Organoelectronics. *Adv. Mater.* **2015**, *26*, 7931 – 7958.